DISSERTATION

# DETERMINATION OF THE INTERFACIAL ELECTRONIC STRUCTURE AND MORPHOLOGY OF ORGANIC SEMICONDUCTOR MATERIALS

Submitted by
Paul G. Schroeder
Department of Chemistry

In partial fulfillment of the requirements
for the degree of Doctor of Philosophy
Colorado State University
Fort Collins, Colorado
Spring 2002

COLORADO STATE UNIVERSITY

December 17, 2001

WE HEREBY RECOMMEND THAT THE DISSERTATION PREPARED UNDER OUR SUPERVISION BY PAUL G. SCHROEDER ENTITLED: DETERMINATION OF THE INTERFACIAL ELECTRONIC STRUCTURE AND MORPHOLOGY OF ORGANIC SEMICONDUCTOR MATERIALS, BE ACCEPTED AS FULFILLING IN PART REQUIREMENTS FOR THE DEGREE OF DOCTOR OF PHILOSOPHY.

Committee on Graduate Work

Elliot Bernstein

Nancy Levinger

Alan Van Orden

Siu Au Lee

Adviser – Bruce Parkinson

Department Head

## ABSTRACT OF DISSERTATION

## DETERMINATION OF THE INTERFACIAL ELECTRONIC STRUCTURE AND MORPHOLOGY OF ORGANIC SEMICONDUCTOR MATERIALS

Thin films of *p*-quaterphenyl, *p*-sexiphenyl, coronene, and pentacene were each deposited sequentially in multiple steps onto different substrates including highly oriented pyrolytic graphite (HOPG), $SnS_2$, and Au(111). The energy level offsets at the interfaces between each organic semiconductor film and the respective substrate were subsequently measured using a combination of X-ray and ultraviolet photoelectron spectroscopy (XPS, UPS) *in situ* after each growth step. The organic materials used have significantly delocalized molecular orbitals, and were chosen for their potential applications in organic semiconductor devices and that they allowed for more thorough analysis of the interface. HOPG and $SnS_2$ are layered materials that have nearly atomically flat van der Waals surfaces that could be cleaved in vacuum allowing for fundamental investigations of interfacial dipoles and the existence of band bending effects at the interfaces of organic materials. The gold substrate allowed for more applied studies into the contact interfaces used for organic thin film transistors.

The combined methods of UPS and XPS were used to more precisely determine the orbital offsets at the organic interfaces by separating out band bending, or final state screening related shifts, from the total work function measured with UPS. In addition, a method using low intensity XPS work function measurements was successfully developed to separate out sample charging artifacts from the true shifts.

Several of these systems, particularly those consisting of pentacene, were also characterized for the surface adsorption and film morphology using scanning tunneling microscopy (STM), atomic force microscopy (AFM), and temperature programmed desorption (TPD). The STM images revealed ordering of pentacene in several distinct unit cells with respect to the Au(111) surface. Different growth patterns of pentacene deposited on Au(111) and $SnS_2$ were observed based on the analysis of the ultra-violet photoelectron spectra and AFM.



Paul G. Schroeder
Department of Chemistry
Colorado State University
Fort Collins, CO 80523
Spring 2002

**Acknowledgments**

I would first like to express my gratitude to Professor R. Schlaf at University of South Florida (Department of Electrical Engineering) for his assistance with the evaluation and interpretation of the photoelectron spectra as well as many helpful discussions pertaining to this work. I would like to thank M.W. Nelson for his assisting with much of the instrumentation and laboratory setup. I would also like to thank C.B. France and J.B. Park for their assistance in many of the experiments presented in Chapters 3,4 and 5. J.C. Forsythe is acknowledged for his work on the instrumentation of the temperature programmed desorption. Prof. Bruce A. Parkinson and the Parkinson research group at Colorado State University are gratefully acknowledged for their support and for discussions pertaining to this work. Finally, I would like to thank my parents for their moral support throughout my time in graduate school. Partial support for this work under the Department of Energy contract (DE-F603-96ER14625) is also acknowledged.

## Table of Contents

## Index of Figures

**Index of Tables**

## List of Acronyms

AES: Auger electron spectroscopy
$Alq_3$: tris (8-hydroxyquinolinato) aluminum
BE: binding energy
CB: conduction band
CBM: conduction band maximum
ClInPc: chloroindium phthalocyanine
D.C.: direct current
DOS: density of states
EAR: electron affinity rule
eD: interface dipole
$E_F$: Fermi level energy
$Gaq_3$: tris (8-hydroxyquinolinato) gallium
HBEC: high binding energy cutoff
HOMO: highest occupied molecular orbital
HOPG: highly oriented pyrolytic graphite
ITO: indium tin oxide
KE: kinetic energy
LEED: low energy electron diffraction
LUMO: lowest unoccupied molecular orbital
MO: molecular orbital(s)
OFET: organic field effect transistors
OLED: organic light emitting diodes
OTFT: organic thin film transistors
*p*-4P: *para*-quaterphenyl
*p*-6P: *para*-sexiphenyl
PE: polarization energy
PES: photoelectron (*or photoemission*) spectroscopy
PIES: Penning ionization electron spectroscopy
PLED: polymer light emitting device
PPP: poly-paraphenylenes
PTCDA: 3,4,9,10-perylenetetracarboxylic-dianhydride
QCM: quartz crystal microbalance
RGA: residual gas analysis
SAM: scanning Auger microscopy
SE: secondary edge
STM: scanning tunneling microscopy

**Acronyms *continued...***

TMD: transition metal dichalcogenide
TPD: temperature programmed desorption
TPD: N,N'-diphenyl-N,N'-(3-methylphenyl)-1,1'-biphenyl-4,4'-diamine
UHV: ultra high vacuum
UV: ultraviolet
UPS: ultraviolet photoelectron spectroscopy
VB: valence band
VBM: valence band maximum
VDW: van der Waals
VL: vacuum level
VT-STM: Variable-Temperature scanning tunneling microscope
WF: workfunction
XPS: x-ray photoelectron spectroscopy
ZnPc: zinc phthalocyanine

## Objectives:

Establishing a fundamental understanding of the chemical, physical and morphological properties of organic semiconductor materials at the interface of metal, inorganic semiconductor, or organic semiconductor materials will enable improved efficiencies and performance of organic light emitting devices (OLEDs) and organic thin film transistors (OTFTs). While much research has been conducted on interfaces involving organic semiconductor materials, there still remain certain unresolved aspects.

The first issue is establishing a universally accepted method for measuring the charge injection barriers at these interfaces. This issue has been addressed extensively in the literature where much progress has been made [1-4]. One of the more common techniques for measuring the energy level offsets is ultraviolet photoelectron spectroscopy (UPS). In addition, it is well established that the assumption of vacuum level alignment at these interfaces, according to the electron affinity rule (EAR), is invalid [5,6]. A measurement of the interfacial dipole barrier is crucial to understanding the behavior of these systems, however we wish to establish an improved method for more accurately measuring the magnitude of the interface dipole barrier.

The issue of band bending in these systems has posed more of a challenge. Experiments have yielded results that support the existence of band bending in organic molecular solids [7-10] while others refute that notion [11-13]. Furthermore, there are

several phenomena including chemical reactions, sample charging artifacts, and polarization induced screening of remaining charges following photoemission, each of which can produce measurements that resemble band bending and complicate interpretation of the photoemission data. One of the objectives of this research is to assess the presence and effects of each of the phenomenon, and incorporate them into the evaluation procedure for determining the energy level alignment at such interfaces.

In this research, we use a combined method of ultraviolet photoelectron spectroscopy and x-ray photoelectron spectroscopy to measure the energy level alignment at several model interfaces of organic semiconductors and various substrates. We believe this to be an improvement over using UPS alone and allows the issues of interfacial dipoles and the validity of band bending in comparison to final state screening effects to be particularly addressed.

The morphology of organic films is of fundamental interest to surface science, but we also want to investigate the relevance of film morphology to the electronic behavior of organic semiconductors. The orientation of the organic molecules at an inorganic or metallic interface can affect the conductivity of the organic film, the magnitude of the charge injection barriers and interface dipole, as well as the types of electronic surface states that will be present [14,15]. Some of this research includes characterization of the surface adsorption and film morphology of pentacene thin films to further elucidate the

relationship between the molecular orientation with respect to the substrate and the electronic properties of the interface.

**References:**


[1] J. Ishii, K. Sugiyama, E. Ito, K. Seki, Adv. Mater. 11 (8) (1999) 605.

[2] G. Koller, R. I. R. Blyth, S. A. Sardar, F. P. Netzer, M. G. Ramsey, Appl. Phys. Lett. 76 (7) (2000) 927.

[3] A. Rajagopal, C. I. Wu, A. Kahn, J. Appl. Phys. 83 (5) (1998) 2649.

[4] K. Sugiyama, D. Yoshimura, T. Miyamae, T. Miyazaki, H. Ishii, Y. Ouchi, K. Seki, J. Appl. Phys. 85 (9) (1999) 4928.

[5] H. Ishii, K. Seki, IEEE trans. elect. devices 44 (8) (1997) 1295.

[6] H. Ishii, K. Sugiyama, D. Yoahimura, E. Ito, Y. Ouchi, K. Seki, IEEE J. Sel. Top. Quant. Elec. 4 (1) (1998) 24.

[7] R. Schlaf, P. G. Schroeder, M. W. Nelson, B. A. Parkinson, P. A. Lee, K. W. Nebesny, N. R. Armstrong, J. Appl. Phys. 86 (3) (1999) 1499.

[8] R. Schlaf, B. A. Parkinson, P. A. Lee, K. W. Nebesny, N. R. Armstrong, J. Phys. Chem. B 103 (15) (1999) 2984.

[9] Y. Park, V. Choong, E. Ettedgui, Y. Gao, B. R. Hsieh, T. Wehrmeister, K. Mullen, Appl. Phys. Lett. 69 (8) (1996) 1080.

[10] E. Ettedgui, H. Razafitrimo, K. T. Park, Y. Gao, B. R. Hsieh, J. Appl. Phys. 75 (11) (1994) 7526.

[11] I. G. Hill, A. J. Mäkinen, Z. H. Kafafi, Appl. Phys. Lett. 77 (12) (2000) 1825.

[12] E. Ito, H. Oji, N. Hayashi, H. Ishii, Y. Ouchi, K. Seki, Appl. Surf. Sci. 175-176 (2001) 407.

[13] D. Schlettwein, K. Hesse, N. E. Gruhn, P. A. Lee, K. W. Nebesny, N. R. Armstrong, J. Phys. Chem. B 105 (21) (2001) 4791.

[14] H. E. Katz, Z. Bao, J. Phys. Chem. B 104 (4) (2000) 671.

[15] M. Kasaya, H. Tabata, T. Kawai, Surf. Sci. 400 (1-3) (1998) 367.

# Chapter 1: Introduction to Organic-Based Electronic Materials

## 1.1 Drive for Organic Electronic Materials

Organic and polymer based thin films are emerging as a class of electronic materials with applications for use in light emitting devices and thin film transistors. Several distinct advantages offered by organic based devices include a high degree of efficiency through energy level variation, a wide range of colors through the use of different compounds, ease of fabrication, and low cost processing. Organic semiconductors present opportunities for new types of industrial or high-tech applications including organic thin film transistors (OTFTs) and organic light emitting devices (OLEDs). The OLEDs could be used in flat panel displays for multimedia applications, automobile in-dash displays, or home appliances. When comparing organic 'solid-state' displays to liquid crystal displays, the solid-state devices offer a wider viewing angle,

have sharper color contrast, faster pixel response time, and have a greater potential for scaling up to large displays. There are already several devices where OLEDs are used in the display, namely cellular telephones and automobile stereos. The OTFTs have potential in thin film organic solar cells, pixel drivers for the OLEDs, or "smart" cards.

Electroluminescence in organic semiconductors has been known for some time [1,2], but the efficiency of organic light emitting devices was not increased significantly until Tang and VanSlyke used *tris*-(8-hydroxyquinoline) aluminum ($Alq_3$) as the luminescent material and N,N'-diphenyl-N,N'-(3-methylphenyl)-1,1'-biphenyl-4,4'-diamine (TPD) as the hole transporter to create an organic heterojunction [3]. The utilization of the organic heterojunction was the significant step toward fabricating an effective device. Previous electroluminescence attempts used only single organic layers sandwiched between two metallic electrodes, but the light output was extremely low. This was attributed to the majority of the carriers (electrons or holes) migrating to the opposite electrode instead of recombining with an opposite carrier in the luminescent material. Two organic layers, with a potential energy barrier at the organic/organic interface, maximizes the rectifying behavior of the heterojunction allowing for an increased probability of radiative recombination in the luminescent material. Since this revelation, organic semiconductors and conjugated polymers have been extensively explored as possibilities for OLEDs or polymer light emitting devices (PLEDs).

A diagram of the energy levels in a simple bilayer OLED is shown in Fig. 1.1.A. A low work function metal cathode such as Al or Mg:Ag alloy, is used to inject electrons into the lowest unoccupied molecular orbital (LUMO) of the organic electroluminescent layer. A high work function transparent anode such as indium tin oxide (ITO) is used to inject holes (electron vacancies) into the highest occupied molecular orbital (HOMO) of the hole transport material. Both the electron and hole transport layers typically have a thickness on the order of several hundred nanometers. Each of these carriers migrates through their respective transport medium toward the opposite electrode. The holes are then injected into the HOMO of the electroluminescent layer. The electrons however, have a reduced probability of being injected into the hole transport layer since the choice of hole transport materials is partly chosen so that its LUMO is at a higher energy than the LUMO of the electron transport material. This energy barrier at the organic/organic heterojunction helps confine both the electrons and holes in the luminescent material. An electron-hole pair then has a chance of being confined to an individual molecule creating an electronically excited state molecule. With the increased probability of creating the excited state molecule, there is an increased probability for radiative recombination.

A diagram of the construction of a simple bilayer device as proposed by Tang and VanSlyke [3] using $Alq_3$ and TPD as the electron transport/luminescent and hole transport materials respectively is shown in Fig. 1.1.B. Numerous modifications and additions to this basic design have been proposed extensively in the literature including:

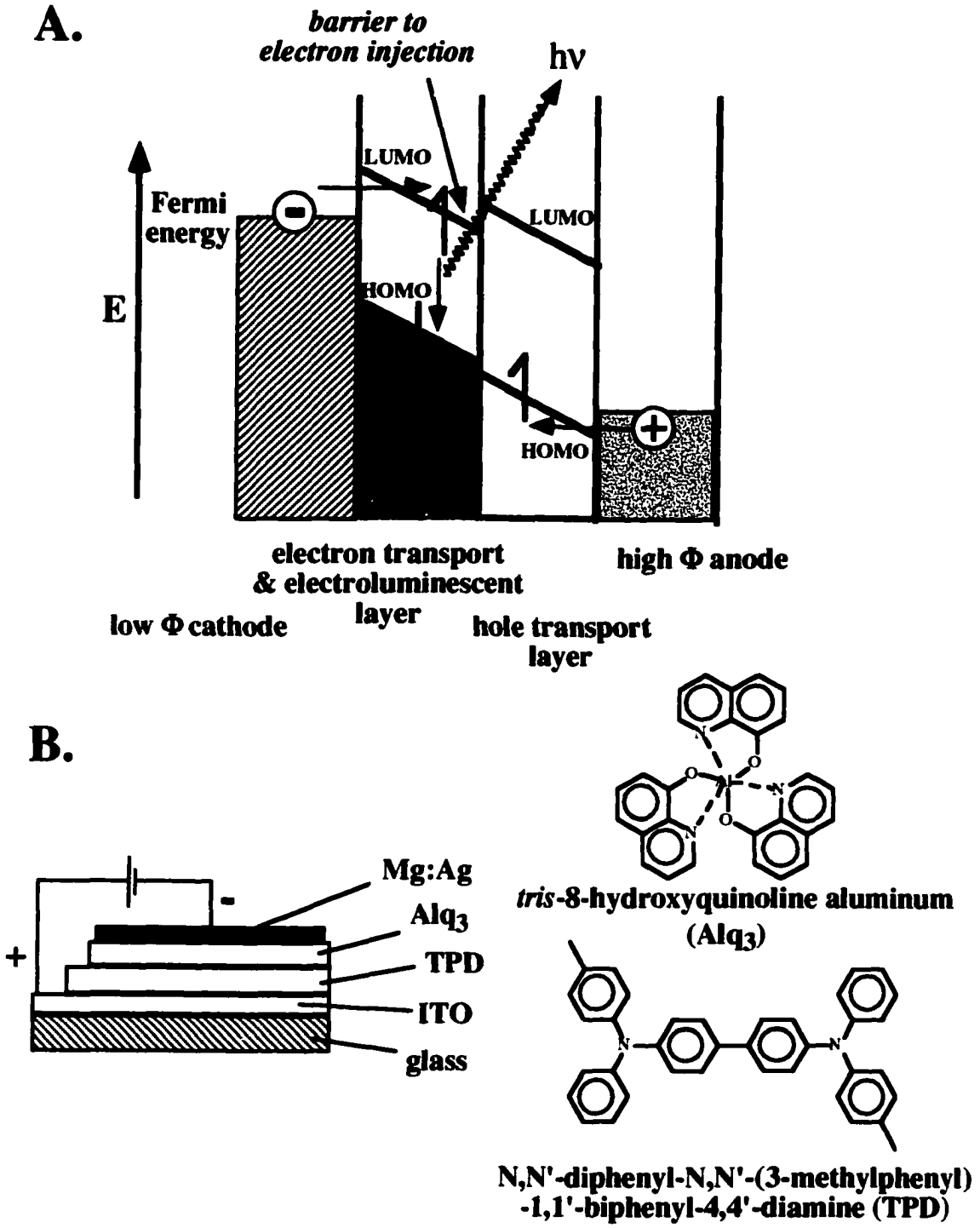


**Fig. 1.1:** **A.** Diagram of the energy levels for a simple bilayer organic light emitting device (OLED). **B.** Diagram of the construction of an experimental OLED originally proposed by Tang and VanSlyke (1987) using the electron transport and luminescent molecule $Alq_3$ and the hole transport molecule TPD.

using different electron transport/luminescent materials [4-9], stacking multiple layers of organic materials for improved device engineering [10-17], doping of varied colored dyes into the electron transport layer [18-24], and varying the hole transport material [25-31]. The aforementioned references are only representative of the extensive literature on OLEDs. In addition, there has been extensive research on polymer based LEDs [32-42], however the remainder of this work will be focused on small molecule devices.

Organic thin film transistors (OTFT) are another system where organic semiconductor materials are being investigated [43-53]. An example of an experimental OTFT device is diagrammed in Fig. 1.2.A. This is a simple organic field effect transistor where the organic film is vapor deposited or spin coated onto a heavily doped Si wafer with a ~300 nm oxide layer. Gold source and drain contacts are evaporated on top of the organic film. Under device operation, a negative potential is applied to the source contact and a positive potential to the drain contact. The Si substrate acts as the gate electrode, controlling current flow through the organic film by increasing or decreasing the gate bias [54]. The interfaces between the source or drain contacts and the organic semiconductor film are crucial parameters that affect the charge injection rates and voltage onsets of these types of devices. Figure 1.2.B is a detailed energy level diagram of a Schottky contact [55], that is formed when a metal and semiconductor are brought into contact. In the above OTFT device, the Schottky contact would occur at the interface between the organic semiconductor film and the gold contacts.

**A.**

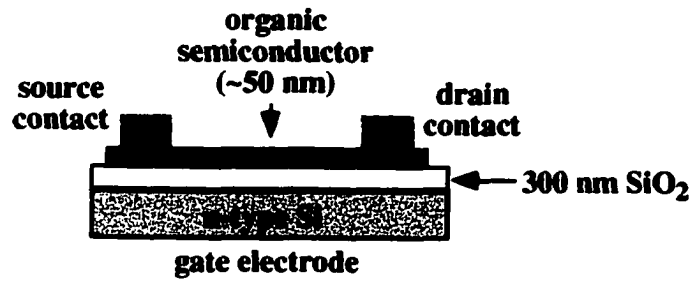


**B.**

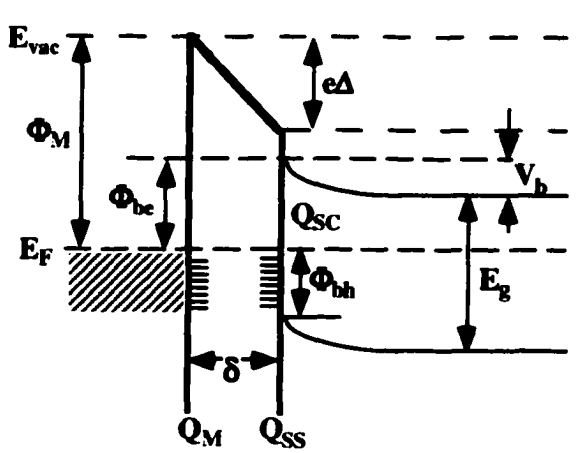


$\Phi_M$ = work function of metal
$\Phi_{be}$ = barrier height for electron injection
$\Phi_{bh}$ = barrier height for hole injection
$E_{vac}$ = energy level of the vacuum
$E_F$ = Fermi energy level
$e\Delta$ = interface dipole potential
$V_b$ = band bending/built in potential
$E_g$ = band gap of semiconductor
$Q_{SC}$ = space-charge density in semiconductor
$Q_M$ = surface charge density on metal
$Q_{SS}$ = surface-state density on semiconductor
$\delta$ = thickness of interfacial layer

**Fig. 1.2** **A.** Diagram of the construction of an experimental organic thin film field effect transistor (FET). **B.** Detailed energy level diagram of a Schottky contact. For the organic thin film transistor, this diagram would be relevant for the interface between the organic semiconductor and the metallic source or drain contacts. *Energy level diagram based on diagram in M. Pope and C.E. Swenberg (1999).*

Figure 1.2.B diagrams the full effects of surface states, interface dipole potentials, and band bending on the interface between a semiconductor and a metal. These effects will be discussed in further detail below.

Literally hundreds of organic and organometallic molecules have been studied for OLED and OTFT applications. A sampling of these molecules, primarily those molecules studied in detail in subsequent chapters, is shown in Fig. 1.3. The one feature that all organic electronic materials possess is a conjugated $\pi$-electron system at the core of the molecule. This delocalization of electron orbitals gives the molecules the ability to support positive or negative carriers, often leading to relatively high mobilities in the film or single crystal. The molecules *p*-sexiphenyl and *p*-quaterphenyl are both poly-*para*-phenylenes that are relatively efficient electron transport materials that have been investigated in the literature [56-63]. Coronene and 3,4,9,10-perylenetetracarboxylic dianhydride (PTCDA) are also transport materials that have also been investigated [63-70]. Pentacene is an example of an organic thin film transistor material that has been of considerable recent interest [46,53,71,72]. Metal quinolates and other organometallic compounds have been explored for their electron transport and luminescent properties [31].

Conductive polymers are also of interest for these types of devices, however there are many difficulties in measuring the energy level alignment at interfaces with polymer

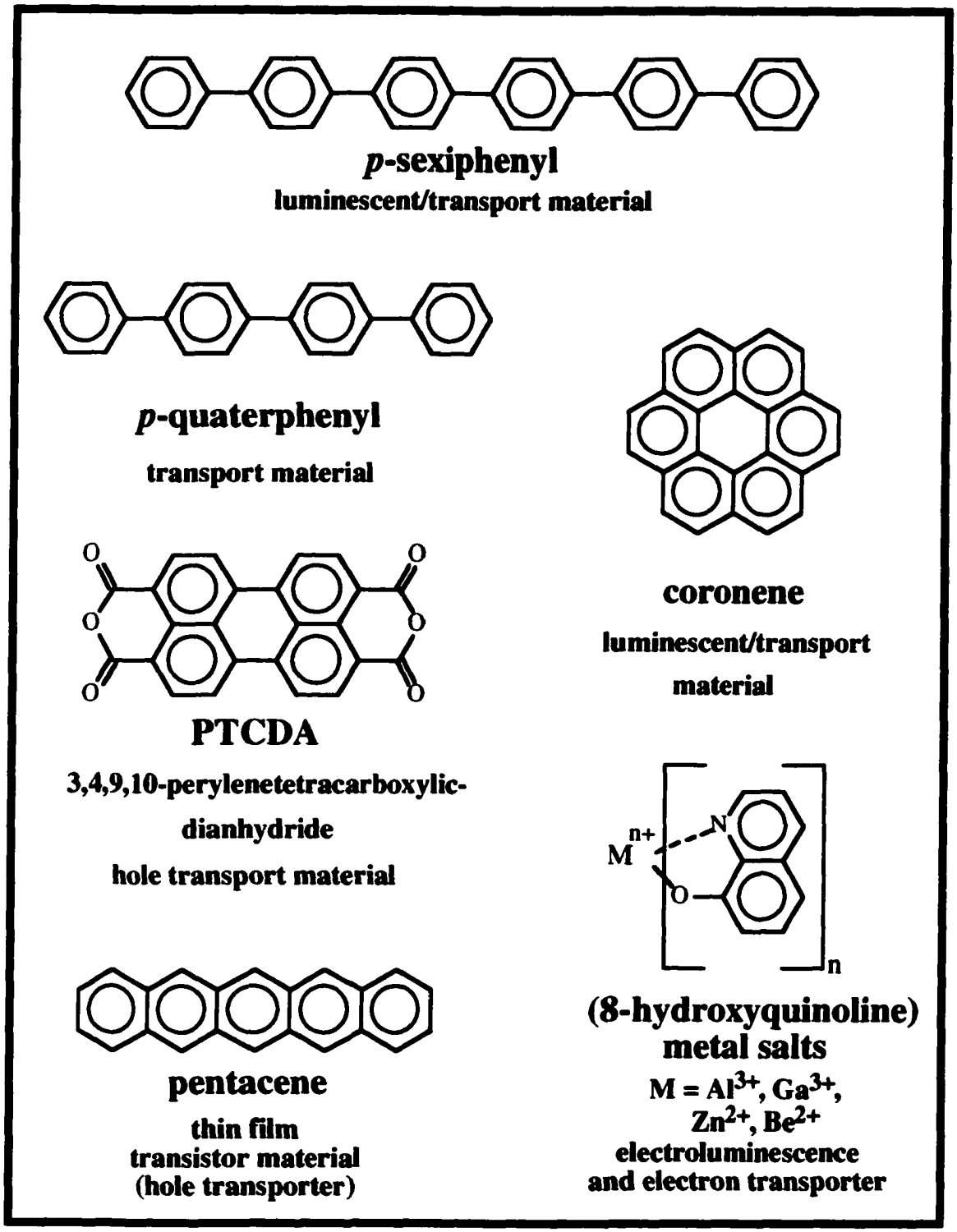


**Fig. 1.3:** A sampling of molecules investigated for application in organic light emitting devices and organic thin film transistors, including those that have been the focus of research in the following chapters.

materials. The small molecule films are built up via vacuum evaporation, allowing a high degree of control over the film thickness as well as a means for growing very clean and pure films. Polymer films need to be spin coated onto substrates from solution, which limits the needed precise control of the film thickness. In fact, creating monolayer and sub-monolayer films is virtually impossible. Furthermore, there are inherent contaminants in polymer films that can severely hinder the ability to measure the energy levels of the material of interest. These contaminants can be due to the solvent, residual catalysts from the polymer synthesis, residual polymer precursors, and synthesis byproducts. In this research, small molecules have been used exclusively for the purposes of measuring the electronic behavior of the interfaces of organic films, and staying within the boundaries in which the experimental procedure is feasible.

In all organic and polymer based electronic devices, there are a number of fundamental and engineering issues that must continue to be explored in order to make such devices commercially viable. These include modifying the materials for improved electron and hole transport, optimizing the kinetics of time dependent carrier trapping and detrapping, improving recombination and emission efficiencies, increasing molecular stability and device lifetime, and understanding/optimizing interface effects and injection barriers [45,73]. There is a strong need to understand the charge injection characteristics from metallic electrodes into the organic film. For example, a very low work function metal would be ideal for the cathode. Calcium, with a work function of 2.2 eV, would be

the preferred material except for the fact that calcium oxidizes easily. It is necessary to have a detailed understanding of the injection characteristics and chemical behavior of the interface to be able to select an electrode material that allows for high injection efficiency yet is chemically stable. The primary objective of this research has been to elucidate the electronic properties of the interfaces in organic based electronic devices by measuring the energy levels at the interfaces as well as investigate the morphology of organic thin films on metal substrates.

This research focuses on the need to understand the electronic and morphological properties of these organic interfaces. Ultimately, a thorough comprehension of the interfaces can lead to better engineering of the previously mentioned devices. The origins and measurement of the core-electron peak shifts and the attribution to band bending and/or changes in the polarization environment will be discussed. These core peak shifts are entirely attributed to band bending in the systems in Chapter 2, however as measurements were done on additional systems, it was realized that polarization energies and their effect on the charge screening environments needed to be further scrutinized. This is done to some extent for the systems in Chapter 3, and more significantly in Chapter 5 where the gold substrate allowed for a more thorough examination of possible polarization induced shifts. There is a traditional assumption of a common vacuum level (VL) at such interfaces, and the following chapters will verify the invalidity of this assumption through the measurement of interfacial dipoles as well as discussions on

some possible morphological and chemical contributions to interfacial dipoles. A further understanding of interfacial dipoles and band bending will help gain insight on the current-voltage behavior, charge injection characteristics, and efficiency of organic based devices.

## 1.2 Background of Organic Based Electronic Materials

Many of the properties of organic semiconductor materials and conventional inorganic semiconductors are similar. These include an increase in conductivity with increasing temperature [55], and similar junction offset characteristics. One significant difference is the conduction mechanism, explained as a carrier 'hopping' process instead of band formation that occurs in bulk inorganic semiconductors.

In conventional inorganic semiconductors and metals, each atom has covalent or metallic bonds, respectively, to each of its neighboring atoms forming what is viewed as an infinite molecular lattice [74]. Energy bands are formed when there is an overlap of a large number of atomic orbitals in the continuous solid leading to molecular orbitals that are closely spaced in energy. Organic semiconductors consist of covalent bonds within each molecule, however, they lack the covalent or metallic bonding over an infinite molecular lattice. The molecules in an organic semiconductor crystal or film are relatively closely packed though, leading to some overlap of their molecular wavefunctions. The interaction between adjacent molecules leads to energy level splitting. When the number of organic molecules on a 1 $cm^2$ film that is 100 nm thick

can exceed a population of $10^{17}$ cm$^{-3}$, the splitting of this number of energy levels leads to the formation of energy bands. While the conduction mechanism in organic systems is known to be more of a hopping process, there can (and should) be the formation of valence/conduction bands or band-like energy levels in the organic materials. This may not be an exact physical equivalent to band behavior in inorganic semiconductors, but there is a lack of analogous nomenclature when referring specifically to organic systems. Because there are many similarities in band-like behavior between organic and inorganic systems, the concept of bands will be treated in a universal sense.

A feature that is relevant to organic and conventional inorganic materials as well as metals is the concept of the Fermi level ($E_F$). For metals, the Fermi level is defined as the energy where the probability of an electron occupying that state is 1/2 provided that the temperature of the metal is 0 K [74]. This population probability (P) of the energy levels is based on the Fermi-Dirac distribution, a version of the Boltzman equation that takes into account the Pauli exclusion principle:

$$P = \frac{1}{1 + e^{(E-E_F)/kT}} \qquad (1.1)$$

This is not an exact equation for semiconductors, since the Fermi level lies in the gap between the valence bands and conduction bands of the semiconductor. As a consequence, there is a zero probability of an electron existing at the Fermi level energy

in semiconductors. In the case of an intrinsic semiconductor where there is a negligible presence of impurities, the Fermi level is defined as

$$E_F = \frac{E_C + E_V}{2} + \frac{3kT}{4} \ln\left(\frac{m_{dh}}{m_{de} M_c^{2/3}}\right) \qquad (1.2)$$

where $E_C$ and $E_V$ are the energy levels of the conduction band and valence band respectively, $m_{dh}$ is the effective mass of the holes, $m_{de}$ is the effective mass of the electrons, and $M_c$ is the number of equivalent minima (of energy states) in the conduction band [74]. When artificial impurities known as dopants, are implanted or infused into the semiconductor to enhance the conductive properties, the position of the Fermi level will depend on the density and type of these dopants.

To raise the Fermi level in inorganic semiconductors such as silicon, the semiconductor is doped with n-type (negative carrier) dopants like phosphorus or arsenic ions. To lower the Fermi level, the silicon can be doped with a p-type (positive carrier) such as boron. Doping of the semiconductor may be accomplished by diffusion of a molten form of the dopant element into the semiconductor matrix, or by ion implantation via a beam of the ionized dopants accelerated up to several keV under an electric field and embedded into the semiconductor.

There are several methods for adjusting the Fermi level in organic and polymer systems. The first, like the inorganic systems, is the implantation of dopants into the organic film [59,75-78]. By evaporating or diffusing in a trace amount of an alkali metal

such as cesium, that will ionize to $Cs^+$ in the organic matrix leaving an extra electron in the conduction band of the organic material leading to n-type conductivity. Likewise by vaporizing a halogen such as molecular iodine, it will ionize to $I^-$ and depleting the organic film of electrons leading to p-type or hole conductivity. These metal or halogen dopants can effectively tune the Fermi level and dramatically increase the conductivity of the organic material. A distinct disadvantage to metallic or halogen dopants is that these charged species are not permanently bound in the organic lattice like in inorganic semiconductors. Therefore, these dopants can diffuse through the organic matrix toward the oppositely charged electrode under bias conditions thereby removing the dopants from the organic material.

Another way to adjust the Fermi level in an organic material is to modify the chemistry of the molecules themselves. This can be accomplished by changing the functional groups on the molecules [9,79-84]. It should be noted that in addition to tuning the Fermi level, changing these methods of doping or modifying the functional groups on the organic molecules can also raise or lower the positions of the HOMO and LUMO of the molecule, which may or may not be the desired result. This may also enhance or reduce the carrier mobilities and affect luminescent properties.

Two distinct electronic phenomena, that may occur at interfaces involving a semiconductor material, are bending of the electronic energy bands and the formation of an interface dipole. When two materials with different Fermi energies are brought into

contact with each other, there is a thermodynamic drive toward Fermi level equilibration. In the case of a metal-semiconductor interface (Fig. 1.4.A), a higher work function metal is brought into contact with a semiconductor with a slightly lower work function value. As the Fermi levels equilibrate, there will be a "pinning" of the valence and conduction band edges at the interface, and the valence and conduction bands will bend as under the induced potential energy field. This creates a Schottky type contact as shown in Fig. 1.4.B. The region where the band bending occurs is known as the space charge region. The space charge region extends from a few tens of nanometers up to several microns into the bulk of the material.

Figure 1.4.C shows a diagram of p-type (left) and n-type (right) semiconductors being brought into contact with each other. Again, the Fermi levels will thermodynamically equilibrate inducing an electric potential across the interface under which bends the bands. This situation where two semiconductors are brought into contact is known as a p-n junction (Fig. 1.4.D). When both sides of this p-n junction are silicon, just differently doped, this creates what is known as a homojunction. If two different base materials (e.g. those with different band gaps) are brought into contact, a heterojunction is formed.

There is the question of whether a space charge field is really able to form in organic materials. As previously mentioned, there is the presence of band-like energy states in organic materials. However, in order for band bending to occur at an interface,

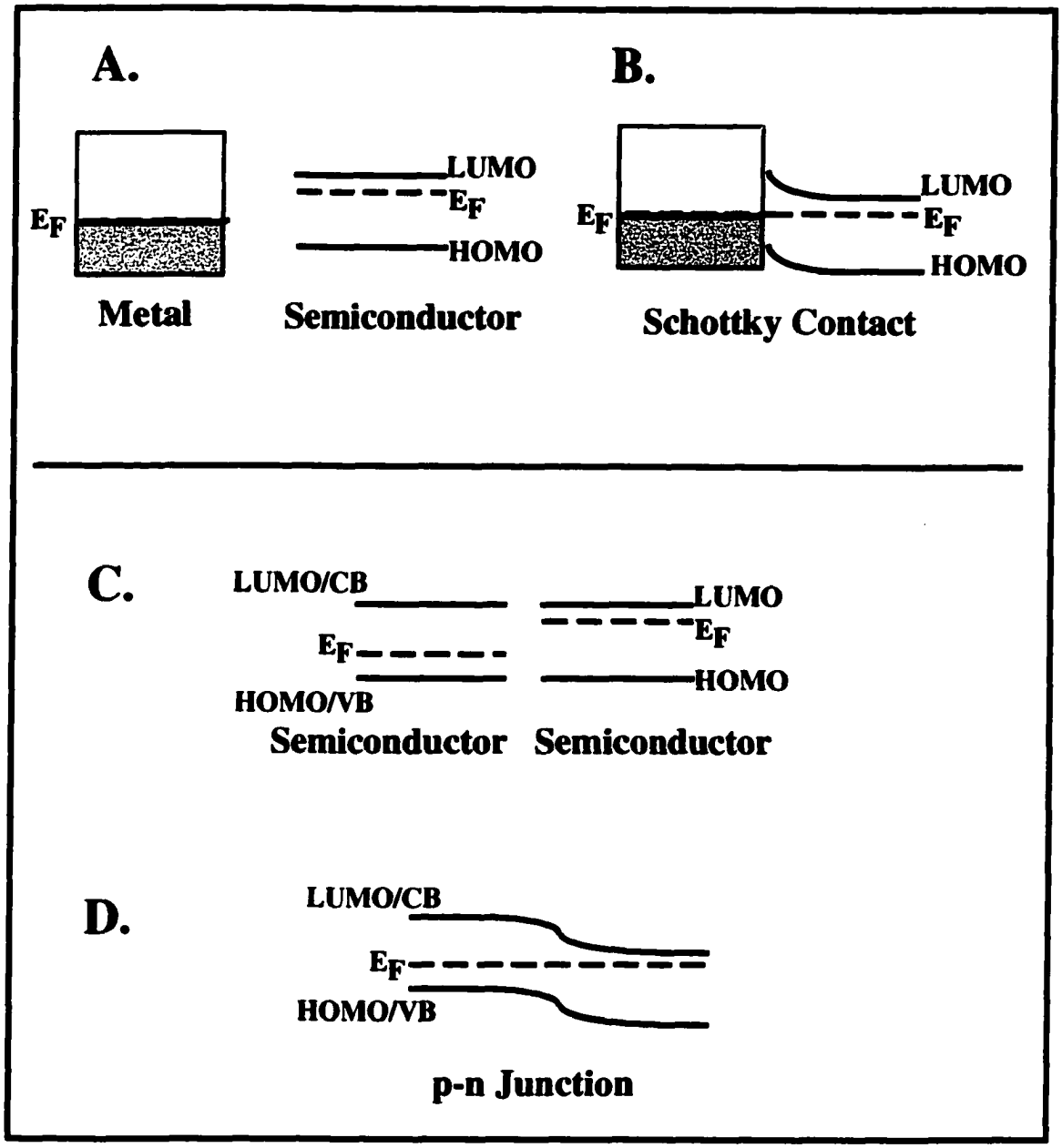


**Fig. 1.4:** Diagram of "band bending" in a semiconductor material. In the top part, a metal and a semiconductor (A.) with different Fermi energies are brought into contact. The Fermi energies are thermodynamically brought into equilibrium creating a Schottky contact (B.). In (C.) two semiconductors with different Fermi energies are brought into contact forming a p-n junction (D.).

stationary dopants or charges in the organic material are required to support the space charge field. In inorganic semiconductors such as silicon, the dopants are covalently bound in the silicon lattice forcing them to be stationary. But in organic films, both electrons and holes are mobile, and impurity atoms or compounds are absent in these films. Even if impurity atoms were present, they are not covalently bound to the molecular solid, and therefore could have the ability to diffuse through the organic film under an applied electric field. Furthermore, the magnitude of the band bending is directly dependent on the concentration of the dopants as can be expressed by a general form of the Poisson equation in relation to the band bending potential $V_0$

$$\frac{d^2V}{dx^2} = \frac{-dE}{dx} = \frac{-eN_D}{\varepsilon_r\varepsilon_0} \qquad (1.3)$$

where e is the electronic charge, $N_D$ is the dopant density, $\varepsilon_0$ is the permittivity, and $\varepsilon_r$ is the dielectric constant of the organic medium. When V is integrated with respect to x, and then setting $x = d_n$ as the width of the space charge region, the relation between dopant density and band bending magnitude can be determined.

$$V_0 = \frac{N_D e d_n^2}{2\varepsilon_r\varepsilon_0} \qquad (1.4)$$

As will be discussed in later chapters, a dopant concentration $>10^{15}$ dopants·cm$^{-3}$ is needed to support a measurable ( 0.05 eV) space charge field. It is unlikely there is that high a concentration of impurities in the organic film.

Measuring the extent of band bending in an organic material is further complicated by the method of the measurement. Band bending is usually determined from the peak shifts of the core electrons measured using x-ray photoelectron spectroscopy (XPS) as will be discussed below. The issue at hand is whether these core level peak shifts are attributed to band bending or to other phenomena such as final state screening shifts. Final state screening is always present in photoemission spectra. This is a result of a polarizable medium surrounding the atom where the photoejected electron originated that screens the remaining positive charge after the electron has been ejected. This screening of the remaining positive charge lowers the effective ionization energy of the photo-ejected electron. This is why the work function values and ionization potentials of all materials in the solid phase have a lower value than the gas phase ionization energy of an atom or molecule of that same material.

The ability of a medium to screen the remaining charge is dependent on the polarization energy of that material, and is defined as the difference between the gas phase and solid phase ionization potentials. The polarization energies of metals range from 1.7 eV for aluminum to 5.9 eV for mercury while most organic compounds generally have polarization energies from 1.6-3.0 eV, usually closer to the lower value [85]. If the organic molecules had sufficiently low polarization energies, it could be postulated that when measuring the photoelectron spectra, the remaining charges in first monolayer of the film would be effectively screened by the more polarizable substrate.

Then additional molecular layers deposited on top would be screened to a lesser degree resulting in a shift of the photoelectron spectra to slightly higher binding energies [85,86]. This exact effect was in fact observed in the photoelectron spectra of Xe deposited on Pd(001) where a strong shift (> 1 eV) of the Xe 4d line was observed between the first xenon monolayer and multilayer coverages [87].

Final state screening effects caused by changes in the polarizability of the medium can cause shifts in the photoelectron spectra of the organic on metal interfaces that can be confused with band bending related shifts. This then relates back to the question of whether the formation of a space charge field (e.g. band bending) could really occur in the organic material. To partially answer this question, it should be pointed out that band bending related shifts, as determined using XPS, were observed in several organic/organic interfaces where the polarization energies are very close in value [69]. For organic semiconductor on metal interfaces, this issue was addressed by Schlaf et. al. [88] where it was determined that the polarizability of most organic molecules investigated for OLED and thin film transistor purposes can be sufficient to screen the holes resulting from the photoemission process. Core-level peak shifts, due to changes in polarization energies, would be expected to be more prevalent on substrates such as gold where the polarization energy is substantially larger than that of the organic materials. Part of this work involves trying to further address this issue and discuss the possible

origins of these shifts (particularly in chapter 5) in the organic semiconductors as was observed using photoelectron spectroscopy.

The Mott-Schottky model for interfaces predicts the magnitude of the injection barrier by assuming alignment at the vacuum energy level according to the electron affinity rule (EAR). However, as will be shown, the Mott-Schottky model is not necessarily valid for many of these interfaces due to the formation of interfacial dipoles. An interface dipole is a potential drop that occurs immediately (typically within one atomic or molecular layer) at the interface between two different materials. The magnitude of the interface dipole can range from 0 to greater than 1 eV. There are several factors that may contribute to the formation of the interface dipole, all based on surface or interface states. The first contributing factor is charge transfer effect known as a quantum dipole [89] (Fig. 1.5.A), where electrons are injected from one material into the other. In the band diagram, this or any type of interface dipole is represented by a step in the vacuum energy level ($E_{vac}$) as shown in Fig. 1.5.B. A polar molecule adsorbed on a substrate leads to a permanent or molecular dipole (Fig. 1.5.C, and could also induce an image charge (Fig. 1.5.D) if the substrate is metallic. Adsorbing a molecule on a chemically reactive surface can induce a charge dipole at the interface (Fig. 1.5.E). There can also be a surface rearrangement (Fig. 1.5.F), where a polarizable atom is adsorbed on a metallic surface such as xenon adsorbed on palladium [87]. The dipole is attributed to the tailing part of the metal's electronic cloud into the vacuum is pushed back by repulson

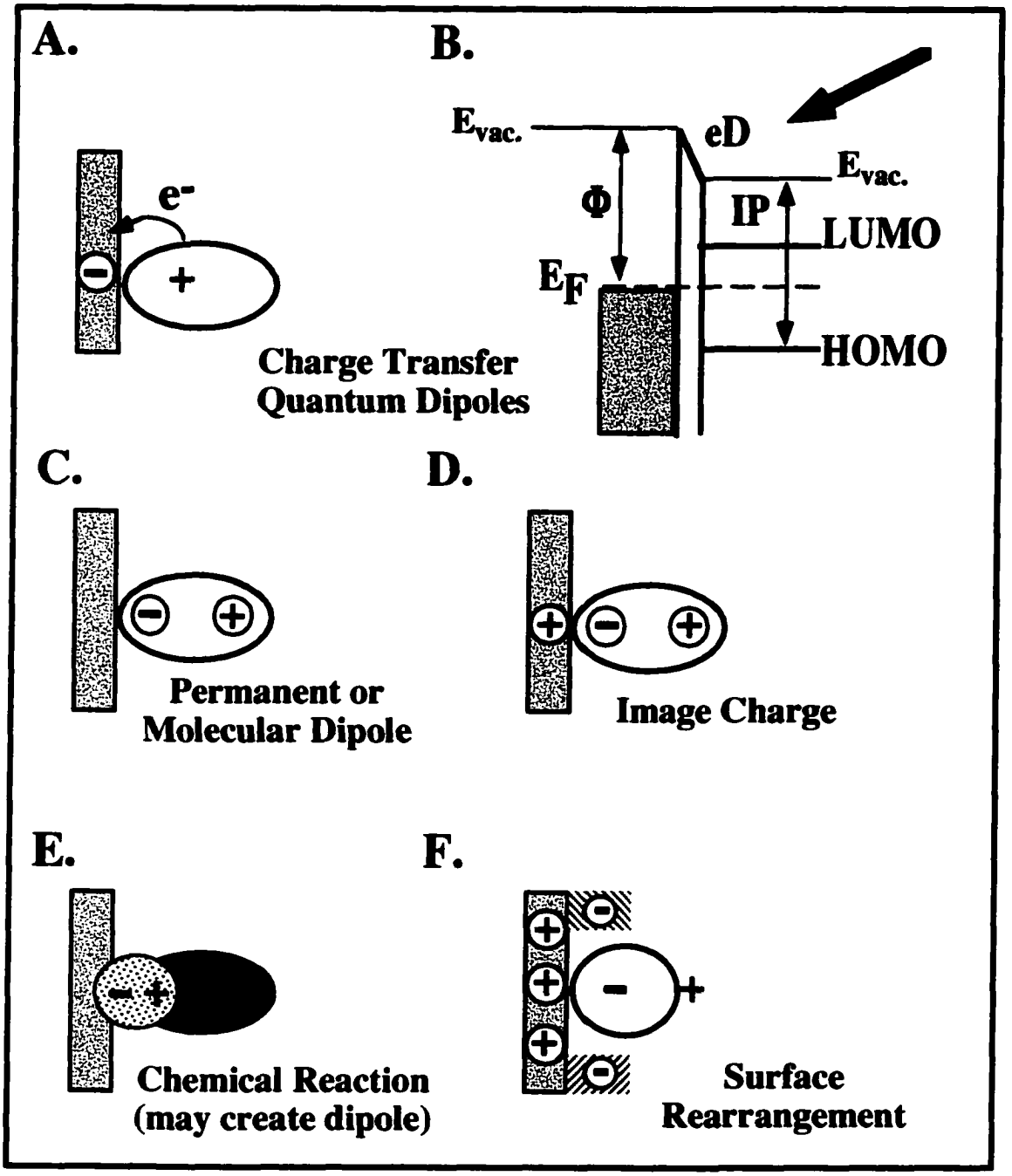


**Fig. 1.5:** Factors that can lead to the formation of an interface dipole potential. Fig. 1.5.B. shows how an interface dipole is represented by a step in the vacuum energy level.

with the electron cloud of the adsorbate leaving a positive charging effect on the vacuum side [73].

The conventional belief was that the charge injection processes could be understood by simply estimating the barrier height between the Fermi level of the metal and the HOMO or LUMO of the organic material as done using the Mott-Schottky model for interfaces. It has become very clear that this yields an inaccurate depiction of the energetics of the interface. Modifications are needed to establish a more correct model of these interfaces. As an example, it has recently been proposed by Baldo and Forrest [90] that the rate limiting step in charge injection from a metal into an organometallic film is the charge hopping out of the interfacial molecular sites whose energy distribution is broadened by the interfacial dipole field. If thermionic emission over the metal/organic semiconductor interface barrier were to describe the transport characteristics, the current density J would be predicted by the Richardson-Schottky equation [74],

$$J = A^* T^2 \exp[-(\phi_B - \sqrt{qF/4\pi\varepsilon})/k_B T] \qquad (1.5)$$

where A* is the Richardson constant, $\phi_B$ is the injection barrier, q is the electronic charge, F is the electric field, $\varepsilon$ is the organic permittivity, $k_B$ is Boltzmann's constant, and T is the temperature. However, there are large discrepancies between this model and actual current-voltage behavior of actual devices. The fits of the above equation to the experimental data yields a Richardson constant that is ten orders of magnitude lower than

would be expected for an electron in an organic medium. Also the curves do not obey Arrhenius [exp(1/$k_B$T)] behavior below room temperature. It is clear that a modification to this model to account for interface states is necessary to establish a more thorough understanding of the charge injection processes at these interfaces.

Baldo and Forrest recently proposed [90] a model for the current density where the limiting step is injection from the interface states into the bulk of the organic medium.

$$J(E_F) = \frac{aq}{\sqrt{2\pi\sigma_B^2}} \int_{-\infty}^{\infty}\int_{-\infty}^{\infty} n_I(E_I, E_F) R(E_B - E_I - aqF) \times \exp\left[-\frac{1}{2}\left(\frac{E_B}{\sigma_B}\right)^2\right] dE_I dE_F \qquad (1.6)$$

Here, a is the average intermolecular spacing, $\sigma_B$ is the width of the bulk charge distribution, $E_I$ is the energy of the interfacial sites, $E_B$ is the energy of the charge in the bulk, and $R(E_B - E_F - aqF)$ is the polaron hopping rate as a function of the energy difference between adjacent hopping sites and the applied electric field [91,92]. A polaron is a charge (electron or hole) coupled to a phonon on a molecule or within in a molecular lattice and is suitable for describing charge states in an organic film [74]. The charge density per unit energy at the interface is given by $n_I(E_I,E_F)$ which was determined by Fermi-Dirac statistics [90],

$$n_I(E_I, E_F) = \frac{N_I/\sqrt{2\pi\sigma_I^2}}{1+\exp[(E_I - E_F)/k_B T]} \exp\left[-\frac{1}{2}\left(\frac{E_I}{\sigma_I}\right)^2\right] \qquad (1.7)$$

where $N_t$ is the density of the interfacial sites, and $\sigma_t$ is the energetic distribution of the sites in the first organic layer at the interface. This model is based upon a broad, dipole-induced Gaussian distribution of energy sites located at the interface. The current-voltage behavior as well a temperature dependence of several experimental devices more closely matched this model than the Richardson-Schottky model, demonstrating that charge injection from the dipole-induced interface states into the bulk of the organic film is a crucial aspect the transport characteristics of organic based electronic devices. While these results or similar models may be valid for certain organic interfaces, the Richardson-Schottky equation may still be valid for other systems. Regardless, the interface dipole should be considered when trying to understand charge injection characteristics. Results, such as that previously stated, reinforce the need to be able to precisely measure the presence and magnitude of the interface dipole in order to further understanding the behavior of organic based devices.

### 1.3 Experimental Procedure in Energy Level Alignment

All of our experiments were performed in an Omicron Multiprobe® ultra-high vacuum (UHV) surface analysis system (Fig. 1.6). The commercial system was equipped with an analysis chamber with capabilities for X-ray photoelectron spectroscopy (XPS), ultraviolet photoelectron spectroscopy (UPS), Auger/scanning Auger spectroscopy/microscopy (AES,SAM), residual gas analysis (RGA) mass

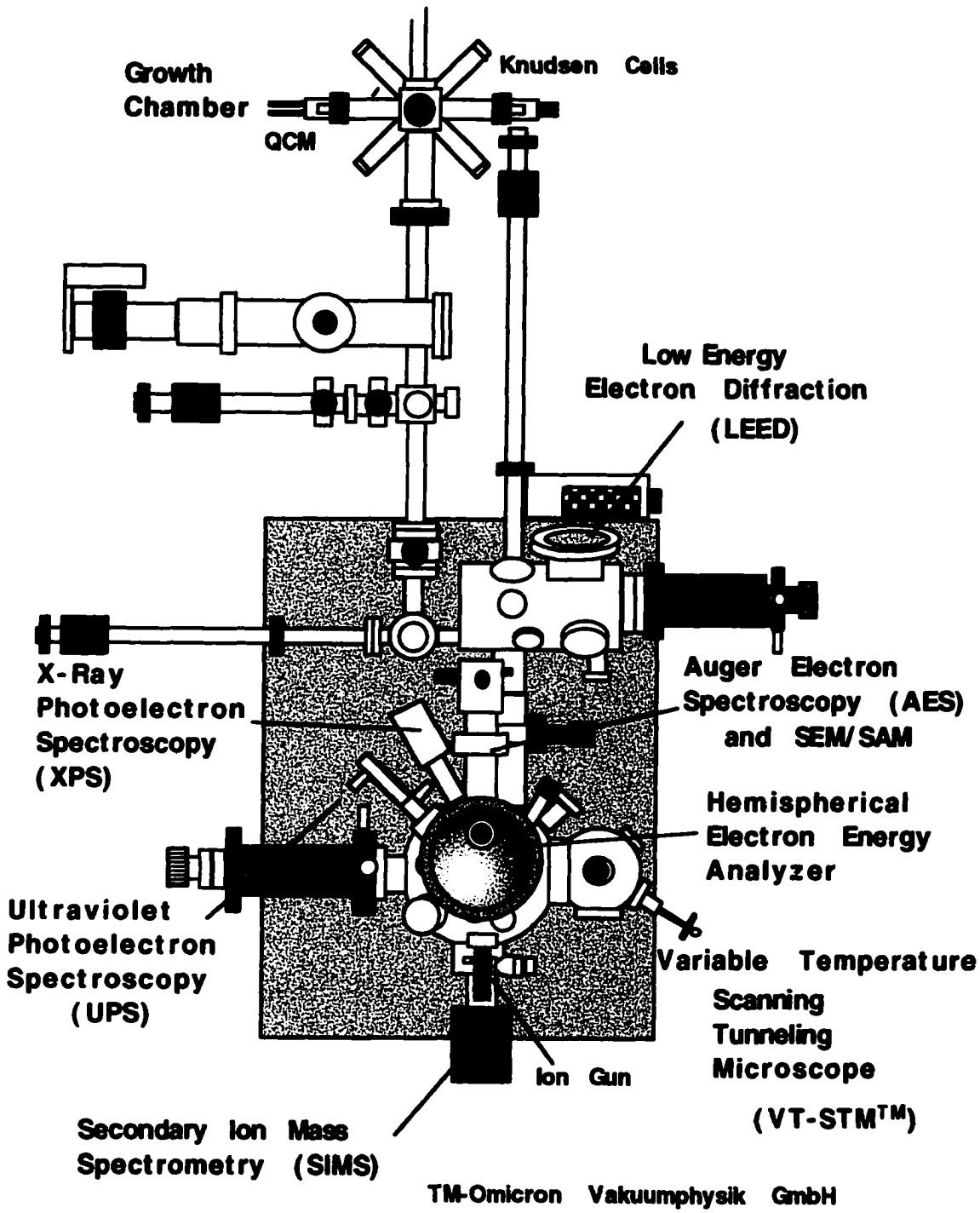


**Fig. 1.6:** Ultra-high vacuum (UHV) Omicron Multiprobe® surface analysis instrument.

spectrometry that can also be used for temperature programmed desorption (TPD), and scanning tunneling microscopy (STM); and a second chamber equipped with low energy electron diffraction (LEED). The base pressure in both of these chambers is $5 \cdot 10^{-11}$ mbar.

A home-built physical vapor deposition chamber was added on, attached to the sample entry chamber. This chamber is equipped with a quartz crystal microbalance (QCM), a sample heater, and home-built Knudsen-type sources. A diagram of the deposition setup is shown in Figure 1.7. The organic material of interest is placed in a boron nitride crucible that is wrapped with a resistively heated tungsten wire. A type-K (Alumel/Chromel) thermocouple is inserted into a bored hole in the bottom of the crucible. The Knudsen source is mounted on a UHV electrical feedthrough flange that is connected to a Eurotherm® temperature controller and a Sorensen® power supply. The temperature of the source can be precisely controlled to within ±1°C. A tantalum foil shield with a 5 mm aperture is placed over the end of the source to help collimate the molecular beam and to thermally shield the source. The QCM is mounted on a linear motion device and can be moved into the path of the evaporating molecules where the deposition rate of the organic film can be determined. The sample can be moved into the path of the source mounted either on the magnetically coupled transfer rod, or placed into the sample heater which is also mounted on a linear motion translator. In most of our experiments, a deposition rate of 4Å/min is established for precise control of the film

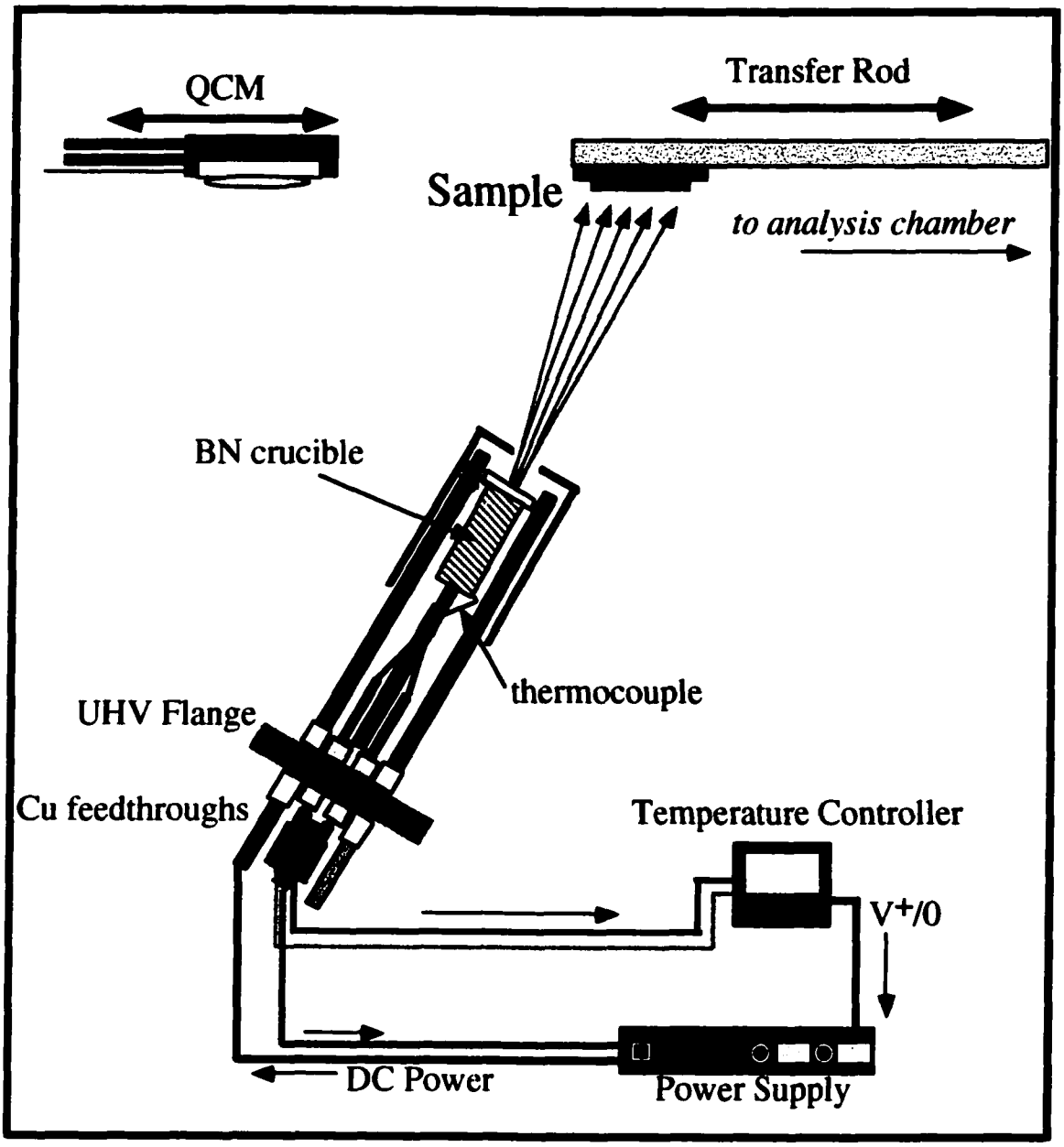


**Fig. 1.7:** Deposition process: The organic compound is held in a boron nitride crucible that is wrapped with a resistively heated tungsten wire and is mounted on a UHV flange. The temperature is monitored with a thermocouple and controlled with a Eurotherm™ temperature controller that is connected to a power supply. A quartz crystal microbalance (QCM) can be moved into the path of the source to monitor the deposition rate.

thickness at monolayer and sub-monolayer coverages. The base pressure of this chamber is $1 \cdot 10^{-8}$ mbar.

Photoemission spectroscopy (PES) is an experimental technique used to determine characteristic energies of the electrons in a sample. PES is based on the photoelectric effect first explained by Einstein in 1906. The fundamental equation behind photoemission spectroscopy is:

$$BE = h\nu - KE - \phi \qquad (1.8)$$

where BE is the characteristic binding energy of an electron in a given shell of a particular atom, KE is the kinetic energy of the electron as measured by the hemispherical electron energy analyzer, hv is the light source energy, and $\phi$ is the characteristic work function of the analyzer. The binding energies of core electrons are fairly well defined, however, they can be shifted by up to several eV depending on the atom's oxidation state, chemical bonding, or any surrounding electric field potential. The binding energy of the valence electrons, as measured with UPS, are attributed to the highest occupied molecular orbitals or valence band structure of the material being measured.

The "band-lineup" experiments, discussed in the following chapters, use PES to probe the electron energy levels of the interface between two different materials. Details

of the measurement process as applied to specific systems in subsequent chapters are described below.

To specifically investigate the interface dipole phenomena and the possible occurrence of band bending at the interfaces involving organic materials, it is necessary to choose clean and essentially atomically flat substrates. The two substrates chosen for the majority of these experiments are $SnS_2$ and highly oriented pyrolytic graphite (HOPG). $SnS_2$ is a layered material with a repeating three-layer sandwich of the chalcogenide sulfur at the top and bottom and the tin in the middle. The bonding within each sandwich layer is covalent with ionic character, however the adjacent sandwich layers are held together by weak van der Waals (VDW) forces. Figure 1.8.A shows a cross sectional diagram of the layered structure of $SnS_2$. The van der Waals plane bisects each covalently bonded sheet. HOPG is also a layered material where each two-dimensional layer consist of covalent $sp^2$ hybridized carbon. Adjacent layers of graphite are also held together with VDW forces as shown in Fig. 1.8.B. One advantage of these layered materials is that they can easily be cleaved, by peeling away the topmost layers, exposing clean, atomically flat terraces up to several hundred nanometers wide. Surface sulfur and carbon atoms have saturated bonding [93], and do not react chemically with the deposited organic film.

The substrates were glued on to the sample holder using a conductive epoxy (EPO-TEK® H20E) compatible with UHV applications. $SnS_2$ and HOPG are vacuum

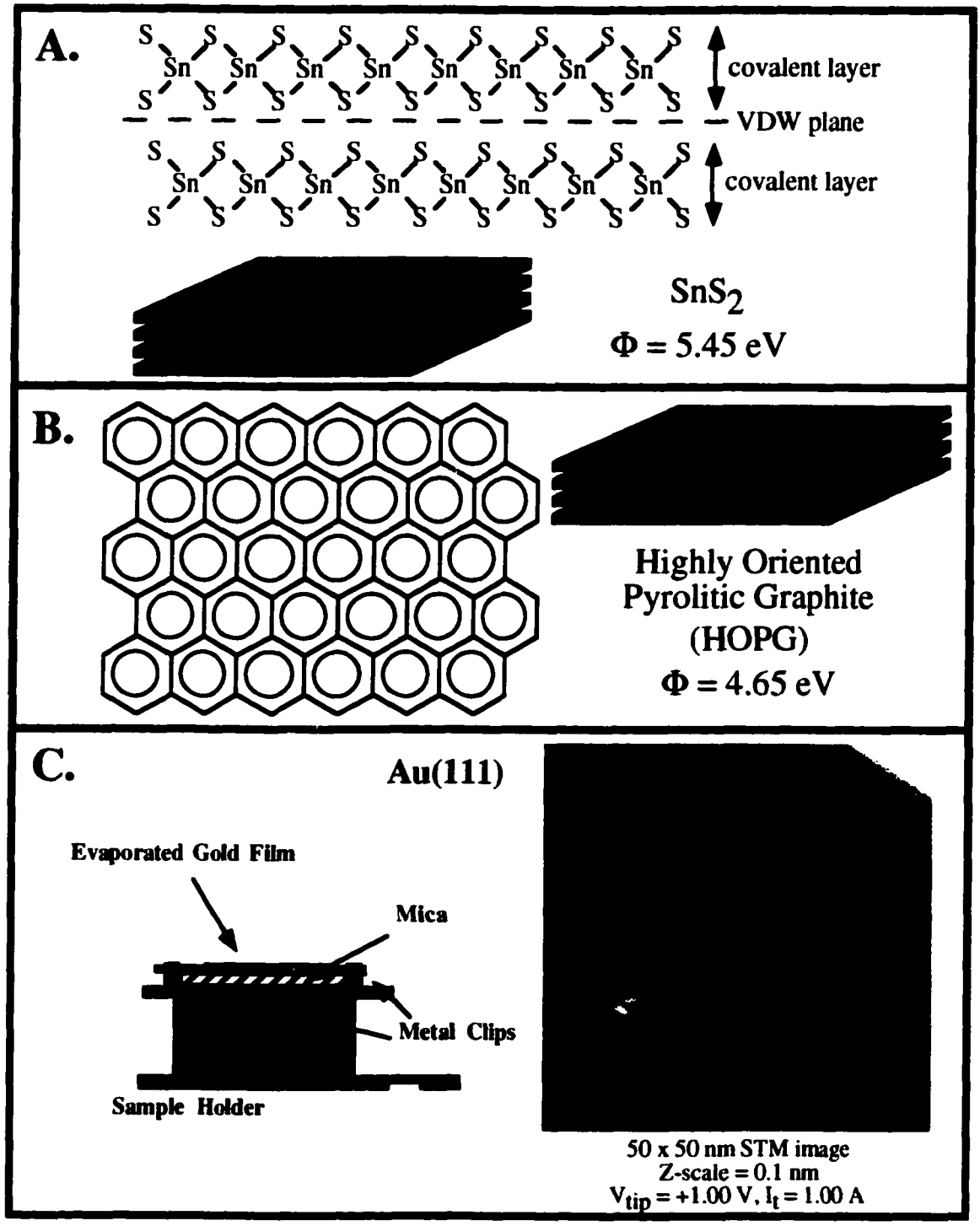


**Fig. 1.8:** Three substrates used in the experiments in the following chapters are the layered semiconductor material $SnS_2$ (A), the semi-metal highly oriented pyrolytic graphite (HOPG) also a layered material (B), and the (111) surface of gold (C). The STM image in Fig. 1.8.C. shows the characteristic 22 x $\sqrt{3}$ reconstruction of the Au(111) surface.

cleaved using a metal foil (0.1 mm thick) glued onto the surface. The metal foil is bent into an 'L' shape then one face is glued onto the layered material surface using a standard acrylic epoxy with the other face of the foil sticking perpendicular from the sample surface. The foil then is knocked off using an adjacent transfer rod arm in the vacuum system. Since the van der Waals forces between the layers of the substrate materials are weaker than the bonding forces of the epoxies, the sample typically will cleave in the middle of the layered material. This allows an atomically flat, freshly cleaved substrate in the UHV without the presence of any significant ambient contaminants.

In addition to investigating the fundamentals aspects of band bending and interface dipoles, a more practical system was also investigated. The focus here was on the interface between pentacene and Au(111). As discussed above, pentacene single crystals and thin films are known for having high carrier mobilities, and gold is frequently used as the source and drain contacts in experimental thin film transistors. We specifically chose the (111) surface of the gold for the purpose of having a well-defined surface for which to study the electronic structure of the interface, as well as imaging the morphology using scanning tunneling microscopy.

The Au(111) surface may be prepared from cleaving along the (111) plane of a single crystal of gold, or by annealing a vacuum evaporated gold film. In our experiments, the vacuum evaporated gold method was used. A freshly cleaved piece of mica (about 2 $cm^2$) was mounted on a sample plate (Fig. 1.8.C) and subsequently heated

to 350°C in the sample manipulator at $10^{-10}$ mbar for 24 hours to completely clean the mica surface. The substrate was then placed in the deposition chamber sample heater and heated to 300°C before and during the deposition of the gold. The gold was treated in concentrated $HNO_3$ prior to placing it into a tungsten wire basket in the deposition chamber. The tungsten wire basket was resistively heated at approximately 40 watts to evaporate the gold onto the mica substrate. The resulting gold film (~1 μm thick) was then moved to the analysis chamber where several cycles of sputtering with the argon ion gun (1 kV, 30 mA ion current, 15 minutes), followed by annealing for 30 minutes at 350°C yielded the clean Au(111) surface. The quality of the Au(111) surface was verified using low energy electron diffraction, and from the 22 x $\sqrt{3}$ reconstruction present in STM images as shown in Fig. 1.8.C.

After cleaving the layered material in the sample entry chamber, or preparation of the metal film, the substrates are characterized in the analysis chamber using XPS and UPS. XPS is used to determine the chemical purity and surface cleanliness as well as for measuring the first spectra for the determination of the magnitude of the core-level peak shifts. As previously stated, the core-level peak shifts could be attributed to band bending, changes in the screening environment, or a combination of both. The UPS is used to determine the work function and the band structure (Fermi edge or valence band) of the substrate. At this point the position of the sample and He lamp are optimized to

maximize the signal intensity and verify that the substrate spectra matches previously published spectra [94,95].

After analysis of the energy levels of the substrate, the sample is moved into the deposition chamber, where a very thin film of the organic smiconductor of typically 0.1 Å (or about 5% of one monolayer) is deposited onto the substrate. The sample is then moved back into the analysis chamber where the XPS and UPS measurements are repeated. After this, the sample is moved back into the deposition chamber for deposition of another 0.1 Å to bring the total film thickness to approximately 0.2 Å, then moved back to the analysis chamber. This process is repeated, generally from twelve to fifteen times, doubling the total film thickness each time. The final film thickness after the twelve to fifteen steps in the experiment is usually between 250 Å and 1000 Å. The purpose of building up to a relatively thick film is to establish a film thickness where the occupied molecular orbital positions can be measured with a high degree of accuracy as well as reach a point where flat band potential can be assumed. Care must be taken not to build up too thick a film since sample charging could commence. Chapter 2 addresses how sample charging is measured and then considered in the data evaluation procedure.

A diagram showing the potential energy wells typical of a molecular solid is shown on the left side of Fig. 1.9, where the atomic nuclei in each molecule are defined as the bottom of the wells. A molecular solid in these cases is defined as an organic single crystal or an organic thin film where there is a lack of covalent bonding between

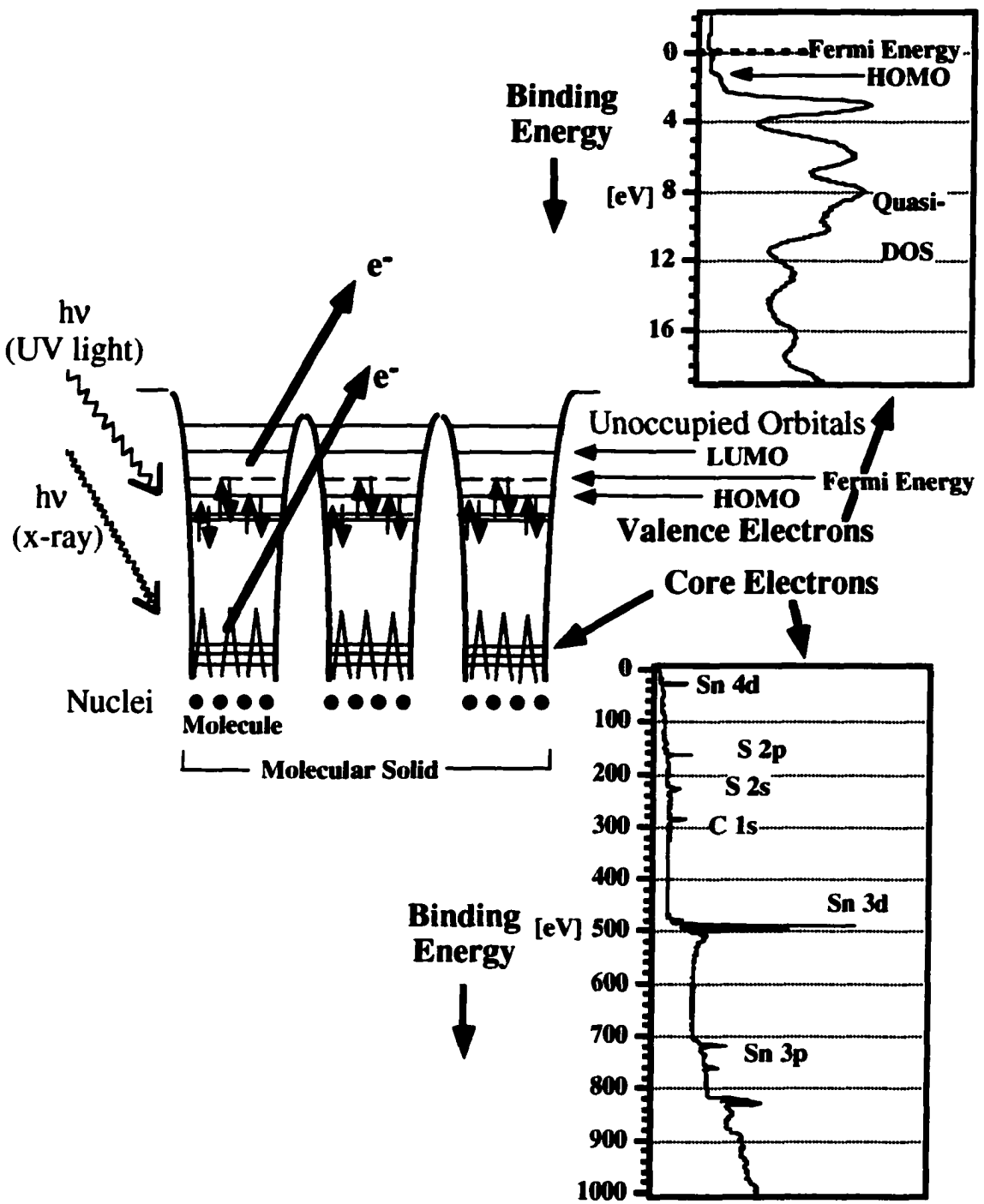


**Fig. 1.9:** A potential energy well diagram for a molecular solid showing the core and valence electron energy levels. X-ray photoelectron spectroscopy (XPS) is used to probe the energy levels of the core electrons. Ultraviolet photoelectron spectroscopy (UPS) is used to probe the energetics of the valence electrons yielding a quasi-density of states of the valence electron energy distribution for the sample.

the individual molecules. The primary intermolecular forces present are usually van der Waals forces, however, other forces such as hydrogen bonding or dipole-dipole interactions may be present in a number of these organic systems. The tops of the potential energy wells are defined as the vacuum energy level. While the true definition of the vacuum energy level $V_\infty$ the energy of an isolated electron at rest in the vacuum (or at infinite distance from the sample), the vacuum reference in PES is the energy of an electron just outside the surface of the sample $V_s$. As previously mentioned, this is acceptable since we are interested in determining the energy levels relative to adjacent layers in the samples and not relative to the energy of an electron at $V_\infty$ [73]. The ionization potential is the energy between the HOMO and the vacuum and the electron affinity is the energy between the LUMO and the vacuum. Organic semiconductor materials have an electronic band gap ($E_g$) that is analogous to the optical absorption gap, and is the difference between the HOMO and LUMO. It is important to mention that this optical absorption gap is not necessarily the same magnitude as the electronic band gap of the material. This is primarily due to the large excitonic binding energy on the order of 0.5 eV, resulting in the measured optical gap being smaller than the actual electronic band gap [55]. This, however, still allows a crude estimate of the LUMO position to be made, and does not interfere with the primary investigations of band bending or polarization induced shifts, and charge dipoles at the interfaces. The core electrons are

deep down in the potential energy wells where the binding energies can range from several tens up to many thousands of electronvolts.

In each of the measurement steps, the core-level energy positions of each of the elements in both the substrate and organic overlayer are measured with XPS, as diagramed in the example in the lower right part of Fig. 1.9. The x-ray source is a twin anode source where either the Mg Kα source peak ($h\nu$ = 1253.6 eV) or the Al Kα source peak ($h\nu$ = 1486.6 eV) can be selected. The valence electron (or highest occupied molecular orbital) energy levels are probed with ultraviolet light using He I radiation (21.21 eV) or He II radiation (40.81 eV). This light is generated from a differentially pumped helium discharge lamp, where the He I light corresponds to the $n = 1 \leftarrow 2$ transition in the Lyman series for the helium atom, and the He II light corresponds to the first line of the Lyman series for the $He^+$ ion. The corresponding spectra yield a quasi-density-of-states diagram (upper right of Fig. 1.9) where the binding energies are determined from equation (1.8). The objective of this procedure is to observe and measure the changes in the photoelectron spectra measured right at the interface, within the first monolayer of the organic film, and then follow the additional changes in the photoelectron spectra as organic film is built up to establish bulk-like characteristics.

Evaluation of the data, as well as display of all the spectra and graphs, was performed using Igor Pro® software by Wavemetrics Inc. The first feature measured is

the core-level shifts as determined using XPS. These shifts are frequently attributed to the amount of band bending occurring in the material, but could also be due to changes in the polarization environment as the transition from substrate to overlayer occurs. To evaluate these shifts, a unique element in the substrate, such as the Sn 3d peak in $SnS_2$, is typically selected and its binding energy is measured throughout the experiment [96]. The shift of this core-level binding energy between the vacuum cleaved substrate [$BE_{vac.cl.}$(sub.)] and that with a thick film deposited on top [$BE_{thick}$(sub.)] reflects the extent of the core-level shifts ($\Delta$CL(substrate)) in the substrate.

$$\Delta CL(substrate) = BE_{thick}(sub.) - BE_{vac.cl.}(sub.) \qquad (1.9)$$

A unique element in the organic overlayer is also selected and the binding energy position is determined at the first point where a Gaussian-Lorentzian curve can be fit to the spectra. This is typically around 0.4 Å thickness of the organic film. The binding energy shift between this "thin film" peak [$BE_{thin}$(film)] and a thick film peak [$BE_{thick}$(film)] yields the change in the core-level position [$\Delta$CL(film)] in the organic film.

$$\Delta CL(film) = BE_{thick}(film) - BE_{thin}(film) \qquad (1.10)$$

The work function ($\Phi$) of the sample is measured with UPS, and is evaluated by subtracting the high binding energy cutoff ($E_{HBEC}$) of the inelastically scattered electrons from the He I source energy ($h\nu$ = 21.21 eV).

$$\Phi = h\nu - E_{HBEC} \qquad (1.11)$$

The magnitude of the sample work function is measured throughout the experimental procedure, and the change of the work function ($\Delta\Phi$) between the vacuum cleaved substrate ($\Phi_{sub.}$) and that of the thick film ($\Phi_{film}$) is determined.

$$\Delta\Phi = \Phi_{film} - \Phi_{sub.} \qquad (1.12)$$

This work function change is a result of both the magnitude of band bending or changes in polarization energies and the interface dipole (eD) in the sample. Subtracting the core-level shifts, as measured with XPS, from the total work function change yields the magnitude of the interface dipole.

$$eD = \Delta\Phi - \left[\Delta CL(sub.) + \Delta CL(film)\right] \qquad (1.13)$$

The positions of the valence bands (VB) or highest occupied molecular orbitals are determined from the low binding energy region of the UP-spectra. The lowest binding energy peak cutoff determines the energy position of the VB or HOMO relative to the Fermi level. The conduction band (CB), or lowest unoccupied molecular orbital (LUMO) cannot be directly measured with photoelectron spectroscopy [97]. The position of the CB or LUMO can be estimated by incorporating the optical "band gap" measured from optical absorption spectroscopy, into the evaluation procedure. By measuring each of these spectral shifts as a function of film thickness, a precise diagram of the electronic energy levels at the interface can be obtained.

Photoelectron spectroscopy generally yields measurements within ± 0.1 eV of the absolute value of the electron binding energy being probed. The source of the error margins is generally attributed to slightly different properties of different electron analyzers that are used to measure the kinetic energy of the electrons. In these measurements of the energy levels at the interfaces, the values obtained of are based on shifts of peak positions in the photoelectron spectra. Since the same experimental setup is used for each of the measurement steps in an experiment the margin of error will be smaller, typically on the order of ± 0.03 eV relative error, due to offsets being subtracted out. Generally an error margin between ± 0.05 and 0.07 eV is assumed for the reported values of the barrier heights, band bending magnitudes, and interfacial dipoles.

The procedure of using photoelectron spectroscopy to determine the energy level offsets at organic interfaces, has been applied to a number of systems by several different research groups. Some research has focused on organic/organic interfaces to measure the energy level offsets at the all organic interface that would occur in a bilayer or multi-layer device [98-102]. There are some difficulties when using photoelectron spectroscopy to measure the energy levels at the organic/organic interfaces. For instance, the bottom organic film could exhibit a significant amount of surface roughness and could lead to discrepancies in the measurement of the interfacial dipole. This can also make it difficult to separate out the position of the HOMO for each of two organic layers,

because the sampling depth of the photoelectrons in the UPS measurements is upwards of three times the inelastic mean free path of the photoelectrons in the sample (5-20Å) [103]. Sample charging effects also need to be considered if the organic materials being investigated have a relatively low conductivity. Photoelectron spectroscopy is still an effective technique for probing the energy levels of organic/organic interfaces provided that the above mentioned considerations are taken into account.

Much of what determines device efficiency is governed by the charge injection rates at the electrodes used to contact the organic materials. Therefore, a significant amount of research has focused on the energy level alignment between an organic semiconductor and a metallic or inorganic semiconductor electrode [104-111]. The measurement of the energy levels and barriers at metal or inorganic interfaces can also reduce some of the uncertainties present for the organic/organic interfaces. Aside from the higher conductivity of these substrates (which reduces the possibility of sample charging), very smooth or single crystal metals or inorganic semiconductors can be used as the substrate. This insures a well-defined interface for very precise measurements of the energy level offsets.

Some of these groups [98,102,104,105] have used variations of the technique described above, but most measured the offsets using only UPS. Using UPS alone can usually give a reasonable approximation of the barrier height for electron or hole injection between two materials, however this neglects the degree of band bending

occurring near the interface, and/or may yield an inaccurate measurement of the magnitude of the interface dipole. When looking at the interfaces of organic materials where both components have similar Fermi levels, the presence of band bending is likely to be negligible, therefore using UPS alone would suffice for the determination of the energy level alignment for these interfaces. In addition, band bending may not occur in all organic films but XPS should be done to verify whether or not band bending does occur.

Another advantage of measuring the X-ray photoelectron spectra is the ability to obtain an idea about the growth modes of the organic films. By comparing the peak intensities of the core-spectra for the substrate and overlayer peaks as a function of the film thickness, one can determine whether the film is depositing in a layer-by-layer fashion, island-like growth, or a combination of these modes such as Stranski-Karastanov growth [112]. Assessing the growth pattern of the films is included in the evaluation procedures for each of the systems studied in this work.

There have been a limited number of publications where XPS measurement of core-level peak shifts were incorporated into the measurement process [109,113,114]. Research in our group has addressed this measurement more extensively. In most of this previous work, the core-level peak shifts were all assumed to be attributed to band bending, and changes in polarization environments was only minimally discussed, even though the origins of these peak shifts remains to be completely resolved. Peak shifts in

some of the systems studied could very well be attributed to band bending, particularly for the organic/organic interfaces where the polarization environments are likely to be roughly the same. This may not be the case for the organic/inorganic or organic/metal interfaces, however because band bending is assumed to be a possible origin of these shifts in the published papers. The energy level alignment at the interface between $Alq_3$ and TPD, one of the more extensively studied systems for OLEDs, was measured using XPS along with UPS [96]. In this case, a moderate amount of band bending (0.14 eV) was measured in the $Alq_3$ layer while a negligible amount ($\leq$ 0.02 eV) was measured in the TPD layer. Stronger band bending was observed in other organic/organic interfaces such as that of 3,4,9,10 perylenetetracarboxylic dianhydride (PTCDA) on zinc phthalocyanine (ZnPc) or chloroindium phthalocyanine (ClInPc) [69]. When PCTDA was deposited onto the inorganic semiconductor $SnS_2$, 0.75 eV of band bending was observed in the PTCDA layer [70]. This was primarily due to a large difference between the work functions of PTCDA ($\Phi$ = 4.26 eV) and $SnS_2$ ($\Phi$ = 5.09 eV).

There has also been a focus on organic/metal interfaces with particular emphasis on the charge injection at these Schottky contacts. Measurements were performed on the tris (8-hydroxyquinolinato) galllium ($Gaq_3$)/Pt interface, which yielded strong band bending (1.47 eV) in the organic film as well as a strong interface dipole (0.71 eV) [115]. This work also detailed the discrimination between sample charging and band bending related shifts in the photoelectron spectra. The $Gaq_3$ is the gallium analog of the

extensively used $Alq_3$ molecule. The purpose of using the gallium quinolate was that the Ga core-level peaks in the XPS are much more intense than the Al core-level peaks, and therefore much easier to track. $Gaq_3$ was also investigated for similar purposes on silver and magnesium interfaces [116,117].

Many of these systems had chemical reactions occurring at the interfaces and/or had a diffuse boundary between the two films. The procedure of energy level alignment using photoelectron spectroscopy can usually measure the interfaces with a high degree of accuracy, but interpretation of the origins of the peak shifts can often be cumbersome especially with these complicated interfaces. It would be ideal to complement the photoemission experiments with other surface science techniques to establish a more thorough comprehension of the molecular and electronic properties of the interface.

## 1.4 Investigation of the Morphology of Organic Interfaces

To further understand the electronic behavior of organic semiconductor materials at interface boundaries, morphological effects need to be considered. The orientation of the organic molecules at interfaces may affect the magnitude of the charge injection barriers as well as the interface dipoles. Molecular ordering at the interfaces can lead to increased mobility of carriers through the organic material in this region.

Two techniques in our laboratory, intended to investigate the morphology of these interfaces, are low energy electron diffraction (LEED), and scanning tunneling

microscopy (STM). LEED is a diffraction technique where incident electrons from a thoriated tungsten filament are impinged upon a sample surface and then diffracted back towards a phosphorescent screen. The corresponding LEED pattern on the phosphorescent screen is related to the surface structure and atomic/molecular dimensions by Bragg's Law

$$n\lambda = d\sin\theta \qquad (1.14)$$

where $n$ is the diffraction order, d is the lattice spacing, $\theta$ is the diffraction angle relative to the surface normal, and $\lambda$ is the de Broglie wavelength of the incident electrons.

$$\lambda = \frac{h}{\sqrt{2 \cdot KE \cdot m_e}} \qquad (1.15)$$

where h is Planck's constant, $m_e$ is the electron mass, and KE is the kinetic energy of the electrons. The primary difference between LEED and x-ray diffraction techniques is that the incident electrons do not penetrate more than a few Ångströms into the sample, and therefore LEED is significantly more surface sensitive. LEED was used to verify the surface structure of the various substrates such as the (111) face of the gold [118]. The organic materials did not yield a strong diffraction pattern, and in many cases were damaged by the incident electron beam, therefore LEED was not used in determining the orientation of the organic films relative to the substrates although many attempts to do so were made.

Scanning tunneling microscopy (STM) is a technique first invented by Binning and Rohrer [119], where an atomically (or nearly atomically) sharp tip is held within electron tunneling distance (several Å) of the sample surface. When an appropriate bias, usually between several tenths of a volt and several volts (of either + or – polarity on the tip), is then applied between the tip and sample, electron tunneling is possible, provided that the sample is not insulating. A simple diagram for one-dimensional tunneling in the field emission regime from a metal in an external electric field is shown in Fig. 1.10A. This is a highly simplified diagram just to show an electronic wavefunction as the electron tunnels across a barrier (vacuum gap). There are a number of proposed models for the tunneling mechanism in STM, each with some validity for various different systems. The bottom line in each of these models is that the tunneling current between the tip and sample exponentially depends on the tip-surface separation:

$$I \propto \exp(-2\kappa s) \tag{1.16}$$

With $\kappa$ as the tunneling decay constant:

$$\kappa = \frac{(2m\phi)^{1/2}}{\hbar} \tag{1.17}$$

where $\phi$ is the effective local potential barrier height, $\hbar$ is the Planck constant, and m is the effective mass of the tunneling electron. In the three dimensional tunneling models for STM, the matching of the wavefunctions across the interface becomes extremely complicated due to effects such as different electronic density of states in the tip and/or

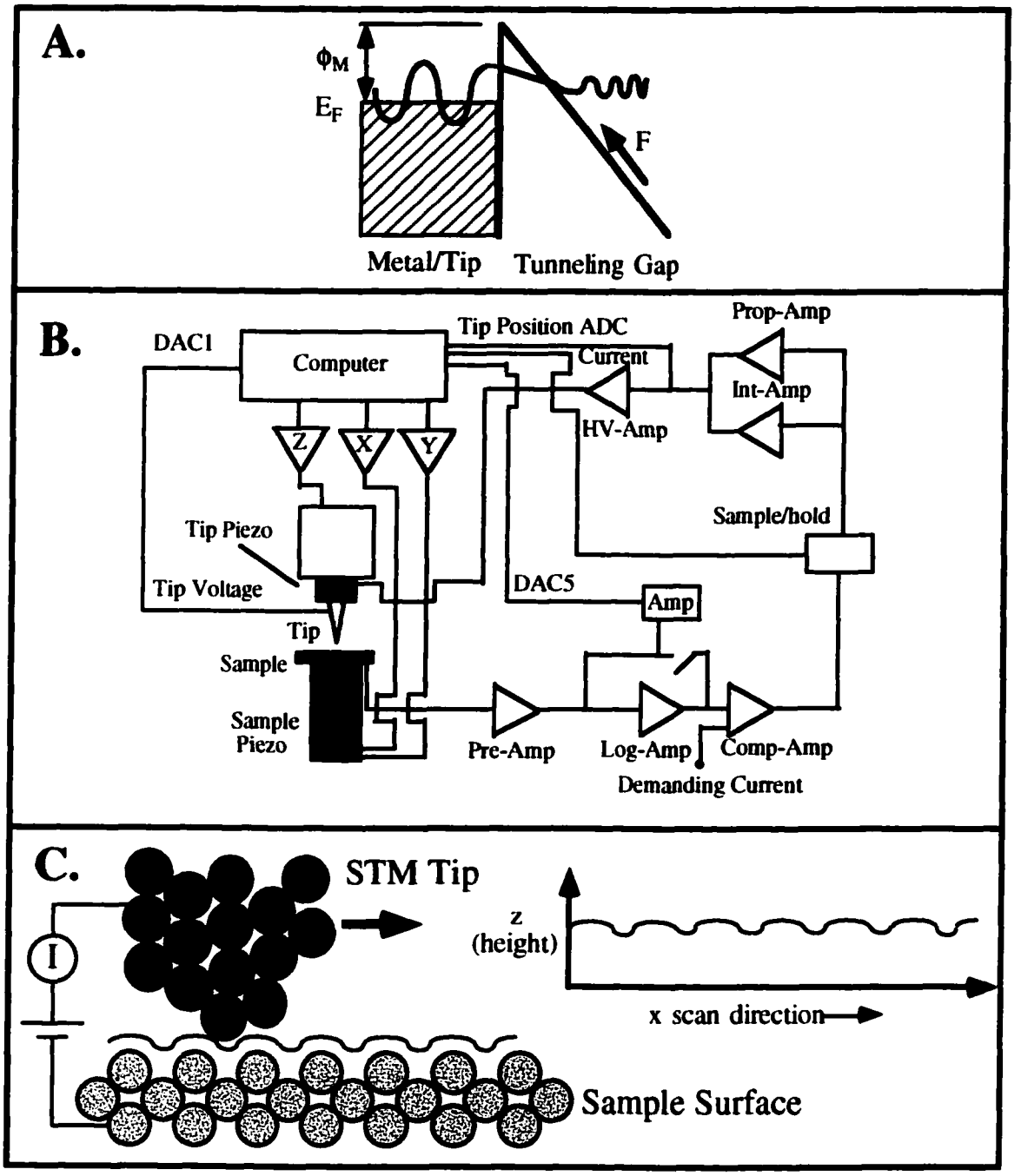


**Fig. 1.10:** **A.** Simplified schematic of field emission from metals in an external electric field based on Fowler-Nordheim tunneling. **B.** General electrical schematic for a feedback circuit in scanning tunneling microscopy. **C.** Constant current mode for an STM tip scanning with atomic resolution over a sample surface. On the right is a graphical depiction of the surface topography for a single scan line.

the sample or angle dependence of the tip wavefunction [93]. As a result, interpretation of STM images can often be difficult when trying to separate electronic structure effects from topographic features. Regardless, for the purposes of our experiments, STM is a useful tool for investigating local morphology of small molecules on surfaces.

Either the sample or the tip can be mounted on a piezo-electric tube for rastering in the x and y directions to obtain a two-dimensional image of the sample surface. The sample size that can be imaged with STM ranges from a few square nanometers up to several hundred square microns. The tip, attached to a piezo-electric mount, is modulated through a feedback loop (Fig. 1.10 B.) to maintain a constant tip to sample distance throughout the scan. The STM tip may be made of a variety of materials, but DC electrochemically etched tungsten (in 4M KOH) is used in experiments applied to this research. The two primary modes in which STM functions are constant current, and constant height. The constant current mode is the more commonly used method where the tunneling current is set to a constant value, usually between 0.05 and 2 nanoamperes. An electronic feedback mechanism measures the differential change in the tunneling current and then adjust the tip piezo accordingly to maintain the tunneling current at the preset value. This is shown schematically in Fig. 1.10.C. where the STM tip traces over the topography of the sample surface. On the right is a graphical depiction of a single scan line in the x direction of an STM image, where the z-scale or height is measured from the motion of the tip piezo as adjusted to maintain constant tunneling current. In the

constant height mode, the tip piezo is not adjusted and the corresponding image reflects the changes in the tunneling current. Since the tunneling current is exponentially dependent on the tip-to-sample distance, very subtle differences in the surface can be detected with STM. Molecular resolution is commonly achieved, and atomic resolution may be achieved with a clean sample surface, and a high quality tip. All of the STM images presented in this work were scanned in the constant current mode.

The STM in our laboratory is an Omicron® variable temperature microscope. To minimize vibrations, the STM base plate is suspended by four springs and equipped with a mechanism for eddy current dampening. In addition, the entire UHV system is mounted on air legs to further reduce mechanical vibrations, essential for achieving high-resolution STM images.

In our experiments, thin films of an organic semiconductor material between sub-monolayer and several monolayers are deposited onto the substrate surface then imaged with scanning tunneling microscopy. The obtained STM images are a convolution of topography and electronic state densities. There is frequently a bias dependence on the optimal tunneling conditions, often attributed to the different electronic states of the organic adsorbate. Molecular resolution images may be challenging to interpret since they may show molecular orbitals that are different from the molecular structure. Once molecular or atomic resolution is obtained in STM images, much insight about the spatial orientation of the molecules relative to each other as well as the orientation with respect

to the substrate can be deduced. The molecular orbital shapes of the organic compounds can lead to variations in the ionization energy, electron affinity, and work function of a molecular film depending on the orientation, when there is preferential molecular ordering on the surface. This in turn would influence the magnitudes of the injection barriers and charge injection behavior. Insight into the relationship between the molecular structure and electronic properties may help explain the energy levels at these interfaces. In addition, the understanding of how organic molecules are oriented on a metallic surface is of fundamental interest to the field of surface science.

The combined experimental focus of both the energetics of organic semiconductor interfaces, probed using photoelectron spectroscopy, and the morphology of the films, probed primarily using scanning tunneling microscopy, will help develop a full 'picture' of the chemical and physical phenomena at these interfaces.

A thorough understanding of the electronic and morphological properties at the interfaces of organic electronic materials requires the utilization of multiple surface science techniques. The advantage of having multiple techniques as well as the deposition chamber included in a single ultra-high vacuum system is that different properties of a single sample can be determined without ever breaking the vacuum. It is imperative that these properties be measured under UHV, since ambient conditions could easily oxidize the organic films and/or contaminate the sample surface, either of which could severely affect the accuracy of the measurements.

As emphasized throughout this chapter, most of the following experiments are focused on 'model' interfaces with the objective of precisely determining the presence and magnitudes of electron and hole injection barriers, band bending, and interfacial dipoles. While some of these systems are not necessarily applicable to specific devices, detailed measurements of the interfacial energetics can lead to a better understanding of the underlying physical phenomena governing the behavior of organic based electronic devices.

**References**


[1] M. Pope, J. Chem. Phys. 38 (1963) 2042.

[2] W. Mehl, W. Buchner, Krist. Z. Phys. Chem. 47 (1965) 76.

[3] C. W. Tang, S. A. VanSlyke, Appl. Phys. Lett. 51 (12) (1987) 913.

[4] Y. Hamada, T. Sano, M. Fujita, T. Fujii, Y. Nishio, K. Shibata, Jpn. J. Appl. Phys. pt 2 32 (4A) (1993) L514.

[5] N. Donzé, P. Péchy, M. Grätzel, M. Schaer, L. Zuppiroli, Chem. Phys. Lett. 315 (5-6) (1999) 405.

[6] Y. Hamada, T. Sano, M. Fujita, T. Fujii, Y. Nishio, K. Shibata, Jpn. J. Appl. Phys. pt. 2 32 (4A) (1993) L511.

[7] Y. Hamada, T. Sano, M. Fujita, T. Fujii, Y. Nishio, K. Shibata, Chem. Lett. (1993) 905.

[8] Y. Hamada, H. Kanno, T. Sano, H. Fujii, Y. Nishio, H. Takahashi, T. Usuki, K. Shibata, Appl. Phys. Lett. 72 (16) (1998) 1939.

[9] M. Matsumura, T. Akai, Jpn. J. Appl. Phys. 35 (1996) 5357.

[10] Z. Y. Xie, J. S. Huang, S. Y. Liu, Y. Wang, Y. Q. Li, J. C. Shen, Appl. Phys. Lett. 74 (5) (1999) 641.

[11] J. Kido, Y. Iizumi, Appl. Phys. Lett. 73 (19) (1998) 2721.

[12] G. Gu, G. Parthasarathy, S. R. Forrest, Appl. Phys. Lett. 74 (2) (1999) 305.

[13] G. Gu, V. Khalfin, S. R. Forrest, Appl. Phys. Lett. 73 (17) (1998) 2399.

[14] C. Adachi, S. Tokito, T. Tsutsui, S. Saito, Jap. J. Appl. Phys. B 27 (2) (1988) L269.

[15] G. Gu, G. Parthasarathy, P. Tian, P. E. Burrows, S. R. Forrest, J. Appl. Phys. 86 (8) (1999) 4076.

[16] G. Gu, G. Parthasarathy, P. E. Burrows, P. Tian, I. G. Hill, A. Kahn, S. R. Forrest, J. Appl. Phys. 86 (8) (1999) 4067.

[17] A. Dodabalapur, L. J. Rothberg, T. M. Miller, Appl. Phys. Lett. 65 (18) (1994) 2308.

[18] T. Mori, K. Miyachi, T. Mizutani, J. Phys. D: Appl. Phys. 28 (1995) 1461.

[19] H. Mattoussi, H. Murata, C. D. Merritt, Y. Iizumi, J. Kido, Z. H. Kafafi, J. Appl. Phys. 86 (5) (1999) 2642.

[20] Y. Hamada, H. Kanno, T. Tsujioka, H. Takahashi, T. Usuki, Appl. Phys. Lett. 75 (12) (1999) 1682.

[21] G. Sakamoto, C. Adachi, T. Koyama, Y. Taniguchi, C. D. Merritt, H. Murata, Z. H. Kafafi, Appl. Phys. Lett. 75 (6) (1999) 766.

[22] X.-C. Gao, H. Cao, C.-H. Huang, S. Umitani, G.-Q. Chen, P. Jiang, Synth. Met. 99 (1999) 127.

[23] C. W. Tang, S. A. VanSlyke, C. H. Chen, J. Appl. Phys. 65 (9) (1989) 3610.

[24] Y. Hamada, C. Adachi, T. Tsutsui, S. Saito, Jpn. J. Appl. Phys. Pt. 1 31 (6A) (1992) 1812.

[25] G. E. Jabbour, Y. Kawabe, S. E. Shaheen, J. F. Wang, M. M. Morrell, B. Kippelen, N. Peyghambarian, Appl. Phys. Lett. 71 (13) (1997) 1762.

[26] L. S. Hung, C. W. Tang, Appl. Phys. Lett. 74 (21) (1999) 3209.

[27] A. Yamamori, C. Adachi, T. Koyama, Y. Taniguchi, J. Appl. Phys. 86 (8) (1999) 4369.

[28] Y. Shirota, Y. Kuwabara, H. Inada, T. Wakimoto, H. Nakada, Y. Yonemoto, S. Kawami, K. Imai, Appl. Phys. Lett. 65 (7) (1994) 807.

[29] C. Giebeler, H. Antoniadis, D. D. C. Bradley, Y. Shirota, J. Appl. Phys. 85 (1) (1999) 608.

[30] E. W. Forsythe, D. C. Morton, C. W. Tang, Y. Gao, Appl. Phys. Lett. 73 (11) (1998) 1457.

[31] S. R. Forrest, Chem. Rev. 97 (1997) 1793.

[32] A. R. Brown, D. D. C. Bradley, J. H. Burroughes, R. H. Friend, N. C. Greenham, P. L. Burn, A. B. Holmes, A. Kraft, Appl. Phys. Lett. 61 (23) (1992) 2793.

[33] J. H. Burroughes, D. D. C. Bradley, A. R. Brown, R. N. Marks, K. Mackay, R. H. Friend, P. L. Burns, A. B. Holmes, Nature 347 (1990) 539.

[34] P. W. M. Blom, M. J. M. de Jong, C. T. H. F. Liedenbaum, Polym. Adv. Technol. 9 (1998) 390.

[35] J. Kido, M. Kohda, K. Okuyama, K. Nagai, Appl. Phys. Lett. 7 (17) (1992) 761.

[36] Y. Kim, S. Kwon, D. Yoo, M. F. Rubner, M. S. Wrighton, Chem. Mater. 9 (12) (1997) 2699.

[37] G. Yu, C. Zhang, A. J. Heeger, Appl. Phys. Lett. 64 (12) (1994) 1540.

[38] G. Gustafsson, Y. Cao, G. M. Treacy, F. Klavetter, N. Colaneri, A. J. Heeger, Nature 357 (1992) 477.

[39] A. Köhler, D. A. dos Santos, D. Beljonne, Z. Shuai, J.-L. Bredas, A. B. Holmes, A. Kraus, K. Mullen, R. H. Friend, Nature 392 (1998) 903.

[40] M. G. Harrison, J. Grüner, G. C. W. Spencer, Phys. Rev. B 55 (12) (1997) 7831.

[41] X.-T. Tao, Y.-D. Zhang, T. Wada, H. Sasabe, H. Suzuki, T. Watanabe, S. Miyata, Adv. Mater. 10 (3) (1998) 226.

[42] Z. Bao, S. Campbell, Thin Solid Films 352 (1/2) (1999) 239.

[43] H. E. Katz, J. Mater. Chem. 7 (3) (1997) 369.

[44] D. J. Gundlach, Y.-Y. Lin, T. N. Jackson, D. G. Schlom, Appl. Phys. Lett. 71 (26) (1997) 3853.

[45] H. E. Katz, Z. Bao, J. Phys. Chem. B 104 (4) (2000) 671.

[46] J. H. Schön, S. Berg, C. Kloc, B. Batlogg, Science 287 (5455) (2000) 1022.

[47] J. H. Schön, C. Kloc, B. Batlogg, Phys. Rev. B 63 (12) (2001) 125304.

[48] J. H. Schön, C. Kloc, Appl. Phys. Lett. 78 (22) (2001) 3538.

[49] C. D. Dimitrakopoulos, S. Purushothaman, J. Kymissis, A. Callegari, J. M. Shaw, Science 283 (1999) 822.

[50] Z. Bao, A. J. Lovinger, A. Dodabalapur, Appl. Phys. Lett. 69 (20) (1996) 3066.

[51] A. R. Brown, C. P. Jarrett, D. M. de Leeuw, M. Matters, Synth. Met. 88 (1997) 37.

[52] J. G. Laquindanum, H. E. Katz, A. J. Lovinger, J. Am. Chem. Soc. 120 (4) (1998) 664.

[53] J. G. Laquindanum, H. E. Katz, A. J. Lovinger, A. Dodabalapur, Chem. Mater. 8 (11) (1996) 2542.

[54] A. Dodabalapur, L. Torsi, H. E. Katz, Science 268 (1995) 270.

[55] M. Pope, C. E. Swenberg, *Electronic Processes in Organic Crystals and Polymers* (Oxford University Press, Oxford, 1999).

[56] G. Grem, G. Leditzky, B. Ullrich, G. Leising, Adv. Materials 4 (1) (1992) 36.

[57] H. Yanagi, S. Okamoto, T. Mikami, Synthetic Metals 91 (1997) 91.

[58] G. Leising, S. Tasch, C. Brandstatter, W. Graupner, S. Hampel, E. J. W. List, F. Meghdadi, C. Zenz, P. Schlichting, U. Rohr, Y. Geerts, U. Scherf, K. Mullen, Synthetic Metals 91 (1997) 41.

[59] N. Koch, A. Rajagopal, J. Ghijsen, R. L. Johnson, G. Leising, J.-J. Pireauz, J. Phys. Chem. B 104 (7) (2000) 1434.

[60] T. Mikami, H. Yanagi, Appl. Phys. Lett. 73 (5) (1998) 563.

[61] E. Zojer, Z. Shuai, G. Leising, J. L. Brédas, J. Chem. Phys. 111 (4) (1999) 1668.

[62] P. G. Schroeder, M. W. Nelson, B. A. Parkinson, R. Schlaf, Surf. Sci. 459 (2000) 349.

[63] P. G. Schroeder, C. B. France, B. A. Parkinson, R. Schlaf, (to be published) .

[64] K. A. Cho, T. Shimada, M. Sakurai, A. Koma, J. Appl. Phys. 84 (1) (1998) 268.

[65] R. Zhang, H. Zheng, J. Shen, Synth. Met. 105 (1) (1999) 49.

[66] Y. Azuma, S. Akatsuka, K. K. Okudaira, Y. Harada, N. Ueno, J. Appl. Phys. 87 (2) (2000) 766.

[67] C. Kendrick, A. Kahn, S. R. Forrest, Appl. Surf. Sci. 104/105 (1996) 586.

[68] M. C. Gerstenberg, F. Schreiber, T. Y. B. Leung, G. Bracco, S. R. Forrest, G. Scoles, Phys. Rev. B 61 (11) (2000) 7678.

[69] R. Schlaf, B. A. Parkinson, P. A. Lee, K. W. Nebesny, N. R. Armstrong, J. Phys. Chem. B 103 (15) (1999) 2984.

[70] R. Schlaf, P. G. Schroeder, M. W. Nelson, B. A. Parkinson, P. A. Lee, K. W. Nebesny, N. R. Armstrong, J. Appl. Phys. 86 (3) (1999) 1499.

[71] J. H. Schön, C. Kloc, E. Bucher, B. Batlogg, Nature 403 (2000) 408.

[72] J. H. Schön, C. Kloc, B. Batlogg, Appl. Phys. Lett. 77 (16) (2000) 2473.

[73] J. Ishii, K. Sugiyama, E. Ito, K. Seki, Adv. Mater. 11 (8) (1999) 605.

[74] S. M. Sze, *Physics of Semiconductor Devices*, 2nd ed. (John Wiley & Sons, 1981).

[75] C. K. Chiang, C. R. J. Fincher, Y. W. Park, A. J. Heeger, H. Shirakawa, E. J. Louis, S. C. Gau, A. G. MacDiarmid, Phys. Rev. Lett. 39 (17) (1977) 1098.

[76] T. Minakata, M. Ozaki, J. Appl. Phys. 73 (4) (1993) 1819.

[77] N. Koch, G. Leising, L. M. Yu, A. Rajagopal, J. J. Pireauz, R. L. Johnson, J. Vac. Sci. Technol. A 18 (2) (2000) 295.

[78] M. G. Ramsey, M. Schatzmayr, S. Stafstrom, F. P. Netzer, Europhys. Lett. 28 (2) (1994) 85.

[79] X. Zhang, A. S. Shetty, S. A. Jenekhe, Macromolecules 32 (22) (1999) 7422.

[80] S.-J. Chung, J.-I. Jin, C.-H. Lee, C.-E. Lee, Adv. Mater. 10 (9) (1998) 684.

[81] S.-J. Chung, J.-I. Jin, K.-K. Kim, Adv. Mater. 9 (7) (1997) 551.

[82] C. H. Chen, J. Shi, C. W. Tang, Macromol. Symp. 125 (1997) 1.

[83] J. H. Schön, Z. Bao, J. Appl. Phys. 89 (6) (2001) 3526.

[84] C. J. Bloom, C. M. Elliott, P. G. Schroeder, C. B. France, B. A. Parkinson, J. Am. Chem. Soc. 123 (38) (2001) 9436.

[85] N. Sato, K. Seki, H. Inokuchi, J. Chem. Soc. Faraday Trans. 2 77 (1981) 1621.

[86] C. B. Duke, Surf. Sci. 70 (1977) 674.

[87] G. Kaindl, T.-C. Chiang, D. E. Eastman, F. J. Himpsel, Phys. Rev. Lett. 45 (22) (1980) 1808.

[88] R. Schlaf, B. A. Parkinson, P. A. Lee, K. W. Nebesny, N. R. Armstrong, Surf. Sci. Lett. 420 (1) (1999) L122.

[89] R. Schlaf, O. Lang, C. Pettenkofer, W. Jaegermann, J. Appl. Phys. 85 (5) (1999) 2732.

[90] M. A. Baldo, S. R. Forrest, Phys. Rev. B 64 (17) (2001) 085201.

[91] D. Emin, Phys. Rev. B 4 (10) (1971) 3639.

[92] D. Emin, Adv. Phys. 8 (1975) 305.

[93] R. Weisendanger, *Scanning Probe Microscopy and Spectroscopy* (University Press, Cambridge, 1994).

[94] G. Ertl, J. Küppers, *Low Energy Electrons and Surface Chemistry*, 2nd ed. (VCH Verlagsgesellschaft mbH, Weinheim, Ger., 1985).

[95] R. Schlaf, N. R. Armstrong, B. A. Parkinson, C. Pettenkofer, W. Jaegermann, Surf. Sci. 385 (1997) 1.

[96] R. Schlaf, B. A. Parkinson, P. A. Lee, K. W. Nebesny, N. R. Armstrong, Appl. Phys. Lett. 73 (8) (1998) 1026.

[97] The energy levels of the conduction band or lowest unoccupied molecular orbitals can be directly measured using inverse photoemission spectroscopy (IPES). However, uor laboratory is not equipped with this capablitliy.

[98] I. G. Hill, A. Kahn, J. Appl. Phys. 84 (10) (1998) 5583.

[99] N. Sato, M. Yoshikawa, J. Electr. Spect. and Rel. Phen. 78 (1996) 387.

[100] A. Rajagopal, A. Kahn, Adv. Mater. 10 (2) (1998) 130.

[101] T. Maruyama, A. Hirasawa, T. Shindow, K. Akimoto, H. Kato, A. Kakizaki, J. Lumines. 87-89 (2000) 782.

[102] A. Rajagopal, C. I. Wu, A. Kahn, J. Appl. Phys. 83 (5) (1998) 2649.

[103] M. P. Seah, in *Practical Surface Analysis by Auger and X-ray Photoelectron Spectroscopy*, edited by D. Briggs,M. P. Seah (John Wiley and Sons, New York, 1983), p. 181.

[104] K. Seki, E. Ito, H. Ishii, Synthetic Metals 91 (1997) 137.

[105] S. Narioka, H. Ishii, D. Yoshimura, M. Sei, Y. Ouchi, K. Seki, S. Hasegawa, T. Miyazaki, Y. Harima, K. Yamashita, Appl. Phys. Lett. 67 (13) (1995) 1899.

[106] I. G. Hill, A. Rajagopal, A. Kahn, J. Appl. Phys. 84 (6) (1998) 3236.

[107] D. Yoshimura, H. Ishii, S. Narioka, M. Sei, T. Miyazaki, Y. Ouchi, S. Hasegawa, Y. Harima, K. Yamashita, K. Seki, J. Elect. Spect. and Rel. Phen. 78 (1996) 359.

[108] D. Schlettwein, K. Hesse, N. E. Gruhn, P. A. Lee, K. W. Nebesny, N. R. Armstrong, J. Phys. Chem. B 105 (21) (2001) 4791.

[109] J. Yoon, J.-J. Kim, T.-W. Lee, O.-O. Park, Appl. Phys. Lett. 76 (16) (2000) 2152.

[110] Q.-T. Le, E. W. Forsythe, F. Nüesch, L. J. Rothberg, L. Yan, Y. Gao, Thin Solid Films 363 (2000) 42.

[111] G. Koller, R. I. R. Blyth, S. A. Sardar, F. P. Netzer, M. G. Ramsey, Appl. Phys. Lett. 76 (7) (2000) 927.

[112] C. Argile, G. E. Rhead, Surface Sci. Reports 10 (1989) 277.

[113] Y. Park, V. Choong, E. Ettedgui, Y. Gao, B. R. Hsieh, T. Wehrmeister, K. Mullen, Appl. Phys. Lett. 69 (8) (1996) 1080.

[114] E. Ettedgui, H. Razafitrimo, K. T. Park, Y. Gao, B. R. Hsieh, J. Appl. Phys. 75 (11) (1994) 7526.

[115] R. Schlaf, C. D. Merritt, L. A. Crisafulli, Z. H. Kafafi, J. Appl. Phys. 86 (10) (1999) 5678.

[116] R. Schlaf, P. G. Schroeder, M. W. Nelson, B. A. Parkinson, C. D. Merritt, L. A. Crisafulli, H. Murata, Z. H. Kafafi, Surf. Sci. 450 (2000) 142.

[117] R. Schlaf, C. D. Merritt, L. C. Picciolo, Z. H. Kafafi, J. Appl. Phys. 90 (4) (2001) 1903.

[118] *The Handbook of Surface Imaging and Visualization*; *Vol.* , edited by A. T. Hubbard (CRC Press, Inc., Boca Raton, Fl, 1995).

[119] G. Binning, H. Rohrer, C. Gerber, E. Weibel, Phys. Rev. Lett. 49 (1) (1982) 57.

# Chapter 2: Investigation of band bending and charging phenomena in frontier orbital alignment measurements of *para*-quaterphenyl thin films grown on highly oriented pyrolytic graphite and $SnS_2$

Published: P.G. Schroeder, M.W. Nelson, B.A. Parkinson, R. Schlaf, Surf. Sci. 459 (2000) p. 349-364

**Abstract**

Thin films of the polyparaphenylene (PPP) molecule *para*-quaterphenyl (*p*-4P) were grown in ultra high vacuum in a multi-step growth procedure on *in situ* cleaved highly oriented pyrolytic graphite (HOPG) and single crystals of the layered semiconductor $SnS_2$. Prior to growth and after each growth combined X-ray and ultraviolet photoelectron spectroscopy (XPS,UPS) measurements were carried out to determine the electronic structure of the interfaces. PPP organic interfaces are of interest because of the emissive properties of PPP molecules and their potential use in organic light emitting diodes and displays. The large difference between the $SnS_2$ and HOPG work functions ($SnS_2$: 5.38 eV; HOPG: 4.65 eV) allowed the quantitative examination of

band bending occurring in the *p*-4P layer due to the equilibration of the substrate and *p*-4P Fermi levels. The combination of UPS and XPS measurements allowed for separation of band bending, charging, and interface dipole related shifts of the high binding energy cutoff (secondary edge) of the UP-spectra which are needed for the precise determination of the interface dipole and the highest occupied and lowest unoccupied molecular orbital (HOMO, LUMO) alignment relative to the substrate electronic structure.

## 2.1 Introduction

Considerable interest in low molecular weight organic and polymeric semiconductor *p*-phenylenes has developed [1-10] since the initial demonstration of using poly(*para*-phenylene) as the active layer in a blue light-emitting device [11]. In order to tailor the devices to optimize performance characteristics such as onset voltages, electron-hole pair formation and radiative recombination, device lifetime as well as understanding the fundamental attributes and behavior of organic-semiconductor heterojunctions, a thorough understanding of the interfacial electronic structure is essential. The alignment of the highest occupied and lowest unoccupied molecular orbitals (HOMO, LUMO) is especially of interest at organic interfaces since their magnitude strongly affects the charge transfer across the interface.

This sparked considerable research efforts in recent years to determine the frontier orbital alignment at organic interfaces [12-21]. In these experiments the energy level

alignment at organic heterointerfaces is usually determined using ultraviolet photoelectron spectroscopy (UPS) in combination with a multi-step growth procedure of a thin film of one of the materials in contact on a substrate composed of the other. One of the biggest challenges in such orbital line-up measurements is distinguishing between interface dipole related shifts of the high binding energy cutoff of the He I UP-spectra and shifts caused by other phenomena affecting the entire PE-spectrum including the high binding energy cutoff. It was recently shown that band bending can be determined in these organic systems with good precision by additional XPS measurements of core levels of substrate and overlayer [22-26] which is an established technique in the field of inorganic semiconductor interfaces [27-29]. It should be mentioned here that our use of the expression "band bending" relates to this "inorganic origin" of the measurement technique. The source of the observed band bending shifts in organic systems is not clearly understood, yet. However, we chose to use the established inorganic terminology since the observed phenomena are very similar to what is observed in inorganic systems and due to a lack of a special "organic systems language". Therefore, in the following observed band bending effects in our measurements should be taken in this context.

When performing PES on organic interfaces, particular attention needs to be given to the possible occurrence of charging artifacts and final state screening shifts [30] that might be superimposed to the band bending related shifts. It was shown recently that final state screening effects likely do not play a significant role in these measurements

[25]. The results presented in this paper mainly focus on the development of band bending and charging related shifts at organic interfaces. A simple way to distinguish between band bending and charging related shifts is to compare experiments in which the same organic material is deposited on substrates having different work functions. Since charging of an organic semiconductor is mainly attributed to increasing film thickness, experiments where charging occurs should yield similar shifts of the overlayer spectra regardless of the substrate material. Band bending, though, depends on the work function difference between substrate and overlayer materials. In other words, the larger the difference of substrate and bulk overlayer work function the larger the expected band bending.

Following these considerations we used $SnS_2$ and highly oriented pyrolytic graphite (HOPG) as substrates with different work functions. Both substrates are layered materials having a two-dimensional crystal structure composed of van der Waals bonded sandwich layers. These properties result in a high chemical inertness and also allow the preparation of non-reactive and atomically smooth interfaces [31,32]. This is important for such model experiments since interface reactions and morphological effects would also result in peak shifts superimposed to the band bending and interface dipole related shifts. $SnS_2$ is a semiconductor being intrinsically n-type and having a work function of around 5.3 eV. HOPG is a semi-metal having a work function of 4.65 eV. Since *para*-quaterphenyl (*p*-4P) has a work function close to HOPG, the *p*-4P/HOPG interface

should be nearly free of band bending while due to the different work functions of p-4P and $SnS_2$ strong band bending can be expected to develop across the *p*-4P/$SnS_2$ interface.

Our experiments also make use of XPS work function measurements in addition to the standard UPS measurements. Since x-ray guns can be run at very low intensities, the onset of charging phenomena in the UP-spectra can be pinpointed easily by comparison between UPS and XPS values. This allows the determination of the maximum film thickness still allowing UPS measurements without interference of charging effects [26].

## 2.2 Experimental Details

The experiments were carried out in a commercial Omicron Multi-Probe ultrahigh vacuum (UHV) apparatus (base pressure = $5 \cdot 10^{-11}$ mbar) equipped with XPS, UPS and a VSW EA125 single channel hemispherical analyzer. The organic deposition chamber is attached to the analysis chamber allowing the samples to be prepared *in situ*. The base pressure of the growth chamber was $10^{-9}$ mbar. The $SnS_2$ crystal and HOPG were cleaved *in situ* using a glued on metal foil, and subsequently characterized with XPS and UPS prior to deposition. The *p*-4P films were grown by sublimation from a resistively heated BN crucible. The source was held at 100°C for 12 hours prior to deposition to remove residual gases and water vapor from the *p*-quaterphenyl. The *p*-4P films were deposited at a growth rate of about 4Å/s which was determined with a Leybold quartz

crystal microbalance (QCM). The source temperature during growth was 126$^0$C while the substrates were kept at room temperature. After each growth step, the samples were characterized *in situ* using XPS (MgKα, 50 eV pass energy) and UPS (HeI, 21.21 eV; and HeII, 40.81 eV, 10 eV pass energy) in normal emission. A -5.00 V bias was applied to the sample for the UPS measurements to separate sample and spectrometer high binding energy cutoffs. The samples were mounted on a pedestal elevated 5 mm above the sample plate to prevent stray electrons from the manipulator assembly interfering with the UP-spectra [33]. The spectrometer was calibrated to yield the standard values [34] of 75.13 eV for the Cu3p and 932.66 eV for the $Cu2p_{3/2}$ emission lines on an $Ar^+$ sputtered Cu sample. Binding energy zero was determined using the Fermi level position of the Cu sample. The overall analyzer resolution was determined from the width of the Cu Fermi edge (0.20 eV) as shown in Fig. 2.1. Therefore, work function and HOMO cutoff positions determined from the high binding energy cutoffs and HOMO onsets of UP-spectra were corrected for the analyzer broadening by adding 0.1 eV. XPS core level peak positions were determined by a fitting routine given in Reference [35] using IGOR Pro (Wavemetrics) data evaluation software.

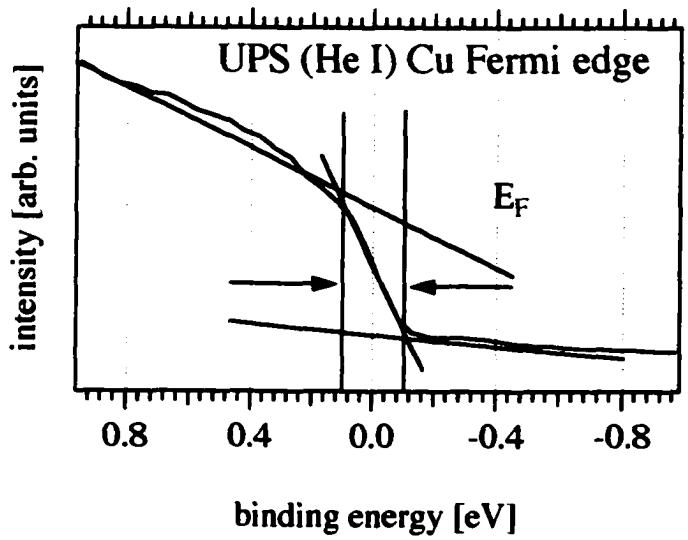


**Fig. 2.1:** Fermi Edge of an $Ar^+$ sputtered Cu sample measured with UPS (He I). The width of the Fermi edge due to analyzer broadening was determined to be 0.2eV giving an overall analyzer resolution of ±0.1eV.

## 2.3 Results

### 2.3.1. *p*-quaterphenyl on $SnS_2$

The *p*-4P film on the vacuum cleaved $SnS_2$ single crystal was grown in ten steps starting at a nominal coverage of 0.5Å up to the final coverage of 256Å. The UP-spectra measured with He I excitation are shown in Fig. 2.2. The schematic structure of *p*-4P is shown as insert in the center part of the Figure. On the left the high binding energy cutoff region of the spectra is shown normalized for better comparison. The graph on the right shows the valence bands/HOMO region magnified. The corresponding spectra measured with He II excitation are shown in Fig. 2.3. The bottom spectra of both figures 2.2 and 2.3 show the emissions from the clean vacuum cleaved $SnS_2$ substrate. The position of the valence band maximum (VBM) of the $SnS_2$ substrate was determined from these spectra by fitting a straight line into their low binding energy onsets and determining the intercept with the binding energy axis. The intercept positions determined are 2.21 eV for the case of the He I spectrum and 2.33 eV for the He II spectrum after adding 0.1 eV to account for the analyzer broadening. In the following band/orbital line-up determination the average between both values (2.27 eV) will be used as VBM position.

The upper spectra in Figs. 2.2 and 2.3 were taken after each subsequent *p*-4P growth step. Development of the *p*-4P molecular orbital structure is evident in both the

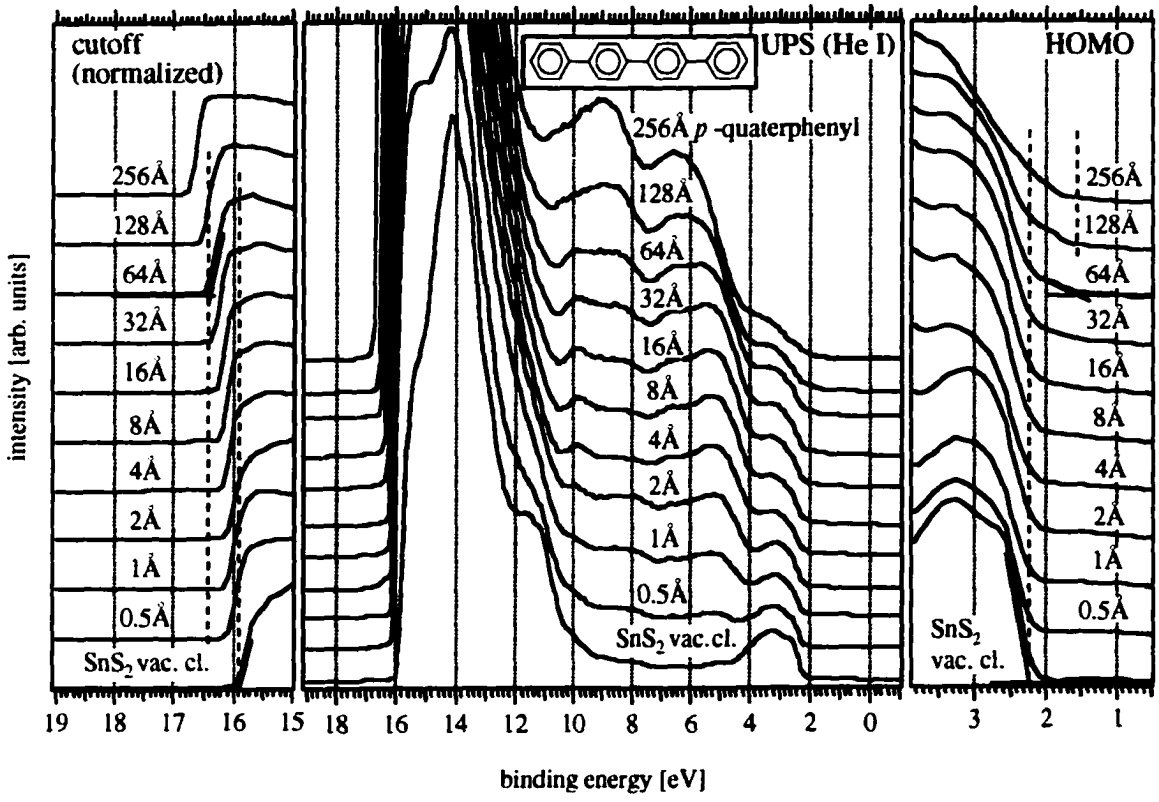


**Fig. 2.2**: HeI UP-spectra of *p*-4P grown on $SnS_2$. The bottom spectra show the vacuum cleaved substrate, while each subsequent growth step is shown above. On the left the high binding energy cutoff is shown normalized. The right part of the figure shows the magnified spectral range in which the *p*-4P HOMO is located. The insert in the center part shows the schematic structure of *p*-4P.

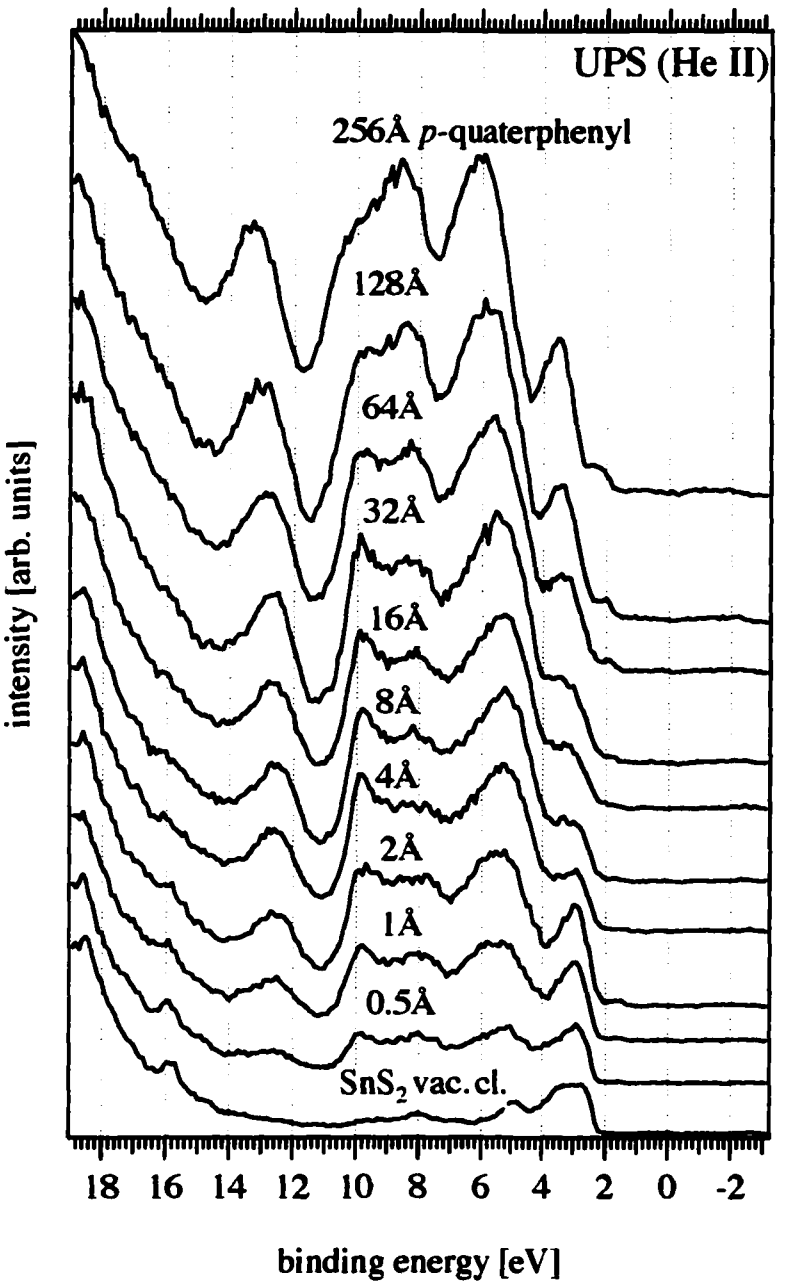


**Fig. 2.3:** HeII UP-spectra of *p*-4P on $SnS_2$.

He I and He II spectra as the spectral features of the $SnS_2$ substrate are attenuated with increasing *p*-4P coverage. The different spectral shape of the He II spectra is mainly caused by a weaker influence of final state effects caused by the higher photon energy [36], and possibly (to a lesser extent) by the different photoionization cross-sections of the C2s and C2p related features of the *p*-4P valence bands. The photoionization cross-sections ratios between 2s and 2p states are 0.2 and 0.7 for He I and He II while amounting to 18 and 66 for Mg Kα and Al Kα excitation energies [37]. This was used to explain the strong intensity differences between UPS and XPS spectra of sexiphenyl valence bands [38]. The cross-section influence when comparing our He I to He II spectra can expected to be much weaker due to the much smaller photoionization cross-section ratio difference. Furthermore, if cross-section effects played a significant role in our experiments the C 2p-related peaks close to the Fermi edge should appear weaker than lower lying C 2s-related peaks when measured with He II excitation compared to He I spectra (compare Ref. [39] for the assignment of the observed UPS peaks). Instead, our results show the opposite supporting the final state effects interpretation.

In addition to the above effects, both He I and He II spectra change shape and shift to higher binding energy as the film thickness increases. The shifts at higher coverages are partially caused by both the development of band bending and by charging artifacts. The spectra of the last three growth steps allow the identification of the weak HOMO feature between 1.8 and 2 eV binding energy. Owing to the onset of charging

phenomena at coverages higher than 64Å (see Section 2.3.2), the 64Å spectra were used for the determination of the HOMO cutoff position. This procedure is shown in Fig. 2.4 containing the magnified HOMO features of the He I and He II 64 Å-spectra (after background removal [40]) including the fitted lines shifted by the analyzer broadening of 0.1 eV. Determination of the intercepts with the x-axis yields 1.60 eV for the He I and 1.71 eV for the He II HOMO cutoff positions. As can be seen in Fig. 2.4, the HOMO shape in the He II spectrum is much more pronounced than in the He I. The He II cutoff position was therefore used in this evaluation of the orbital line-up to determine the HOMO position.

In order to determine the HOMO cutoff position right at the interface, the band bending that occurs across the junction must be included in the evaluation. The band bending is measured from XPS core level spectral shifts. A detailed description of the orbital line-up evaluation procedure can be found in Refs. [22,23]. The relevant core level XP-spectra of the system are shown in Fig. 2.5. The $SnS_2$ substrate related Sn 3d line is shown on the left and the *p*-4P-related C 1s line is on the right. The Sn 3d line becomes attenuated as the *p*-4P coverage increases but is not fully suppressed at the final 256 Å coverage. This indicates mainly island or cluster shaped growth of the *p*-4P layer in comparison to other experiments where good layer by layer growth could be assumed [23]. The C 1s peak appears after the first deposition step and strongly increases as the film becomes thicker. While the Sn 3d peak remains at its initial position (486.85±0.03

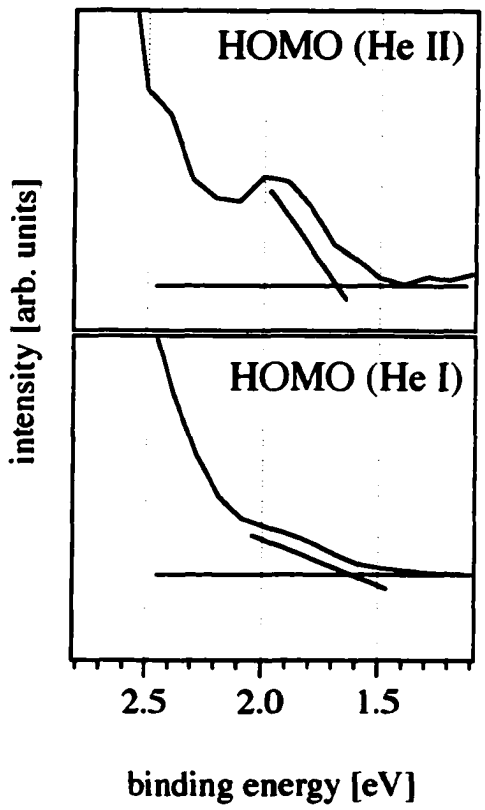


**Fig. 2.4:** Determination of the HOMO cutoff position from the background removed 64Å *p*-4P He I (top) and He II (bottom) spectra. The fitted lines are shifted to account for the analyzer resolution.

eV) throughout the experiment indicating that no band bending occurs in the $SnS_2$ crystal, the C 1s peak shifts to higher binding energy at higher coverages. The C 1s peak starts out at 283.97±0.03eV which represents the average of the 1, 2 and 4 Å peak positions which remain at a constant position (the 0.5 Å spectrum at 283.92 eV was dismissed due to its very low signal-to-noise ratio). This peak then shifts to 284.25 eV at 64 Å and finally to 285.45 eV at 256 Å film thickness. From this shift, the band bending at 64 Å film thickness determined to be

$V_b$(64Å *p*-4P) = 284.25eV - 283.97eV = 0.28eV

We need to point out that the real value might be somewhat smaller, since at 64 Å the band bending is not completely developed yet, i.e. the peak consists of contributions from regions of lesser band bending than the surface of the 64 Å layer. Owing to island growth mode of the layers the influence of this effect is difficult to quantify. The work function of the *p*-4P film after each deposition step was determined by subtracting the high binding energy cutoff positions from the He I energy (21.21 eV). A significant change in the work function is measured as the *p*-4P emissions dominate the spectra at thicker coverage. The initial work function of the clean $SnS_2$ substrate amounts to 5.38 eV. At 64 Å *p*-4P coverage the work function decreases to 4.88 eV (corresponding to 0.50 eV change) and then further to 4.57 eV at 256 Å. Fig. 2.6 shows both the work function change and the shift of the C1s peak relative to its first occurrence at 0.5 Å versus the *p*-4P coverage. Both the curves are aligned at their 64 Å points to graphically

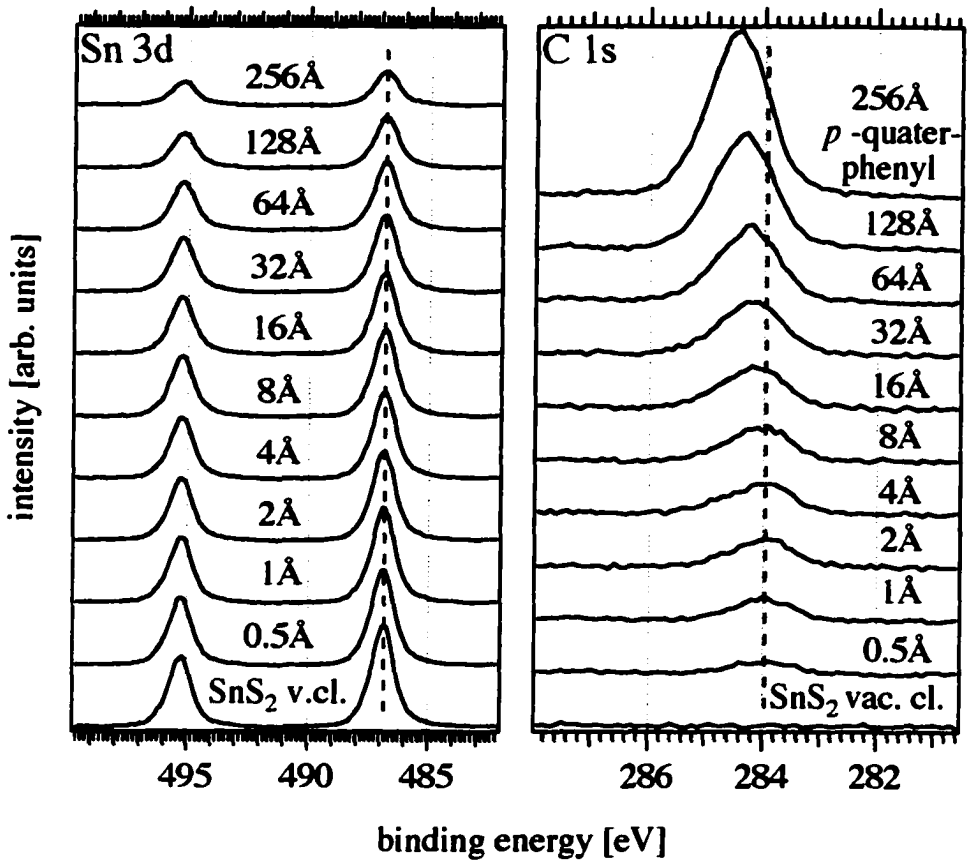


**Fig. 2.5:** Core level spectra of the C1s (right) and Sn3d (left) peaks for the *p*-4P on $SnS_2$ band lineup. A shift attributed to band bending is clearly visible in the C1s spectra while virtually no shift is detected in the Sn3d indicating that band bending in this heterojunction almost solely occurs in the organic layer.

demonstrate the occurrence of the interface dipole eD, corresponding to the difference between total band bending $V_b$ (determined from the C 1s shift) and total work function change (determined from the high binding energy cutoff shift). This results from the fact that the high binding energy cutoff shift is caused by interface dipole *and* band bending while core level peak shifts are only band bending related (if chemical interface reactions and final state shifts can be excluded which is probably the case in this system [25]). More details regarding this evaluation method can be found in Refs. [23,26]. Comparing the starting points of the two curves in Fig. 2.6 it is evident that the total work function change exceeds the C 1s shift between clean substrate and 64 Å overlayer. The interface dipole eD is the difference between total work function change and total C 1s shift, provided that charging related shifts can be avoided. This was accomplished by aligning two curves (Fig. 2.6) at the highest coverage where charging artifacts can still be safely dismissed, which was determined to be at 64 Å thickness for this system. This way, the dipole can be determined directly from the graph as the difference between the starting points of both curves amounting to

eD = 0.50eV - 0.28eV = 0.22eV

The offset between the $SnS_2$ VBM and the HOMO cutoff of the *p*-4P layer can now be determined by subtracting the initial $SnS_2$ VBM position (2.27 eV) and the band bending related shifts (0.28 eV) from the HOMO cutoff of the *p*-4P at 64 Å (1.71 eV) giving

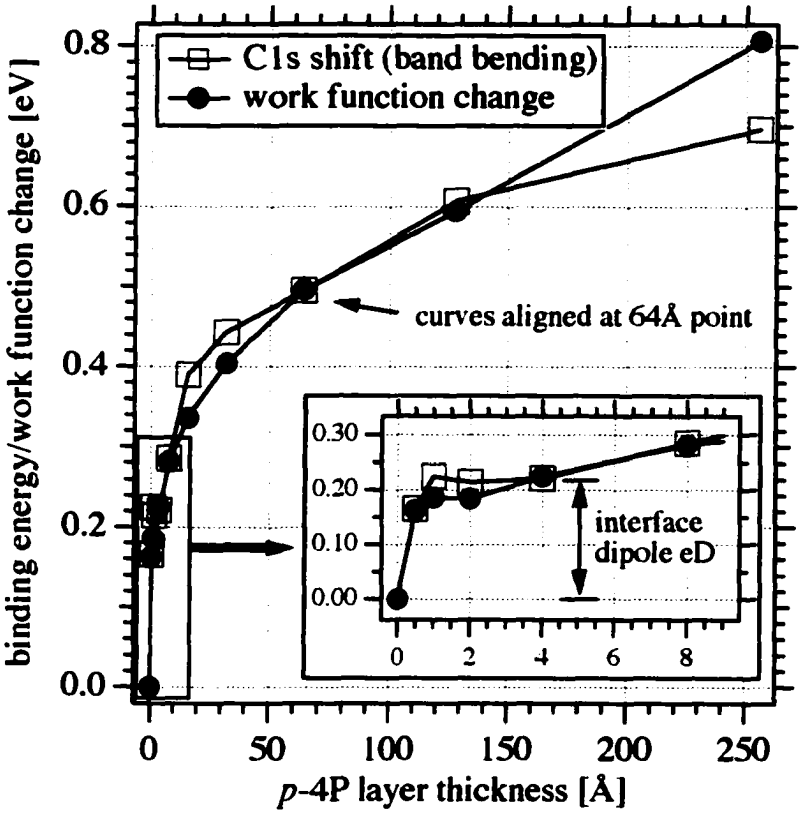


**Fig. 2.6:** *p*-4P on $SnS_2$: Comparison between C1s shift (open symbols) and work function change (solid symbols). Both curves are aligned at the 64Å point which is considered to be the last one without charging shifts in the UP-spectra. The difference between the starting points of the curves corresponds to the interface dipole eD related part of the work function change.

$\Delta HOMO_{cutoff}$ = 1.71eV - 2.27eV - 0.28eV = -0.84eV.

The negative value here indicates that the HOMO cutoff of the *p*-4P is at a lower binding energy than the VBM of the $SnS_2$.

The LUMO positions of the substrate and overlayer cannot be directly measured with UPS, but can be estimated by subtracting the difference of the known optical gaps of the materials from the ΔHOMO cutoff. The value used for the $SnS_2$ was 2.18 eV which is an average of the optical absorption measurements given in Ref. [29] and references therein. The HOMO/LUMO gap of the *p*-4P was determined to be 4.43 eV based on optical absorption measurements[4]. Due to the large excitonic binding energies in organic materials which can be of the order of 0.5 eV or larger [41] this value can only be regarded as a crude estimate giving a lower limit for the "electronic" band gap. Using the optical gap, the resulting barrier between the LUMO of the *p*-4P and the conduction band maximum (CBM) of $SnS_2$ was determined to be

$\Delta LUMO_{cutoff}$ = -0.84eV - 4.43eV + 2.18eV = -3.09eV.

The determined electronic structure of the $SnS_2$/*p*-4P interface is shown schematically in the top part of Fig. 2.7. The ionization energy $E_{ion}$ of *p*-4P was calculated by adding HOMO cutoff position (1.71 eV) to the work function (4.88 eV) of the 64 Å layer of the $SnS_2$ experiment yielding $E_{ion}$= 6.59 eV. Using the VBM position of

the clean $SnS_2$ substrate (2.27 eV) and its work function (5.38 eV) $E_{ion}$ of the $SnS_2$ sample was determined to be 7.65eV. This value differs somewhat from earlier reported numbers [23] which is probably related to the still experimental stage of $SnS_2$ crystal growth resulting in varying crystal quality. The considerably smaller value of 7.14 eV that is reported in Ref. [29] is a result of a different high binding energy cutoff evaluation procedure that did not take the analyzer broadening (about 0.3 eV) into account.

With regard to measurement errors it should be noted that often an error margin of about ±0.1 eV is assigned to photoemission measurements. This error margin refers to the determination of the *absolute* values for ionization energy, work function and core level peaks. The source for these errors is easily located in the case of the position determination of UP-spectra-related cutoff features (HOMO and high binding energy cutoffs). The evaluation of these features strongly depends on the way the lines are fitted into the edges. XPS core-level peak positions, however, can be determined very accurately owing to the well-defined peak shapes in combination with very precise peak fitting procedures. We estimate that for the case of good signal to noise ratio, errors in peak positions can be ±0.03 eV. Therefore, the main source of errors in absolute XPS peak positions results more likely from mis-calibration of the electron analyzers. Since for the determination of orbital offsets, band bending and interface dipole only differences of absolute energy values are used, the errors that have to be considered for these quantities are probably much smaller. This results from the fact that the UPS

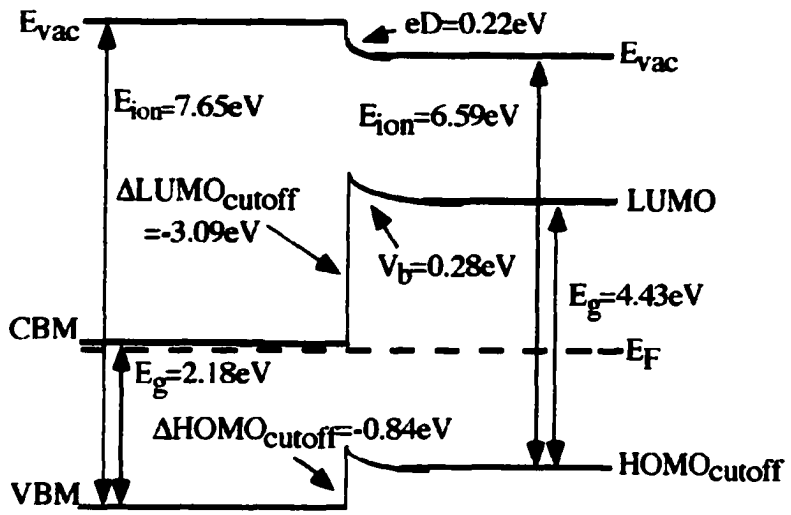


$SnS_2$ 64Å *p*-4P

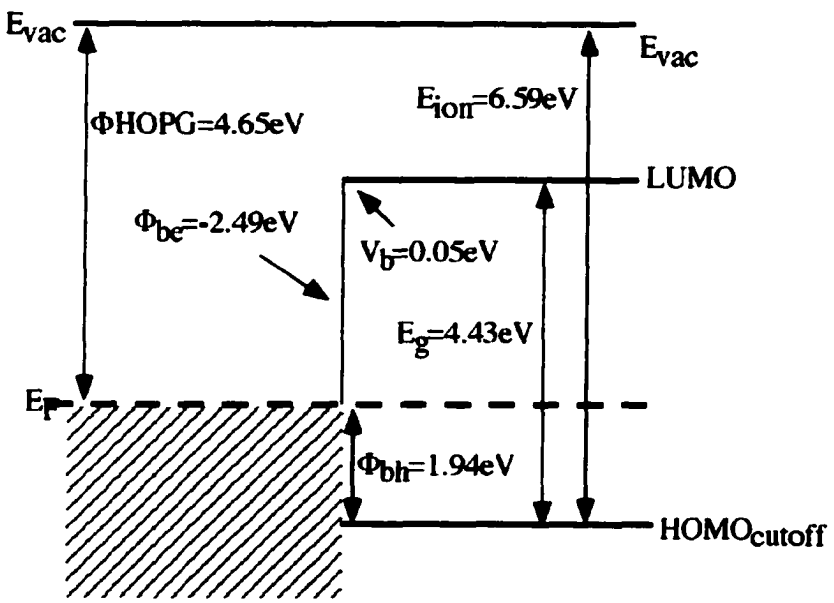


HOPG 64Å *p*-4P

**Fig. 2.7:** Schematic of the electronic structure of the *p*-quaterphenyl/$SnS_2$ (top) and the *p*-quaterphenyl/HOPG (bottom) interfaces at 64Å *p*-4P layer thickness as determined from the PES measurements.

cutoffs most likely all deviate by the same values since the same evaluation procedure is used for all of them. Also, XPS peaks monitored during a growth sequence will be shifted by the same values throughout the experiment. Therefore, we believe that that the overall measurement errors in orbital offsets and interface dipoles are in the range of about ±0.05 eV.

### 2.3.2. *p*-quaterphenyl on HOPG

On HOPG the *p*-4P film was grown in 12 steps starting at 0.2 Å nominal coverage to a final film thickness of 512 Å. Figs. 2.8 and 2.9 show the He I and He II UP-spectra before and during the growth session. The VBM/HOMO and the high binding energy cutoff regions of the He I spectra are shown in more detail in the right and left portions of Fig. 2.8 respectively. The high binding energy cutoff spectra are shown normalized. The bottom spectra of both Figures show the HOPG substrate after cleavage in vacuum. The He I substrate spectrum has only two distinct features being the strong conduction band related peak at 13.5 eV and the weak valence band feature at about 2.5-3 eV. The He II spectrum shows a broad valence bands related peak at about 6.5 eV. After deposition of the *p*-4P layers these features become attenuated, while the molecular orbital emissions of the *p*-4P start to dominate the spectra. Comparison of the spectral shapes of the He I and He II spectra with the corresponding spectra of the $SnS_2$/*p*-4P sequence reveals some intensity and shape differences between spectra of comparable layer thickness. At lower

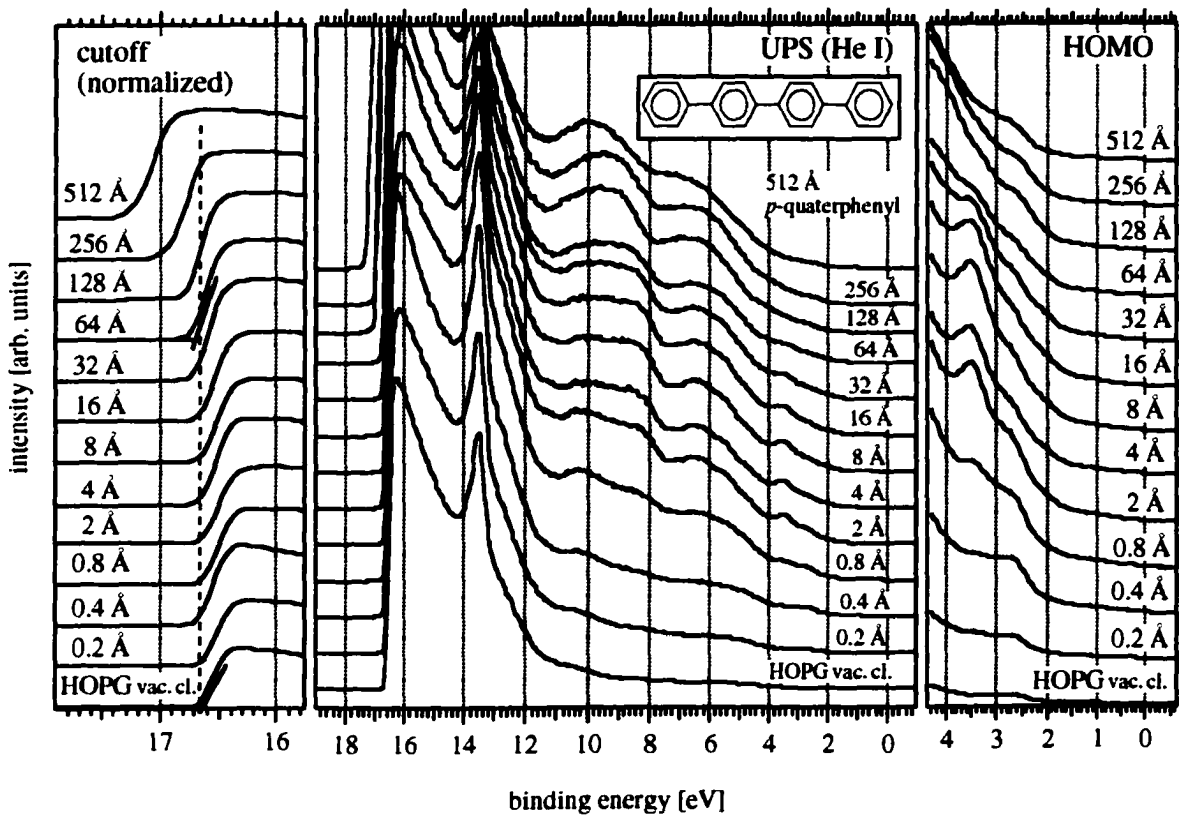


**Fig. 2.8:** HeI UP-spectra of the *p*-4P growth sequence on HOPG. Center: Full spectra. Left: High binding energy cutoff normalized. Right: Magnified region of the UP-spectra where the *p*-4P HOMO appears at increasing *p*-4P layer thickness. The bottom spectra show the vacuum cleaved HOPG substrate. The spectra above were taken after each *p*-4P growth step.

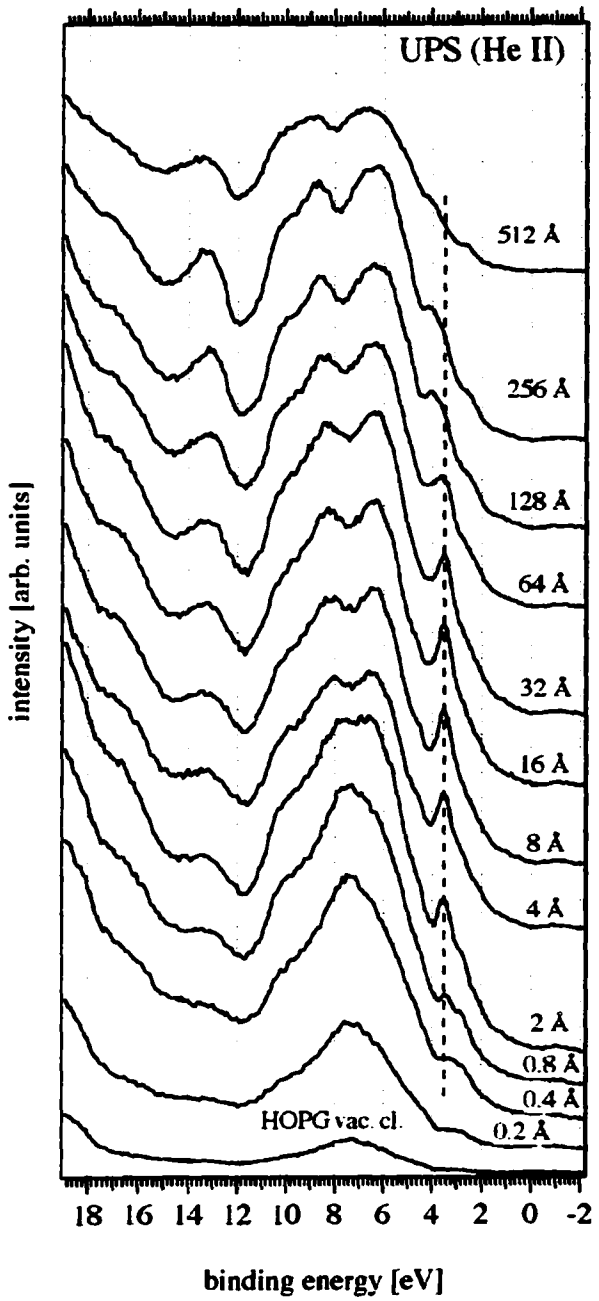


**Fig. 2.9:** HeII UP-spectra of *p*-4P on HOPG.

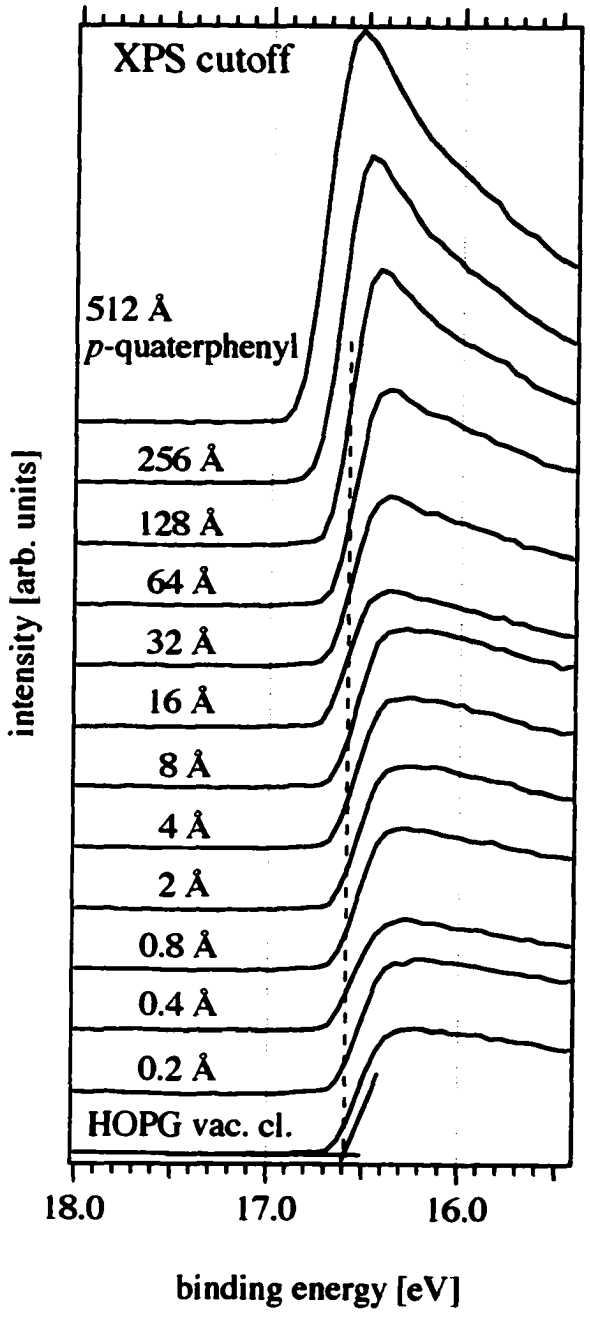


**Fig. 2.10:** *p*-4P on HOPG: XPS high binding energy cutoff. Comparison with the UPS high binding energy cutoff spectra show the onset of charging phenomena after the 64Å growth step in the UP-spectra.

coverages this is related to the different spectral shape of the substrate electronic structure and possibly also to a differing electronic interaction between substrate and over-layer. At higher film coverage this might be related to an earlier onset of charging phenomena due to more pronounced island growth for the case of the HOPG substrate (see below).

In order to determine the *p*-4P layer thickness at which charging artifacts start becoming significant we measured the high binding energy cutoff of the XP-spectra with retracted x-ray gun (to lower the photon flux) [26]. These spectra are shown in Fig. 2.10. Comparison with the high binding energy cutoff of the UP-spectra (Fig. 2.8, left) shows that the shifts of the XP-cutoff shift less at higher coverages than the corresponding UP-cutoffs. Fig. 2.11 compares the work function values derived from both sets of spectra versus the *p*-4P layer thickness. The work function values were determined by subtracting the high binding energy cutoff position from the He I excitation energy (21.21 eV) and adding 0.1 eV to compensate for the analyzer broadening. The work function of HOPG was determined to be 4.65 eV. The insert shows the 0-60 Å coverage range magnified demonstrating the close agreement between XPS- and UPS-derived work functions. Starting at 128 Å the curves deviate significantly indicating the onset of charging shifts in the UP-spectra. Therefore, the 64 Å spectra were chosen for the determination of the electronic structure of both interfaces.

In the XP-spectra the C 1s peaks of both HOPG and *p*-4P strongly overlap (see below) while no other elemental peaks are available which would allow for

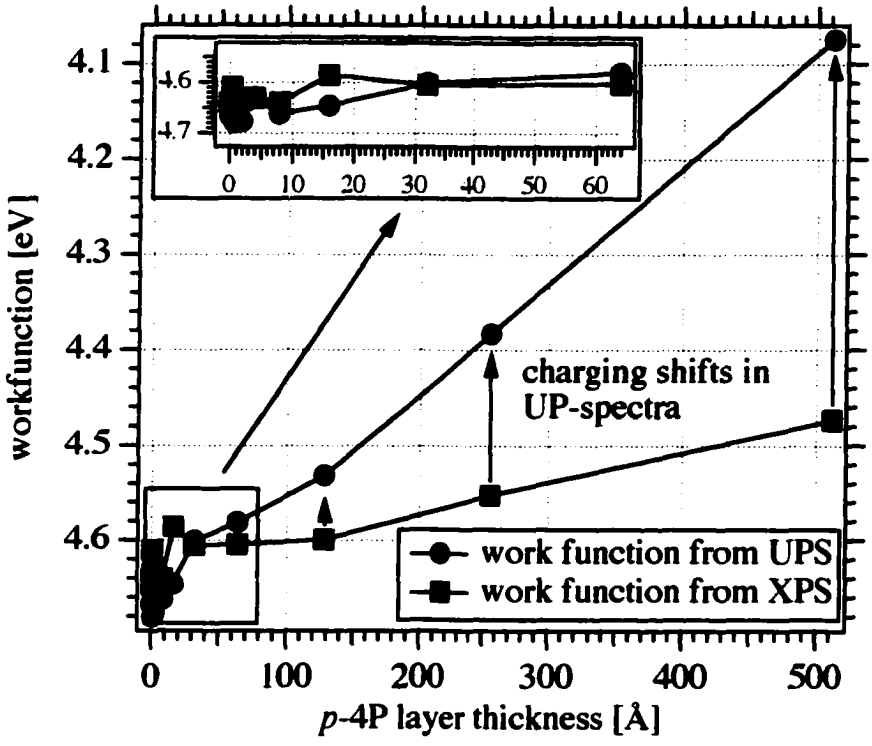


**Fig. 2.11:** Top: Work function change as a function of *p*-4P layer thickness. Both XPS (square symbols) and UPS (round symbols) derived values are plotted. The insert shows the 0 to 64Å range in more detail. It is evident that both curves start to deviate at *p*-4P layer thickness exceeding 64Å indicating the onset of charging phenomena in the UP-spectra.

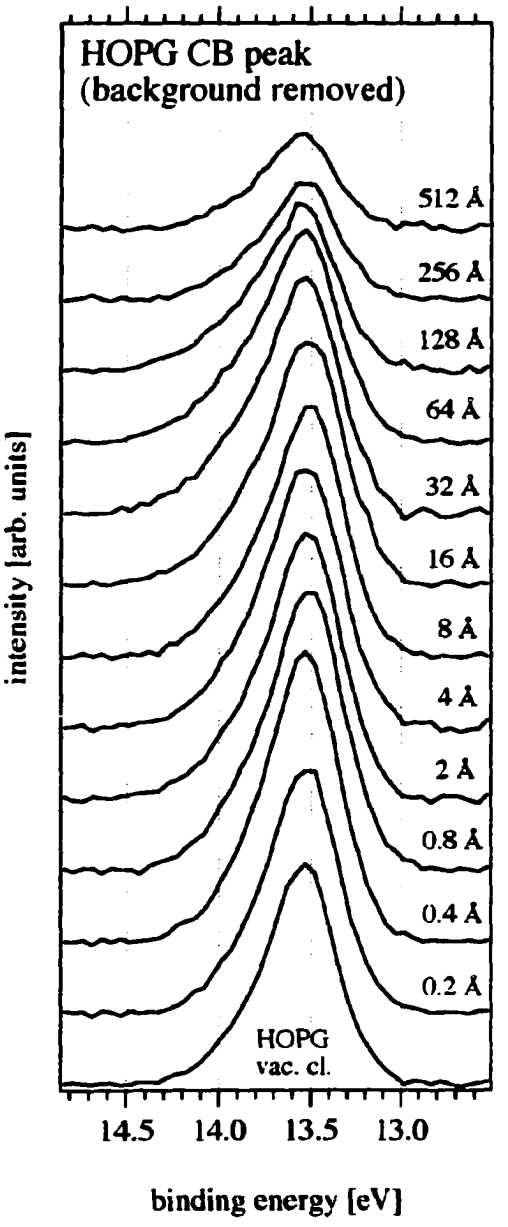


**Fig. 2.12:** UPS He I HOPG conduction band related peak at 13.5eV. Even at 512Å the peak is still visible indicating cluster growth mode.

distinguishing between substrate and over-layer emission intensity. As a result, the only spectral feature allowing an estimation of the growth mode of *p*-4P on HOPG is the conduction band-related UPS peak at 13.7 eV. This peak is shown in Fig. 2.12 after the background was removed by fitting a third-order polynomial into the surrounding spectral area. It is clear that this peak becomes only partially attenuated as the *p*-4P thickness increases which indicates that the *p*-4P film grew in a pronounced island growth mode. In a comparable experiment where a chloroindium phthalocyanine (ClInPc) film was grown on HOPG [25], this peak was completely suppressed between the 64 Å and 128 Å growth steps. It is well known that phthalocyanines grow epitaxially on layered materials in a layer-by-layer fashion [42-44].

Since the charging effects cause a blurred shape of the 64 Å and higher UP-spectra, the weak HOMO peak cannot be identified very clearly. Only a weak shoulder seems to appear in both the He I and He II spectra, which cannot be evaluated with high accuracy. This complicates the determination of the orbital line-up at the interface. The unchanged position of the high binding energy cutoff between clean substrate and the 64 Å *p*-4P layer shows, however, that no interface dipole occurs at this interface. It is possible to circumvent the charging problem by using the ionization energy $E_{ion}$ of *p*-4P as determined from the *p*-4P on $SnS_2$ experiment (6.59 eV). Using $E_{ion}$, Schottky's rule can be applied to calculate the hole injection barrier $\Phi_{bh}$ (HOMO offset) relative to the Fermi level of the HOPG by aligning HOPG and *p*-4P at the vacuum level. Using the

HOPG work function of 4.65eV, $\Phi_{bh}$ is then determined by subtracting the HOPG work function from $E_{ion}$ yielding $\Phi_{bh}$ = 1.94 eV.

The position of the electron injection barrier (LUMO offset relative to HOPG Fermi level) is estimated by subtracting the optical gap of *p*-4P (4.43 eV) from $\Phi_{bh}$, yielding $\Phi_{bc}$ = 1.94 - 4.43 eV = -2.49 eV.

In order to draw the final picture of the *p*-4P/HOPG electronic structure the amount of band bending in the *p*-4P layer needs to be determined. Fig. 2.13 shows the XP-spectra of the C 1s peak during the growth series. This peak remains at a constant position throughout the experiment, indicating that the C 1s positions of HOPG and the *p*-4P layer are at similar positions and that no significant band bending occurs as the layer grows thicker. However, from the evolution of the UP-spectra it can be deduced that some weak band bending occurred at the interface. The insert in Fig. 2.11 shows the evolution of the work function of the growth steps up to 64 Å. It is evident that only a weak gradual shift occurs which amounts to about 0.05 eV. This shift coincides with the slight shift of the peaked feature at about 3.6 eV of the He II spectra (Fig. 2.9). Therefore, we can conclude that 0.05 eV band bending developed in the 64 Å layer. The schematic on the bottom of Fig. 2.7 summarizes the determined electronic structure of the *p*-4P/HOPG interface.

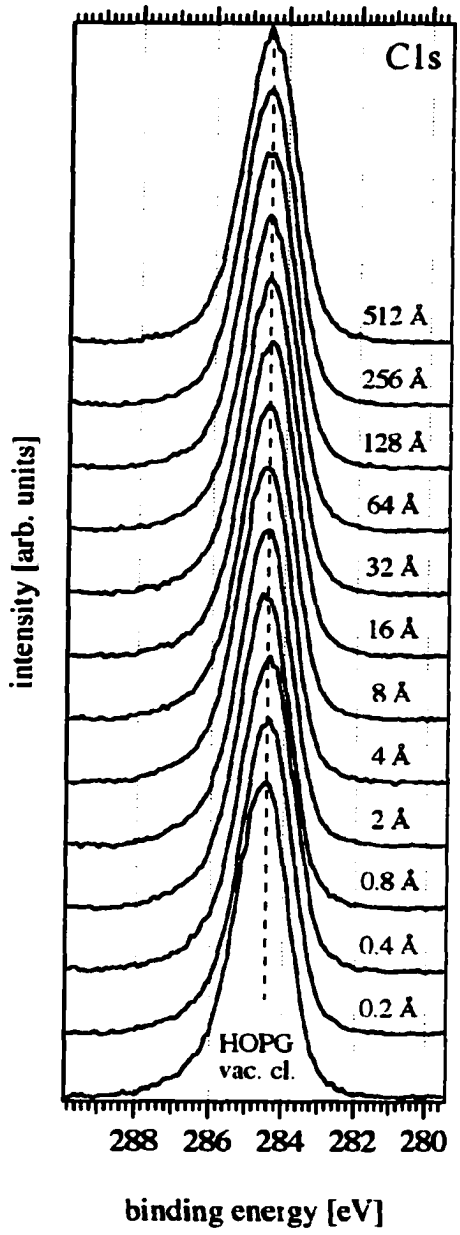


**Fig. 2.13:** *p*-4P on HOPG: Evolution of the C1s XPS core level peak as the *p*-4P layer grows thicker. The stable position of the peak indicates that no significant band bending occurs at this interface.

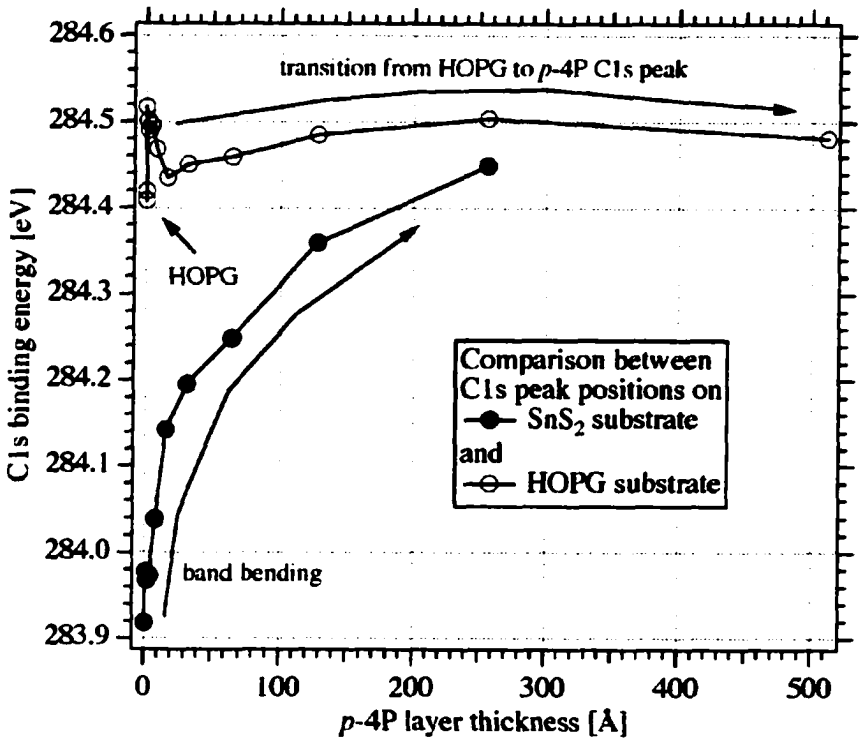


**Fig. 2.14:** Comparison of the C1s peak positions of the HOPG and the $SnS_2$ experiments. It is evident from the curves that at the $SnS_2$ interface strong band bending occurs. As the *p*-4P layer on $SnS_2$ grows thicker the C1s position converges with the nearly constant C1s position measured on the HOPG substrate. This demonstrates that the detected shifts are band bending related.

## 2.4 Discussion

The positions of the C 1s peak of both the *p*-4P on HOPG and $SnS_2$ experiments relative to the *p*-4P layer thickness are shown in Fig. 2.14. Although the peak remains at a constant position during the experiment on HOPG, it starts out at about 0.5 eV lower binding energy in the case of the $SnS_2$ experiment. As the *p*-4P layer grows thicker the $SnS_2$ position converges with the HOPG. This is exactly what is expected when the shifts are band bending related. The large work function of the $SnS_2$ crystal will cause the *p*-4P electronic structure to align at lower binding energy right at the interface (closer to the Fermi level) than in the case of HOPG. This causes the C 1s peak of the thin *p*-4P layers on $SnS_2$ to appear at lower binding energy (see Fig. 2.7). As the *p*-4P layer grows thick enough to develop a sufficiently large space charge region to compensate for the initial Fermi level difference (contact potential), it will start to assume its own bulk Fermi level position that is independent of the substrate. This clearly demonstrates that band bending is responsible for the strong C 1s shift observed.

Regarding the reasons for the band bending effects observed we can only speculate so far that the doping of the layers either occurs due to trace impurities in the organic material or due to X-ray/UV radiation created defects which act as dopants. PES is not sensitive enough to detect the minute stoichiometric changes or extremely low concentration of impurities sufficient to cause significant doping effects. It is also possible that charged species within the organic material diffuse to equilibrate the

substrate and over-layer Fermi levels similar to what is assumed to be the cause for band bending effects observed in systems involving thin LiF layers [45].

The curves in Fig. 2.14 also demonstrate that no charging effects occurred in the XPS core-level peak measurements. Otherwise, similarly strong C 1s shifts should have been observed in both experiments. However, our experiments clearly indicate that in UPS measurements charging occurs. The additional XPS work function measurements of the HOPG experiment (compare Figs. 2.10 and 2.11) show that the UPS and XPS high binding energy cutoff positions start to deviate after the *p*-4P layer thickness exceeds 64 Å. The significantly higher binding energies of the UPS cutoffs at high coverages show that charging occurred during these measurements. The reason for the charging shifts during UPS measurements is a result of the magnitudes higher photon flux of the UV source compared to that of the x-ray gun used for XPS. This makes the additional XPS (low intensity) work function measurements an ideal 'probe' for the onset of charging phenomena in UP-spectra. However, we need to point out here, that even the low intensity XPS work function measurements still cause some charging shifts at the highest coverages. From Fig. 2.14 it is evident that the C1s peak does not shift significantly between the 128 and 512 Å layers of the HOPG experiment while the XPS work function decreases by about 0.12 eV. This can be explained by the fact that during the XPS work function measurements, the x-ray gun is operated about 5 cm away from the sample in its retracted position, whereas during core level peak measurements the gun is located as

close to the sample as possible to get maximum intensity. It is well known that standard non-monochromatic x-ray sources, such as the one used in these experiments, produce their 'own' secondary electrons due to photoemission processes in the Al Bremsstrahlung filter and in the nozzle of the gun [46]. These low energy electrons cause the end of the x-ray gun to act as an intrinsic flood gun that replenishes the photo-emitted electrons of the sample, reducing charging effects. The reason that the XPS work function measurements need to be carried out with retracted gun lies in the presence of these electrons. Since a –5 V bias potential is applied to the sample during work function measurements, the secondary electrons from a x-ray gun that is close to the sample are also attracted into the analyzer. This would result in erroneous work function measurements (i.e. the high binding energy cutoff of the gun assembly materials would be superimposed on the sample cutoff). Retraction solves the problem, since only an insignificant amount of these electrons reaches the analyzer (and sample). Tests on a variety of clean metal substrates showed that the XPS and UPS high binding energy cutoffs coincide within 0.05 eV accuracy if the x-ray gun is operated at 5 cm distance [47].

Comparing the orbital line-up of the HOPG with the $SnS_2$ interface shows another significant difference besides the occurrence of band bending. The $SnS_2$ interface shows a small 0.22 eV interface dipole offsetting the *p*-4P orbitals relative to the $SnS_2$ bands while they align directly at the vacuum level without a dipole at the HOPG interface.

The reason for this probably lies in the different electronic interaction of *p*-4P with HOPG and $SnS_2$. In the case of $SnS_2$, recent results on heterojunctions [29,48] between layered semiconductors similar to $SnS_2$ suggest that the small dipole might be a result of the occurrence of a quantum dipole due to tunneling of carriers across the large orbital/band offsets of this interface. A similar experiment at the $SnS_2$ and PTCDA interface [23], which has much smaller orbital offset than the *p*-4P interface, concluded that this interface is dipole free. This would support the quantum dipole explanation since quantum dipoles depend on the magnitude of the band offsets at semiconductor heterojunctions. The absence of such a dipole at the HOPG/*p*-4P interface can possibly be related to the strong similarities in the chemical nature of HOPG and a *p*-quaterphenyl film which are probably responsible for the very similar work functions and C 1s peak positions. Interface dipoles are the direct result of localized charge transfer at the interface. In the absence of structural effects or reactions, an interface between similar materials should therefore have only insignificant dipoles.

Some more evidence for the different types of interaction at both of the interfaces can be found in the spectral shapes of the UP-spectra. At higher coverages the thick film spectra of both systems closely resemble the UP-spectra of the slightly larger PPP oligomer *p*-sexiphenyl (*p*-6P) [49]. These spectra also correspond well to the density functional theory simulated UP-spectra of *p*-6P [3]. At low *p*-4P film coverage (0.2-16 Å), significant differences from the above experiments are observed (primarily in the He

II spectra). On HOPG a very distinct sharp peak develops at about 3.5 eV. This peak is not present in series on $SnS_2$, but here a similar feature develops at about 9.8 eV (see Fig. 3) and then blends into the adjacent valence band peak towards lower binding energy as the *p*-4P layer grows thicker. The locations of both of these features correspond to energetic regions of the substrate band structures where the density of states (DOS) is vanishing in normal direction to the crystal surface (Δ direction of the hexagonal Brillouin zone of the crystals) [50,51]. This allows the assumption that a similar effect takes place in the *p*-4P layers as was observed in the case of ultrathin InSe layers grown epitaxially on HOPG [51]. Owing to the lack of overlap with the substrate DOS at the two locations, the molecular states of the *p*-4P molecules are not broadened by chemical interaction with the substrate. The *p*-4P molecules do retain their molecular states as long as the layer is thin enough to prevent the broadening caused by intermolecular interaction. As the films reach a certain thickness the bulk electronic structure of *p*-4P develops becoming independent of the substrate DOS. To determine conclusively whether these features are true molecular states, experiments on well ordered films using synchrotron radiation allowing the measurement of the band dispersion would need to be conducted.

It is difficult to compare the *p*-4P growth modes between the two systems. While the $SnS_2$ substrate offers the Sn or S peaks to be compared with the solely *p*-4P related C1s peak, the *p*-4P/HOPG system only allows an estimation using the *p*-4P thickness

dependent attenuation of the HOPG conduction band (CB) feature of the HeI UP-spectra (Fig. 2.12). In the case of the $SnS_2$/*p*-4P system, the comparison of the C1s and Sn3d peak intensities vs. the *p*-4P layer thickness allows the conclusion that Stranski-Krastanov growth occurs in these systems [52]. The top graph of Fig. 2.15 shows that during the very first growth steps the intensity of the C1s peak decreases very fast while a similar steep decrease of the Sn 3d peak is noted. Then the slope of the intensity curves decreases for both peaks. This indicates that the *p*-4P layer grows at first as a flat layer leading to the fast intensity change observed in the beginning while the following layers grow in a clustered fashion resulting in a slower intensity change since less surface area is covered per deposited amount of *p*-4P. These results are consistent with observations made at *p*-4P layers deposited on KCl (001) surfaces [4]. It is important to point out that the interaction between KCl and *p*-4P is probably differs considerably from the investigated layered materials interfaces due to the ionic and three-dimensional character of KCl.

The bottom graph in Fig. 2.15 shows the comparison of the Sn 3d and the HOPG CB peak normalized intensities indicating differences between the growth modes. As is evident from Fig. 2.12 the first two HOPG CB spectra have somewhat lower intensities than the third one (probably caused by slightly differing operation conditions of the UV lamp). Therefore, we did not use these first two spectra but instead normalized the HOPG curve on the third one. In order to compare the Sn 3d with the HOPG curve with

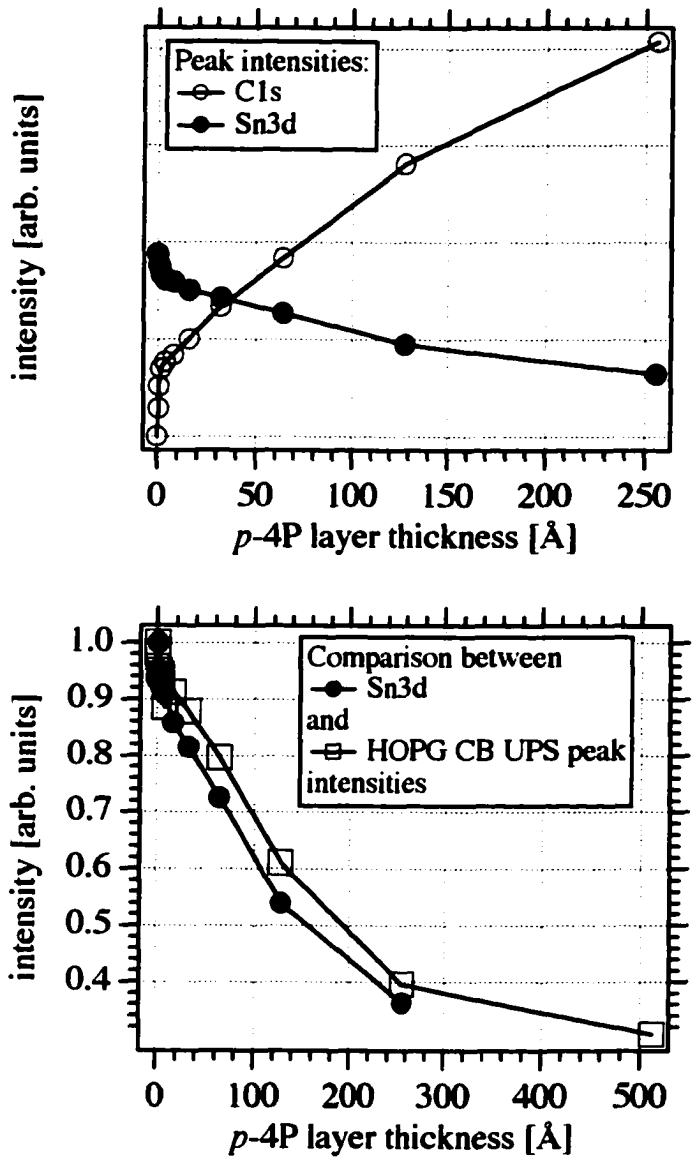


**Fig. 2.15:** Top: $SnS_2$/*p*-4P interface: Cross section corrected intensities of the C1s and Sn3d core peaks as a function of *p*-4P layer thickness. The fast change during the early growth stages in combination with the slow change at larger thickness reveals a growth pattern indicative of the Stranski-Krastanov growth mode. Bottom: Comparison between $SnS_2$ and HOPG experiments. The HOPG conduction band related UPS peak at 13.5eV becomes attenuated more slowly than the Sn3d peak despite the larger escape depth of the Sn3d electrons. This indicates a more strongly clustered growth mode of the *p*-4P layer on the HOPG substrate than on $SnS_2$.

consistency, the Sn 3d curve was also normalized on the third point. It is evident that the HOPG CB intensities become attenuated somewhat slower than the Sn 3d. Taking into account the lower escape depth of the UPS electrons of the HOPG peak it can be concluded from Fig. 2.15 that the *p*-4P films grow more clustered on HOPG than on $SnS_2$. This is in agreement with the observation that the UP-spectra of the thicker *p*-4P coverages on HOPG seem to become blurred earlier due to the onset of charging effects being related to the earlier development of thicker clusters.

## 2.5 Conclusion

Thin films of *p*-quaterphenyl (*p*-4P) were grown in multiple steps on vacuum cleaved $SnS_2$ and highly oriented pyrolytic graphite (HOPG). The alignment of the HOMO and LUMO of *p*-quaterphenyl relative to the valence/conduction bands of the $SnS_2$ as well as the Fermi level of the HOPG were determined by combined X-ray and ultraviolet photoemission spectroscopy. These measurements were performed during multi-step *in situ* growth sequences of *p*-4P on both substrate materials. Comparison of the spectral XPS and UPS shifts observed in both experiments allows the conclusion that band bending occurs in the *p*-4P layers with the magnitude of band bending depending on the work function of the substrate. While the HOPG interface was essentially free of band bending (0.05 eV) at the $SnS_2$ interface a value of 0.28 eV was found at 64 Å *p*-4P thickness. The onset of charging shifts in the UP-spectra depending on the *p*-4P layer

thickness was determined by using XPS work function measurements. This allowed band bending and charging related spectral shifts of the UP-spectra to be separated. At the $SnS_2$/*p*-4P interface a small 0.22 eV dipole was determined and is possibly related to the formation of a quantum dipole due to tunneling of charge carriers across the interface. The hole injection barriers (HOMO offsets) at the two interfaces were determined to be 1.94 eV between the *p*-4P HOMO cutoff and HOPG Fermi level and -0.84 eV between $SnS_2$ valence band maximum and *p*-4P HOMO cutoff.

**Acknowledgements**

We are grateful to H. Yanagi for helpful discussions.

## References


[1] M.G. Ramsey, M. Schatzmayr, S. Stafstrom and F.P. Netzer: Europhys. Lett. 28(2) (1994) 85.

[2] G. Leising, S. Tasch, F. Meghdadi, L. Athouel, G. Froyer and U. Scherf: Synthetic Metals 81 (1996) 185.

[3] N. Koch, L.-M. Yu, V. Parente, R. Lazzaroni, R.L. Johnson, G. Leising, J.-J. Pireauz and J.-L. Bredas: Adv. Mater. 10(13) (1998) 1038.

[4] T. Mikami and H. Yanagi: Appl. Phys. Lett. 73(5) (1998) 563.

[5] M.S. Miao, P.E. Van Camp, V.E. Van Doren, J.J. Ladik and J.W. Mintmire: J. Chem. Phys. 109(21) (1998) 9623.

[6] M.A. Keegstra, V. Cimrová, D. Neher and U. Scherf: Macromol. Chem. Phys. 197(8) (1996) 2511.

[7] S. Narioka, H. Ishii, K. Edamatsu, K. Kamiya, S. Hasegawa, T. Ohta, N. Ueno and K. Seki: Phys. Rev. B 52(4) (1995) 2362.

[8] A. Piaggi, G. Lanzani, G. Bongiovanni, A. Mura, W. Graupner, F. Meghdadi, G. Leising and M. Nisoli: Phys. Rev. B 56(16) (1997) 10133.

[9] H. Yanagi, S. Okamoto and T. Mikami: Synthetic Metals 91 (1997) 91.

[10] H. Yanagi and T. Mikami: Applied Physics Letters 73(5) (1998) 563.

[11] G. Grem, G. Leditzky, B. Ullrich and G. Leising: Adv. Materials 4(1) (1992) 36.

[12] H. Ishii and K. Seki: IEEE trans. elect. devices 44(8) (1997) 1295.

[13] H. Ishii, K. Sugiyama, D. Yoahimura, E. Ito, Y. Ouchi and K. Seki: IEEE J. Sel. Top. Quant. Elec. 4(1) (1998) 24.

[14] I.G. Hill and A. Kahn: J. Appl. Phys. 84(10) (1998) 5583.

[15] S.T. Lee, X.Y. Hou, M.G. Mason and C.W. Tang: Appl. Phys. Lett. 72(13) (1998) 1593.

[16] S.T. Lee, Y.M. Wang, X.Y. Hou and C.W. Tang: Appl. Phys. Lett. 74(5) (1999) 670.

[17] Y. Park, V.E. Choong, B.R. Hsieh, C.W. Tang, T. Wehrmeister, K. Müllen and Y. Gao: J. Vac. Sci. Technol. A 15(5) (1997) 2574.

[18] A. Rajagopal, C.I. Wu and A. Kahn: J. Appl. Phys. 83(5) (1998) 2649.

[19] A. Rajagopal and A. Kahn: Adv. Mater. 10(2) (1998) 130.

[20] K. Seki, E. Ito and H. Ishii: Synth. Met. 91 (1997) 137.

[21] H. Ishii, K. Sugiyama, E. Ito and K. Seki: Adv. Mater. 11(8) (1999) 605.

[22] R. Schlaf, B.A. Parkinson, P.A. Lee, K.W. Nebesny and N.R. Armstrong: J. Phys. Chem. 103 (1999) 2984.

[23] R. Schlaf, P.G. Schroeder, M.W. Nelson, B.A. Parkinson, P.A. Lee, K.W. Nebesny and N.R. Armstrong: J. Appl. Phys. 86(3) (1999) 1499.

[24] R. Schlaf, B.A. Parkinson, P.A. Lee, K.W. Nebesny and N.R. Armstrong: Appl. Phys. Lett. 73(8) (1998) 1026.

[25] R. Schlaf, B.A. Parkinson, P.A. Lee, K.W. Nebesny and N.R. Armstrong: Surf. Sci. Lett. 420 (1999) L122.

[26] R. Schlaf, C.D. Merritt, L.A. Crisafulli and Z.H. Kafafi: J. Appl. Phys. 86(10) (1999) 5678.

[27] J.R. Waldrop and R.W. Grant: Physical Review Letters 43(22) (1979) 1686.

[28] K. Horn: Applied Physics A51 (1990) 289.

[29] R. Schlaf, O. Lang, C. Pettenkofer and W. Jaegermann: J. Appl. Phys. 85(5) (1999) 2732.

[30] G. Kaindl, T.-C. Chiang, D.E. Eastman and F.J. Himpsel: Phys. Rev. Lett. 45(22) (1980) 1808.

[31] W. Jaegermann and H. Tributsch: Prog. Surf. Sci. 29(1/2) (1988) 1.

[32] W. Jaegermann: "*Surface Studies of Layered Materials in Relation to Energy Converting Interfaces*" in "*Photoelectrochemistry and Photovoltaics of Layered Semiconductors*", A. Aruchamy(ed.) (Kluwer Academic Publishers, Dordrecht, (1992).

[33] R. Schlaf, P.G. Schroeder, M.W. Nelson, B.A. Parkinson, C.D. Merritt, L.A. Crisafulli, H. Murata and Z.H. Kafafi: Surf. Sci. 450 (2000) 142

[34] M.P. Seah: Surf. Interf. Anal. 14 (1989) 488.

[35] I. Kojima and M. Kurahashi: J. Electron. Spectr. Rel. Phen. 42 (1987) 177.

[36] G. Ertl and J. Küppers: "*Low Energy Electrons and Surface Chemistry* " 2nd (VCH Verlagsgesellschaft mbH, Weinheim, Germany, 1985).

[37] J.J. Yeh and I. Lindau: Atomic Data and Nuclear Data Tables 32 (1985) 1.

[38] K. Seki, U.O. Karlsson, R. Engelhardt, E.-E. Koch and W. Schmidt: Chem. Phys. 91 (1984) 459.

[39] J.L. Bredas, R.R. Chance, R. Silbey, G. Nicolas and P. Durand: J. Chem. Phys. 77(1) (1982) 371.

[40] X. Li, Z. Zhang and V.E. Henrich: J. Electron Spectrosc. Relat. Phenom. 63 (1993) 253.

[41] M. Pope and C.E. Swenberg: "*Electronic Processes in Organic Crystals and Polymers* " (Oxford University Press, Oxford, 1999).

[42] C. Ludwig, B. Gompf, J. Petersen, R. Strohmaier and W. Eisenmenger: Z. Physik B93 (1994) 365.

[43] A. Schmidt, L.-K. Chau, A. Back and N.R. Armstrong: in "*Phthalocyanines*", C. Leznoffand A.P.B. Lever(ed.) (VCH Publications, New York, 1996) pp.307-341.

[44] C.D. England, G.E. Collins, T.J. Schuerlein and N.R. Armstrong: Langmuir 10 (1994) 2748.

[45] R. Schlaf, B.A. Parkinson, P.A. Lee, K.W. Nebesny, G. Jabbour, B. Kippelen, N. Peyghambarian and N.R. Armstrong: J. Appl. Phys. 84(12) (1998) 6729.

[46] G. Beamson and D. Briggs: "*High Resolution XPS of Organic Polymers-The Scienta ESCA300 Database* " (Wiley&Sons, 1992).

[47] R. Schlaf: unpublished results

[48] R. Schlaf, O. Lang, C. Pettenkofer, W. Jaegermann and N.R. Armstrong: J. Vac. Sci. Technol. A15(3) (1997) 1365.

[49] P.G. Schroeder, C.B.France, B.A. Parkinson and R. Schlaf: in press

[50] R.H. Williams, R.B. Murray, D.W. Govan, J.M. Thomas and E.L. Evans: J. Phys. C: Sol. State Phys. 6 (1973) 3631.

[51] A. Klein, O. Lang, R. Schlaf, C. Pettenkofer and W. Jaegermann: Phys. Rev. Lett. 80(2) (1998) 361.

[52] C. Argile and G.E. Rhead: Surface Sci. Reports 10 (1989) 277.

# Chapter 3: Orbital alignment at *p*-sexiphenyl/ $SnS_2$, *p*-sexiphenyl/HOPG and coronene/$SnS_2$, coronene/HOPG interfaces measured with photoemission spectroscopy

Submitted to: *Journal of Applied Physics*
P.G. Schroeder, C.B. France, B.A. Parkinson*, and R. Schlaf

**Abstract**

The energy level alignment at the interfaces between *para*-sexiphenyl/$SnS_2$, *para*-sexiphenyl/highly oriented pyrolytic graphite(HOPG), coronene/$SnS_2$, and coronene/HOPG were determined using *in situ* thin film deposition in combination with x-ray and ultraviolet photoemission spectroscopy (XPS, UPS) measurements. The organic thin films were grown in multiple steps by vapor deposition, then sequentially characterized *in situ* after each growth step. The vacuum cleaved single crystals of $SnS_2$ and HOPG substrates provided clean, atomically flat and chemically inert surfaces, allowing for the investigation of the phenomena of band bending and interface dipoles without the interference of chemical reactions or morphological problems. Due to the

distinctly different work functions of the HOPG ($\Phi$ = 4.65 eV) and $SnS_2$ ($\Phi$ = 5.45 eV) substrates, the observed shifts in the binding energies of the organic overlayer related XPS core level emission lines could possibly be associated with band bending resulting from Fermi level equilibration between the organic thin films and substrates. Different polarization energies of the two substrates however, complicates the ability to precisely distinguish band bending related shifts from final state screening shifts. Low intensity XPS work function measurements enabled the detection of the overlayer-thickness-dependent onset of charging phenomena in the UPS measurements. This allowed the precise determination of the highest occupied molecular orbital (HOMO) alignment of the organic molecules at the investigated interfaces.

### 3.1 Introduction

Organic based electronic materials have emerged as areas of intense research due to their potential in a variety of opto-electronic devices [1-3]. Determination of the electronic structure of interfaces between electrodes and organic materials or between different organic materials using photoemission spectroscopy (PES) has become a vivid field of research [4-14] since the charge transfer across these interfaces strongly influences the performance of the organic devices.

While such measurements are well understood and frequently used on inorganic semiconductor interfaces[15-17], their application in systems containing organic

semiconducting materials is relatively new and still under development. There are three prominent issues regarding this measurement technique, namely sample charging, band bending, and final state screening shifts (due to differences of polarization energies of the molecules at the interface and within the overlayer). The polarization energy is defined as the difference between the gas phase and condensed phase ionization energies of a particular element or molecule. The greater the polarization energy, the more effectively the solid material will be able to shield the remaining positive charge (hole) after an electron is ejected from the sample via the photoelectric process. Charging and final state screening effects are artifacts, which need to be considered and removed during the evaluation. Band bending on the other hand occurs due to Fermi level equilibration across the interface and is part of its electronic structure. The main problem of such measurements is to distinguish between spectral shifts caused by these effects.

While charging artifacts can be relatively easily controlled [5], distinguishing between final state screening effects and band bending is more difficult and likely cannot be resolved using photoelectron spectroscopy alone. Using photoelectron spectroscopy in combination with Kelvin probe measurements has been previously done [18] and does offer the possibility of distinguishing between the two. In both cases overlayer thickness dependent spectral shifts occur in the overlayer related emission lines. Due to this superposition of shifts it is nearly impossible to distinguish between such shifts in only one experiment. One way to investigate these phenomena is to measure several

interfaces composed of the same overlayer but substrates having different work functions (i.e. varying Fermi level positions relative to the overlayer material). If band bending is the cause for the observed shifts, their magnitude will depend proportionally on the work function of the substrate (if interface dipoles are absent). If final state screening is responsible then the shifts should rather depend on the differences in screening capabilities of the substrate materials.

The results presented in this paper represent such a series of experiments: Two different organic materials were each deposited on two different layered substrate materials, $SnS_2$ and highly oriented pyrolytic graphite (HOPG) having *distinctively different work functions* ($SnS_2$: $\Phi$=5.5 eV; HOPG: $\Phi$=4.65 eV). Due to their layered crystal structure, both substrate materials are ideal model systems for such an investigation since atomically abrupt interfaces can be achieved, which are free of structural dipoles and chemical reactions [19,20]. The only forces between organic overlayer and the substrates are of van der Waals origin, i.e. peak shifts resulting from chemical/structural dipoles at the interface are expected to be negligible[16]. However, these two substrates also have different screening capabilities where the $SnS_2$ substrate is likely to have a larger polarization energy (PE = 2.5 – 3.0 eV) than HOPG (PE = 1.2 eV) which is expected to be closer to that of the organic thin films [21]. As a result, either of these effects are expected to induce similar shifts in the core-level spectra measured using XPS. Careful analysis though, of these core-level energy shifts as a function of the film

thickness can provide some insight on the origins of these shifts. The organic materials used are interesting due to their electronic properties: *P*-sexiphenyl is a short chain poly(*para*-phenylene) which has been extensively studied due to its conductivity properties and the possible use as an active layer in an organic light emitting device (OLED) [22-26]. Coronene is of interest for its transport properties, and is of particular interest in this paper due to its simple structure that is similar to highly oriented pyrolytic graphite (HOPG) [27-29].

### 3.2. Experimental Details

All *in situ* experiments were performed in a commercial Omicron Multi-Probe ultrahigh vacuum (UHV) apparatus (base pressure = 5 x $10^{-11}$ mbar) equipped with x-ray photoelectron spectroscopy (XPS), ultraviolet photoelectron spectroscopy (UPS), and a VSW EA125 single channel hemispherical analyzer. The organic physical vapor deposition chamber (base pressure = 1 x $10^{-9}$ mbar) is attached to the analysis chamber allowing the samples to be prepared *in situ*. The $SnS_2$ crystals and HOPG were cleaved *in situ* using a glued on metal foil, and characterized with XPS and UPS prior to deposition. The organic films were grown by sublimation from resistively heated boron nitride crucibles. The *p*-6P source was held at 110°C, and the coronene source was held at 90°C for 12 hours each prior to deposition to outgas lower vapor pressure contaminants. The thin films were deposited at a rate of 4Å/min, which was monitored

by a Leybold quartz crystal microbalance (QCM). The source temperature during growth was 97°C for the coronene, and 190°C for the *para*-sexiphenyl (*p*-6P) while the substrates were kept at room temperature. After each growth step, the samples were characterized *in situ* using XPS (MgKα, 50 eV pass energy) and UPS (HeI, 21.21 eV; and HeII, 40.81 eV, both with 10 eV pass energy) in normal emission. A -5.00 V bias was applied to the sample for the UPS measurements to separate the sample and spectrometer high binding energy cutoffs. The samples were mounted on a pedestal elevated 5 mm above the sample plate to prevent stray electrons from the manipulator assembly interfering with the ultraviolet photoelectron (UP)-spectra [30]. The spectrometer was calibrated to yield the standard values [31] of 75.13 eV for the Cu 3p and 932.66 eV for the Cu $2p_{3/2}$ emission lines on an $Ar^+$ sputtered Cu sample. Binding energy zero was determined using the Fermi level position of the Cu sample. The overall analyzer resolution of 0.20 eV was determined from the width of the Cu Fermi edge [7]. Therefore, work function and the highest occupied molecular orbital (HOMO) cutoff positions determined from the high binding energy cutoffs and HOMO onsets of UP-spectra were corrected for the analyzer broadening by adding/subtracting 0.1 eV. XPS core level peak positions were determined by a fitting routine given in Ref. [32] using IGOR Pro (Wavemetrics) data evaluation software. A vacuum deposited coronene film on quartz was used to obtain the solid state absorption spectrum that was measured using a Varian Cary-500 UV-VIS-NIR Spectrophotometer.

With regard to the errors in the above and the following evaluations it should be noted that often margins of about ±0.1 eV are assigned to photoemission measurements. This error margin refers to the determination of the *absolute* values for ionization energy, work function and core level peaks. The source of errors is easily located in the case of the position determination of UP-spectra related cutoff features, specifically the highest occupied molecular orbital and high binding energy cutoff (HOMO and HBEC). The evaluation of these features strongly depends on the way the lines are fitted into the edges. In these experiments, we are measuring the relative shifts in peak position that can be determined very accurately due to the well-defined peak shapes in combination with very precise peak fitting procedures. We estimate that for the case of good signal to noise ratio, errors in peak positions can be on the order of ±0.03 eV or better. Therefore, the main source of errors in absolute XPS peak positions results more likely from miscalibration of the electron energy analyzers. The UPS cutoffs and XPS peaks monitored during a growth sequence most likely all deviate by the same values since the same evaluation procedure is used for all measurements. The magnitude of the orbital offsets and interface dipole barriers are each determined from the addition or subtraction of between two and six total spectral measurements and therefore, the overall measurement errors are estimated to be in the range of about ±0.05-0.07 eV.

## 3.3. Results

### 3.3.1. *p*-sexiphenyl on $SnS_2$

Fig. 3.1 shows the UP-spectra sequence for the *p*-6P/$SnS_2$ interface. The bottom spectra were measured on the vacuum cleaved $SnS_2$ crystal. The upper spectra were measured after each of the 13 *p*-6P deposition steps, starting with a nominal coverage of 0.1 Å and progressively increasing in thickness up to the final coverage of 512 Å. The center part of Fig. 3.1 shows the complete spectra revealing the evolution of the valence bands emissions of the sample surface throughout the transition from the $SnS_2$ substrate to the *p*-6P film. The left part of this figure shows a magnification of the normalized high binding energy cutoff region of the UP-spectra. On the right is a magnified spectral region of the valence band edge/HOMO of the sample. To determine the work function and the valence band maximum (VBM) of the sample at each growth step, a straight line was fitted into the high and low binding energy positions of the UP-spectra. A 0.1 eV shift was added to the determined work function and the VBM positions to account for the energy broadening of the analyzer. This is indicated by the 0.1 eV offset lines drawn in the Figure. The arrows in the right part of Fig. 3.1 and in the He II spectra in Fig. 3.2 show the onset of the HOMO of the *p*-6P. The pronounced band structure of the *p*-6P in the He II spectra very closely correlates with the density functional theory calculation of *p*-6P by N. Koch and coworkers [33].

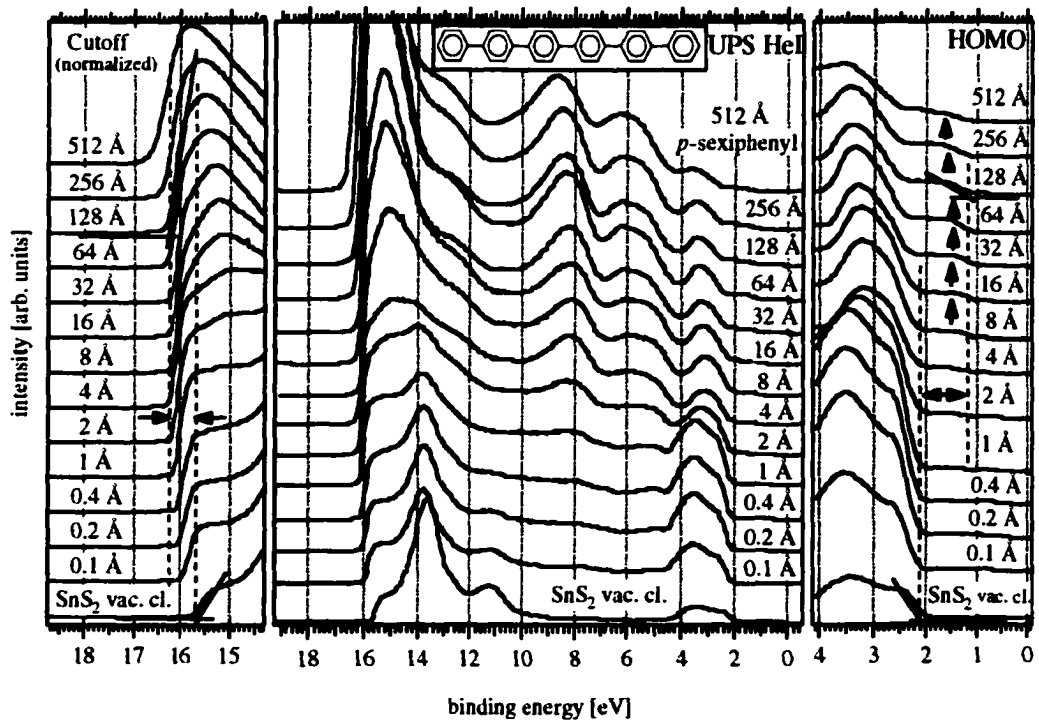


**Fig. 3.1.** He I UP-spectra of *p*-6P grown on $SnS_2$. The bottom spectra shows the vacuum cleaved substrate while the offset spectra were measured after each subsequent growth step. The high binding energy cutoff is magnified on the left part of the figure to show the overall shift in the work function of the sample. A magnified spectral range where the $SnS_2$ valence band and *p*-6P HOMO peaks are located is shown on the right.

Precise determination of the barrier between the HOMO of the *p*-6P and the VBM of the $SnS_2$ at the interface, requires measurement of the band bending occurring at the interface to be included in the evaluation. A detailed description of the evaluation procedure for determining the energy level alignment is given in previous work [4,6]. Measurement of the shifts of the core electron peaks with X-ray photoelectron spectroscopy (XPS), for both the substrate and the overlayer, allows the determination of the extent of band bending. The left side of Fig. 3.3 shows the Sn 3d peaks of the vacuum cleaved substrate (bottom) and their attenuation as thicker layers of the *p*-6P are added. A slight binding energy shift in the Sn 3d peak position indicates that there is a small amount of band bending occurring in the $SnS_2$ substrate. This is similar to the energy level alignment measurement of PTCDA/$SnS_2$ [4]. On the right side of Fig. 3.3 the C 1s core spectra is shown with the evolving intensity of the C 1s peak after each growth step. As can be seen in the C 1s spectra for the vacuum cleaved $SnS_2$, a trace quantity (estimated to be about 1-3% surface coverage) of adventitious carbon is present on the surface. The binding energy of approximately 285.5 eV of this trace C1s peak is indicative of hydrocarbon contamination of the sample plate on which the cleaved crystal was mounted. Carbon is the only element in *p*-6P that can be measured with XPS, so the C 1s contamination peak must be contended with in the evaluation. This contamination peak interferes with the determination of the position of the C 1s peak attributed to the *p*-6P, particularly in the first several growth steps.

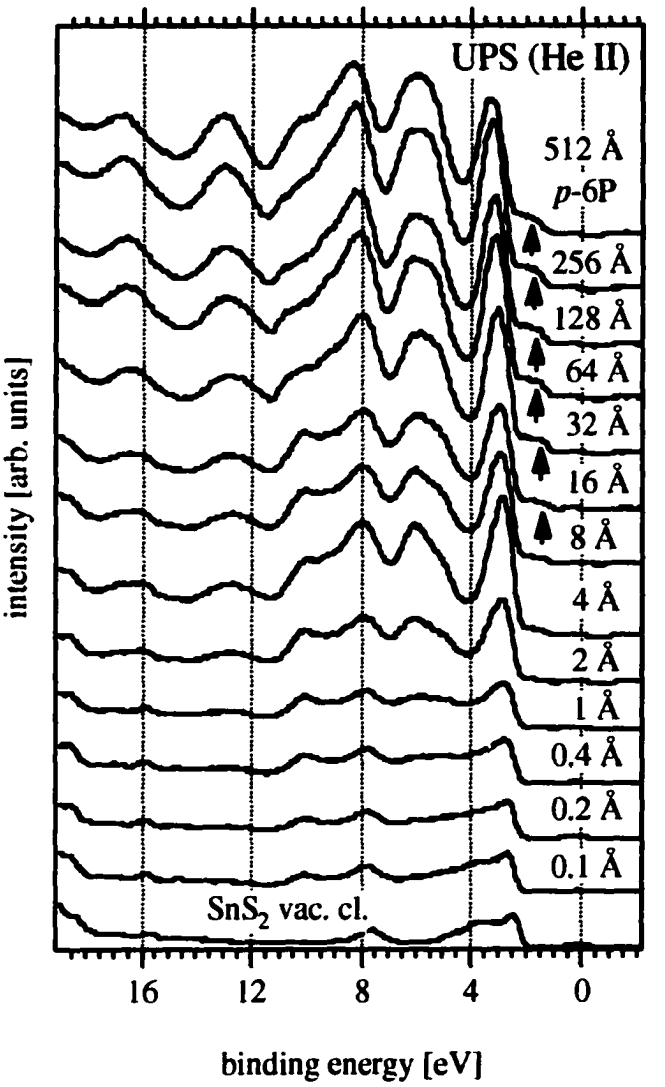


**Fig. 3.2.** He II UP-spectra of *p*-6P on $SnS_2$.

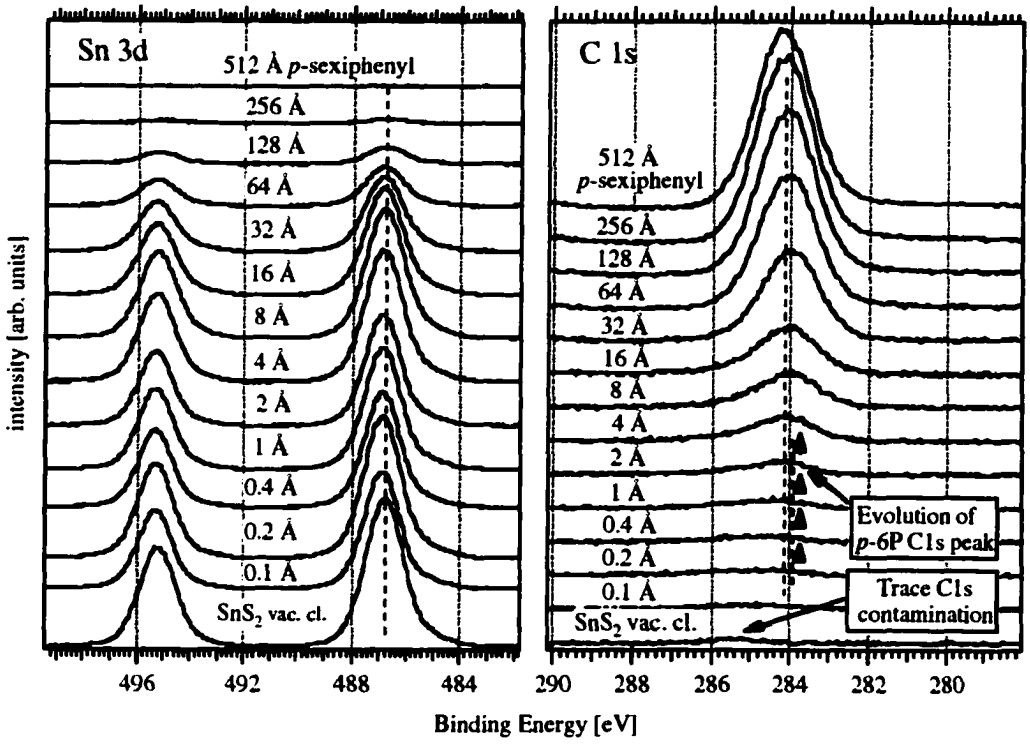


**Fig. 3.3.** Core level spectra as determined from X-ray photoelectron spectroscopy. The left shows the attenuation of the Sn 3d peak as the thickness of the *p*-6P films increases. On the right is the *p*-6P C 1s peak. The vacuum cleaved substrates did show slight carbon peak at about 285.5 eV indicating a trace amount of (a high oxidation state) carbon contamination. Peak fitting procedures described in the text explain how the contamination C 1s and *p*-6P C 1s peaks were differentiated. A shift of 0.21 eV was measured in the C 1s spectra whereas there was a slight shift in the Sn 3d (0.16 eV), indicating the presence of band bending and/or changes in the polarization environment.

However, this carbon contamination peak is at a significantly higher (>1eV) binding energy than the peak attributed to the *p*-6P. A careful peak fitting procedure that incorporates both the contamination C 1s peak and the C 1s peak for the organic layer was used to distinguish the contamination peak from the *p*-6P related peaks that start to dominate the spectrum at about 2-4 Å coverages. The fitting procedure allowed for separating the two peaks to determine the actual binding energy of the C 1s peak that is attributed to the deposited molecules. This was accomplished by first, fitting the initial C 1s contamination peak, on the vacuum cleaved substrate before deposition of the organic layer, with a Gaussian-Lorentzian function. These fit parameters for the C 1s contamination peak were then constrained when fitting two Gaussian-Lorentzian functions to the spectra for the first several growth steps of the organic layer [34].

The initial core-level peak shifts [$\Delta CL(SnS_2)$] in the substrate caused by the first overlayer deposition is determined from the 0.16 eV shift Sn 3d emission line between the vacuum cleaved substrate and the 128 Å layer. The initial binding energy of the *p*-6P C1s peak was determined to be 283.91 eV, which is the average C 1s binding energy for the 0.1, 0.2, 0.4, 1, and 2 Å growth steps. These are all sub-monolayer (ML) thickness, where one ML is estimated to be ~6 Å and the molecules are presumed to initially lie flat on the substrates as observed in other experiments [25]. The binding energy for the "thick" *p*-6P film (128Å) was determined to be 284.12 eV, based on the largest thickness of the *p*-6P film where spectra could be measured reliably, since it is just prior to the

onset of sample charging in the UP-spectra. The thickness at which sample charging begins is discussed below. The difference in the C1s binding energy, between the thick film (128Å) and initial growth steps of the *p*-6P film was determined to be [ΔCL(C1s) = 0.21 eV)].

The measured shift in the work function of the sample between the bare substrate and the thick film is often directly used as the magnitude of the interface dipole (eD) [35-38]. Since both band bending contributions and final state screening effects also influence the measured work function, the core-level peak shifts should be subtracted from the total work function shift to get an accurate determination of the magnitude of the interface dipole barrier. The work function at each growth step is evaluated by subtracting the analyzer broadening corrected high binding energy cutoff (Fig. 3.1, left side) of the UP-spectra from the He I source energy (21.21 eV). The total shift of the work function at the 128Å *p*-6P layer was 0.52 eV. Subtracting the total core-level peak shifts [ΔCL(Sn 3d) = 0.16 eV; ΔCL(C 1s) = 0.21 eV] gives a corrected interface dipole magnitude of eD = 0.15 eV

The energy offset between the VBM of the $SnS_2$ substrate and the highest occupied molecular orbital (HOMO) of the *p*-6P film was evaluated by subtracting the VBM of the vacuum cleaved $SnS_2$ substrate (2.11 eV) and core-level shifts (0.16 and 0.21 eV) from the HOMO cutoff (lowest binding energy edge of the UP-spectra) of the *p*-6P at 128Å (1.18 eV) resulting in

$\Delta HOMO_{cutoff}$= HOMO(128Å *p*-6P) - VBM($SnS_2$) – $\Delta$CL(Sn3d) – $\Delta$CL(C1s)

= 1.18 - 2.11 - 0.16 – 0.21 eV = -1.30 eV.

The positions of the conduction band's unoccupied molecular orbitals cannot be measured directly with photoelectron spectroscopy. Therefore, the conduction band minimum (CBM)/lowest unoccupied molecular orbital (LUMO) offset can only be determined by including the optical absorption band gap of the two materials into the evaluation. The value of the band gap used for the $SnS_2$ crystal is 2.18 eV, which is the average of the optical absorption measurements given in reference [16] and references therein. The band gap between the HOMO and LUMO for *p*-6P of 3.80 eV was obtained from the used average gap energies determined by optical absorption measurements in references [26,39,40]. It is important to indicate that the optical gap values for organic materials can only be used as estimates of their HOMO-LUMO gap since they do not account for the large excitonic binding energies of the molecules of the order of 0.5 eV [41]. In addition, the electronic band gap of $SnS_2$ is probably slightly larger for the same reasons, but incorporating these values into the evaluation still provides a reasonable approximation of the electron injection barriers. The offset between the LUMO of the *p*-6P and the conduction band maximum (CBM) of the $SnS_2$ was determined by subtracting the difference of the band gaps from $\Delta HOMO_{cutoff}$ (-1.30 eV) which yields

$\Delta LUMO_{cutoff} = \Delta HOMO_{cutoff} - (E_g(p\text{-}6P) - E_g(SnS_2)) = -1.30 - (3.80 - 2.18\ eV) = -2.92\ eV.$

The negative values of both the $\Delta HOMO_{cutoff}$ and the $\Delta LUMO_{cutoff}$ indicate that the HOMO and LUMO of the *p*-6P are at a lower binding energy than the VBM and CBM respectively of the $SnS_2$ crystal.

A schematic of the complete electronic structure of the interface is shown in the top part of Fig. 3.4. The ionization potential of the $SnS_2$ was evaluated by adding the VBM position (2.11 eV) to the work function (5.53 eV), yielding

$E_{ion}$= VBM($SnS_2$) + $\Phi$($SnS_2$) = 2.11 + 5.53 eV = 7.64 eV.

The ionization potential for the *p*-6P grown on $SnS_2$ was determined similarly by adding the position of the $HOMO_{cutoff}$ for the 128Å layer to the work function of the same layer, giving $E_{ion}$=6.19 eV.

### 3.3.2. *p*-6P on HOPG

The *p*-6P film was also grown sequentially on a vacuum cleaved substrate of HOPG in twelve steps as seen in Fig. 3.5. As was done in the *p*-6P/$SnS_2$ system, the high binding energy cutoff is shown normalized in the left part of the figure. In this system, only a nominal shift (<0.1 eV) is detected in the high binding energy cutoff. This indicates the existence of only a weak interface dipole or band bending related shift at the *p*-6P/HOPG interface. Furthermore, it indicates that this system does not show significant charging effects even at the thickest investigated layer. With the exception of

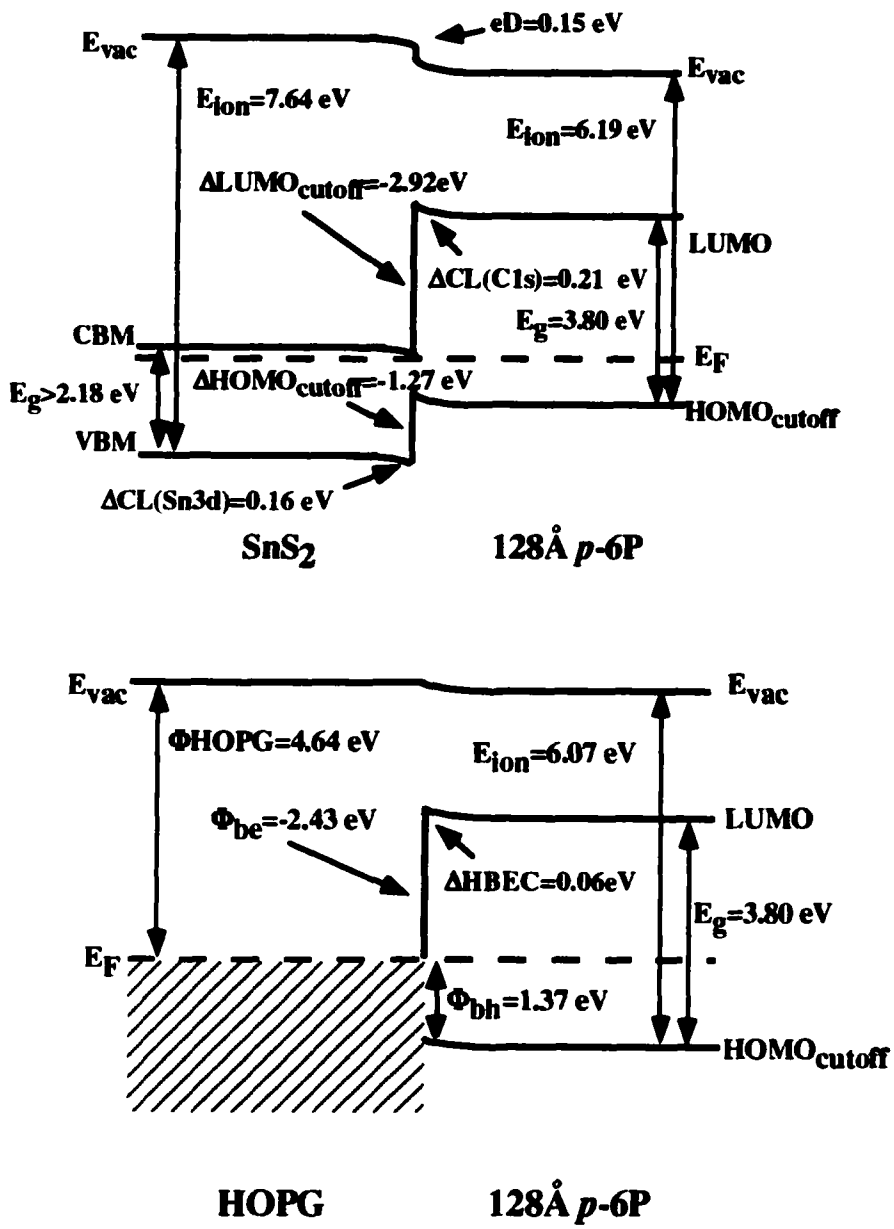


**Fig. 3.4.** Schematic of the electronic structure of *p*-sexiphenyl/$SnS_2$ (top) and *p*-6P/HOPG (bottom) interfaces. The 128Å *p*-6P layers were used for the final thickness since it was determined that this was the thickest point of the organic layer where sample charging did not occur.

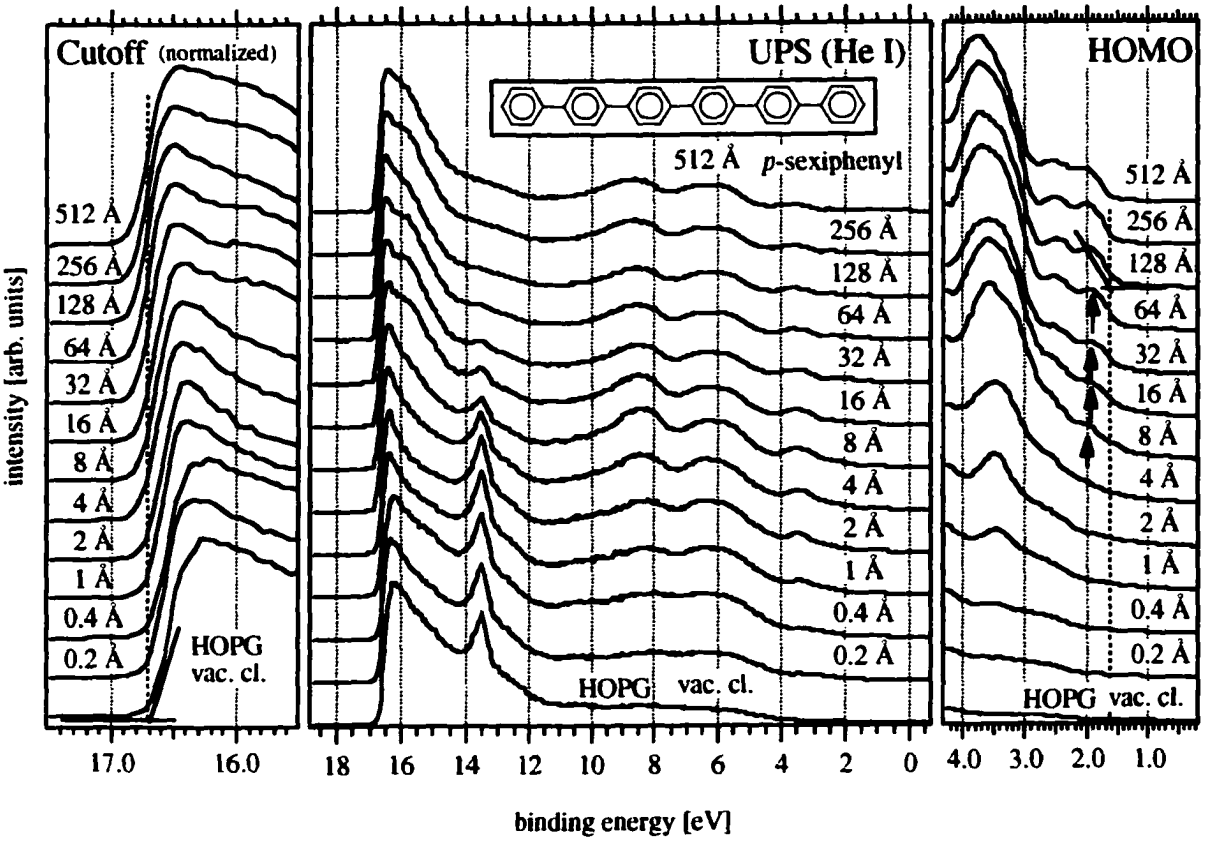


**Fig. 3.5.** He I UP spectra of *p*-6P deposited on HOPG. The center shows the full UP-spectrum for the vacuum cleaved substrate (bottom) and each subsequent growth step. The right side shows a magnified spectral region to clearly reveal the evolution of the HOMO of the *p*-6P as indicated by the arrows. The left part of the figure shows the normalized high binding energy cutoff.

the presence of a strong, probably conduction band related peak at 13.5 eV (resulting from electrons inelastically scattered into conduction band states above the vacuum level) [42], the UP-spectrum of the vacuum cleaved HOPG substrate is essentially featureless providing a low background for viewing the emerging valence band emissions, including the HOMO of the *p*-6P, as the thickness of the organic film is increased. This is evident in the right part of Fig. 3.5, where the arrows point out the spectral region for the onset of the *p*-6P HOMO emissions.

Fig. 3.6 shows the C 1s core levels, as measured with XPS, parallel the UPS measurements. It is evident that the emission line remains almost at a constant position during the entire growth procedure. Due to the chemical similarities of *p*-6P and HOPG (only $sp^2$ carbon atoms), very little can be determined regarding band bending or final state screening related shifts. However, the barrier heights for this system can still be estimated and used to test the validity of the measurement process. This is probably a result of the similar chemical structures of HOPG and *p*-6P. A weak shift of ($\Delta$HBEC = 0.06 eV) was observed in the high binding energy cutoff of the UP-spectra, suggesting only a very small change in polarization energies exist and likely a negligible amount of band bending occurs. The fact that the shift in the HBEC was gradual with respect to the film thickness indicates the absence of an interface dipole.

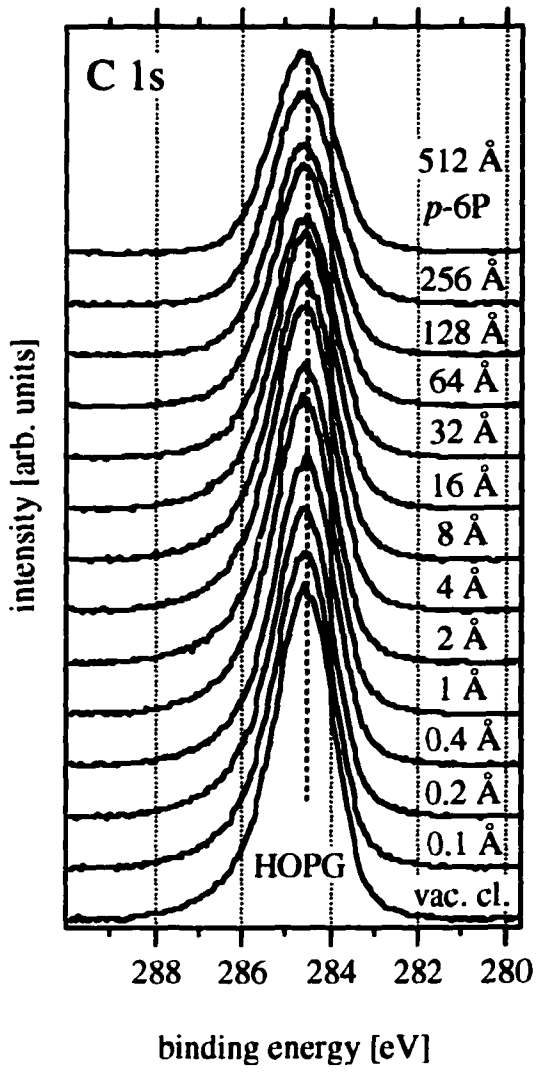


**Fig. 3.6.** *p*-6P on HOPG: The C 1s XPS core-level peak as the thickness of the *p*-6P layer is increased. The almost constant peak binding energy indicates that there is no significant band bending occurring at the *p*-6P/HOPG interface.

The HOPG substrate is electronically treated as a semi-metal due to the absence of a true absorption gap. Therefore, the offsets of interest for the *p*-6P/HOPG interface are the barrier height between the Fermi level of the HOPG and the $HOMO_{cutoff}$ (hole injection barrier($\Phi_{bh}$)), and the $LUMO_{cutoff}$ (electron injection barrier ($\Phi_{be}$)) of the *p*-6P. The hole injection barrier height ($\Phi_{bh}$) is the difference between the $HOMO_{cutoff}$ of the *p*-6P and the Fermi level of the HOPG. This was determined by subtracting the work function of the HOPG substrate ($\Phi$HOPG = 4.64 eV) as well as the shift in the high binding energy cutoff ($\Delta$HBEC = 0.06 eV) from the measured ionization potential of the 128 Å layer ($E_{ion}$ = 6.07 eV) of the *p*-6P film. This gives a barrier height of

$\Phi_{bh} = E_{ion}$(128Å *p*-6P) - $\Phi$HOPG - $\Delta$HBEC = 6.07 - 4.64 - 0.06 eV = 1.37 eV.

The electron injection barrier $\Phi_{be}$ (between the HOPG Fermi level and the LUMO of the *p*-6P) is evaluated by subtracting the optical absorption gap of the *p*-6P (3.80 eV as determined above) from the hole injection barrier

$\Phi_{be} = \Phi_{bh} - E_g$(*p*-6P) = 1.37 eV - 3.80 eV = -2.43 eV.

A schematic of the electronic structure of the *p*-6P/HOPG interface is depicted in the bottom of Fig. 3.4. The barrier offsets and interface dipole as evaluated above are shown. The same evaluation procedure as done for the *p*-6P on $SnS_2$ was applied to obtain the ionization potential of *p*-6P on HOPG yielding 6.07 eV. The slight

discrepancy in the ionization potential for *p*-6P on $SnS_2$ versus HOPG is likely due to possible morphological differences between the two samples.

### 3.3.3. Coronene on $SnS_2$

The coronene was also evaporated onto a vacuum cleaved $SnS_2$ substrate starting at a nominal coverage of 0.1Å and sequentially increased up to a final film thickness of 256Å. The He I UP-spectra of this experiment are shown in the left part of Fig. 3.7. The structure, work function and VBM of the He I spectra of the vacuum cleaved $SnS_2$ crystal is nearly identical to that of the crystal used for the *p*-6P experiment. As the film thickness is increased, the coronene molecular bands start to dominate the spectra, including the evolution of the coronene HOMO at approximately 1.5 eV binding energy. There is also a more dramatic shift of the high binding energy cutoff at the higher film coverage than occurred in the *p*-6P systems. This is attributed to the coronene film charging at a lower thickness than *p*-6P possibly due to coronene having a lower conductivity or poorer charge transfer at the interface.

The thickness at which charging in the UP-spectra occurred was again determined by measuring the corresponding XPS high binding energy cutoff positions. Fig. 3.8 shows the XPS (right) and UPS (left) cutoff spectra in direct comparison. It is evident that the UP-spectra shift much more strongly during the last few deposition steps than

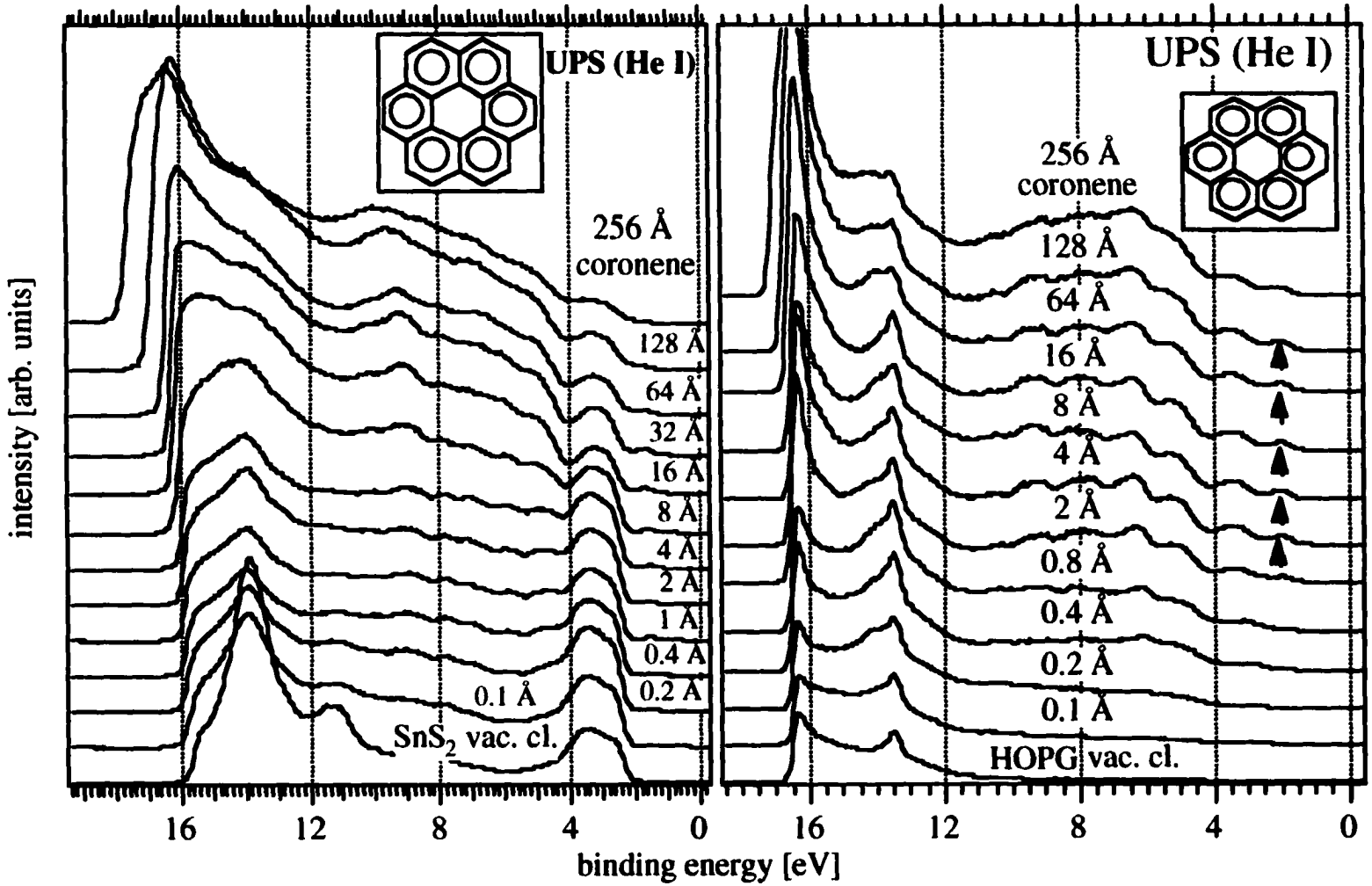


**Fig. 3.7.** He I UP-spectra of coronene films grown on $SnS_2$ (left) and HOPG (right). The spectra for the vacuum cleaved substrates are shown at the bottome of each, while the additional spectra were taken after each additional growth step.

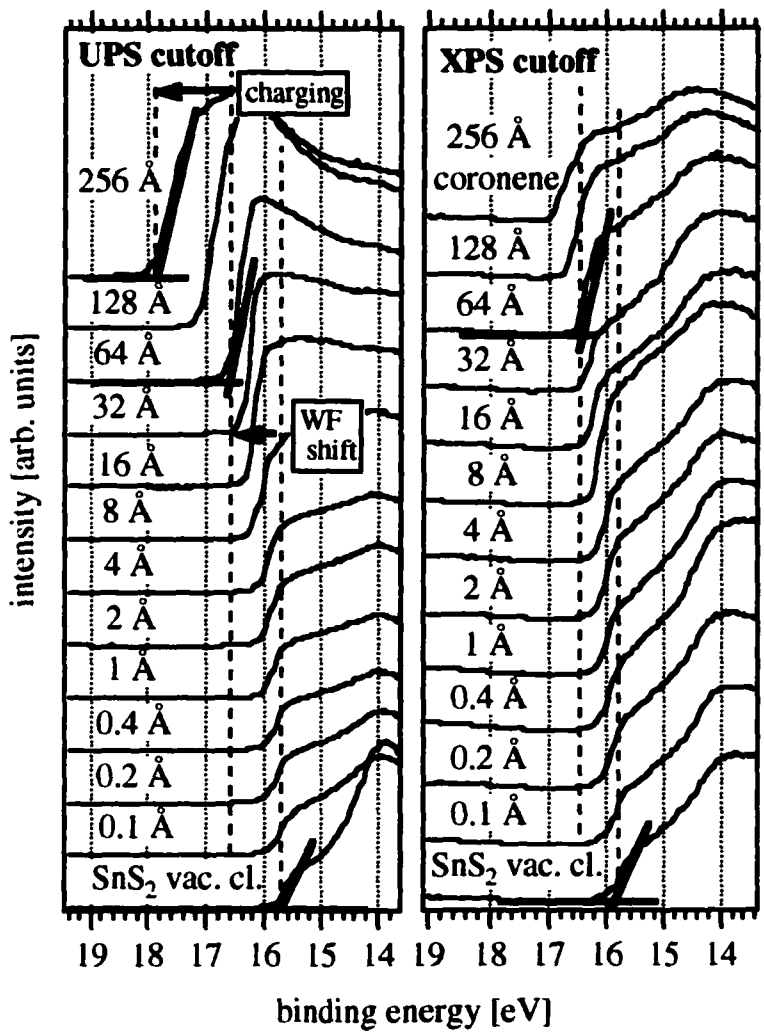


**Fig. 3.8.** High binding energy cutoff for coronene grown on $SnS_2$ as determined from both UPS (left) and XPS (right). The greater shift in the UP-spectra of the cutoff point between 64 Å and 256 Å indicates the onset of sample charging attributed to a greater photon flux from the helium lamp than the x-ray source.

XPS. Fig. 3.9 shows the work function values derived from these spectra, demonstrating the onset of charging phenomena in the UP-spectra after the 64 Å deposition step.

To evaluate the core-level peak shifts occurring in the substrate and coronene film, the XPS of Sn3d (substrate) and C1s (overlayer) peaks were measured. In Fig. 3.10, the C 1s spectra of the coronene film is shown on the left, whereas the Sn 3d spectra attributed to any shifts occurring in the $SnS_2$ substrate are shown on the upper right. As was the case in the *p*-6P grown on $SnS_2$ and of *p*-quaterphenyl grown on $SnS_2$ [7], there was a slight (0.08 eV) binding energy shift in the Sn 3d peak. The shifts in the Sn 3d peaks in both this system and in the *p*-6P on $SnS_2$ were toward a higher binding energy. This is the opposite direction of what would be expected if the shifts were due to changes in the final state screening environment, therefore a band bending is likely to be present in the $SnS_2$ substrate, and is not unexpected because the $SnS_2$ crystals are doped inorganic semiconductors.

The 0.19 eV shift of the C 1s lines, shown on the left, indicates the possible development of band bending due to the large work function of $SnS_2$. This could also be attributed to changes in the polarization energies between the substrate and the bulk coronene film. The bottom C 1s spectrum shows a weak emission at about 285.2 eV caused by ambient contaminants present on the sample plate. The same fitting procedure as described in the *p*-6P/$SnS_2$ results section was applied to separate the contamination

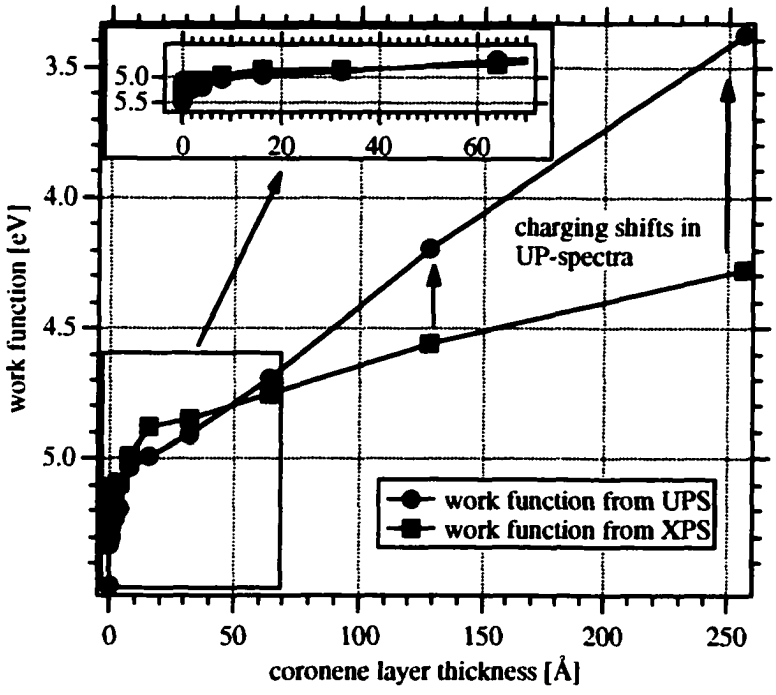


**Fig. 3.9.** Work function change determined with both UPS (round symbols) and XPS (square symbols) as a function of coronene film thickness grown on $SnS_2$. The inset shows the range from 0 Å to 64 Å in more detail. The curves start to deviate when the coronene film thickness exceeds 64 Å indicating the onset of sample charging in the UP-spectra.

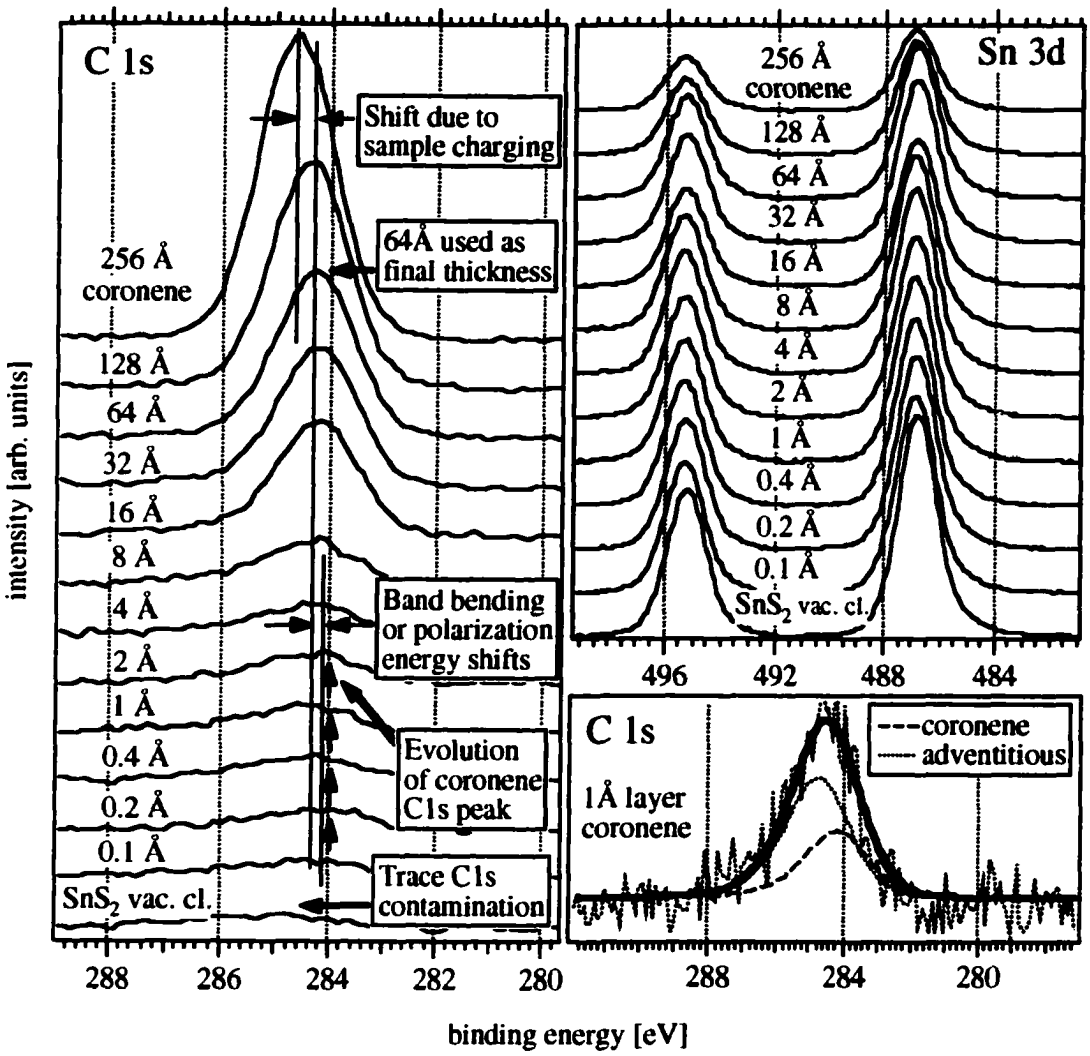


**Fig. 3.10.** Coronene grown on $SnS_2$: the C 1s (left) and Sn3d (upper-right) XPS peaks are shown as the coronene film thickness is increased. The stability of the Sn 3d peak position reveals there is a negligible amount of band bending occurring in the $SnS_2$ substrate. There are core-level shifts occurring in the coronene layer as indicated by the shift between the position of the initial evolution of the coronene C 1s peak and the final point of measurement (before the onset of charging) at 64 Å. The C 1s peak of the coronene was distinguished from that of the trace adventitious carbon by fitting two separate Gaussian-Lorentzian peaks under each of the first five growth steps. An example of this is shown in the bottom right part of the figure. The adventitious carbon peak is shown at the higher binding energy (~285.5 eV) as initially seen in the vacuum cleaved substrate, whereas the coronene C 1s peak is centered around 284.1 eV. The total fit (dark line) and experimental data are also shown.

emissions from those of the coronene film. The bottom right part of Fig. 3.10 shows an example of this fit (in this case using the 1 Å thickness of coronene), where the fine dashed line is the fit of the initial contamination peak, and the broader dashed line shows the evolution of the C 1s coronene peak.

By using the above-described fitting procedure, it was determined that the initial position of the C 1s coronene peaks was at a binding energy of 284.10 eV. This constitutes the average of the 0.2, 0.4, and 1 Å growth steps of coronene. To determine the magnitude of the core-level peak shifts in the coronene layer, this initial binding energy position was subtracted from the binding energy of the 64 Å thick film that was determined to be 284.29 eV. This yields a magnitude of $\Delta$CL(64Å coronene) = 0.19 eV occurring in the coronene film.

The total work function shift from the vacuum cleaved $SnS_2$ substrate (5.49 eV) to the 64 Å layer of coronene (4.69 eV) was determined to be 0.80 eV. Subtracting the core-level binding energy shifts from the total work function shift yields the magnitude of the interface dipole barrier (eD)

$eD = \Delta\Phi(tot) - \Delta CL(Sn\ 3d) - \Delta CL(C1s) = 0.80 - 0.08 - 0.19\ eV = 0.53\ eV.$

The offset between the VBM of the $SnS_2$ crystal and the 64 Å layer of coronene is determined by subtracting the $SnS_2$ VBM position (2.24 eV), and the core-level binding

energy shifts (0.08 and 0.19 eV), from the HOMO position of the 64Å layer of coronene (1.25 eV). This yields a value of $\Delta HOMO_{cutoff} = -1.26$ eV.

The offset between the CBM of the $SnS_2$ crystal and the LUMO position of the coronene was determined by subtracting the difference between the optical absorption gaps of coronene (3.29 eV) and the $SnS_2$ substrate (2.18 eV), from the $\Delta HOMO_{cutoff}$(-1.26 eV). This yields

$$\Delta LUMO_{cutoff} = \Delta HOMO_{cutoff} - (E_g(\text{coronene}) - E_g(SnS_2)) =$$

$$-1.26 \text{ eV} - (3.29 - 2.18 \text{ eV}) = -2.37 \text{ eV}.$$

The optical absorption gap of coronene was determined by taking the absorption spectra of a ~50 nm thick film of coronene evaporated onto a quartz substrate. The resulting spectra (Fig. 3.11) revealed the lowest energy absorption peak at 377 nm (3.29 eV), which represents the minimum distance of the HOMO/LUMO gap for a coronene film.

### 3.3.4. coronene on HOPG

The UPS He I spectra of coronene deposited on HOPG is shown in the right part of Fig. 3.7. The evolution of the band structure of the coronene becomes evident at 2 Å thickness and above. The HOPG conduction band (CB)-related peak at 13.5 eV remains visible even after deposition of 512 Å, indicating a more clustered growth mode for

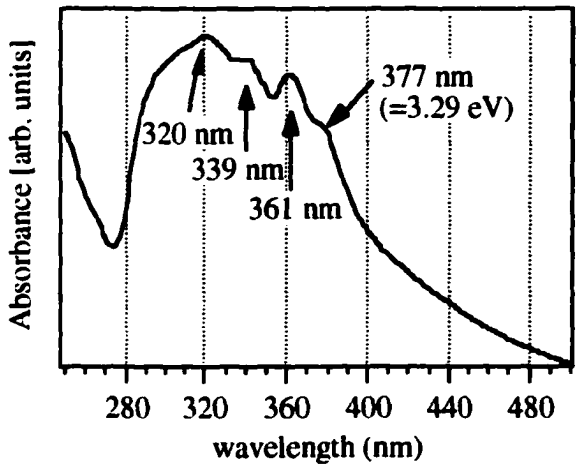


**Fig. 3.11.** Absorption spectrum of a coronene film. The optical band gap for coronene was determined to be 3.29 eV (377 nm) based on the lowest energy absorption peak.

coronene on HOPG than it was observed in the case of *p*-6P. It is also evident that the work function (determined from the high binding energy cutoff side of the spectra) remains essentially constant throughout the procedure, until charging starts to set in at 128 Å. The C 1s spectra (Fig. 3.12) for this system shows a relatively constant binding energy, but any measured shifts are disregarded since there appeared to be a highly clusted growth of the coronene film which negates the validity of the measurements in the peak shifts.

Determining the hole/electron injection barriers between the coronene HOMO/LUMO and the Fermi level of the HOPG is completed in the same manner as was done for the *p*-6P/HOPG sample. The ionization potential of the coronene layer $E_{ion}$ was determined by adding the low binding energy onset ($HOMO_{cutoff}$ = 1.33 eV) and work function (4.57 eV) of the 64 Å coronene layer, yielding $E_{ion}$ = 5.90 eV. The hole injection barrier $\Phi_{bh}$ was calculated by subtracting the work function of the vacuum cleaved HOPG substrate (4.63 eV) from the ionization potential of the coronene (5.90 eV), giving $\Phi_{bh}$ = 1.27 eV. The electron injection barrier $\Phi_{be}$ was determined by subtracting the optical absorption gap energy of coronene ($E_g$ = 3.29 eV) from the hole injection barrier ($\Phi_{bh}$ = 1.27 eV) which yields $\Phi_{be}$ = -2.02 eV.

Schematics of the band line-ups of coronene deposited on $SnS_2$ and on HOPG are shown in Fig. 3.13. The coronene/$SnS_2$ interface (top) shows a strong interface dipole

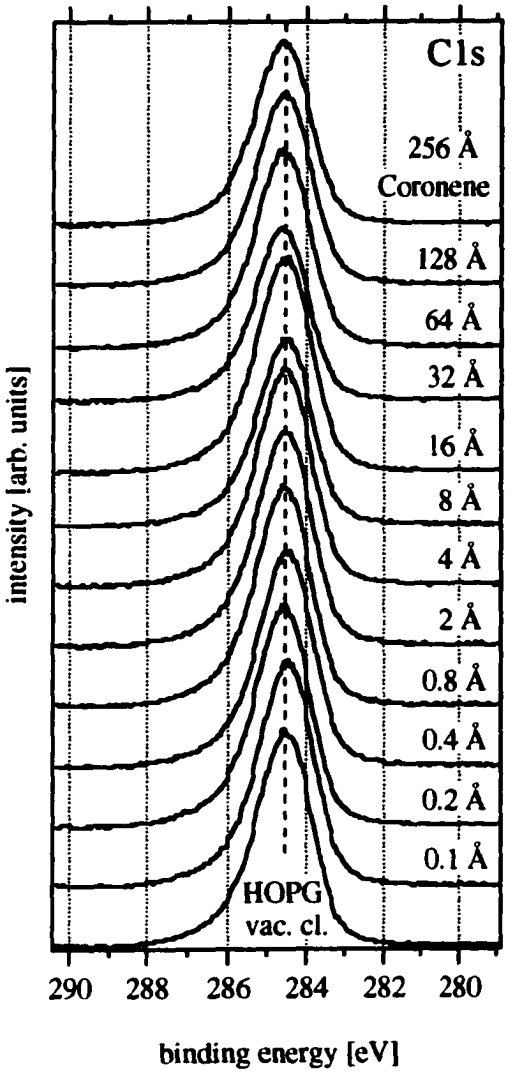


**Fig. 3.12.** C 1s core level emission for coronene on HOPG. The relatively constant peak binding energy indicates a negligible amount of band bending or change in the polarization energy.

(0.53 eV) and a small magnitude of core-level binding energy shifts [ ΔCL(Sn 3d) = 0.19 eV; ΔCL(C 1s) = 0.08 eV] whereas the coronene/HOPG interface reveals little to no electronic perturbations at the interface.

### 3.4. Discussion

Usually the main goal of measurements such as those presented here is to determine the magnitude of the carrier injection barriers at interfaces. These barriers largely determine the carrier injection properties, which in turn, influence the efficiency and power consumption of organic devices. Theoretically, (assuming the HOMO levels do not form bands leading to a broadening of the HOMO peak) these barriers could be measured by growing a monolayer of one of the two materials on top of the other and measure the HOMO position with respect to the Fermi level (metallic substrate) or valence band edge/HOMO position (semiconducting/organic substrate). However, since in practical measurements the monolayer HOMO usually has an intensity too weak to be discerned from the usually much stronger substrate valence region emissions, thicker layers need to be grown to precisely measure the HOMO position. Usually the substrate and overlayer will have both different work functions (Fermi level positions) and different polarization energies leading to changes in the final state screening environment. It can be expected that band bending or changes in polarization energies,

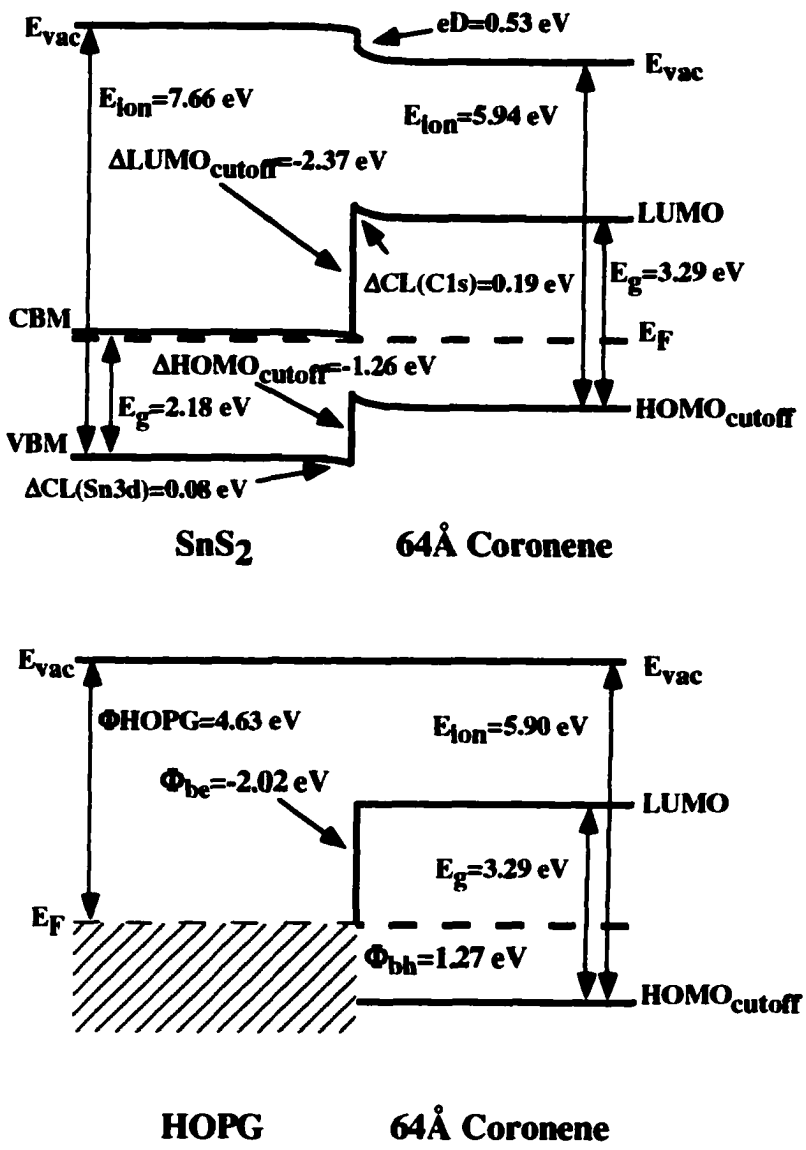


**Fig. 3.13.** Schematic of the electronic structure of the coronene/$SnS_2$ (top) and coronene/HOPG (bottom) interfaces.

either of which will interfere with measurements of the orbital offets, will occur at those interfaces. Regardless of the origin of the core-level binding energy shifts, they need to be taken into account when the HOMO position at the interface is determined by subtracting the core-level energy shift from the "thick layer" HOMO position. These shifts have been found and attributed to band bending in several organic systems [4-6,30] where peak shifts occur similar to those found in inorganic systems[15]. However, due to the usually low conductivity of most organic materials, the band bending related origin of these shifts is controversial and other explanations along the lines of polarization energy differences [43,44] have been suggested [13,14,45].

Our earlier experiments on organic molecule/HOPG interfaces [7,46] suggest that at least on HOPG, no significant final state screening shifts occur (PES peak shifts caused due to differences in polarization energies across an interface are frequently called "final state screening shifts" [47,48]). This conclusion is supported by the fact that the polarization energy shift between a single sheet of graphite and bulk HOPG is estimated to be about 1.2 eV [21], which is in the range of the solid state/gas phase polarization energy shifts of 1-2eV found for many organic molecules [21,49]. Hence, if organic molecules are grown on HOPG, their screening environment is not much different from what they would experience in their own solid-state matrix. Consequently, no significant peak shifts occur, since the final state screening remains constant throughout the organic overlayer.

Similar to what was demonstrated in the *p*-4P systems on the same substrates, the observed peak shifts in the *p*-6P and coronene systems differ depending on the substrate work function. Typically, one way to prove the occurrence of band bending in a particular material is to investigate interfaces with substrates of different work functions. If band bending occurs, the observed shifts will depend on the work function of the particular substrate. However, for this scenario to be valid, both of the substrates investigated would need to have similar polarization energies. $SnS_2$ does have a higher work function than HOPG, however the polarization energy is also at least 1 eV higher.

There is some evidence that at least some of the core-level binding energy shifts could be band bending related. This is shown in Fig. 3.14, where in the top graph, the C 1s binding energy shifts are compared for the two *p*-6P interfaces. While the C 1s peak remains essentially at the same position on the HOPG substrate (open symbols), a significant shift towards the position of the HOPG curve is evident for the *p*-6P on the $SnS_2$ crystal (filled symbols). The initial shifts in the core-level binding energies are likely attributed to a change in the final state screening environment as a result in the changing polarization energies between the $SnS_2$ substrate and the *p*-6P or coronene organic materials. This is followed by a more gradual shift toward higher binding energies between the ~10 Å and 128 Å film thickness where the core holes remaining after the photoelectric process are relatively uniformly surrounded by equivalent organic molecules. The fact that a gradual shift in the core-level binding energy still occurred

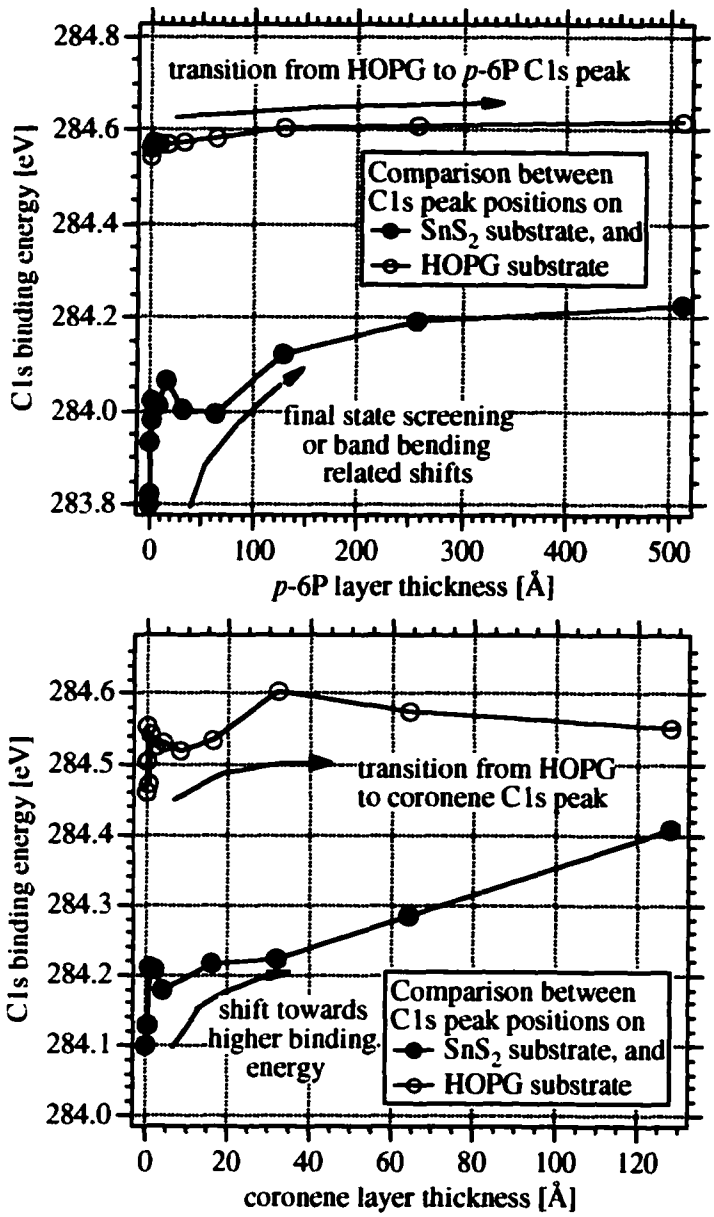


**Fig. 3.14.** Top: Comparison between the C 1s peak positions on the $SnS_2$ substrate (filled symbols) and on HOPG (open symbols) as a function of *p*-6P film thickness. The shift of the C 1s on the $SnS_2$ substrate is attributed to changes in the final state screening environment and possibly band bending occurring in the organic layer, which is a result of the different polarization energies and different work functions between the two materials. The same effect is not observed for the *p*-6P/HOPG interface since the two materials have both similar work functions and polarization energies. Bottom: C 1s peak positions on the $SnS_2$ substrate and on HOPG as a function of coronene film thickness.

after the final state screening environment became relatively constant is an indication that some degree of band bending could still occur in the organic material. As can be seen in Fig. 3.14, these shifts are typically on the order of 0.1 eV which is approaching the limits of the analyzer resolution, and prevents determination of the precise band bending magnitude.

As the film thickness increases, it appears that the C 1s binding energy for *p*-6P on $SnS_2$ starts to converge with that of the *p*-6P/HOPG interface (Fig. 3.14, top), similar to what was observed in the *p*-4P/HOPG and *p*-4P/$SnS_2$ systems [7]. Assuming band bending does occur in the organic films, the fact that these binding energies have not converged completely, even at 512 Å, indicates that the full width of the space charge region of the *p*-6P film has not been realized in these systems (on both interfaces the peak positions should converge if the layer exceeded the depletion region width). This is consistent with the fairly low dopant density expected in these materials. A similar result is obtained when plotting the C 1s peak positions in the case of the coronene interfaces which is shown in the bottom graph of Fig. 3.14. Precise measurement of the binding energies out to the full width of the space charge region of the organic material is also limited by the measurement process as a result of sample charging as discussed above.

If the shifts were band bending related, the origin of the necessary dopant density to support the required space charge field is not clear. While the *p*-6P and coronene thin films are considered to have semi-conducting properties, the actual conductivity of a

molecular solid is quite low [41]. It would therefore be expected that the extent of the band bending observed on our overlayer thickness scale would be expected to be relatively low. The dopant density required to support the magnitude of band bending measured in the organic material is likely in the $10^{15-17}$ $cm^{-3}$ range [50]. Under electrically neutral conditions, it is unlikely that the organic materials are able to support dopant concentrations that high [13]. While trace impurities in the organic layers could act as dopants, it is not probable that the active impurity concentration is high enough to support the observed band bending related shifts. A more likely cause of the band bending related shifts in these systems might be the measurement process itself. The x-ray or UV radiation can possibly cause damage to the organic molecules creating defects which may act as dopants. Low energy radical cations and/or anions due to oxidation or reduction by inelastically scattered electrons could behave as dopants. Soft-x-ray damage to *p*-terphenyl as applied to optical coatings has been investigated [51]. It was determined that the x-rays did degrade its efficiency as an organic phosphor although the types of defects created from the radiation induced damage was not discussed. X-ray damage to organic self-assembled monolayers (SAMs) has been reported [52], and it has been determined that the damage is primarily caused by the secondary electrons since the x-rays themselves do not interact strongly with the materials. Experiments investigating the effects of low energy secondary electrons on alkanethiolates on gold have revealed that one of several irradiation induced chemical modifications is the partial

dehydrogenation leading to C=C double bond formation [53-55]. While the chemistry of *p*-6P or coronene is substantially different than that of SAMs, these results indicate that chemical species induced by x-rays/secondary electrons could have energy states, which lie in the optical gap of the organic film. This indicates that there might be some measurement related influence on the amount of band bending measured, but more experiments are needed to draw a more conclusive explanation. Detection of any impurities or chemical species created by the measurement process is probably not possible due to the extremely low concentration of these species (less than one part in $10^7$).

An analysis of the XPS core-level intensities can be used to analyze the growth mode of *p*-6P on $SnS_2$. The relative x-ray absorption cross-section corrected intensities of the Sn 3d (substrate) and C 1s (organic film) peaks are plotted as a function of the *p*-6P film thickness in Fig. 3.15. The sharp change in the relative intensities in the first few molecular layers followed by a more gradual change in the intensities is indicative of the Stranski-Krastanov growth mode [56]. The evolution of the C 1s and Sn 3d peak intensities of the coronene on $SnS_2$ system suggest the same type of growth pattern. This growth pattern is also consistent with that of the *p*-quaterphenyl grown on $SnS_2$ [7].

Due to carbon being the only unique identifiable element in both *p*-6P and HOPG, XPS cannot be used to distinguish between the chemical identity of the substrate and the organic overlayer. While in the *p*-4P/HOPG system the conduction band (CB)-related

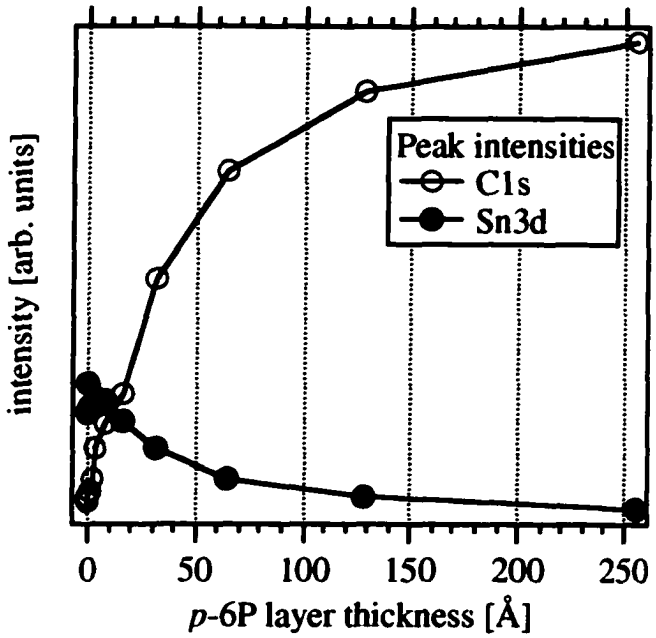


**Fig. 3.15.** $SnS_2$/*p*-6P interface; the C 1s and Sn 3d core peak intensities as a function of the *p*-6P layer thickness. The peaks were corrected for their X-ray absorption cross-sections. The rapid change in the first 8 Å followed by the reduced change at greater thickness indicates a layer-by-layer growth pattern in the first couple of monolayers followed by an increasingly clustered growth pattern. This is representative of the Stranski-Krastanov growth mode.

peak at about 13.5 eV in the He I spectra could be used for the evaluation of the growth modes, this is not possible in the case of *p*-6P since it has some emission features in that spectral range (compare UP-spectra of the *p*-6P/$SnS_2$ system in Fig. 3.1). This leads to an overlap similar to the C1s case making a sensible evaluation of the growth modes in this system impossible based on our data.

## 3.4. Conclusion

Thin films of *p*-sexiphenyl (*p*-6P) and coronene were grown in multiple steps on vacuum cleaved $SnS_2$ and highly oriented pyrolytic graphite (HOPG). The samples were characterized in situ between each growth step using a combination of UPS and XPS, to determine the energy alignment of the HOMO and LUMO of the organic to the valence/conduction bands of the $SnS_2$, or the Fermi level of HOPG. At the *p*-6P/$SnS_2$ interface, the interface dipole was determined to be 0.15 eV, and the VBM/HOMO offset was determined to be -1.27 eV, while the CBM/LUMO offset was -2.89 eV. For the coronene/$SnS_2$ sample, the interface dipole was 0.53 eV, the VBM/HOMO offset was -1.26 eV, and the CBM/LUMO offset was -2.37 eV. The interfaces of both *p*-6P and coronene deposited on HOPG had a negligible interface dipole, whereas the hole injection barriers were $\Phi_{bh}$ = 1.37 and 1.27 eV, and the electron injection barriers were $\Phi_{be}$ = -2.43 and -2.02 eV respectively.

The observed XPS peak shifts detected in these four systems strongly supports the notion that band bending and changes in the final state screening environment affect the magnitudes of the measured orbital offsets at interfaces involving organic materials. Precise separation of band bending and polarization energy contributions using photoelectron spectroscopy remains unresolved. Both phenomena affect the measured values of the orbital offsets, so the core-level binding energy shifts should be incorporated into the evaluation procedure. Significant shifts in the core-level binding energies were determined for both the *p*-6P/$SnS_2$ [$\Delta$CL(Sn 3d) = 0.16 eV; $\Delta$CL(C 1s) = 0.21 eV] and coronene/$SnS_2$ [$\Delta$CL(Sn 3d) = 0.08 eV; $\Delta$CL(C 1s) = 0.07 eV] interfaces attributed to either the higher work function or greater polarization energy of $SnS_2$. The HOPG interfaces, on the other hand, showed only negligible degree core-level energy shifts, matching the much lower work function and similar polarization energy of HOPG, which is of similar magnitude like the organic materials in contact.

**Acknowledgements**

Support by the Petroleum Research Fund (PRF# 35836-GB7) is gratefully acknowledged.

**References**

[1] C. W. Tang, S. A. VanSlyke, Appl. Phys. Lett. 51 (12) (1987) 913.

[2] J. R. Sheats, H. Antoniadis, M. Hueschen, W. Leonard, J. Miller, R. Moon, D. Roitman, A. Stocking, Science 273 (1996) 884.

[3] H. E. Katz, Z. Bao, J. Phys. Chem. B 104 (4) (2000) 671.

[4] R. Schlaf, P. G. Schroeder, M. W. Nelson, B. A. Parkinson, P. A. Lee, K. W. Nebesny, N. R. Armstrong, J. Appl. Phys. 86 (3) (1999) 1499.

[5] R. Schlaf, C. D. Merritt, L. A. Crisafulli, Z. H. Kafafi, J. Appl. Phys. 86 (10) (1999) 5678.

[6] R. Schlaf, B. A. Parkinson, P. A. Lee, K. W. Nebesny, N. R. Armstrong, J. Phys. Chem. B 103 (15) (1999) 2984.

[7] P. G. Schroeder, M. W. Nelson, B. A. Parkinson, R. Schlaf, Surf. Sci. 459 (2000) 349.

[8] Y. Park, V. Choong, E. Ettedgui, Y. Gao, B. R. Hsieh, T. Wehrmeister, K. Mullen, Appl. Phys. Lett. 69 (8) (1996) 1080.

[9] H. Ishii, H. Oji, E. Ito, N. Hayashi, D. Yoshimura, K. Seki, J. Lumines. 87-89 (2000) 61.

[10] G. Koller, R. I. R. Blyth, S. A. Sardar, F. P. Netzer, M. G. Ramsey, Appl. Phys. Lett. 76 (7) (2000) 927.

[11] I. G. Hill, A. Rajagopal, A. Kahn, Y. Hu, Appl. Phys. Lett. 73 (5) (1998) 662.

[12] A. Rajagopal, C. I. Wu, A. Kahn, J. Appl. Phys. 83 (5) (1998) 2649.

[13] I. G. Hill, A. J. Mäkinen, Z. H. Kafafi, Appl. Phys. Lett. 77 (12) (2000) 1825.

[14] J. Ishii, K. Sugiyama, E. Ito, K. Seki, Adv. Mater. 11 (8) (1999) 605.

[15] K. Horn, Appl. Phys. A 51 (4) (1990) 289.

[16] R. Schlaf, O. Lang, C. Pettenkofer, W. Jaegermann, J. Appl. Phys. 85 (5) (1999) 2732.

[17] J. R. Waldrop, R. W. Grant, Phys. Rev. Lett. 43 (22) (1979) 1686.

[18] E. Ito, H. Oji, N. Hayashi, H. Ishii, Y. Ouchi, K. Seki, Appl. Surf. Sci. 175-176 (2001) 407.

[19] W. Jaegermann, H. Tributsch, Progress in Surface Science 29 ((1/2)) (1988) 1.

[20] W. Jaegermann, "*Surface Studies of Layered Materials in Relation to Energy Converting Interfaces*" in *Photoelectrochemistry and Photovoltaics of Layered Semiconductors*, edited by A. Aruchamy (Dluwer Academic Publishers, Dordrecht, 1992).

[21] N. Sato, K. Seki, H. Inokuchi, J. Chem. Soc. Faraday Trans. 2 77 (1981) 1621.

[22] G. Grem, G. Leditzky, B. Ullrich, G. Leising, Adv. Materials 4 (1) (1992) 36.

[23] G. Leising, S. Tasch, F. Meghdadi, L. Athouel, G. Froyer, U. Scherf, Synthetic Metals 81 (1996) 185.

[24] Y. Z. Wang, R. G. Sun, F. Meghdadi, G. Leising, A. J. Epstein, Appl. Phys. Lett. 74 (24) (1999) 3613.

[25] H. Yanagi, S. Okamoto, Appl. Phys. Lett. 71 (18) (1997) 2563.

[26] A. Piaggi, G. Lanzani, G. Bongiovanni, A. Mura, W. Graupner, F. Meghdadi, G. Leising, M. Nisoli, Phys. Rev. B 56 (16) (1997) 10133.

[27] K. A. Cho, T. Shimada, M. Sakurai, A. Koma, J. Appl. Phys. 84 (1) (1998) 268.

[28] C. D. England, G. E. Collins, T. J. Schuerlein, N. R. Armstrong, Langmuir 10 (8) (1994) 2748.

[29] A. W. McKinnon, M. E. Welland, S. J. D. Warren, Thin Sol. Films 257 (1995) 63.

[30] R. Schlaf, P. G. Schroeder, M. W. Nelson, B. A. Parkinson, C. D. Merritt, L. A. Crisafulli, H. Murata, Z. H. Kafafi, Surf. Sci. 450 (2000) 142.

[31] M. P. Seah, Surf. Interf. Anal. 14 (1989) 488.

[32] I. Kojima, M. Kurahashi, J. Electron Spec. Rel. Phen. 42 (1987) 177.

[33] N. Koch, L.-M. Yu, V. Parente, R. Lazzaroni, R. L. Johnson, G. Leising, J.-J. Pireauz, J.-L. Bredas, Adv. Mater. 10 (13) (1998) 1038.

[34] All peak fitting procedures were incorporated into the IGOR software (Wavemetrics). A singlet Gaussian-Lorentzian function was fitted to the adventitious C1s peak on the vacuum cleaved substrate. The fit parameters (For the case of *p*-6P: Binding Energy = 285.19eV, FWHM = 1.85eV, assymmetry factor = -0.1, and Gaussian/Lorentzian ratio = 0.93) were determined for the adventitious C1s peak. The fit paramters for the adventitious C1s peak were then constrained at or near their original values, while another Gaussian-Lorentzian function was fit to the C1s peak attributed to the sexiphenyl or coronene. Since organic molecules were being deposited on the surface, the intensity of the initial contamination peak was reduced (a constrained amount) for each growth step to allow for the best overall fit that would match the real data. The FWHM and the asymmetry factor for the organic film C1s peak were held constant and to that of the original adventitious peak to insure reasonable C1s peak shapes, while some parameter range flexibility was allowed, particularly for the intensities and Gaussain/Lorentzian ratio, to yield the best fit to the experimental data.

[35] A. Rajagopal, A. Kahn, Adv. Mater. 10 (2) (1998) 130.

[36] I. G. Hill, A. Rajagopal, A. Kahn, J. Appl. Phys. 84 (6) (1998) 3236.

[37] K. Sugiyama, D. Yoshimura, T. Miyamae, T. Miyazaki, H. Ishii, Y. Ouchi, K. Seki, J. Appl. Phys. 85 (9) (1999) 4928.

[38] S. Narioka, H. Ishii, D. Yoshimura, M. Sei, Y. Ouchi, K. Seki, S. Hasegawa, T. Miyazaki, Y. Harima, K. Yamashita, Appl. Phys. Lett. 67 (13) (1995) 1899.

[39] M. Era, T. Tsutsui, S. Saito, Appl. Phys. Lett. 67 (17) (1995) 2436.

[40] T. Mikami, H. Yanagi, Appl. Phys. Lett. 73 (5) (1998) 563.

[41] M. Pope, C. E. Swenberg, *Electronic Processes in Organic Crystals and Polymers* (Oxford University Press, Oxford, 1999).

[42] R. S. Williams, P. S. Wehner, J. Stöhr, D. A. Shirley, Phys. Rev. Lett. 39 (5) (1977) 302.

[43] N. O. Lipari, P. Nielsen, J. J. Ritsko, A. J. Epstein, D. J. Sandman, Phys. Rev. B 14 (6) (1976) 2229.

[44] C. B. Duke, Surf. Sci. 70 (1977) 674.

[45] M. Keil, P. Samorí, D. A. dos Santos, T. Kugler, S. Stafström, J. D. Brand, K. Müllen, J. L. Brédas, J. P. Rabe, W. R. Salaneck, J. Phys. Chem. B 104 (16) (2000) 3967.

[46] R. Schlaf, B. A. Parkinson, P. A. Lee, K. W. Nebesny, N. R. Armstrong, Surf. Sci. Lett. 420 (1) (1999) L122.

[47] G. Kaindl, T.-C. Chiang, D. E. Eastman, F. J. Himpsel, Phys. Rev. Lett. 45 (22) (1980) 1808.

[48] K. Jacobi, Phys. Rev. B 38 (9) (1988) 6291.

[49] K. Seki, Mol. Cryst. Liq. Cryst. 171 (1989) 255.

[50] To estimate the dopant density required to support the observed band bending, the Poisson equation can be solved in relation to the potential $V_o$. The general form of the Poisson equation is $d^2V/dx^2 = -dE/dx = - eN_D/\varepsilon_r\varepsilon_o$, where $N_D$ is the dopant density, e is the elementry charge ($1.602 \times 10^{-19}$ C), the permittivity $\varepsilon_0 = 8.854 \times 10^{-14}$ F/cm, and $\varepsilon_r$ is the dielectric constant of the organic medium (approximated to be 3.0). Integrating V with respect to x, setting $x = d_n$ (width of space charge region) and rearranging to solve for $N_D$ yields $N_D = (2\varepsilon_r\varepsilon_o V_o)/(e(d_n)^2)$. Setting the estimated space charge region $d_n$ for the *p*-6P film at 2000Å ($2.0 \times 10^{-5}$ cm), yields $V_0$ for *p*-sexiphenyl to be 0.46 eV, and $N_D = 4 \times 10^{15}$ cm$^{-3}$. This calculated value naturally only represents a rough estimate for the dopant density since the full width of the space charge region is not known, however graphical approximation of the point where the C1s binding energy graphs on $SnS_2$ might meet the C1s graphs on HOPG (which is probably close to the flat band binding

energy of the C1s levels in the bulk of the organic materials) suggest that 2000Å might be a resonable estimate for the space charge region width.

[51] E. L. Benitez, M. L. Dark, D. E. Husk, S. E. Schnatterly, C. Tarrio, Appl. Optics 33 (10) (1994) 1854.

[52] P. E. Laibinis, R. L. Graham, H. A. Biebuyck, G. M. Whitesides, Science 254 (1991) 981.

[53] M. Zharnikov, S. Frey, K. Heister, M. Grunze, Langmuir 16 (6) (2000) 2697.

[54] M. Zharnikov, S. Frey, A. Gölzhäuser, W. Geyer, M. Grunze, Phys. Chem. Chem. Phys. 1 (13) (1999) 3163.

[55] K. Heister, M. Zharnikov, M. Grunze, L. S. O. Johansson, A. Ulman, Langmuir 17 (1) (2001) 8.

[56] C. Argile, G. E. Rhead, Surface Sci. Reports 10 (1989) 277.

# Chapter 4: Energy Level Alignment and Two-Dimensional Structure of Pentacene on Au(111) Surfaces

Submitted to Journal of Applied Physics
P. G. Schroeder, C. B. France, J.B. Park, and B. A. Parkinson*

**Abstract**

X-ray photoemission (XPS), ultraviolet photoemission spectroscopy (UPS) and scanning tunneling microscopy (STM) have been used to determine the energy level alignment and the molecular ordering of monolayer and submonolayer pentacene films on Au(111) in ultrahigh vacuum. Pentacene evaporated onto the van der Waals surface of $SnS_2$ was used as a comparison non-interacting substrate. A large interface dipole was measured for pentacene on Au(111) (0.95 eV) whereas pentacene on $SnS_2$ showed a relatively small interface dipole (0.26 eV). The different interface dipoles are related to the different orientations of the pentacene molecules due to different pentacene substrate

interaction energies. Differences in the UPS spectra also support changing molecular orientations on the two substrates. STM images of pentacene on Au(111) revealed that the molecules lay flat on the substrate and orient parallel to each other, forming striped structures that are commensurate with the Au(111) lattice. The pentacene coverage influences the packing of the striped structures that can form a variety of unit cells. Three related unit cells with pentacene molecules tilted ((2 x $2\sqrt{7}$), (2 x $\sqrt{31}$), and (2 x $\sqrt{39}$)) or perpendicular (2 x $3\sqrt{3}$) to the row direction were identified on Au(111).

## 4.1. INTRODUCTION

Crystals and thin films of highly purified pentacene have recently shown to exhibit hole mobilities of 1.4 $cm^2/V$ s and 0.25 $cm^2/V$ s respectively,[1,2] rather high values for an organic material. The high mobilities increase the likelihood of applications such as thin film transistors[3-5] and photovoltaic devices.[6,7] In experimental transistor devices, Si or $SiO_2$ has typically been used as the substrate for deposition of the pentacene film while gold has been used as the source and drain contacts in the field effect transistors constructed with pentacene. The positions of the energy levels in the pentacene with respect to the work function of gold and the spatial orientation of the molecular orbitals at the pentacene/gold interface will determine the ease or difficulty of charge transfer across this interface. Facile charge transfer or good blocking behavior will be important for efficient device operation. We report on the energy level alignment

and the structure of pentacene monolayers on the Au(111) surface and compare this to the non-interacting substrate $SnS_2$.

## 4.2. EXPERIMENTAL METHODS

All experiments were performed in a commercial Omicron Multi-Probe® ultrahigh vacuum (UHV) apparatus (base pressure = 5 x $10^{-11}$ mbar) equipped with a variable temperature scanning tunneling microscope (VT-STM), low energy electron diffraction (LEED), x-ray photoelectron spectroscopy (XPS), ultraviolet photoelectron spectroscopy (UPS), and a VSW EA125 single channel hemispherical analyzer. The organic physical vapor deposition chamber (base pressure = 1 x $10^{-9}$ mbar) is attached to the analysis chamber allowing the samples to be prepared *in situ*. To prepare the Au(111) film, a 2 $cm^2$ mica sample was heated for 24 hours in UHV to 300°C to evaporate surface contaminates. A gold film, approximately 1 μm thick, was then deposited from a resistively heated tungsten wire basket onto the mica substrate. The substrate temperature was held at 300°C during deposition, and then annealed at 350°C for three hours. The chemical purity of the film was determined using XPS, and LEED patterns revealed that the surface was predominately Au(111). STM images of the bare gold revealed the characteristic 22 x $\sqrt{3}$ reconstruction of the Au(111) surface.[8] The pentacene films were grown by sublimation from a resistively heated boron nitride

crucible. The source was held at 120°C for 12 hours prior to each deposition to outgas any lower vapor pressure contaminants. A 2 Å film was deposited onto the Au(111) substrate at a rate of 4Å/min, monitored using a Leybold quartz crystal microbalance (QCM). The source temperature during growth was 138°C while the gold substrate was kept at room temperature. The constant current STM images were obtained at positive tip biases, ranging from 0.5 to 1.0 V, with tunneling currents between 0.1 and 0.2 nA. Typical image acquisition times were 3-5 min. The height scale of the molecular corrugations was between 1 and 2Å for all images. A background plane fit was the only processing feature applied to the images.

## 4.3. RESULTS

The energy level alignment of the pentacene/Au and the pentacene/$SnS_2$ interfaces were measured using photoemission spectroscopy.[9] The UPS measurements, in conjunction with XPS measurements, allow the determination of the energy level alignment at metal/semiconductor or semiconductor/semiconductor interfaces. Details of the procedure for determining the energy level alignment of such interfaces using photoemission spectroscopy are described elsewhere.[10-14] A moderate shift of 0.25 eV was observed in the high binding energy cutoff edge of the UP-spectra between the vacuum cleaved $SnS_2$ substrate and a 2 Å thick film (or about one monolayer) of pentacene (Fig. 4.1A). The UPS revealed a strong shift of 0.87 eV (Fig. 4.1B) in the high

binding energy cutoff edge between the bare gold substrate and 2 Å thick film of the pentacene, indicating the presence of a significant interface dipole. This interface dipole is most likely attributed to a charge transfer, or a quantum dipole, from the pentacene into the Au since a molecular dipole is not possible due to pentacene's lack of a permanent dipole.

The normalized He II spectra (Fig. 4.1C) show the valence band of the bare Au(111) substrate, the vacuum cleaved $SnS_2$ crystal and the changes in the spectra as 4 Å of pentacene is deposited on each of these substrates. The photoemission peaks attributed to pentacene emerge after a few Ångstroms of deposition, although the very large initial intensity of the Au 5d valence peaks still dominate the spectra. The UPS (He II) of a 500 Å thick pentacene film is also shown to indicate the intensity and positions of the valence peaks (labeled a-h) for the bulk pentacene. Each of these peaks correlate closely on both substrates with the exception of peak c at binding energy of 4.4-5.2 eV. This peak, that is very intense on the $SnS_2$ and weak on the Au substrate, corresponds to the $\pi$ molecular orbitals that are delocalized along the long axis of the pentacene molecules.[15] The large work function shift of the pentacene on the gold substrate as well as the significant difference in intensity of peak c in the He II spectra are indications that there is a difference in the interaction energies and the orientation of the pentacene molecules on the two substrates.

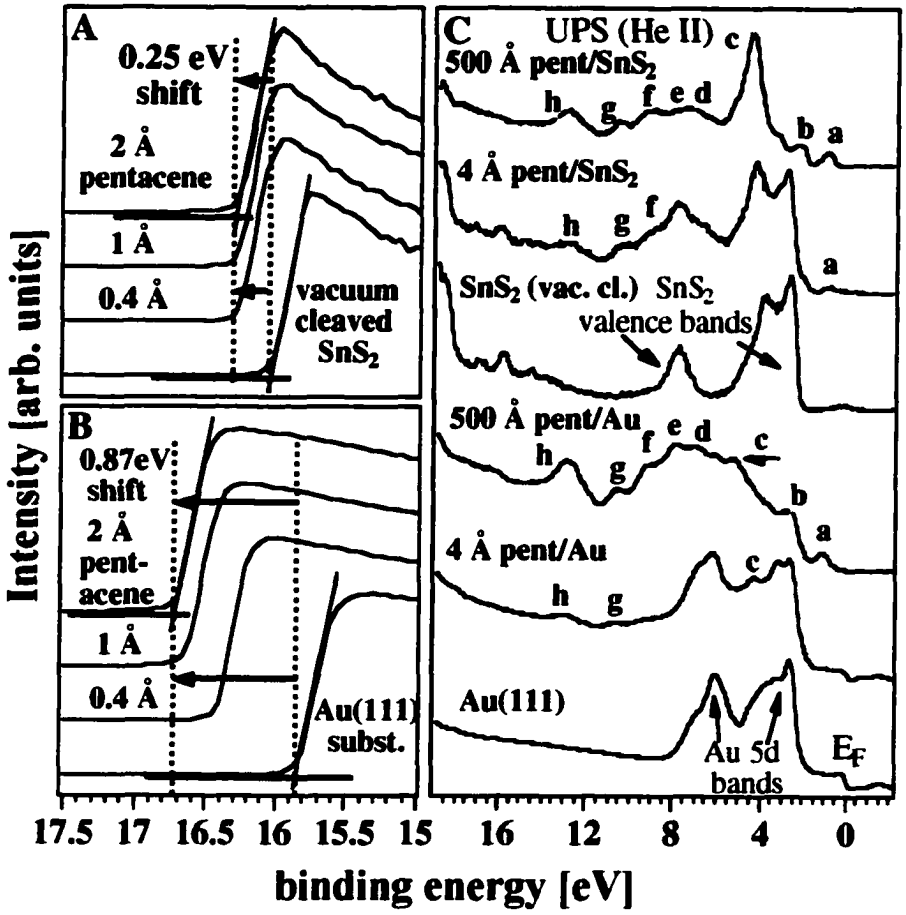


**FIG. 4.1.** (A) UPS (He I) showing the high binding energy cutoff for pentacene deposited on a vacuum cleaved $SnS_2$ substrate. The work function of the sample is determined by subtracting the binding energy from the source energy (21.21 eV). (B) UPS (He I) showing the high binding energy cutoff for pentacene deposited on a Au(111) substrate. (C) UPS (He II) spectra of the valence band regions for pentacene deposited on Au(111) and $SnS_2$ substrates.

Band diagrams of pentacene on Au(111) and on $SnS_2$ determined from the photoemission experiments are summarized in Fig. 4.2. Details of this experiment are discussed elsewhere[9]. The magnitudes of the electron and hole injection barriers as well as small core-level energy shifts, as measured with XPS, were determined. These core-level shifts could be attributed to band bending[10] or changes in the final state screening environment[16,17]. The phenomenon emphasized herein is the strong interface dipole that is represented as a step in the vacuum level in the energy level diagram. The interface dipole at the pentacene/Au(111) interface (Fig. 4.2, top), as determined from the full measurement process up to 512 Å of pentacene is 0.95 eV. For comparison, a similar experiment was performed for pentacene deposited on the layered semiconductor $SnS_2$ (Fig. 4.2, bottom). In this experiment, the magnitude of the interface dipole is substantially smaller than for the pentacene on gold (0.26 eV). This is very likely due to a much lower charge transfer across the interface that may be related to differences in the morphology of the pentacene on the two substrates. The ~0.3 eV difference in ionization energies of the 512 Å pentacene film on the two substrates also suggests that the morphology of the films is different since ionization potentials are usually dependent on the molecular orientation.

Scanning tunneling microscopy was used to investigate the molecular arrangement of the pentacene molecules on the Au(111) and $SnS_2$ substrates. No ordered structures have yet been observed on $SnS_2$, presumably since the molecule-substrate

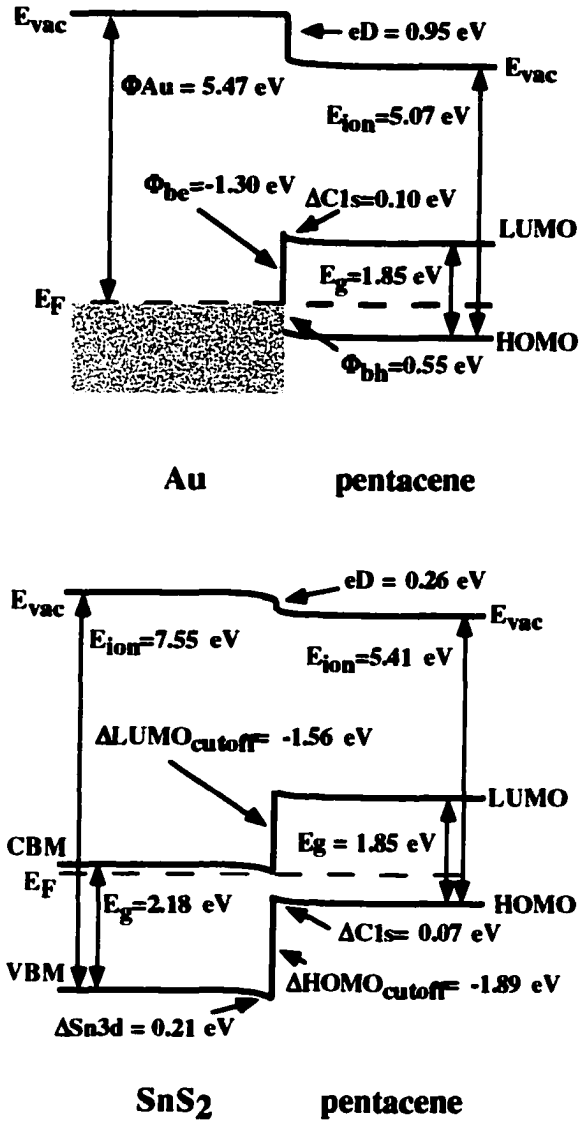


**FIG. 4.2.** Band diagrams of the pentacene/Au(111) interface (TOP) and the pentacene/$SnS_2$ interface (BOTTOM). A larger charge dipole is measured at the pentacene/Au interface (represented by a step in the vacuum energy level) than the pentacene/$SnS_2$.

interaction is likely to be very weak due to the van der Waals surface of the $SnS_2$. In this system, the molecule-molecule interaction may dominate the surface morphology resulting in a reduced interaction between the molecule and substrate, likely disorder in the thin films of pentacene, and a correspondingly low surface dipole. Figure 4.3 shows an STM image of an area of the Au substrate with several visible terraces. The pentacene molecules form long rows or stripes that are usually straight, although they are observed to curve to follow the step edges of the gold substrate or to bend around terminated rows of pentacene molecules.

Analysis of higher resolution STM images like those shown in Figure 4.4, suggests that the pentacene molecules are lying flat on the substrate and are commensurate with the Au(111) lattice. The molecular width of pentacene molecules, measured by cross-section analysis of the images, was determined to be 5.55 ± 0.17 Å, just slightly larger than the *para*-hydrogen-hydrogen inter-nuclear distance of 5.03 Å for pentacene in the bulk crystal structure[18]. This is also close to the estimated van der Waals width of the pentacene molecules of 5.98 Å.

The high-resolution STM images (Figure 4.4) reveal that the outer rings of the individual pentacene molecules appear brighter in the STM images. We attribute this to the pentacene molecular orbital that is accessed under these tunneling conditions on the Au(111). Double-lobed features were also observed in STM studies of pentacene

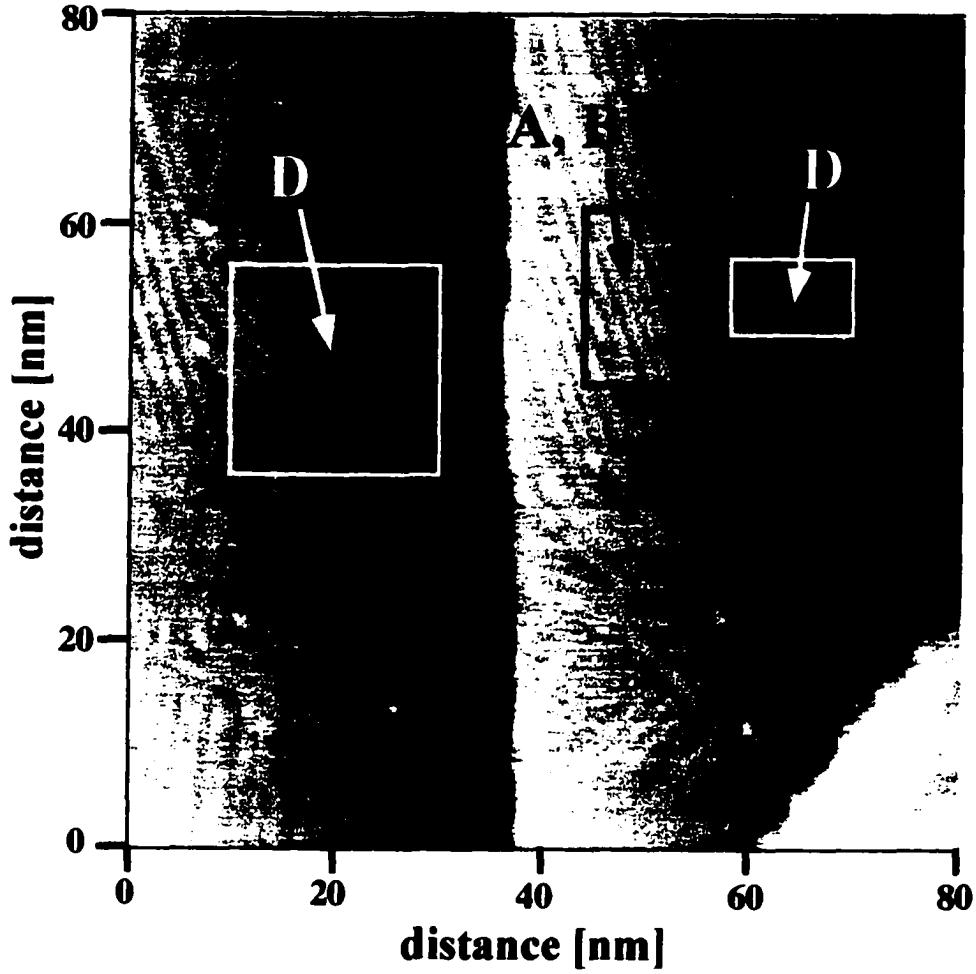


**FIG. 4.3.** STM (80 x 80 nm) image of a 0.8 to 1.0 monolayer of pentacene deposited on Au(111). A substrate step edge is observed down the center of the image. The black box shows a region of closely spaced rows consisting of type A, B and/or C unit cells. The white boxes show regions containing type D unit cells.

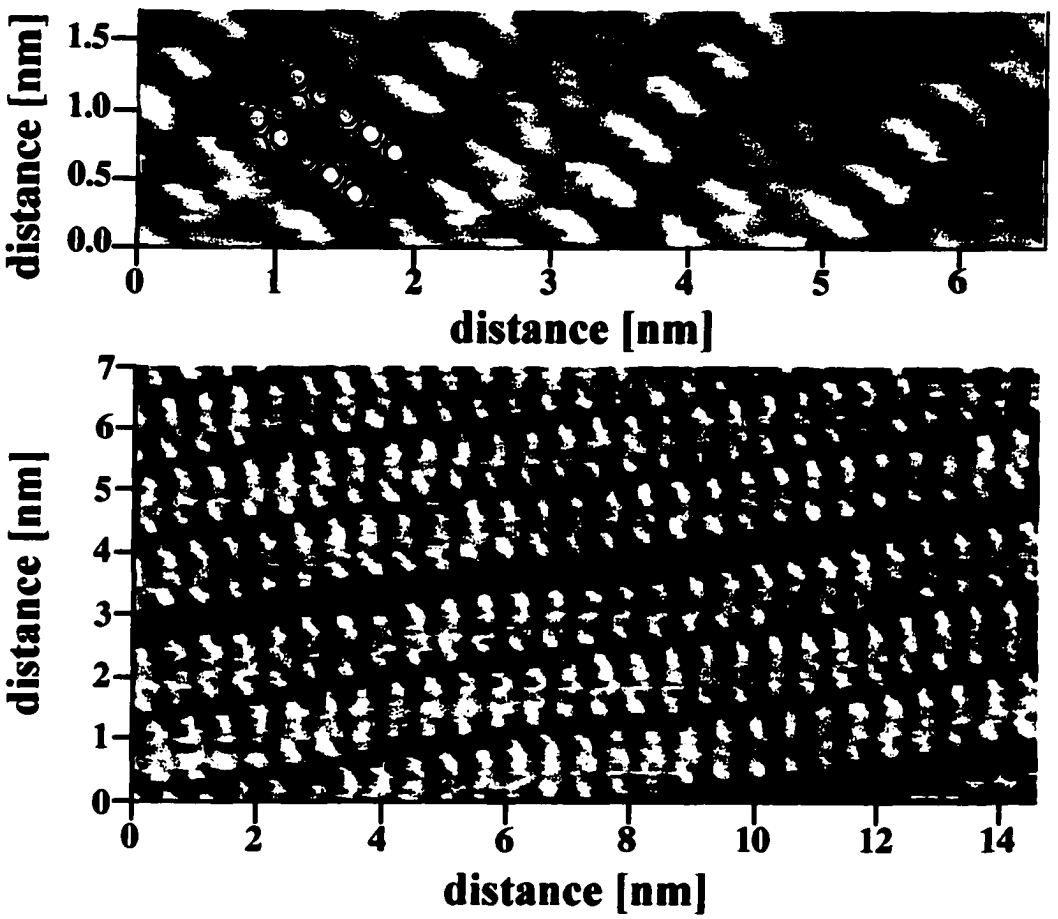


**FIG. 4.4.** (TOP) STM image of pentacene molecules with type A unit cell where the pentacene molecules are in line with those in the adjacent row. (BOTTOM) STM image of pentacene where the molecules are more staggered relative to those in the adjacent row corresponding to the type B or C unit cells. The region containing extra space between the rows corresponds to the type D unit cell.

adsorbed on a Si(100) 2x1 surfaces and were explained by the spatial distributions of the pentacene orbitals in contact with the Si dimers.[19]

## IV. DISCUSSION

The relative peak intensities in the UPS (Fig. 4.1) reveal differences in the morphology of pentacene films on the two substrates. The intense peak at 4.4-5.2 eV (peak c in Fig. 4.1C) is in the region of the UP-spectrum corresponding to the high binding energy $\pi$ bands for polyaromatic molecules. As previously stated, peak c is attributed to the diffuse $\pi$ molecular orbitals oriented along the long axis of the pentacene molecule. The intense band at 4.4-5.2 eV in the UPS for the pentacene on $SnS_2$ therefore indicates that the pentacene molecules are lying flat or only slightly tilted relative to the surface normal even as the film approaches a bulk state of pentacene. It is known that pentacene molecules initially lie flat on graphite substrates due to a strong commensuration with the hexagonal graphite lattice followed by a slight degree of molecular tilting upwards as the film thickness increases.[20] It is therefore very likely that the pentacene molecules also lie flat on the $SnS_2$ substrate (which is also a hexagonal van der Waals surface), but the molecule-substrate interaction energy is probably lower due to a lower degree of lattice matching.

This peak is slightly present in the UP-spectra for the 4 Å (or approximately one monolayer) of pentacene on gold which is consistent with the notion that for very thin

(one to several monolayers) films of pentacene are oriented flat on the gold surface as observed with STM. This peak is attenuated for thicker films of pentacene on the gold surface indicating a change in the morphology. Other experiments and analysis have revealed that thicker films of pentacene on gold form polycrystallites where the molecules are oriented perpendicular to the substrate surface and will be discussed in more detail in future work.[9]

The geometry of the pentacene molecule can produce commensurate structures on the gold lattice with the outer rings lying directly above substrate atoms, as shown in the diagrams in Figure 5. Deciphering the exact unit cell for each pentacene domain is not always possible since the differences in unit cell distances in the proposed geometries are often rather subtle. We however propose four predominant and at least one probable unit cell geometries of pentacene on the Au(111) lattice based on a statistical analysis of the measurement distances between adjacent pentacene molecules in the STM images as well as the relative orientation of the pentacene molecules to each other. In each of the proposed geometries, the $\pi$ orbitals of the outer rings lie on top of the Au atom underneath, leading to an increased molecule substrate interaction. Adjacent pentacene molecules within a row are then separated by one Au atom. A histogram of 240 measurements of row widths taken from 23 different images is shown in the bottom of Figure 4.5. The row widths were measured perpendicular to the row direction. Two distinct peaks in the row-width histogram are observed centered at 15 Å and 17.5 Å with

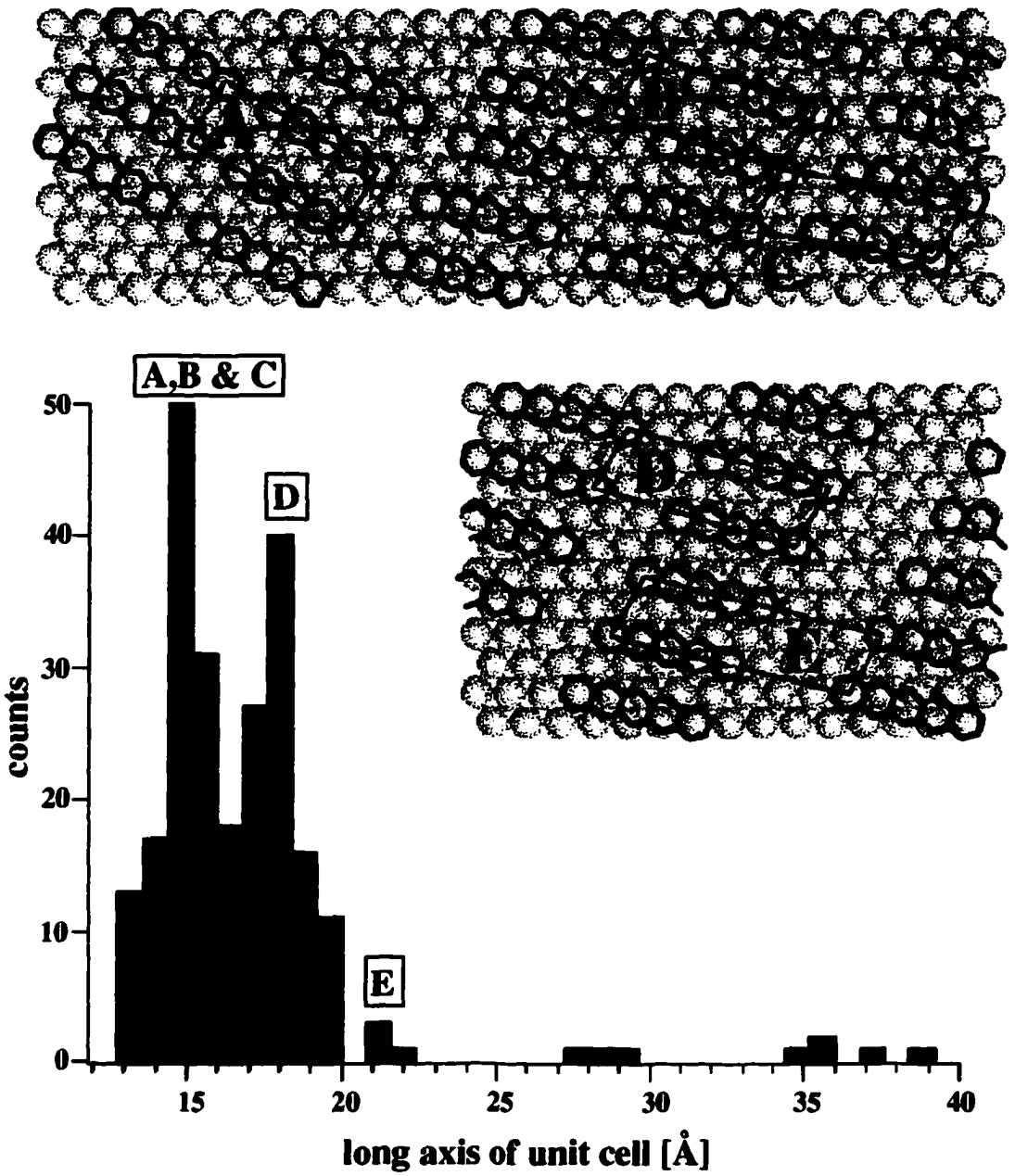


**FIG. 4.5.** (TOP) Diagram of four types of unit cells for pentacene molecules adsorbed on the Au(111) lattice. Type A has a (2 x $3\sqrt{3}$) relationship with the Au(111) surface. Type B has a (2 x $2\sqrt{7}$) unit. Type C has a (2 x $\sqrt{31}$) unit cell. Type D is similar to type B, except for an extra row of gold atoms between adjacent rows of pentacene molecules yielding a (2 x $\sqrt{39}$) unit cell. Larger spacings such as type E (2 x $2\sqrt{13}$) are also possible.

a small peak at 21.5 Å. The histogram, plus analysis of the high-resolution STM images, suggests that variety of unit cells are exhibited by pentacene on Au (111). Several rows exhibited a Type A adsorption configuration, as diagramed in Figure 4.5 (top; left), where the individual molecules lie perpendicular to the row direction (a (2 x $3\sqrt{3}$) unit cell) with respect to the underlying Au(111)). The type A unit cell has a unit cell length of 14.65 Å corresponding to a packing density of the molecules of 1.21 x $10^{12}$ molecules·cm$^{-2}$, the highest of any structure we have observed. Type B (Fig. 4.5: top; middle), is a (2 x $2\sqrt{7}$) unit cell that has a slightly lower packing density (1.19 x $10^{12}$ molecules·cm$^{-2}$), but is much more prevalent in the STM images. The type B unit cell leads to a calculated unit cell length of 14.9 Å. Type C (2 x $\sqrt{31}$) unit cell, also shown in Figure 4.5 (top: center), corresponds to a calculated unit cell length of 15.7 Å and has a slightly different offset of the molecules in the two rows than the type B cell. The difference between the type B and C unit cells is the position of the end ring of the pentacene molecule is offset by one row of Au atoms relative to that of the neighboring pentacene in the adjacent row for the type B unit cell. In type C, the end of the pentacene ring starts in the same row of Au atoms as the nearest neighbor in the adjacent row. The bottom STM image in Figure 4.4 consists primarily of types B or C unit cells, however limitations on the lateral resolution in the STM prevented distinguishing between these two unit cell types. In this image, the pentacene molecules appear staggered relative to those in the adjacent row. The

molecules in the STM image in the top of Figure 4.4 appear to be colinear with those in the adjacent row, consistent with the proposed type A unit cell. For the type A unit cell, the unit cell length is equivalent to the calculated row width (14.65 Å) since the molecules are arranged perpendicular to the row direction. In type B and C unit cells, the molecules are slanted relative to the perpendicular direction of the row, so the measured row width does not reflect the calculated unit cell length. The measured average row widths for types A, B, and C was 14.8 ± 0.9 Å, which is in range of the $3\sqrt{3}$ gold atom distance of 14.65 Å that corresponds to the distance perpendicular to the row directions for each of these unit cell types. It was therefore not possible to distinguish the type A unit cell from the type B or C unit cells without high resolution scans like Figure 4 that show the relative alignment of the molecules.

The type D unit cell had a larger spacing that is equivalent to one additional gold atom between the rows of pentacene molecules. An area showing the type D ($2 \times \sqrt{39}$) unit cell is shown in the white boxes in the image in Figure 4.3 and at higher resolution in the bottom image of Figure 4.4, where there is a larger space between two rows. This structure is also diagramed in Figure 4.5 (middle). The second peak in the histogram in Figure 4.5 is centered at 17.5 Å and coincides with the type D unit cell. This distance is close to the calculated row separation distance of 17.1 Å and is within the standard deviation of the measured value of 17.8 ± 1.9 Å. All the types of unit cells have an a-axis

equal to two gold atoms corresponding to a molecular separation of 5.64 Å, in excellent agreement with the average measured width of 5.55 ± 0.17 Å of individual pentacene molecules. While this corresponds well to the 5.03 Å separation distance determined from crystallography, it is a smaller separation distance than the van der Waals width of 5.98 Å for the pentacene molecules. This close separation distance for unit cells B-E is explained by the interdigitation of the hydrogen atoms between adjacent molecules within the rows due to the molecules tilting within a row. However, this interdigitation is not possible for the type A unit cell where the hydrogen atoms between the molecules are directly in line with each other. There would be even greater steric hindrance between the hydrogen atoms at the C1 and C2 positions of the pentacene molecules in adjacent rows. We speculate that there is a slight tilting up of the pentacene molecules from the Au(111) surface to increase the packing and reduce the steric interaction of the hydrogen atoms in the Type A structure. The tilting could be a prelude to edge on adsorption at even higher coverages. We have observed that at lower coverages the pentacene molecules still retain the striped morphology but tend to have larger spacings between rows of pentacene molecules such as in the type D unit cell. The small occurrence of slightly larger row widths in the histogram in Figure 4.5 (E) may be associated with an additional Au atoms between pentacene rows. Data at larger separations would represent additional gold atoms or entire missing rows. More experiments are underway to quantitate these observations.

## V. SUMMARY

In summary, we investigated the energy level alignment between pentacene molecules on Au and the non-interacting substrate $SnS_2$. On the Au(111) surface a relatively high surface dipole is measured indicating a stronger molecule-substrate interaction than on $SnS_2$ where the pentacene is unlikely to strongly interact with the van der Waals surface. STM images revealed that the molecules form ordered rows of parallel molecules on the Au(111) surface with the molecules flat on the surface, indicating a strong molecule-substrate interaction, consistent with the large interface dipole measured with UPS. The molecular rows showed several distinct separation distances and molecular orientations within the rows, leading us to propose the existence of four predominant pentacene two-dimensional unit cells that are commensurate with the Au(111) lattice.

## ACKNOWLEDGEMENTS

We would like to thank Dr. John Stickney for helpful discussions. This work has been supported by the Department of Energy under contract DE-F603-96ER14625.

**References:**

[1] J. H. Schön, C. Kloc, R. A. Laudise, B. Batlogg, Phys. Rev. B 58 (19) (1998) 12952.

[2] X. L. Chen, A. J. Lovinger, Z. Bao, J. Sapjeta, Chem. Mater. 13 (4) (2001) 1341.

[3] J. G. Laquindanum, H. E. Katz, A. J. Lovinger, A. Dodabalapur, Chem. Mater. 8 (11) (1996) 2542.

[4] Y.-L. Lin, D. J. Gundlach, S. F. Nelson, T. N. Jackson, IEEE trans. elect. devices 44 (8) (1997) 1325.

[5] J. H. Schön, S. Berg, C. Kloc, B. Batlogg, Science 287 (5455) (2000) 1022.

[6] J. H. Schön, C. Kloc, E. Bucher, B. Batlogg, Nature 403 (2000) 408.

[7] J. H. Schön, C. Kloc, B. Batlogg, Appl. Phys. Lett. 77 (16) (2000) 2473.

[8] J. V. Barth, H. Brune, G. Ertl, R. J. Behm, Phys. Rev. B 42 (15) (1990) 9307.

[9] P. G. Schroeder, C. B. France, J. B. Park, J. C. Forsythe, B. A. Parkinson, unpublished results .

[10] R. Schlaf, P. G. Schroeder, M. W. Nelson, B. A. Parkinson, P. A. Lee, K. W. Nebesny, N. R. Armstrong, J. Appl. Phys. 86 (3) (1999) 1499.

[11] R. Schlaf, P. G. Schroeder, M. W. Nelson, B. A. Parkinson, C. D. Merritt, L. A. Crisafulli, H. Murata, Z. H. Kafafi, Surf. Sci. 450 (2000) 142.

[12] R. Schlaf, C. D. Merritt, L. A. Crisafulli, Z. H. Kafafi, J. Appl. Phys. 86 (10) (1999) 5678.

[13] P. G. Schroeder, C. B. France, B. A. Parkinson, R. Schlaf, (to be published) .

[14] P. G. Schroeder, M. W. Nelson, B. A. Parkinson, R. Schlaf, Surf. Sci. 459 (2000) 349.

[15] H. Ozaki, J. Chem. Phys. 113 (15) (2000) 6361.

[16] E. Ito, H. Oji, N. Hayashi, H. Ishii, Y. Ouchi, K. Seki, Appl. Surf. Sci. 175-176 (2001) 407.

[17] N. Sato, K. Seki, H. Inokuchi, J. Chem. Soc. Faraday Trans. 2 77 (1981) 1621.

[18] R. B. Campbell, J. M. Robertson, J. Trotter, Acta. Cryst. 14 (1961) 705.

[19] M. Kasaya, H. Tabata, T. Kawai, Surf. Sci. 400 (1-3) (1998) 367.

[20] Y. Harada, H. Ozaki, K. Ohno, Phys. Rev. Lett. 52 (25) (1984) 2269.

# Chapter 5: Energy level alignment and morphology of pentacene deposited on Au(111) and $SnS_2$


## Abstract

The energy level alignment at the pentacene on gold and pentacene on $SnS_2$ interfaces were determined using *in situ* thin film deposition in combination with x-ray and ultraviolet photoemission spectroscopy (XPS, UPS) measurements. The organic thin films were grown in multiple steps by vapor deposition, then sequentially characterized *in situ* after each growth step. The pentacene/Au(111) interface is an Ohmic contact that yielded a strong (0.95 eV) interfacial dipole barrier. The vacuum cleaved single crystals of $SnS_2$ substrate provided clean, atomically flat and chemically inert surfaces, allowing for the investigation of the core-level energy shifts and interface dipoles without the interference from chemical reactions or problems with the substrate morphology. Low intensity XPS work function measurements enabled the detection of the overlayer-

thickness-dependent onset of charging phenomena in the UPS measurements. This allowed the precise determination of the highest occupied molecular orbital (HOMO) alignment of the organic molecules at the investigated interfaces. Scanning tunneling microscopy and temperature programmed desorption (TPD) of pentacene on gold allowed for a more complete understanding of the morphological properties of pentacene and how this influences band structure. Current-voltage measurements of doped and undoped pentacene/$SnS_2$ interfaces verified the existence of a rectifying junction and demonstrated the photoconductivity of the pentacene.

## 5.1 Introduction

Pentacene has been recently determined to be one of the most promising candidates for organic thin film field effect transistors (FET) [1-3] or photovoltaic devices [4,5] due to its high field effect mobility of 1.4 $cm^2/Vs$ for the single crystal [6] at room temperature, and upwards of $10^4$-$10^5$ $cm^2/V{\cdot}s$ at very low temperature [7]. Both single crystals and thin films of pentacene have been used to fabricate transistor devices. Typically a $Si/SiO_2$ substrate has been used as the substrate and the gate electrode, while gold has been used as the contact material for the source and drain electrodes. There have been several studies of pentacene deposited on Si or $SiO_2$ [8,9], however there have been very few studies into the electronic and morphological properties of the pentacene/gold interface. A further understanding of hole/electron injection or blocking

abilities as well as the orbital overlap at the source and drain contacts, provides insight into the current-voltage characteristics of pentacene FET devices. Determining the barrier offsets between an organic semiconductor film and a contact/electrode material to elucidate the electronic characteristics of the interface can greatly enhance device performance. Determining the energy level offsets at the pentacene/$SnS_2$ interface probes the properties of a p-n type heterojuction involving an organic and inorganic semiconductor. The nearly atomically flat van der Waals surface of the $SnS_2$ substrate also functions as a model substrate to further investigate fundamental properties of the organic semiconductor interface.

A common procedure for determining the energy level offsets is photoemission spectroscopy [10-16]. Ultra-violet photoelectron spectroscopy (UPS) is used to determine the work function and position of the occupied molecular orbitals/valence bands of the sample. X-ray photoelectron spectroscopy (XPS) is also included in our measurements to distinguish the interface dipole from either the band bending or final state screening related shifts in the work function, as well as assist in the determination of the growth modes of the organic films.

Determination of the binding energy of the molecules to the substrate can help lead to a better understanding of the properties of the interface, particularly the interfacial dipole. A strong interfacial dipole barrier is indicative of electrostatic forces between the substrate and overlayer. Temperature programmed desorption (TPD) is used to measure

the binding energies of molecules to a substrate surface. TPD measurements of pentacene on different substrates will help determine whether there is an increased bonding or electrostatic binding between the organic film and a substrate where a large interface dipole is present.

## 5.2 Experimental

All *in situ* experiments were performed in a commercial Omicron Multi-Probe® ultrahigh vacuum (UHV) apparatus (base pressure = 5 x $10^{-11}$ mbar) equipped with variable temperature scanning tunneling microscopy (VT-STM), low energy electron diffraction (LEED), temperature programmed desorption (TPD), x-ray photoelectron spectroscopy (XPS), ultraviolet photoelectron spectroscopy (UPS), and a VSW EA125 single channel hemispherical analyzer. The organic physical vapor deposition chamber (base pressure = 1 x $10^{-9}$ mbar) is attached to the analysis chamber allowing the samples to be prepared *in situ*. The 1 $cm^2$ $SnS_2$ crystal was cleaved *in situ* using a glued on metal foil, and characterized with XPS and UPS prior to deposition. The gold film was prepared by heating a mounted 2 $cm^2$ mica sample for 24 hours in UHV to 300°C to vaporize surface contaminates. The substrate temperature was heated to 300°C in the deposition chamber where the gold was then evaporated from a tungsten wire basket onto the mica substrate. Small molybdenum clips were attached to the outer edges of the

sample to ensure the gold film would be electrically grounded. The pentacene films were grown by sublimation from a resistively heated boron nitride crucible (source temperature was 142°C). The source was held at 120°C for 12 hours prior to deposition to outgas lower vapor pressure contaminants. The thin films were deposited at a rate of 4Å/min., monitored using a Leybold quartz crystal microbalance (QCM). After each growth step, the samples were characterized *in situ* using XPS (MgKα, 50 eV pass energy) and UPS (HeI, 21.21 eV; and HeII, 40.81 eV, both with 10 eV pass energy) in normal emission. A -5.00 V bias was applied to the sample for the UPS measurements to separate the sample and spectrometer high binding energy cutoffs. The $SnS_2$ substrates were doped n-type at a carrier concentration of about 7 x $10^{16}$ $cm^{-3}$ was mounted on a pedestal elevated 5 mm above the sample plate to prevent stray electrons from the manipulator assembly interfering with the ultraviolet photoelectron (UP)-spectra. Elevation of the gold sample was not necessary due to the sufficiently large sample size. The spectrometer was calibrated to yield the standard values [16-18] of 75.13 eV for the Cu 3p and 932.66 eV for the Cu $2p_{3/2}$ emission lines on an $Ar^+$ sputtered Cu sample. Binding energy zero was determined using the Fermi level position of the Cu sample. The overall analyzer resolution of 0.20 eV was determined from the width of the Cu Fermi edge. Therefore, work function and the highest occupied molecular orbital (HOMO) cutoff positions, determined from the high binding energy cutoffs and HOMO onsets of UP-spectra, were corrected for the analyzer broadening by adding/subtracting

0.1eV. XPS core level peak positions were determined by a fitting routine using IGOR Pro (Wavemetrics) data evaluation software. A vacuum deposited pentacene film on quartz was used to obtain the solid state absorption spectrum that was measured using a Varian Cary-500 UV-VIS-NIR Spectrophotometer.

The pentacene on gold STM images were obtained in constant current mode at positive tip biases ranging from 0.5 to 1.0 V, with tunneling currents between 0.1 and 0.2 nA. Image acquisition times are between 3-5 min. A background plane fit was the only processing feature applied to the STM images.

Atomic force microscopy was performed in tapping mode using a Digital Instruments Nanoscope® III Multiprobe AFM. The cantilevers used were Nanodevices Metrology Probes™ Multi75 with a force constant of 3 N/m and a resonance frequency of approximately 75 kHz.

Temperature programmed desorption (TPD) spectra (for details see Appendix A) were obtained using a Stanford Research Systems quadrupole mass spectrometer with a residual gas analyzer. The mass to charge ratio of 140 amu was selected for monitoring during acquisition of the TPD spectra because it was a major fragmentation peak of pentacene and there was little analyzer noise in that region of the mass spectrum. The substrate temperature was monitored with a Raytek® Ranger MX® infrared thermopile detector.

Current-voltage measurements were performed on a home-built electrical characterization station. The sample organic thin film devices were made by first gluing a thin $SnS_2$ crystal onto a stainless steel washer using a conductive epoxy. The pentacene was deposited on the $SnS_2$ crystal through a 5 mm diameter mask in our UHV deposition chamber. A 50 nm gold film was then deposited through a 3 mm diameter mask at $5x10^{-6}$ torr in a Denton DV-502A vacuum deposition chamber. The samples were placed on a micromanipulator with an annealed gold ball pressed down on the gold film as one contact and a metal probe pressed on the stainless steel washer as the other. The voltage were applied using a EG&G Model 174A polarographic analyzer, with the signal monitored using a Stanford Research Systems SR830 DSP Lock-In amplifier and recorded using MacLab/4e (ADInstruments) and Echem v.1.5.1 software.

## 5.3 Results of Energy Level Alignment Measurements

### 5.3.1 Pentacene on Au(111)

The pentacene film was grown sequentially on a vacuum deposited gold substrate in multiple steps. The UPS (He I) for pentacene on gold is shown in Fig. 5.1. The full spectra are shown in the center part of the figure with the bottom spectra being the UPS for the bare gold substrate. The changes in the band structure are evident as thicker layers of pentacene are deposited on the substrate. The high binding energy cutoff is shown normalized in the left part of Fig. 5.1. A very significant shift in the high binding

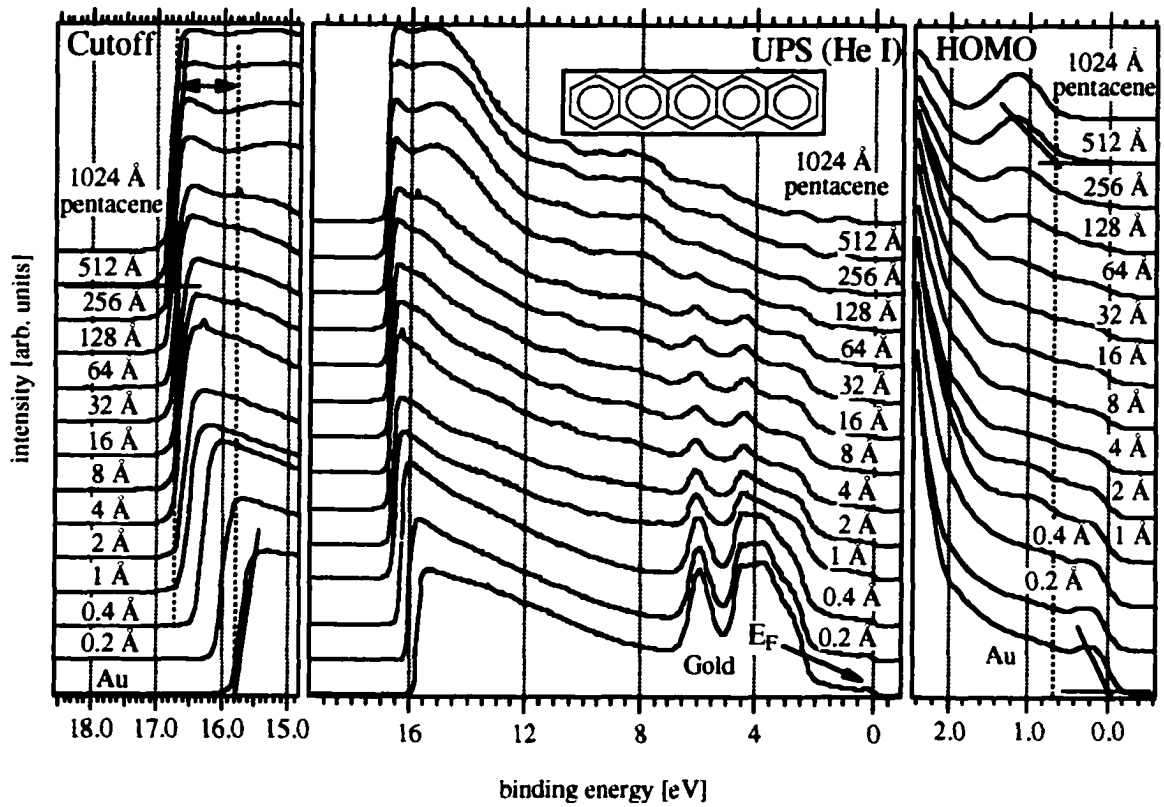


**Fig. 5.1** UPS He I spectra of pentacene deposited on Au(111). The center portion shows that full spectra on a binding energy scale. The spectra on the left are the magnified high binding energy cutoff (HBEC) used to determine the sample work function. The right side shows the magnified region where the gold Fermi edge and the HOMO peak of the pentacene are observed.

energy cutoff between the bare gold substrate and one monolayer of pentacene (about 2-4 Å) is clearly evident. This indicates the existence of a very strong charge dipole at this interface. The shift in the high binding energy cutoff is more gradual at this point, indicating only minimal band bending into the bulk of the pentacene. On the right part of Fig. 5.1, the Fermi Edge of the gold (0 eV) is shown along with the evolution of the highest occupied molecular orbital (HOMO) peak of the pentacene as the film thickness is gradually built up to over 1000 Å.

The pentacene on gold interface is a Schottky barrier, therefore the offsets of interest are the barrier height between the Fermi level of the Au(111) and the $HOMO_{cutoff}$ of the pentacene (hole injection barrier($\Phi_{bh}$)), and the $LUMO_{cutoff}$ (electron injection barrier ($\Phi_{be}$)) of the pentacene. The work function of the gold substrate was determined by subtracting the high binding energy cutoff of the UP-spectra from the source energy (21.21 eV) yielding $\Phi$ = 5.47 eV. The $HOMO_{cutoff}$ of the 512Å layer of pentacene was determined from the lowest binding energy edge of the spectra, to be 0.65 eV. The work function for the pentacene film at this same thickness was measured to be 4.42 eV. This gives a total work function shift ($\Delta\Phi$) of:

$\Delta\Phi = \Phi(Au) - \Phi(512Å\ pentacene) = 5.47\ eV - 4.42\ eV = 1.05\ eV.$

To more precisely determine the energetics of an electronic interface, any band bending that might be occurring in the organic material or polarization energy related

shifts that occur at the interface, need to be included in the evaluation. Such shifts are determined by measurement of the shift of the core level photoemission peaks using XPS. The core-level spectra are shown in Fig. 5.2, where C 1s photoemission peaks for the pentacene film are on the left and the Au 4f photoemission peaks are the on the right. The Au 4f peaks, arising from a metal, will not be subjected to any band bending related shifts. There is a subtle (0.10 eV) shift in the C1s spectra between the 0.4 Å layer, the lowest coverage where a Gaussian-Lorentzian peak could be fitted, and the 512 Å layer of pentacene.

Regardless of the origin of the core-level shift, neither band bending nor changes in the polarization environment should contribute to the magnitude of any charge dipole occurring at the interface. So the core-level shift should still be subtracted out from the total work function shift to precisely determine the magnitude of the interface dipole barrier. Subtracting the C 1s core-level shift ($\Delta$C1s) from the total shift in the work function of the sample ($\Delta\Phi$), yields the magnitude of the interface dipole barrier (eD):

$eD = \Delta\Phi - \Delta C1s = 1.05\ eV - 0.10\ eV = 0.95\ eV.$

The magnitudes of the core-level shift and interface dipole are displayed graphically in Fig. 5.3, where the total work function shift (filled symbols) and the C1s core-level shift (open symbols) are plotted vs. pentacene film thickness. The curves are aligned at the

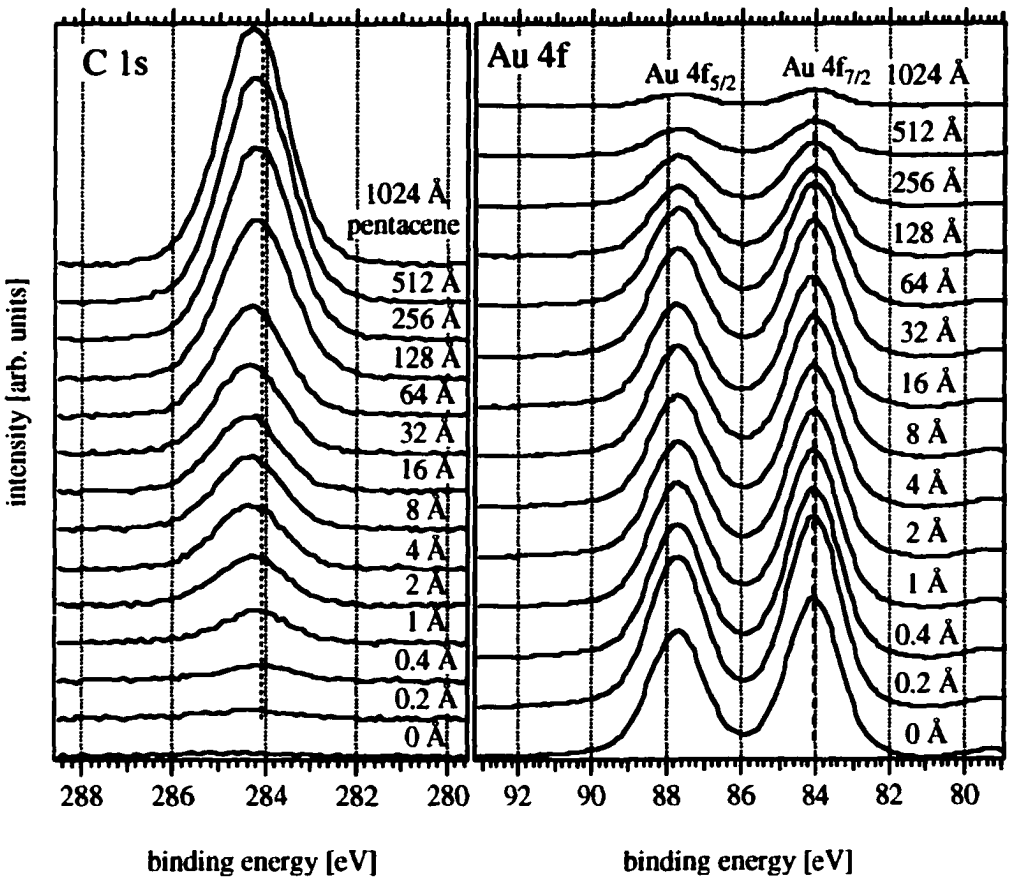


**Fig. 5.2.** XPS of the pentacene C1s (left) and substrate Au 4f (right) peaks as a function of pentacene layer thickness.

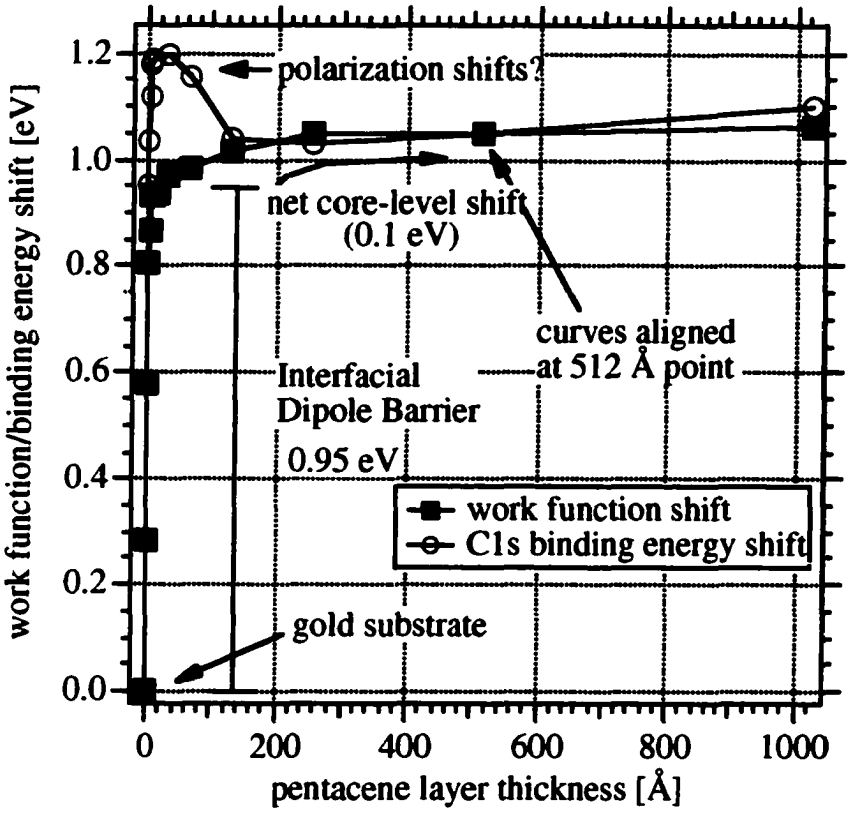


**Fig. 5.3.** Pentacene on Au(111): Plot of the C 1s binding energy shift and work function shift as a function of the pentacene layer thickness. The difference between these shifts yields the magnitude of the interfacial dipole barrier.

512 Å point, which is the thickest point where sample charging effects do not influence the measurements [11,14].

The hole and electron injection barriers ($\Phi_{bh}$ and $\Phi_{be}$) at the pentacene/gold interface are determined by comparing the positions of the HOMO/LUMO of the pentacene relative to the Fermi level of the gold. Subtracting the core-level shift in the pentacene (ΔC1s) from the $HOMO_{cutoff}$ at the 512Å layer results in the hole injection barrier:

$\Phi_{bh} = HOMO_{cutoff}$(512 Å pentacene) – ΔC1s = 0.65 eV – 0.10 eV = 0.55 eV.

The position of the LUMO cannot be measured directly using UPS, however it can be estimated by incorporating the optical absorption gap of the pentacene thin film into the evaluation. Figure 5.4 shows the visible absorption spectrum of a pentacene thin film deposited on a quartz substrate. The maximum absorption peak occurs at 668 nm, which corresponds to a band gap ($E_g$) of 1.85 eV. (It is important to indicate that the optical gap value for organic materials can only be used as an estimate for electronic HOMO-LUMO gap since the large excitonic binding energy of the molecules of the order of 0.5 eV is not accounted for [19]). Subtracting the band gap ($E_g$) from the hole injection barrier results in the electron injection barrier height:

$\Phi_{be} = \Phi_{bh} - E_g$(pentacene) = 0.55 eV – 1.85 eV = -1.30 eV.

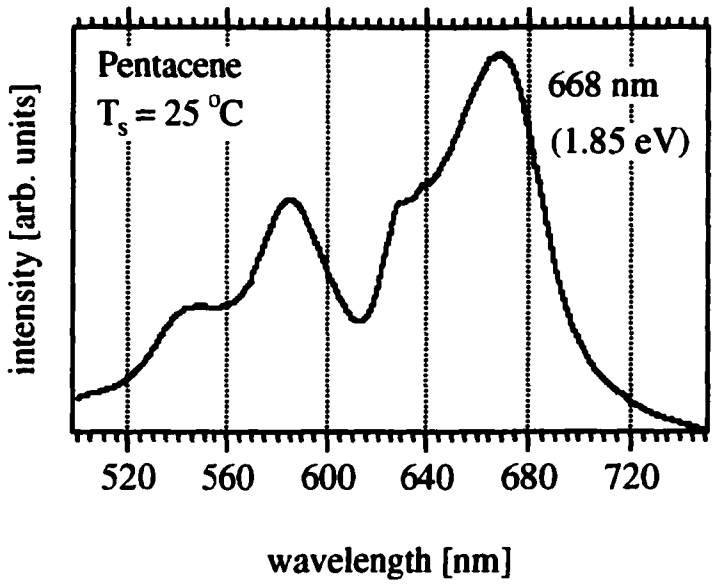


**Fig. 5.4.** Optical absorption spectra of a pentacene film used to estimate the band gap.

The negative sign of this barrier height indicates the $\Phi_{be}$ points upward into the pentacene layer from the Fermi level of the gold in the opposite direction of the $\Phi_{bh}$.

The ionization potential ($E_{ion}$) of the pentacene was determined by adding the work function of the pentacene, at the 512 Å thickness, to the $HOMO_{cutoff}$ of the same spectra yielding:

$E_{ion} = \Phi$(512 Å pentacene) + $HOMO_{cutoff}$ (512 Å pentacene)

= 4.42 eV + 0.65 eV = 5.07 eV

This ionization potential is relatively consistent with the measured value of 4.85 eV for an amorphous pentacene film [20]. The measured energy level alignment of the pentacene/Au interface is summarized in band diagram in the top part of Fig. 5.5.

### 5.3.2. Pentacene on $SnS_2$

The same procedure was applied to the pentacene on $SnS_2$ interface to investigate the behavior of pentacene at the interface of an inorganic semiconductor. Fig. 5.6 shows the UP-spectra sequence for the pentacene/$SnS_2$ interface. The bottom spectrum was measured on the vacuum cleaved $SnS_2$ crystal. The upper spectra were measured after each of the pentacene deposition steps, starting with a nominal coverage of 0.1 Å and progressively increasing in thickness up to the final coverage of 1024 Å. The center part of Fig. 5.6 shows the complete spectra revealing the evolution of the valence

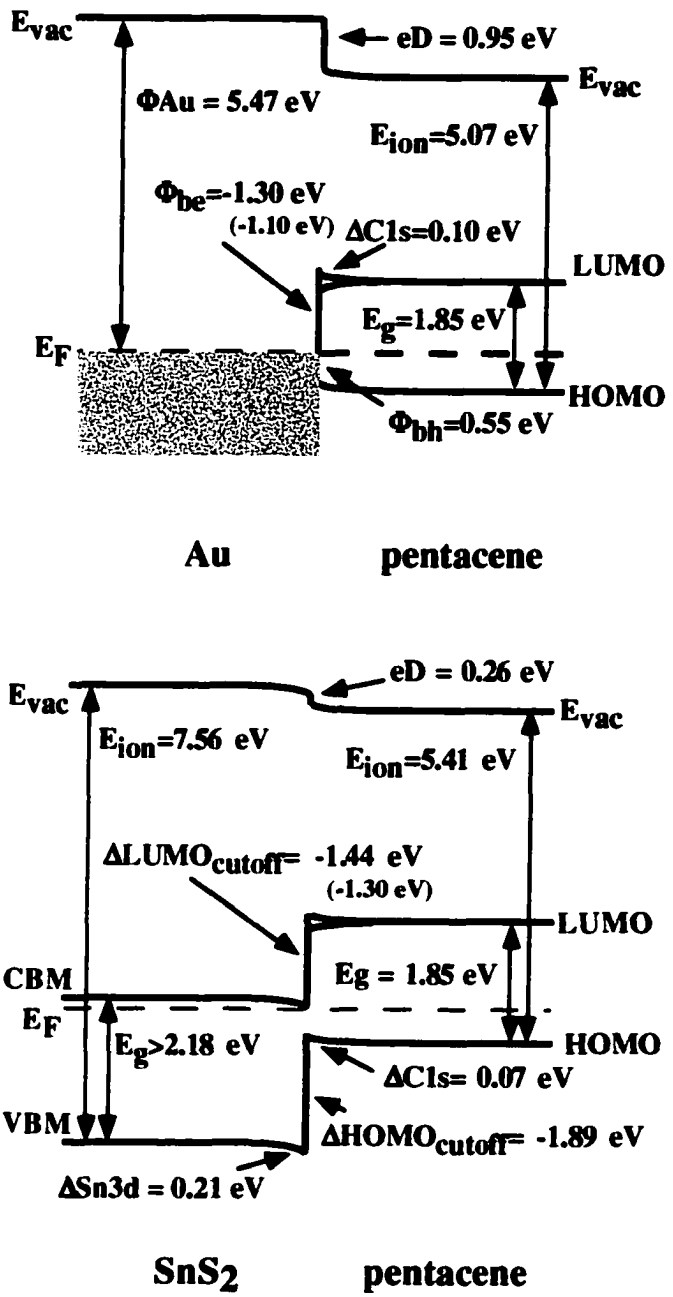


**Fig. 5.5.** Band diagrams of the pentacene/Au(111) (TOP) and pentacene/$SnS_2$ (BOTTOM) interfaces.

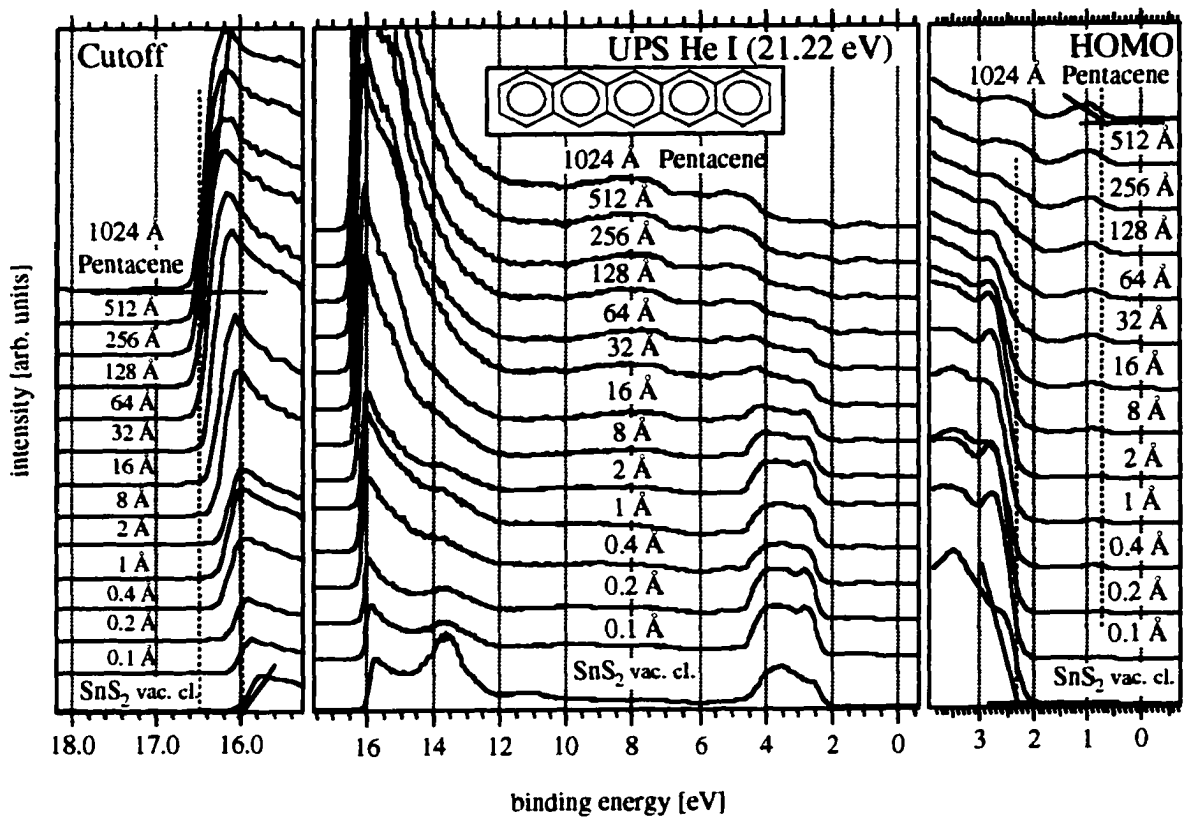


**Fig. 5.6.** UPS He I of pentacene deposited on $SnS_2$. The center portion consists of the full spectra. The left is the high binding energy cutoff (HBEC), while the right is the magnified region of the valence band maxima/HOMO of the $SnS_2$ and pentacene.

photoemission peaks between the $SnS_2$ substrate and the bulk pentacene film. The left part of this figure shows a magnification of the normalized high binding energy cutoff region of the UP-spectra. On the right is a magnified spectral region of the valence band edge/HOMO of the sample.

The core-level shifts were again measured with XPS. The Sn 3d emission peaks are shown in the left part of Figure 5.7. The shift in the Sn 3d emission line from the $SnS_2$ substrate, caused by the pentacene deposition, was determined to be $\Delta Sn3d = 0.21$ eV shift between the vacuum cleaved substrate (binding energy = 486.93 eV) and the thick pentacene film (binding energy = 487.14 eV).

The C 1s spectra are shown on the right side of Fig. 5.7 where the increasing intensity of the C 1s peak is evident. A trace quantity (estimated to be about 1-3% surface coverage) of carbon contamination peak at a significantly higher (>1eV) binding energy than the peak attributed to the pentacene was detected on the vacuum cleaved $SnS_2$ substrate. A peak fitting procedure that incorporates both the contamination C 1s peak and the C 1s peak for the organic layer was used to deconvolute the contamination peak from the pentacene related peaks that start to dominate the spectrum at about 2-4 Å coverages. Details of this fitting procedure, described in reference [21], allowed for the separation of the contamination and the pentacene C 1s peaks to determine the actual binding energy of the C 1s peak that is attributed to the deposited pentacene molecules. An example of this procedure, in the bottom right part of Fig. 5.7, shows the peak for the

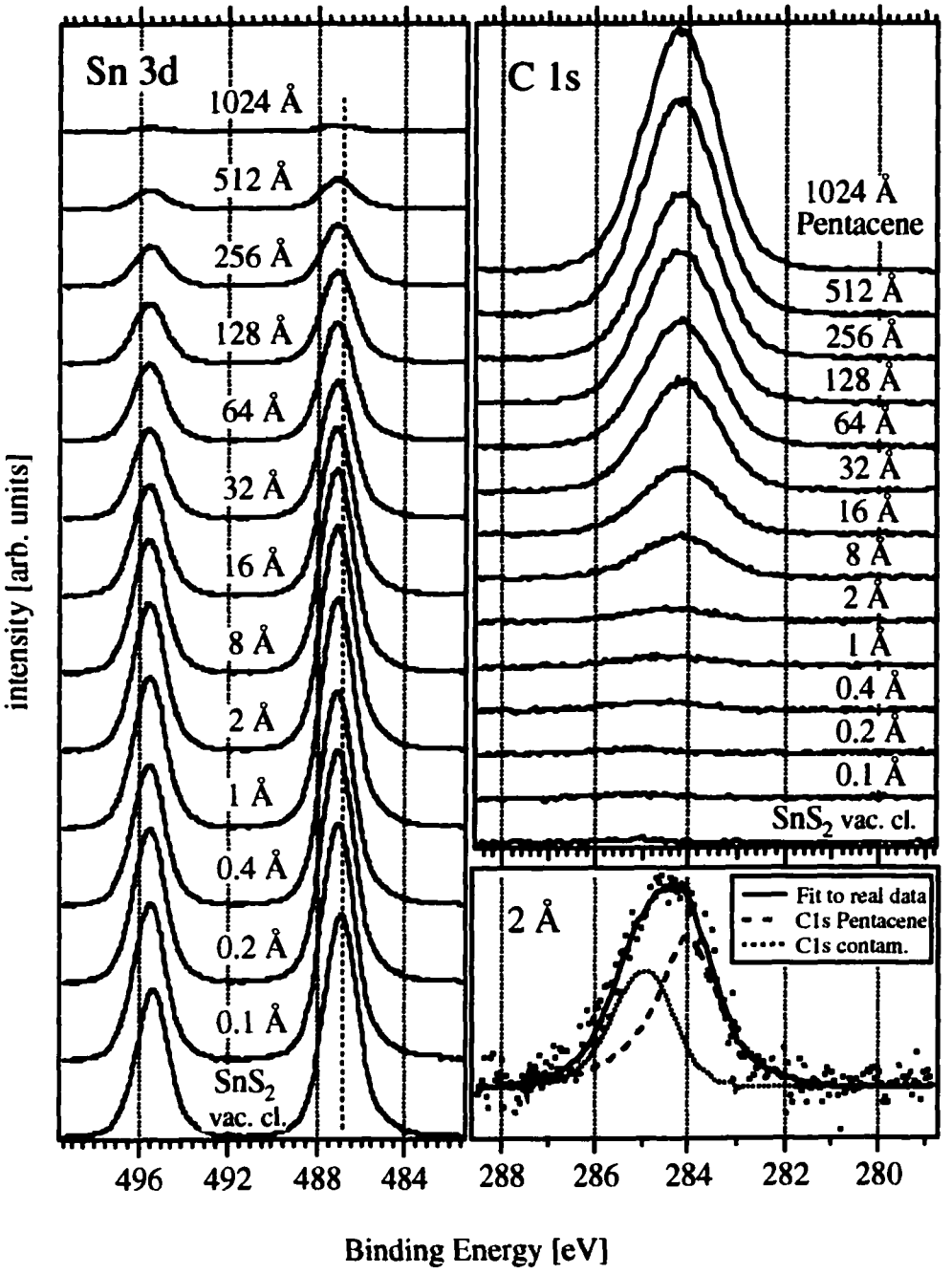


**Fig. 5.7.** XPS core-level peaks of Sn 3d (left) and C 1s (right) for the pentacene on $SnS_2$ interface. The inset at the lower right shows the curve fitting to separate the C 1s signal of the pentacene from that of trace contamination.

2 Å thick pentacene film fit with a Gaussian-Lorentzian function. The initial binding energy of the pentacene C 1s peak was determined to be 284.15 eV, that is the average C 1s binding energy for the 0.2, 0.4, 1, and 2 Å growth steps. The binding energy for the "thick" *p*-6P film (512Å) was determined to be 284.22 eV. This gives a small core-level shift (ΔC1s) of 0.07 eV in the pentacene film.

Adding the core-level shifts of the Sn 3d peaks and the pentacene C 1s emission peaks yields the total core-level shift [CL(tot)] magnitude across the interface:

$CL(tot) = \Delta C1s + \Delta Sn3d = 0.07\ eV + 0.21\ eV = 0.28\ eV.$

The total shift of the work function $\Delta\Phi$ at the between the vacuum cleaved substrate of the $SnS_2$ [$\Phi(SnS_2)$] and the 512 Å layer of the pentacene [$\Phi$(512 Å pentacene)] was determined to be:

$\Delta\Phi = \Phi(SnS_2) - \Phi(512\ Å\ pentacene) = 5.30\ eV - 4.76\ eV = 0.54\ eV.$

Subtracting the total core-level shift (CL(tot) = 0.28 eV) from the work function shift gives the magnitude of the interface dipole:

$eD = \Delta\Phi - CL(tot) = 0.54\ eV - 0.28\ eV = 0.26\ eV.$

The energy offset ($\Delta HOMO_{cutoff}$) between the VBM of the $SnS_2$ substrate and the highest occupied molecular orbital (HOMO) of the pentacene film was evaluated by subtracting the initial VBM position of the $SnS_2$ (2.26 eV) and the total core-level shifts (CL(tot) = 0.28 eV) from the $HOMO_{cutoff}$ of the 512 Å layer of pentacene yielding

$\Delta HOMO_{cutoff} = HOMO_{cutoff}$(512 Å pentacene) - VBM($SnS_2$) - CL(tot)

= 0.65 eV - 2.26 - 0.28 eV = -1.89 eV.

The conduction band maximum (CBM)/lowest unoccupied molecular orbital (LUMO) offset was determined by including the optical band gaps of the $SnS_2$ and pentacene into the evaluation. A common value of the band gap used for the $SnS_2$ crystal is 2.18 eV, which is the average of the optical absorption measurements given in reference [22] and references therein. The electronic band gap however is most likely several tenths of an eV larger and needs to be at least as large as the distance between the VBM and the Fermi level (>2.26 eV), so a value of 2.30 eV provides a reasonable estimate. The optical band gap for the pentacene was 1.85 eV as used from above. The offset between the LUMO of the pentacene and the conduction band maximum (CBM) of the $SnS_2$ was determined by subtracting the difference of the band gaps from $\Delta HOMO_{cutoff}$ (-1.30 eV) which yields

$\Delta LUMO_{cutoff} = \Delta HOMO_{cutoff} - (E_g(\text{pentacene}) - E_g(SnS_2))$

= -1.89 - (1.85 - 2.30 eV) = -1.44 eV.

The negative values of both the $\Delta HOMO_{cutoff}$ and the $\Delta LUMO_{cutoff}$ indicate that the HOMO and LUMO of the pentacene are at a lower binding energy than the VBM and CBM respectively of the $SnS_2$ crystal. A schematic of the complete electronic structure of the interface is diagrammed in the bottom part of Fig. 5.5. The ionization potential of

the $SnS_2$ was evaluated by adding the VBM position (2.26 eV) to the work function (5.30 eV), yielding

$E_{ion}(SnS_2) = VBM(SnS_2) + \Phi(SnS_2) = 2.26 + 5.30\ eV = 7.56\ eV.$

The ionization potential for the pentacene grown on $SnS_2$ was similarly determined by adding the position of the $HOMO_{cutoff}$(512 Å pentacene) to the work function of the same layer [$\Phi$(512 Å pentacene)] giving:

$E_{ion}$(512 Å pentacene) = $HOMO_{cutoff}$(512 Å pentacene) + $\Phi$(512 Å pentacene) =

$= 0.65\ eV + 4.76\ eV = 5.41\ eV.$

Sample charging is often an issue when measuring the orbital offsets of interfaces that have organic materials since the valence band and work function positions can no longer be precisely measured if the sample is charging. Determination of the onset of charging is described in reference [11], where the work function, as measured with both UPS and XPS, is plotted vs. sample thickness. Since the UV helium lamp has photon flux two to three orders of magnitude higher than the X-ray source, the work function measured with UPS has a much greater shift then when measured with XPS once sample charging sets in. Fig. 5.8 shows a graph where both work function lines follow each other very closely throughout the experiment. This indicates that sample charging does not affect the results significantly even at greater than 1000 Å thicknesses, which is an indication of the high conductivity of pentacene thin films [23]. The above energy

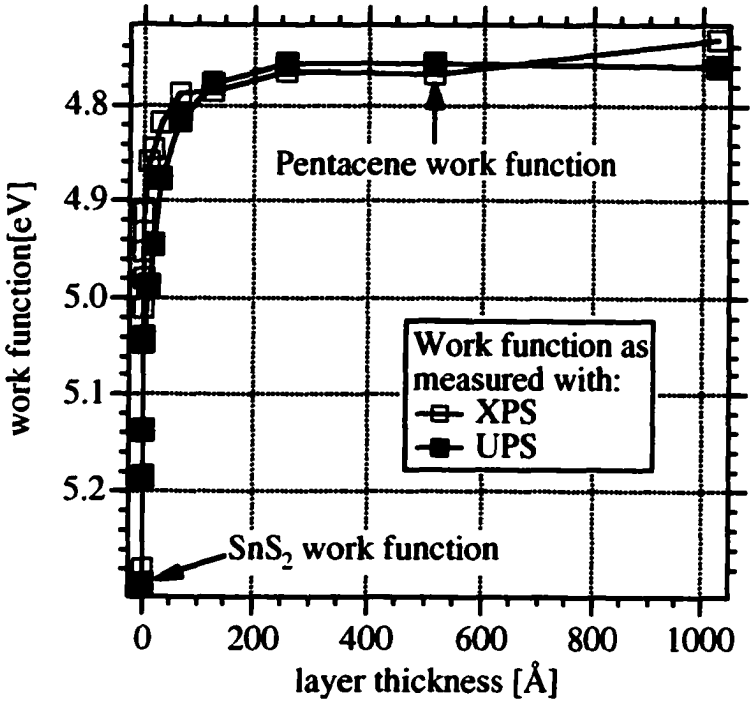


**Fig. 5.8.** Comparison of the sample work function as measured with XPS and UPS as a function of the pentacene film thickness. The work function will shift more significantly under the higher photon flux of the UV lamp upon the onset of sample charging. In this system, there is minimal sample charging even at ≥ 1000 Å thick film of pentacene.

alignments were determination using the values at 512 Å point of pentacene to insure that there would be no influence of sample charging on the measured spectra.

An indication of the growth mode of the pentacene films deposited on the Au(111) substrate can be given by the cross-section corrected intensity of the C 1s and Au 4f peaks (Fig. 5.9, top) plotted as a function of film thickness. The exponential decay of the Au 4f peak and the inverse exponential increase of the C 1s peak indicate that the pentacene film follows a Stranski-Karastanov growth pattern [24]. A similar graph is displayed for the pentacene on $SnS_2$ (Fig. 5.9, bottom) where the same type of growth mode is evident. Layer by layer growth would show a graph where the change of the peak intensities would be linear with respect to the film thickness. Purely island growth would show a lower rate of decay of the substrate peak intensity.

## 5.4 Discussion of Energy Level Offsets and Morphology

Our data does not allow the determination of whether the origin of the core-level peak shift ($\Delta$C1s) in the pentacene layer is due to band bending or to differences in polarization energies. In the pentacene/Au(111) system, the gold substrate has a significantly larger polarization energy than the pentacene (4.9 eV vs. 1.7 eV) [20], so the core hole remaining in the pentacene immediately adjacent to the gold surface should be screened more effectively than those in the pentacene bulk matrix.

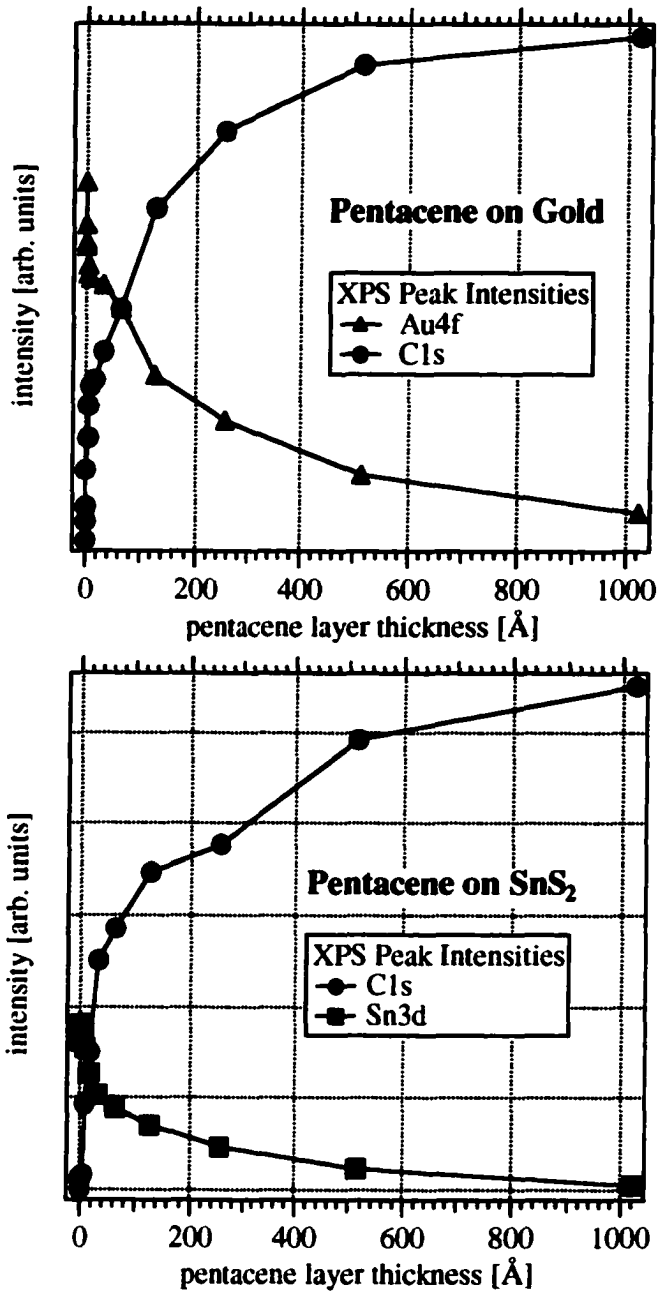


**Fig. 5.9.** Cross section corrected intensities of the XPS core-level peaks plotted as a function of the pentacene film thickness. Both the pentacene on Au(111) (TOP) and pentacene on $SnS_2$ (BOTTOM) revealed Stranski-Karastanov growth patterns.

There is a stronger localized core-level shift near the gold interface. This can be seen in the C 1s binding energy shift of approximately 0.3 eV in Fig. 5.3 between 0 Å and around 16 Å thickness of the pentacene. This strong core-level shift toward higher binding energies in the initial two or three molecular layers is similar to the shifts of the Xe 4f levels over the course of a few monolayers of xenon on Pd(001) as reported in reference [25]. After several molecular layer equivalents of pentacene, the binding energy decreases slightly by approximately 0.2 eV between 16 Å and 128 Å range.

These early shifts can be attributed to the changing polarization environment of the core holes remaining after photo-ejection of the core electron. The initial C 1s binding energy of the first sub-monolayer (0.4 Å) of pentacene is 284.12 eV, which is comparatively low due to the final state screening induced by the strong polarization of the gold substrate. The C 1s binding energy reaches a maximum of 284.41 eV at about the 16 to 32 Å thickness, where the gold surface has already been completely covered by a monolayer of pentacene. At this point, the core hole screening is significantly reduced since the polarization energy of the adjacent pentacene molecules is significantly lower than that of the gold substrate. In addition, most of the C 1s signal still originates from surface molecules where the vacuum does not contribute to final state screening. Beyond several molecular layers (> 32 Å), the remaining core-holes in the pentacene are more thoroughly surrounded by adjacent pentacene molecules leading to a greater polarization

induced screening than in the very thin films (2-32Å) of pentacene, yet still less than the polarization induced screening caused directly by the gold.

It seems clear that the initial core-level binding energy shifts can be attributed to differences in polarization environments between the interface and bulk pentacene. Beyond these localized shifts near the interface, there is the overall net shift of 0.10 eV between the initial C 1s binding energy and the "thick" film (512 Å) of pentacene the origins of which could be attributed to band bending or changes in the final state screening environments. This net shift extends well out into the bulk of the pentacene where the polarization environment becomes relatively constant, and while there could still be contributions from changes in final state screening conditions, it is possible that at least part of this net shift could be attributed to band bending.

Core-level shifts at the pentacene/$SnS_2$ interface may be more difficult to discern since the polarization energies of $SnS_2$ (probably less than 3 eV) and pentacene are likely to be closer in magnitude than pentacene and gold. An important point to make is that the Sn 3d emission peak for the vacuum cleaved substrate is at a lower binding energy than when covered with a pentacene thin film on. This is the opposite of the shift direction that would be expected if adsorbed pentacene molecules were screening the core-holes created in the Sn surface atoms. So, while relaxation effects are likely contributing to the magnitude of the core-level shifts, the fact that the Sn 3d binding energy shift to a higher value with increasing thickness of pentacene indicates that band

bending does occur in the $SnS_2$ substrate. This would be expected since the $SnS_2$ crystal is a moderately doped inorganic semiconductor.

The C1s shift between the very thin (0.4 Å) and thick (512 Å) pentacene layers is very small ($\Delta$C1s = 0.07 eV), almost within the margin of error of the measurement process. This shift could be attributed to band bending in the pentacene film or differences in polarization energies. This 0.07 eV shift constitutes the net shift in the C 1s core-level binding energy.

It should be noted that regardless of the origin of the core-level shifts at the interfaces, they do resemble band bending related shifts. As stated in reference [26], the energy state of hole injection is similar to the hole state created by photoemission both effectively lowering the barrier for hole injection. A similar effect of lowering the electron injection barrier should occur if polarization effects are dominant, however the exact magnitude of this effect remains unknown. It could be assumed that the magnitude of polarization effects for an electron would be similar to that for a hole, except that the direction of the band shift would be opposite of that for a hole. The band diagrams in Figure 5.5 reflect the core-level shift modifications to the injection and interfacial dipole barriers. The magnitude of the electron injection barriers ($\Phi_{be}$ and $\Delta LUMO_{offset}$) are the maximum estimated barrier heights where band bending would be assumed. The lower values for the electron injection barriers are labeled in parenthesis in Fig. 5.5 to point toward a lower limit to the range for the barrier height. The actual electron injection

barrier heights are likely to be lower due to screening of the electron from a polarization environment.

To further investigate the origins of the strong interface dipole barrier (0.95 eV) at the pentacene/gold interface, the binding energies of the pentacene molecules on the gold surface were measured using temperature programmed desorption. The purpose of measuring the binding energies was to determine whether the molecules on the gold surface were bound with a higher binding energy (due to increased electrostatic interactions) than the pentacene molecules in the bulk. The TPD spectra in Fig. 5.10 shows the desorption of an approximately 2 nm thick film (about 5 molecular layers) of pentacene on a Au(111) surface at a heating rate of 15 °C/minute. The mass to charge ratio that was monitored was 140 amu, which is a fragment peak of the pentacene molecule that appeared in a region of the mass spectrum where there was a low noise background. The first strong peak in the TPD spectrum is centered at $T_1$ = 142 °C that, when plugged into the Redhead algorithm, corresponds to an binding energy of 1.21 eV and is attributed to the physisorbed pentacene molecules in the second and third molecular layers on the surface. The temperature of 142 °C also very closely matches the temperature of the source crucible during deposition of the pentacene films. This peak is followed by a significant tailing of the signal as a higher temperature (and binding energy) is reached. Precise peak positions could not be fit into the higher temperature

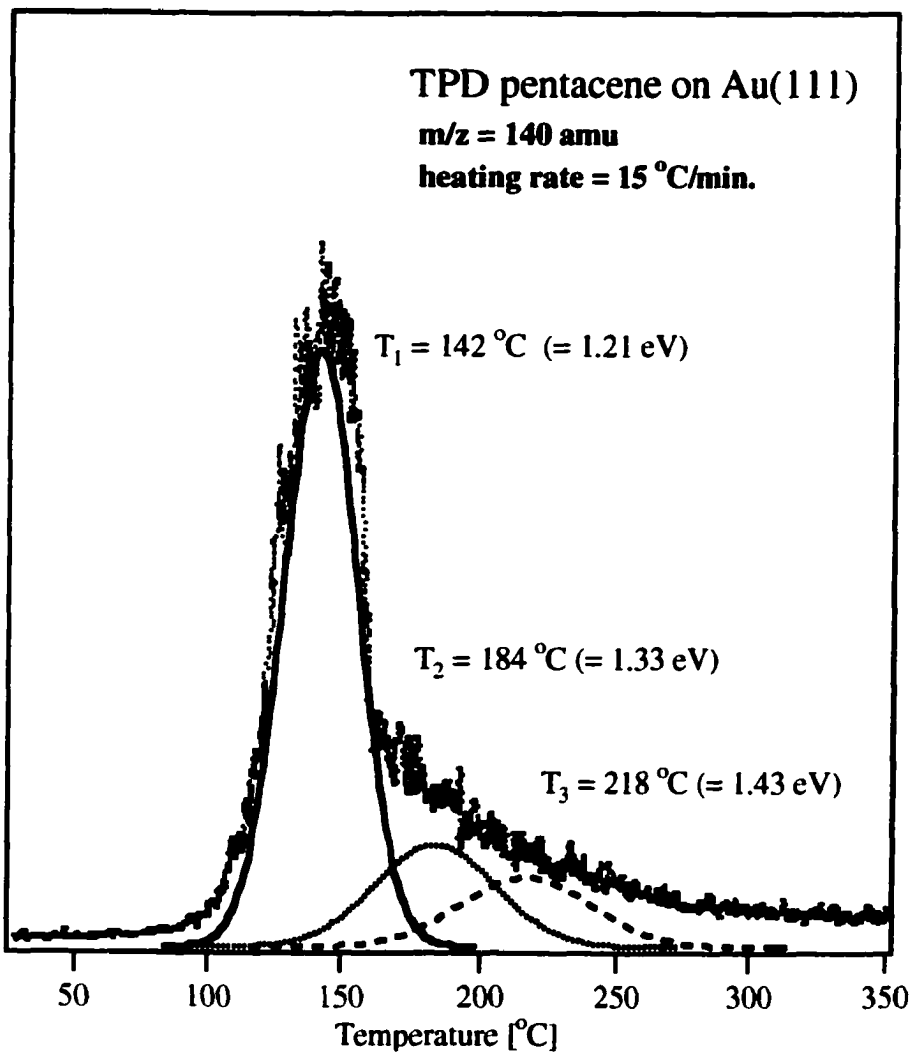


**Fig. 5.10.** Temperature programmed desorption spectra of pentacene on Au(111) using a 140 amu fragment peak. The first peak at 142 °C reflects the physisorbed species. The Gaussian peak fits to the higher binding energy side are approximations and reflect more strongly bound species of pentacene to the Au(111) surface where the effective binding energy increase is attributed to the electrostatic force of the interface dipole.

region of the spectra, although approximate fits could be made. There appeared to have at least two higher binding energy sites of the pentacene molecule on the surface at around $T_2 = 184 \pm 10$ °C and $T_3 = 218 \pm 10$ ° C. Based on TPD experiments of pentacene on $SnS_2$ and on a blank stainless steel sample plate, the $T_2$ peak is likely due to small amounts of pentacene adsorbed on the surrounding sample plate. The $T_3$ peak, corresponding to a binding energy of approximately 1.43 eV, is unique to the gold surface, and appears to be attributed to the first monolayer of pentacene being more strongly bound to the Au(111) surface. This yields an approximate binding energy difference of 0.22 eV between the first layer deposition of the pentacene on gold and the bulk pentacene. While the precision of TPD for this type of experiment is limited, it at least qualitatively verifies that there is a strong, most likely electrostatic, interaction between the pentacene and the gold. This is consistent with the strong relationship of the pentacene molecules to the Au lattice as was observed in the STM images (discussed below).

In comparing the He II spectra for each of these systems (Fig. 5.11), there are a couple of notable characteristics of the spectra as the pentacene film gets thicker on each substrate. Despite the intense valence band photoemission peaks from the Au substrate (Fig. 5.11, left), fairly significant changes are detectable at low coverage of the pentacene. The He II spectra for the 256 Å and above thicknesses can be attributed almost entirely to the pentacene film. The same holds true for the pentacene on $SnS_2$

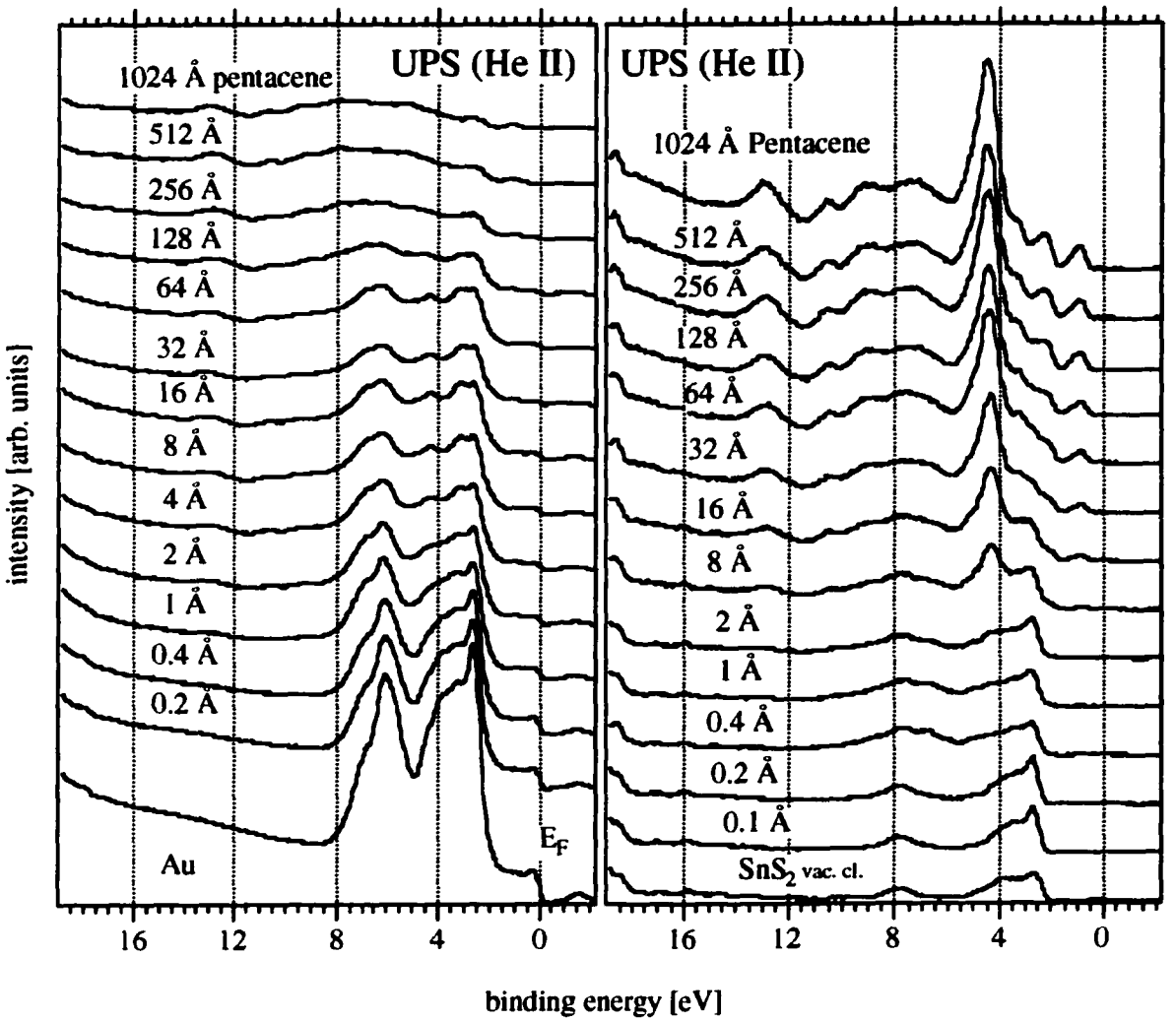


**Fig. 5.11.** Comparison of the UPS He II (hν = 40.81 eV) between the pentacene on Au(111) (LEFT) and pentacene on $SnS_2$ (RIGHT).

(Fig. 5.11, left). While the pentacene photoemission peaks are essentially at the same energies on both substrates, there are differences in the relative intensities of these peaks have certain differences.

The most obvious difference is the presence of the strong valence band peak at approximately 4.4 eV in the pentacene/$SnS_2$ system. This peak starts to emerge at approximately 1 Å average thickness and then continues to get stronger as the film thickness is reached. This same peak appears as a small feature in the pentacene/Au(111) spectra between the 2 Å thickness reaching a maximum intensity around the 64 Å thick film. It then is attenuated as the pentacene thickness exceeds 64 Å. These differences are more evident in Figure 5.12 where the UPS (He II) spectra of the 512 Å thickness of pentacene on $SnS_2$ and gold are plotted together with the 16 Å spectra of pentacene on gold, showing the presence of the 4.4 eV peak for the thinner layers of pentacene. Another noticeable difference in the is the ionization energies of the thick pentacene films on the two substrates. On gold, the ionization energy is 5.07 eV, while it is 5.41 eV on the $SnS_2$ (Fig. 5.5).

The differences in the UP-spectra can be attributed to different morphologies of the pentacene thin films on each of the substrates. Also, ionization energies of molecular solids could be orientation dependent. Exact differences in the morphologies of the films cannot be conclusively determined. However, several pieces of evidence indicate that the pentacene initially lies flat on both substrates, then the film becomes polycrystalline on

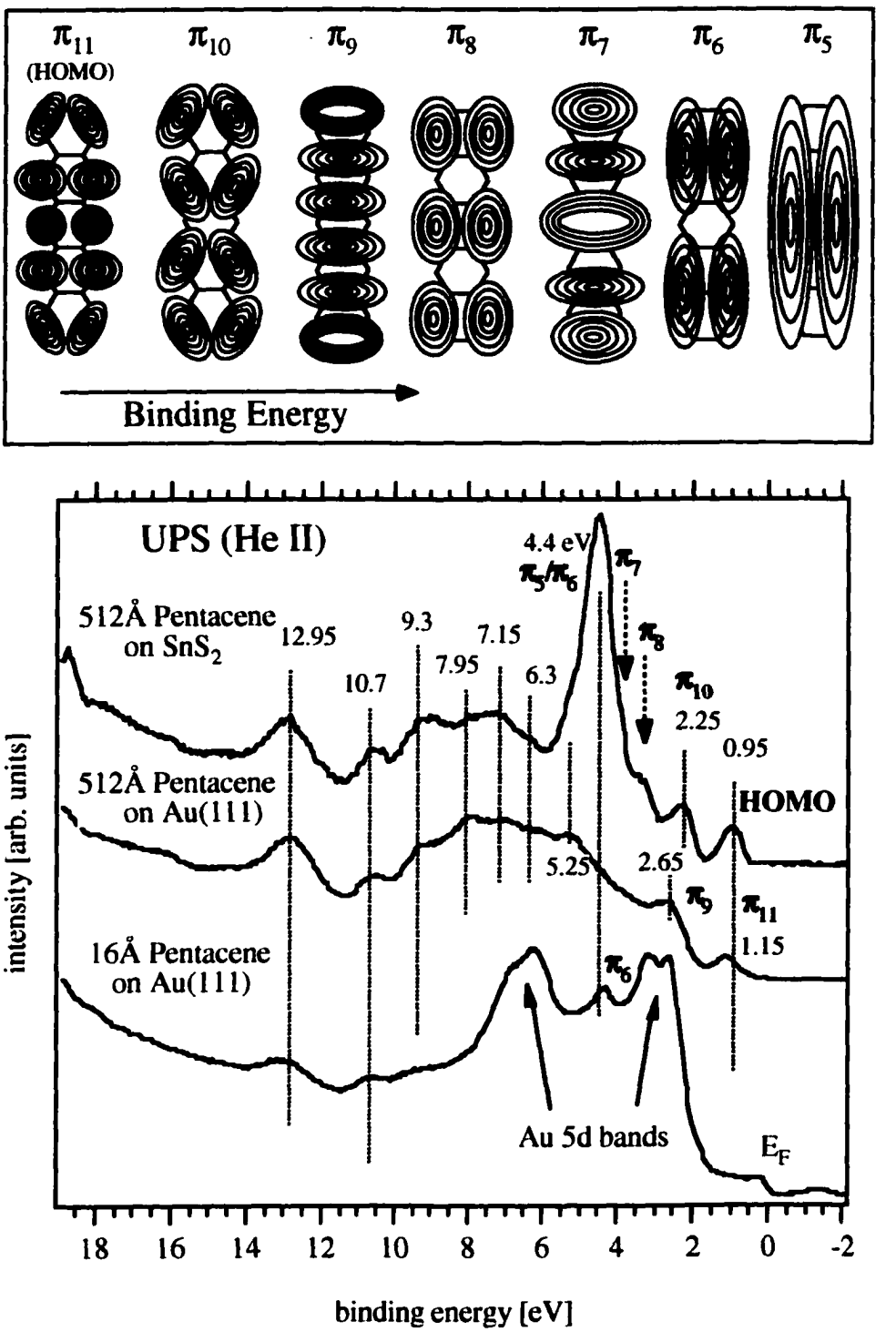


**Fig. 5.12.** Comparison of the UPS He II of the 512 Å thick films of pentacene on the $SnS_2$ and Au(111) surfaces. The 16 Å film of pentacene on the Au(111) surface is also shown for comparison of the peak of the $\pi_5/\pi_6$ band at ~4.4 eV. Molecular orbital diagrams based on diagrams in *H. Ozaki, J. Chem. Phys., 113, p. 6361 (2000).*

the Au(111) surface with the molecules oriented perpendicular to the substrate surface, while on the $SnS_2$ substrate, the molecules appear to either continue to lie flat or only gradually tilt upwards forming 0.5-3 μm molecular domains as will be discussed below and in reference [31].

Figure 5.13 shows the UPS (He I) spectra of a 512 Å film of pentacene on both the gold and the $SnS_2$ substrates where the pure π band region is between the energies of 0 eV and approximately 5 eV while the pure σ band region is generally above 7 eV. A combination of both π and σ bands are found in the region between 5 and 7 eV. Observing changes in intensity of these various bands can help elucidate the growth behavior of the pentacene films. It should be noted that these bands are more clearly resolved in the He II spectra since there is a reduced final state screening as a result of the higher energy incident photon [27]. The peak at 4.4 eV in the He II spectra is in the purely π band spectral region.

For very thin films of pentacene, the molecules are oriented flat on the gold surface as demonstrated in Chapter 4 and in the STM image in Figure 5.14. Although STM was attempted for thin pentacene films on the $SnS_2$ substrate, images could not be acquired. This was most likely due to a weak molecule substrate interaction, so the film did not remain bound to the $SnS_2$ surface during STM imaging, or the molecules adsorb to the tungsten STM tip as it passed over the surface. Studies of pentacene films on

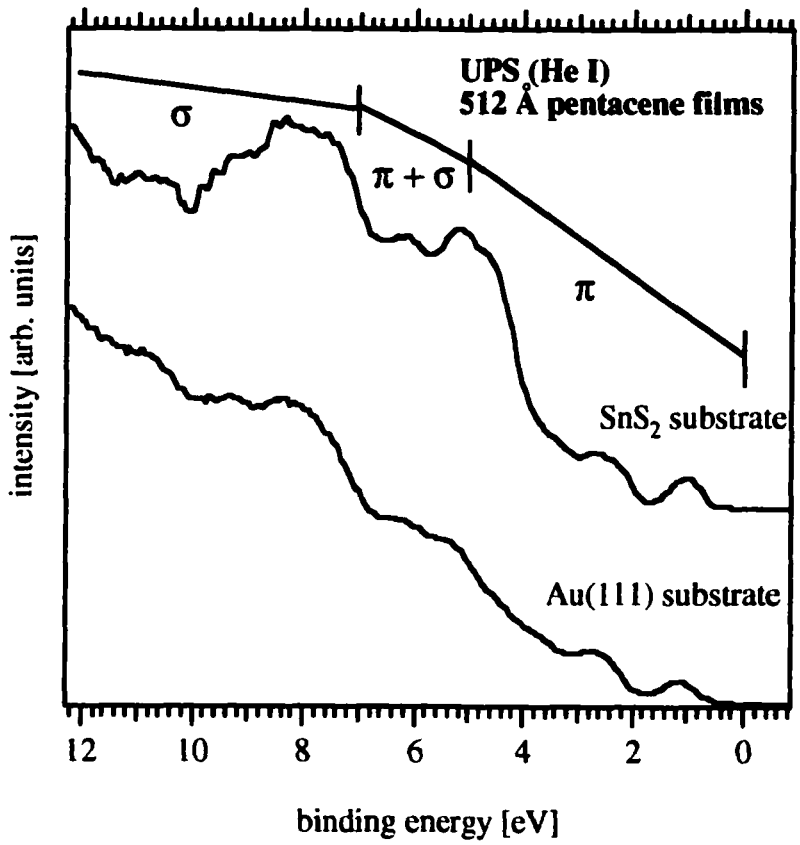


**Fig. 5.13.** UPS He I spectra of 512 Å of pentacene on the $SnS_2$ and Au(111) substrates. The peaks below 5 eV binding energy are purely π-bands. Those above 7 eV are purely σ-bands while those peaks between 5 and 7 eV are a mixture of π and σ bands.

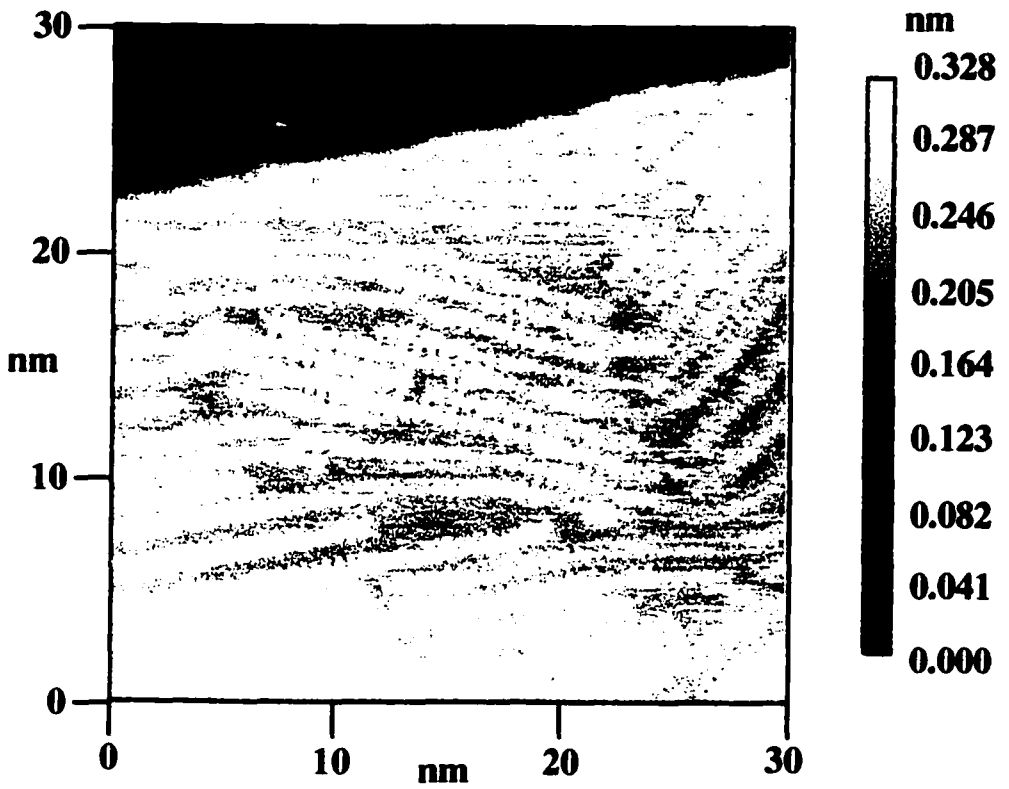


**Fig. 5.14.** STM image (30 x 30 nm) showing the adsorption and ordering of approximately one monolayer of pentacene on a Au(111) surface. The darker region in the top part of the image is a step-edge on the gold surface.

HOPG using UPS and Penning ionization electron spectroscopy have revealed that pentacene molecules lie flat on HOPG at low coverages and then gradually tilt upward with increasing coverage [28]. Penning ionization electron spectroscopy (PIES) is similar to UPS except that the excitation source is a metastable helium atoms, $He^*(2^3S$, 19.82 eV) and is sensitive only to the molecular orbitals at the very outer surface. Since HOPG has many similarities to $SnS_2$ such as low reactivity, a hexagonal close packed surface, and an atomically smooth surface; the initial adsorption of pentacene to each of these substrates is likely to be similar. As a result, it can be concluded the pentacene molecules initially lie flat on both the gold and the $SnS_2$ substrates.

For thicker films, it is known that polycyclic aromatic hydrocarbons, including pentacene, deposited at room temperature on rough metal surfaces, tend to form polycrystalline solids with the *ab* plane of each crystallite parallel to the substrate surface [29-31]. This orientation corresponds to the long axis (or c-axis) of the pentacene molecule oriented perpendicular to the substrate surface [32]. The gold surfaces used in our experiments are not rough but are nearly atomically flat with the predominant (111) face according to LEED and STM. The UPS of thick films of pentacene on the gold surface (Figs. 5.1 and 5.11) is very similar to that of pentacene films of on stainless steel surfaces [31] indicating similarities in morphology.

While we were unable to unambiguously determine the bulk morphology of the thick pentacene films, atomic force microscopy (AFM) images of 100 nm thick films on

both Au(111) and $SnS_2$ did reveal differences between the two films (Fig. 5.15). On the gold surface the pentacene film (Fig. 5.15, TOP) forms randomly spaced domains ranging in size from 500 nm to greater than 1 μm. The pentacene deposited on the $SnS_2$ substrate (Fig. 5.15, BOTTOM) yielded 3-5 μm long and 100-300 nm wide domains of pentacene all oriented in the same general direction. These results were reproducible in different sample spots, and with different scan angles. The pentacene films were rougher on the Au(111) surface (a Z-scale of 300 nm) whereas the pentacene on the $SnS_2$ surface was smoother (Z-scale was 150 nm). This indicates that the pentacene molecules are forming polycrystallites on the gold surface with the molecules oriented perpendicular to the substrate surface, whereas on the $SnS_2$ surface, the molecules seem to be forming smoother films with the molecular orientation likely more parallel to the substrate. The reasons for the unidirectional bulk orientation of the pentacene domains on $SnS_2$, as seen in bottom image in Fig. 5.15, is uncertain but likely attributed to the initial adsorption of pentacene on the substrate.

To explain some of the differences in the UPS He II, band assignments were made for some of the peaks in the spectra. The assignments were based on gas phase UPS of polyaromatic hydrocarbons and solid state UPS of pentacene films on stainless steel and HOPG, where it was determined that pentacene had eleven $\pi$ molecular orbitals [31,33]. These peak assignments would be more conclusive if the spectra were from

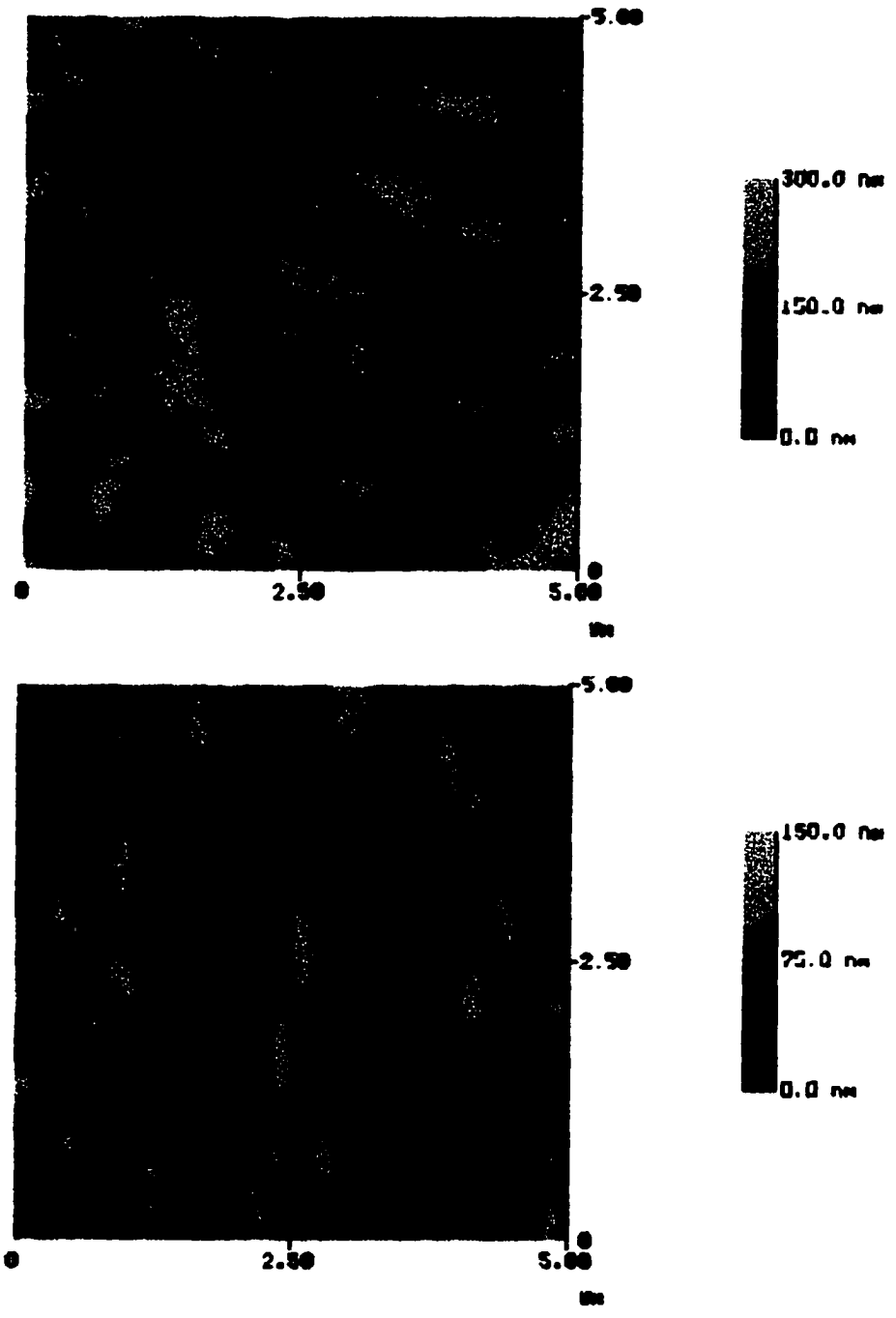


**Fig. 5.15.** Atomic force microscopy images of 1000 Å pentacene films deposited on Au(111) (TOP) and $SnS_2$ (BOTTOM).

PIES, due to its higher surface sensitivity. UPS will nonetheless supply further insight into the different molecular orientations. The peaks in the UPS in Fig. 5.12 at 2.65 eV in the 512 Å thickness of pentacene on the Au(111) substrate corresponds to the $\pi_9$ molecular orbital of pentacene which has five nodes perpendicular to the long axis, and a large electron distribution at the long axis end of the molecule [31]. This indicates that the pentacene molecules in the thick film were oriented perpendicular to the surface as was the pentacene on the stainless steel [31].

The peak at approximately 4.4 eV, which is predominant on the $SnS_2$ substrate, corresponds to the $\pi_5$ or $\pi_6$ molecular orbitals of pentacene that are energetically very close together. The $\pi_5$ and $\pi_6$ orbitals are strongly delocalized with only one node along and zero ($\pi_5$) or one ($\pi_6$) node perpendicular to the longitudinal axis of the pentacene molecules but have a lower electron distribution at the long axis end than the $\pi_9$ orbitals [31]. The fact that one or both of these bands were predominant in the UPS on the $SnS_2$ substrate suggests that the molecules were oriented on the surface at an angle where the electron density cross section normal to the sample surface was very high. In addition, this peak at 4.4 eV was initially present in the UPS for the first few molecular layers of pentacene on gold (up to about 50 Å) then becomes attenuated at higher coverage of pentacene. This supports the notion that the pentacene lies flat for several molecular layers before it starts forming polycrystallites.

The 4.4 eV peak is either very weak or not present in the UPS for thicker films on gold or stainless steel substrates where the molecules are oriented almost perpendicular to the surface. The $\pi_9$ peak at 2.65 eV is not present on the $SnS_2$ substrate indicating that the molecules are not oriented perpendicular to the surface, however, there is a peak at 2.25 eV. This peak can be attributed to the $\pi_{10}$ band that has one node parallel to, and three nodes perpendicular to the longitudinal direction of the pentacene molecule, and is at a lower binding energy molecular orbital than the $\pi_9$ orbital [31]. On the $SnS_2$ substrate, it can be assumed that the presence of the strong $\pi_5$ or $\pi_6$ band peak, the presence of the $\pi_{10}$ peak and the noticeable absence of the $\pi_9$ peak are due to the molecular tilt angle of pentacene likely being very low relative to the $SnS_2$ substrate.

To verify the presence of a rectifying junction of the pentacene/$SnS_2$ interface, and to help validate the energy level alignment measurement using UPS and XPS, current-voltage measurements were performed on sample devices. The I-V curves are shown in Fig. 5.16 where (A) and (B) are of the same 1000 Å thick film with the current is plotted on a linear and logarithmic scale respectively. A 200 Å thick film of pentacene on $SnS_2$ was also measured (Fig. 5.16.C). Forward bias where the pentacene side is biased positive. A simple diagram of the device is shown in Fig. 5.16.D. Each of the pentacene films was doped with low concentrations of bromine by placing the films in a

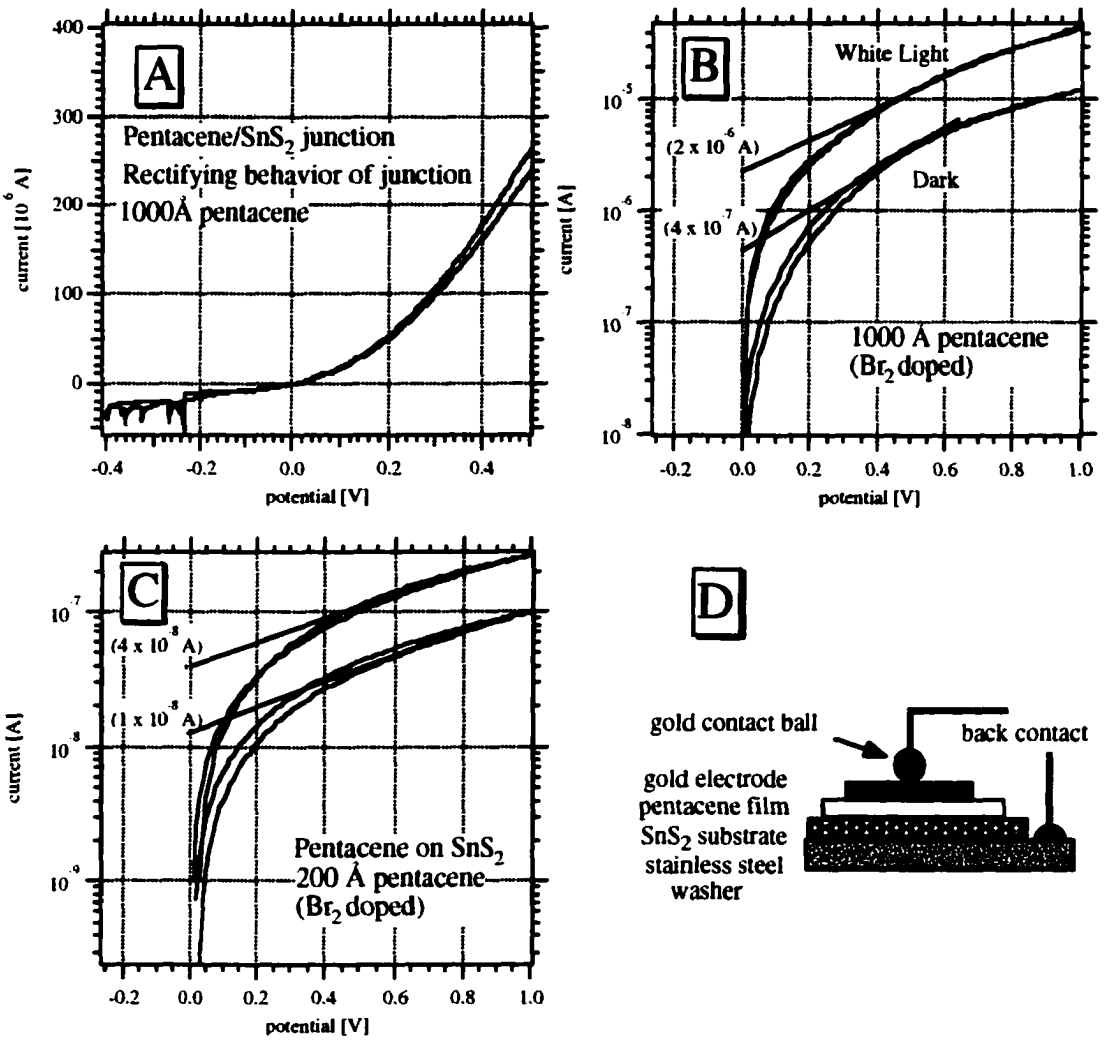


**Fig. 5.16.** Current-voltage curves for pentacene/$SnS_2$ heterojuction. A. I-V curve for 1000 Å film doped with $Br_2$. B. Log(I) vs. V for same sample as (A). C. Log(I) vs. V. for 200 Å doped pentacene film. D. Diagram of device used in I-V measurements.

10 mM solution of $Br_2$ in acetonitrile for several hours to make the pentacene films slightly more conductive to increase the feasibility of the measurements [5].

The first result of the I-V measurements, was the verification that the pentacene/$SnS_2$ interface is a rectifying junction (Fig. 5.16.A). Photoconductivity of the pentacene was also determined from the increase in the current when the sample was illuminated from a tungsten lamp, similar to what was observed in Ref. [34] where the photoconductivity of pentacene single crystals was measured under hydrostatic pressure. There was no detectable open circuit photovoltage for this interface. The deviations from exponential behavior in the I-V curves are likely attributed to recombination, carrier-carrier scattering effects, and possible Auger recombination in the pentacene film [35]. This makes fitting the curves for extrapolating to the value of the current density at zero voltage very difficult, but a rough fit can be made to estimate the barrier height for electron injection at the pentacene/$SnS_2$ heterojuction. Furthermore, the estimations of the barrier heights are based on the Richardson-Schottky equation even though the junction being measured is a p-n heterojunction. The measured barrier heights were between 0.76 and 0.80 eV for the 1000 Å pentacene film (Fig. 5.16.B) and 0.86-0.90 eV for the 200 Å pentacene film as seen in Fig. 5.16.C. These measurements were repeated multiple times on several samples each resulting in similar barrier heights ranging from 0.72-0.90 eV.

These barrier heights for electron injection constitutes just about half of the barrier height of 1.30-1.44 eV measured with the UPS and XPS. The key discrepancies between the two measurement techniques are that I-V measurements are not as accurate for p-n junctions as they are for Schottky contacts [36], and the fact that the measurements were done in air where oxidation could have affected the properties of the pentacene film. There is also the possibility of interference from interface states, recombination within the space charge region in the pentacene film [37]. Discrepancies could also be attributed to incorporation of the optical absorption gap into the electron injection barrier heights for the photoemission measurements whereas the I-V measurements are strictly based on the electronic barrier height. Finally, the standard models for Schottky contacts and p-n junctions as applied to conventional inorganic semiconductors may break down when organic based molecular solids are considered. As a result of these discrepancies, the barrier heights determined from the current versus voltage measurements are considered to be only rough approximations.

## 5.5. Summary

The energy level alignment for the pentacene/Au(111) and pentacene/$SnS_2$ interfaces were determined using a combined method of ultra-violet and x-ray photoelectron spectroscopy. The hole and electron injection barriers for the pentacene/Au(111) interface were determined to be 0.55 eV and –1.30 eV respectively,

while a relatively large interface dipole barrier of 0.95 eV was observed. On the pentacene/$SnS_2$ interface, the hole and electron injection barriers were −1.89 eV and −1.44 eV respectively, and there was a significantly smaller interface dipole magnitude of 0.26 eV. Polarization effects leading to changes in the final state screening environment contribute significantly to the core-level energy shifts, particularly for systems such as the gold/pentacene where the polarization energies of the two materials are significatnly different. Gradual core-level shifts over a longer range of the pentacene film thickness provide evidence of possible band bending contributions as well.

Detailed analysis of the UP-spectra signified distinct differences in the characteristics of the pentacene films on the two substrates and was attributed to the pentacene molecules being oriented perpendicular to the Au(111), and more parallel to the $SnS_2$ substrates. Further experiments were done to explore the morphological differences of the pentacene on the two substrates and relation to the interfacial energy characteristics. UHV STM images revealed ordering of the pentacene molecules lying flat on the Au(111) surface, and commensurate with the Au(111) lattice. AFM was used to investigate the thicker films revealing randomly oriented polycrystallites on the Au(111) surface and a lower surface roughness with oriented domains on the $SnS_2$.

Temperature programmed desorption spectra determined that the first monolayer of pentacene molecules are more strongly bound to the Au(111) surface than to each

other in the bulk pentacene. This helped establish a connection between stronger molecule substrate interactions and a larger interface dipole barrier.

The pentacene/$SnS_2$ interface was determined to be a rectifying junction from current-voltage measurements. The photoconductivity of pentacene was observed, and approximate electron injection barrier heights of 0.76-0.90 eV for were determined. Complexities in the pentacene film and the p-n junction lead to limitations in using electrical measurements for determining the interfacial barrier heights.

**Acknowledgements**

The authors thank C. Bloom for assistance with preparation of the heterojunction devices. R. Schlaf is acknowledged for helpful discussions. This work has been supported by the Department of Energy under contract DE-F603-96ER14625.

**References**


[1] J. H. Schön, S. Berg, C. Kloc, B. Batlogg, Science 287 (5455) (2000) 1022.

[2] Y.-L. Lin, D. J. Gundlach, S. F. Nelson, T. N. Jackson, IEEE trans. elect. devices 44 (8) (1997) 1325.

[3] J. G. Laquindanum, H. E. Katz, A. J. Lovinger, A. Dodabalapur, Chem. Mater. 8 (11) (1996) 2542.

[4] J. H. Schön, C. Kloc, B. Batlogg, Appl. Phys. Lett. 77 (16) (2000) 2473.

[5] J. H. Schön, C. Kloc, E. Bucher, B. Batlogg, Nature 403 (2000) 408.

[6] J. H. Schön, C. Kloc, R. A. Laudise, B. Batlogg, Phys. Rev. B 58 (19) (1998) 12952.

[7] J. H. Schön, C. Kloc, B. Batlogg, Science 288 (5475) (2000) 2338.

[8] M. Kasaya, H. Tabata, T. Kawai, Surf. Sci. 400 (1-3) (1998) 367.

[9] X. L. Chen, A. J. Lovinger, Z. Bao, J. Sapjeta, Chem. Mater. 13 (4) (2001) 1341.

[10] R. Schlaf, P. G. Schroeder, M. W. Nelson, B. A. Parkinson, P. A. Lee, K. W. Nebesny, N. R. Armstrong, J. Appl. Phys. 86 (3) (1999) 1499.

[11] R. Schlaf, C. D. Merritt, L. A. Crisafulli, Z. H. Kafafi, J. Appl. Phys. 86 (10) (1999) 5678.

[12] R. Schlaf, B. A. Parkinson, P. A. Lee, K. W. Nebesny, N. R. Armstrong, J. Phys. Chem. B 103 (15) (1999) 2984.

[13] R. Schlaf, P. G. Schroeder, M. W. Nelson, B. A. Parkinson, C. D. Merritt, L. A. Crisafulli, H. Murata, Z. H. Kafafi, Surf. Sci. 450 (2000) 142.

[14] P. G. Schroeder, M. W. Nelson, B. A. Parkinson, R. Schlaf, Surf. Sci. 459 (2000) 349.

[15] H. Ishii, K. Sugiyama, D. Yoahimura, E. Ito, Y. Ouchi, K. Seki, IEEE J. Sel. Top. Quant. Elec. 4 (1) (1998) 24.

[16] H. Ishii, H. Oji, E. Ito, N. Hayashi, D. Yoshimura, K. Seki, J. Lumines. 87-89 (2000) 61.

[17] I. G. Hill, A. J. Mäkinen, Z. H. Kafafi, Appl. Phys. Lett. 77 (12) (2000) 1825.

[18] S. Narioka, H. Ishii, D. Yoshimura, M. Sei, Y. Ouchi, K. Seki, S. Hasegawa, T. Miyazaki, Y. Harima, K. Yamashita, Appl. Phys. Lett. 67 (13) (1995) 1899.

[19] M. Pope, C. E. Swenberg, *Electronic Processes in Organic Crystals and Polymers* (Oxford University Press, Oxford, 1999).

[20] N. Sato, K. Seki, H. Inokuchi, J. Chem. Soc. Faraday Trans. 2 77 (1981) 1621.

[21] P. G. Schroeder, C. B. France, B. A. Parkinson, R. Schlaf, (to be published) .

[22] R. Schlaf, O. Lang, C. Pettenkofer, W. Jaegermann, J. Appl. Phys. 85 (5) (1999) 2732.

[23] J. H. Schön, C. Kloc, B. Batlogg, Phys. Rev. B 63 (12) (2001) 125304.

[24] C. Argile, G. E. Rhead, Surface Sci. Reports 10 (1989) 277.

[25] G. Kaindl, T.-C. Chiang, D. E. Eastman, F. J. Himpsel, Phys. Rev. Lett. 45 (22) (1980) 1808.

[26] E. Ito, H. Oji, N. Hayashi, H. Ishii, Y. Ouchi, K. Seki, Appl. Surf. Sci. 175-176 (2001) 407.

[27] G. Ertl, J. Küppers, *Low Energy Electrons and Surface Chemistry*, 2nd ed. (VCH Verlagsgesellschaft mbH, Weinheim, Ger., 1985).

[28] Y. Harada, H. Ozaki, K. Ohno, Phys. Rev. Lett. 52 (25) (1984) 2269.

[29] K. O. Lee, T. T. Gan, Chem. Phys. Lett. 51 (1) (1977) 120.

[30] Y. Kamura, K. Seki, H. Inokuchi, Chem. Phys. Lett. 30 (1) (1975) 35.

[31] H. Ozaki, J. Chem. Phys. 113 (15) (2000) 6361.

[32] R. B. Campbell, J. M. Robertson, J. Trotter, Acta. Cryst. 14 (1961) 705.

[33] R. Boschi, E. Clar, W. Schmidt, J. Chem. Phys. 60 (11) (1974) 4406.

[34] Z. Rang, A. Haraldsson, D. M. Kim, P. P. Ruden, M. I. Nathan, R. J. Chesterfield, C. D. Frisbie, Appl. Phys. Lett. 79 (17) (2001) 2731.

[35] S. M. Sze, *Physics of Semiconductor Devices*, 2nd ed. (John Wiley & Sons, 1981).

[36] A. G. Milnes, D. L. Feucht, *Heterojunctions and Metal-Semiconductor Junctions* (Academic Press, New York, 1972).

[37] R. Memming, *Semiconductor Electrochemistry* (Wiley-VCH, Weinheim, Germany, 2001).

## Concluding Remarks and Future Work:

We investigated the frontier orbital alignment of several model systems of organic semiconductor materials using x-ray and ultraviolet photoelectron spectroscopy (XPS, UPS) in combination. This method allowed for a more precise determination of the magnitudes of the electron and hole injection barriers as well as that of the interface dipole. The objective of using the model systems was to determine the validity of the measurement process and to further understand the fundamental behaviors of organic interfaces including the electronic structures and the morphology of the organic semiconductor materials. The layered materials $SnS_2$ and HOPG functioned as nearly ideal substrates that allowed for testing the validity of the measurement process as well as scrutinized investigations into interfacial dipoles, band bending, and final state screening effects. The gold substrate was chosen for its more practical use as an electrical contact material for organic thin film transistor devices, plus it also allowed for in depth studies on the energetics and morphology of metal/organic interfaces.

Table C.1 shows a summary of the energy level alignment measurements for each system completed in this work. The four measurements included in this table are those of

| | Hole injection barrier height (VB or $E_F$/ HOMO offset) | Electron injection barrier height (CB or $E_F$/LUMO offset) | Band bending or polarization energy shift in organic layer | Magnitude of interface dipole barrier (eD) |
|---|---|---|---|---|
| *p*-quaterphenyl/ $SnS_2$ | -0.84±0.04 eV | -3.09±0.05 eV | 0.28±0.05 eV | 0.22±0.07 eV |
| *p*-quaterphenyl/ HOPG | 1.94±0.04 eV | -2.49±0.05 eV | 0.05±0.05 eV | 0 |
| *p*-sexiphenyl/ $SnS_2$ | -1.27±0.04 eV | -2.92±0.05 eV | 0.21±0.05 eV | 0.15±0.07 eV |
| *p*-sexiphenyl/ HOPG | 1.37±0.04 eV | -2.43±0.05 eV | 0.06±0.05 eV | 0 |
| coronene/$SnS_2$ | -1.26±0.04 eV | -2.37±0.05 eV | 0.19±0.05 eV | 0.53±0.07 eV |
| coronene/ HOPG | 1.27±0.04 eV | -2.02±0.05 eV | 0 | 0 |
| pentacene/$SnS_2$ | -1.89±0.04 eV | -1.44±0.05 eV | 0.07±0.05 eV | 0.26±0.07 eV |
| pentacene/ Au(111) | 0.55±0.04 eV | -1.30±0.05 eV | 0.10±0.05 eV | 0.95±0.07 eV |

**Table C.1.** Summary of energy barriers for the systems studied in this research.

primary interest to understanding the device physics and the presented research. These include the electron and hole injection barriers, the electron core-level binding energy shift (that could be attributed to band bending changes in polarization energy) and the interface dipole barrier. One ultimate objective of these types of measurements would be to establish a universal link between the intrinsic properties of the organic semiconductor molecules such as ionization energy, electron affinity, HOMO-LUMO gap, or molecular polarizability and the magnitudes of each of the energy level offsets. This would however require measurements on a very large number of systems with many different

chemical properties. By comparing the work function values of the sample as measured with both the helium lamp and low intensity x-rays, we were able to successfully determine the overlayer-thickness dependent onset of sample charging. This allowed for the determination of the maximum film thickness where the junction offsets can be accurately measured without the interference of charging artifacts.

It still remains a challenge to completely separate band bending effects from final state screening shifts that are attributed to changing polarization energies between the substrate, the thin organic film, and the bulk organic film. However, results in this work conclude that changes in the final state screening environment does contribute significantly to the overall shifts in the orbital binding energies measured with XPS and UPS. There is also some evidence, specifically the more gradual shifts in the core-level binding energies as the organic semiconductor film thickness is increased, that band bending can occur at least to a small extent in organic semiconductors. It should be stated though, that little beyond speculation is known about intrinsic doping in the organic film required to support the band bending related space charge region.

Scanning tunneling microscopy studies of pentacene on the Au(111) surface revealed ordering of the pentecene molecules in striped parallel rows lying flat on and commensurate with the substrate. The four dominant unit cells observed were $(2 \times 2\sqrt{7})$, $(2 \times \sqrt{31})$, $(2 \times \sqrt{39})$, and $(2 \times 3\sqrt{3})$ with respect to the Au(111) lattice.

Comparison of the energy level offsets and the morphology of the pentacene films on the Au(111) and $SnS_2$ substrates demonstrated synergism between the orientation of the molecules at the interface and the magnitudes of the junction offsets, particularly the interface dipole barrier. There appeared to be a stronger molecule-substrate Coulomb interaction between the pentacene and the gold than the $SnS_2$ leading to the larger interface dipole of 0.95 eV versus 0.26 eV for the pentacene/$SnS_2$ interface.

Atomic force microscopy and temperature programmed desorption were used to further analyze the morphology and molecule-substrate binding energy of the pentacene systems. Pentacene was observed to initially lie flat on the gold surface then forms polycrystallites with the molecular orientation perpendicular to the gold surface for films approaching 1000 Å. Current-voltage measurements verified the rectifying behavior of the pentacene/$SnS_2$ heterojunction.

Organic semiconductor materials have similar energetics to conventional inorganic semiconductors, however they usually have significantly lower conductivity, either lack or have low intrinsic doping, yet have a wider range of molecular systems and morphologies. These yield distinct properties for devices made out of organic semiconductors and require unique characterization methods suitable for organic systems.

Future work regarding the energy level offsets and morphology of the interfaces regarding organic semiconductors could potentially lead in a number of possible directions. There has been significant work in the literature focused on the energy level

alignments for the interfaces relevant to organic light emitting devices (OLEDs). There still is room for band alignment measurements for OLED systems, particularly for the electron injection barrier using a chemically stable low work function cathode. However, the primary future directions for research in OLEDs require more of an engineering approach, particularly in the scaling up of device production.

There is significantly more room for expanded fundamental research in the thin film transistor materials. There has been limited research on the measurement of the injection barrier heights between organic thin film transistor materials and metal contacts. In this work, the pentacene/gold interface has been studied in some detail, but there are other organic semiconductors as well as potential contact materials. Polyacenes (including pentacene), thiophenes, phthalocyanines, and perylene deravatives are all examples of organic compounds that could potentially have interesting and useful electronic properties.

In addition, modifying the chemistry of the compounds by incorporating additional functional groups or various heteroatoms (such as sulfur or nitrogen) into the central moiety could alter the band gap, and the positions of the highest occupied and lowest unoccupied molecular orbitals. This provides a useful tool for "tuning" the electron and hole injection barrier heights at the interfaces. In addition to the interfaces between the organic semiconductors and the metal contacts, it is recommended that energy level alignment measurements be investigated for heterojuctions between two

different organic semiconductors. Research on organic based solar energy conversion devices or other heterojunction devices demands detailed measurement of the energy level offsets and a more thorough understanding of the morphology at the interface between the two materials.

It is still questionable whether the more subtle shifts extending into the bulk of the organic materials are band bending related or are attributed to changing of the final-state-screening environment. For the purposes of establishing a basic measurement of the energy level alignment, it is not necessary to build up the organic layers in as many steps as was done in this work. Generally several steps to build up the first several molecular layers is necessary to determine the magnitude of the interface dipole barrier. This would be followed by one or two measurements at larger thickness (greater than 100 Å) to determine the position of the highest occupied molecular orbital of the organic overlayer.

Little is understood about the relation between the morphology of the organic material and the energetic properties of the interface, particularly the interface dipole. While most of the energy level offsets are expected to be primarily dependent on the properties of the bulk constituents at the interface, the interface dipole appears to have a strong dependence on the molecule-substrate interaction and the orientation of the molecules with respect to the substrate. For the next series of experiments, it is recommended that the research is focused on the energy and morphology characteristics of thin films (sub-monolayer to several molecular layers) of organic semiconductors on

metal surfaces. The objectives of this would be a continuation of the investigations of the pentacene on gold followed by expanding to other systems. These experiments should primarily involve determining the morphology of the thin films, at varying thicknesses, using scanning tunneling microscopy. To supplement the scanning probe microscopy work, an estimate of the energy level offsets and the magnitude of the interface dipole barrier can be determined using a "simplified" band lineup measurement as described above. Temperature programmed desorption (TPD) and possibly low energy electron diffraction (LEED) can be used to provide additional insight into the binding energies and long range ordering, respectively, of molecules on a surface.

## Appendix A: Temperature Programmed Desorption

One method of measuring the binding energy between a molecule and a substrate is temperature programmed desorption (TPD). TPD is a widely used technique in surface science to determine surface reaction products and binding energies [1-3]. The premise of TPD is to heat up the sample surface while monitoring the quantity of the products vaporizing off using a mass spectrometer. In our experiments, TPD is used for the purposes of determining the binding energies of small molecule organics to the substrate usually metal in these experiments. From these measurements, clues as to whether the molecules are only physisorbed with van der Waals forces, or whether other forces such as electrostatic (Coulomb) forces or covalent bonding are playing a role in the binding of the first molecular layer to the substrate.

The experimental setup for TPD in our laboratory is depicted in Figure A.1. The sample is mounted on a sample manipulator in an ultrahigh vacuum (UHV) chamber. The substrate temperature is monitored with an infrared thermopile detector through a ZnSe window that is mounted on the UHV chamber. The purpose to using the IR thermometer as opposed to a thermocouple is to establish a more accurate reading of the

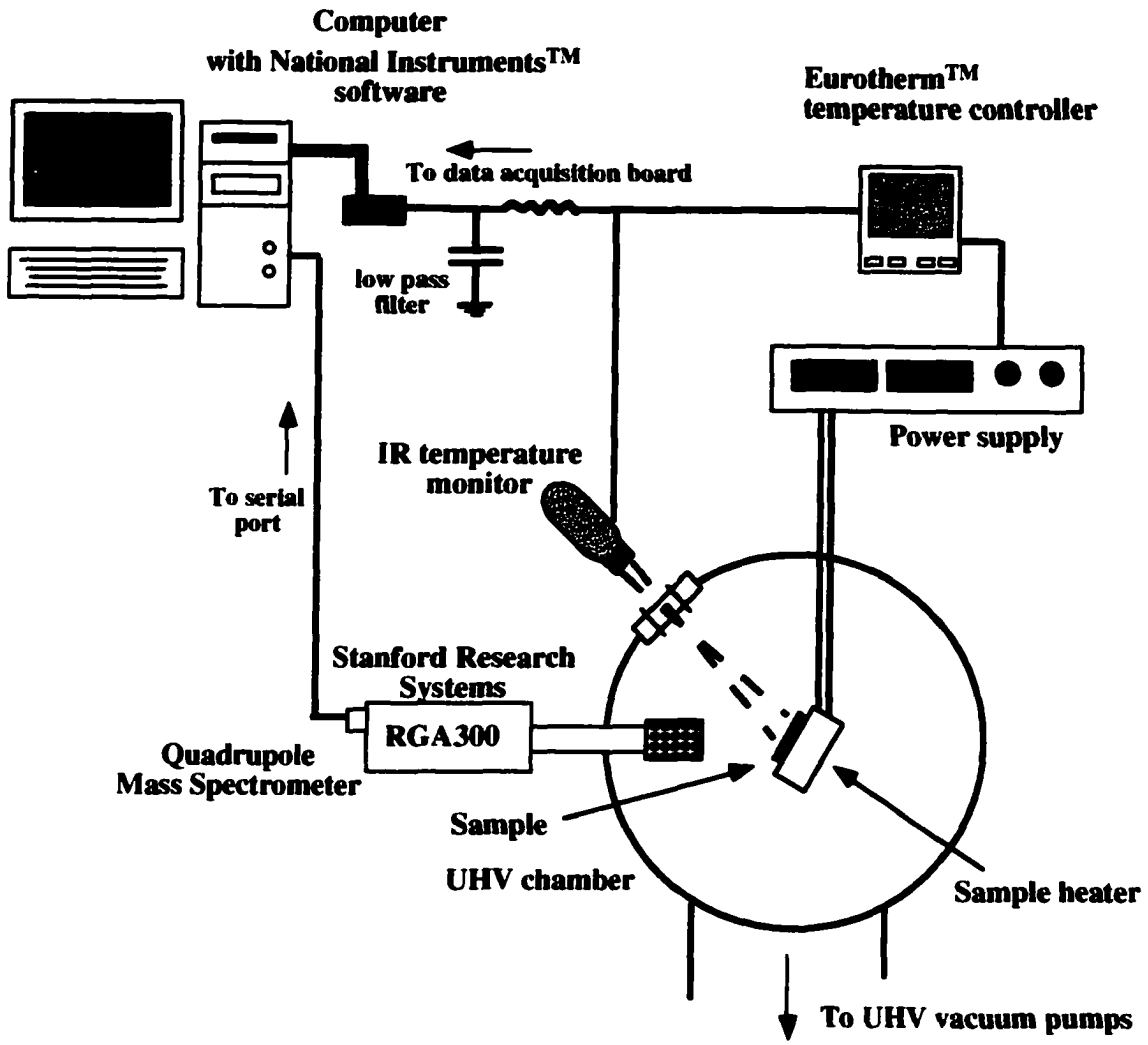


**Fig. A.1** Experimental setup for temperature programmed desorption.

temperature of the actual sample surface, whereas the thermocouple is attached to the sample manipulator approximately 1 cm away from the sample itself [4,5]. A voltage signal output from the IR thermometer is split and sent to both the computer for data recording, and to the Eurotherm® temperature controller. The signal to the computer is

sent through a low-pass filter to null out the high frequency noise ($f \geq 6$ Hz) which was prevalent in the data acquisition software. The Eurotherm® controls the output of the power supply to keep the temperature ramp rate constant. Typical ramp rates used in our experiments vary between 10 and 25 °C/min. As the organic film vaporizes off, the residual gas analyzer; Stanford Research Systems RGA300 quadrupole mass spectrometer consistently monitors a selected mass-to-charge ratio (m/z) position. Since the molecules being vaporized off the surface usually have a neutral charge (at least in the case of the experiments in this work), an ionizing filament is placed in front of the spectrometer head. The selected m/z position may be a parent peak of a molecule or a particular fragment that is predominant in the mass spectrum of that molecule. The mass spectrometer signal is sent to the computer where the intensity of the selected m/z is plotted as a function of the recorded temperature.

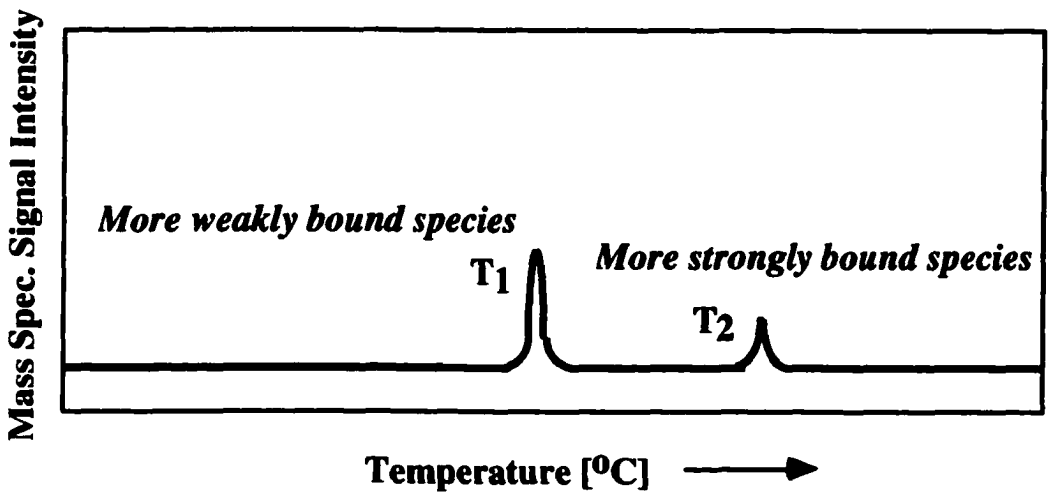


**Fig. A.2** Generic TPD spectrum where the same chemical species is physically or chemically bound to the surface in two distinct forms and energies.

A generic TPD spectrum is shown in Fig. A.2. The center peak position reflects the mean vaporization temperature for a particular molecule or fragment in a specific chemical or physical environment. Multiple peaks in a TPD spectrum reflect the presence of more than one type of binding environment for that chemical species. The peak temperature as well as the temperature ramp rate are then fit into an algorithm such as the Redhead formula (A.1) to determine the binding energy (BE) in Joules [1].

$$BE = N_A kT\left[\ln\left(\frac{Tv}{\alpha}\right) - 3.64\right] \qquad \text{(A.1)}$$

The temperature T is in Kelvin, $N_A$ is Avogadro's number, k is the Boltzman constant, v is a vibrational constant equal to $1 \times 10^{13}$, and $\alpha$ is the temperature ramp rate expressed in °C/second.

**References:**


[1] P. A. Redhead, Vacuum 12 (1962) 203.

[2] C. G. Wiegenstein, K. H. Schulz, J. Scott, Rev. Sci. Instrum. 69 (10) (1998) 3707.

[3] B. R. Chalamala, D. Uebelhoer, R. H. Reuss, Rev. Sci. Instrum. 71 (1) (2000) 320.

[4] M. A. Khan, C. Allemand, T. W. Eager, Rev. Sci. Instrum. 62 (2) (1991) 392.

[5] M. Hoch, Rev. Sci. Instrum. 63 (9) (1992) 4205.

# Appendix B: Hybrid Materials Research Proposal

## Modification of the Organic Moieties in Organic-Inorganic Hybrid Materials to Increase the Conductivity of Thin Film Transistors

**A Proposal Submitted as a Degree Requirement for Chemistry Doctoral Work at Colorado State University**

Paul G. Schroeder
Department of Chemistry
Colorado State University
Fort Collins, CO 80523

**Abstract**

Electronic thin film materials consisting of an organic-inorganic hybrid system provides the potential of combining the ease of processability of organic materials with the superior conductivity of inorganic semiconductors. A hybrid system based on the layered two-dimensional (2D) perovskite structure has been shown to exhibit some unique and interesting electrical properties. A comprehensive research plan is described to systematically vary the organic components, synthesize and cast films of the hybrid material, and determine the structural, chemical, and physical properties of these films. The primary objectives are to establish a relation between the chemistry of the organic components and the facilitation of film self-assembly, as well as determine a method to improve the electrical conductivity of the material. X-ray diffraction and Atomic Force Microscopy will be used to characterize the bulk and surface structures of the films. Current-voltage and Hall measurements will be performed to determine the electrical properties.

**Background**

New applications for field effect transistors (FET's) as an alternative to high speed, but relatively expensive, conventional crystalline silicon FET's have led to intense research in a variety of organic, inorganic and polymer systems. Conjugated organic small molecules, oligomers, and polymers have been investigated extensively since they can be easily fabricated into thin film field effect transistors by evaporation[1], dip coating, ink-jet printing [2,3] or spin coating[4-6]. These systems are limited by their relatively low conductivity, with carrier mobilities usually below 0.1 $cm^2/V{\cdot}s$[7-9], whereas conventional doped silicon has a mobility upwards of 1000 $cm^2/V{\cdot}s$[10]. The inorganic semiconductors' advantage of greater conductivity is often offset by complex and expensive fabrication processes.

Hybrid materials, which consist of both organic and inorganic moieties, have the advantage of combining the simple fabrication processes available for organic systems with the higher conductivity of the inorganic semiconductors. A promising class of hybrid materials, are those with a perovskite structure $ABX_3$ (Fig. B.1) where $A^+$ is an organic cation such as methylammonium, and $BX_3^-$ is an inorganic metal halide anion such as $SnI_3^-$[11]. Inorganic perovskite ($M^{II}M^{IV}X_3$) structures as well as some inorganic-organic hybrid perovskites have been studied for many decades, although most have limited potential for electronic applications. A perovskite structure material with $A_2BX_4$ stoichiometry can form a two-dimensional (2D) structure that stacks into a 3D film with

alternating layers of organic and inorganic components as shown in Figure B.2 [12-14]. Kagen and coworkers at IBM developed a hybrid thin film transistor based on this 2D layering using phenethylammonium cations and tin tetraiodide dianions, $(C_6H_5C_2H_4NH_3)_2SnI_4$. The electron mobility of 0.55 $cm^2/V{\cdot}s$ at a gap voltage of 50 V, which is comparable to that of single crystal pentacene[15].

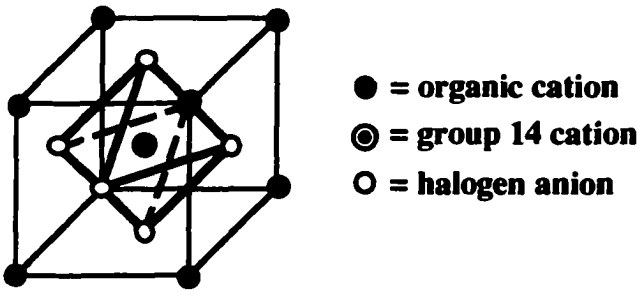


**Fig. B.1** Perovskite structure of inorganic-organic hybrid.

An example of the synthesis of these films utilizes $SnI_2$ and the organic salt $C_6H_5C_2H_4NH_2{\cdot}HI$ in concentrated aqueous HI at 90°C under $N_2$ [15]. The precipitated $(C_6H_5C_2H_4NH_3)_2SnI_4$ crystals were filtered, dried, redissolved, filtered again, and spin coated into films [16]. The organic component facilitates the self-assembly of these materials into an extended framework thin film with alternating layers of the organic moieties and the inorganic component. The extended inorganic component results in conducting channels in the hybrid film if a conducting inorganic metal halide is used. There have been some investigations using different inorganic moieties in these hybrid films such as a transition metal, group 14, or rare earth metal halide [11]. Some of the

group 14 metal halides, particularly $SnI_4^{2-}$ have shown potential for forming electrically conducting hybrid FET's [12-14]. The $SnI_4^{2-}$ will be the inorganic component used for most of the hybrid films in this research, although other metal halide compounds such as $PbI_4^-$, $GeI_4^-$, or $EuI_4^-$ will also be tested [17].

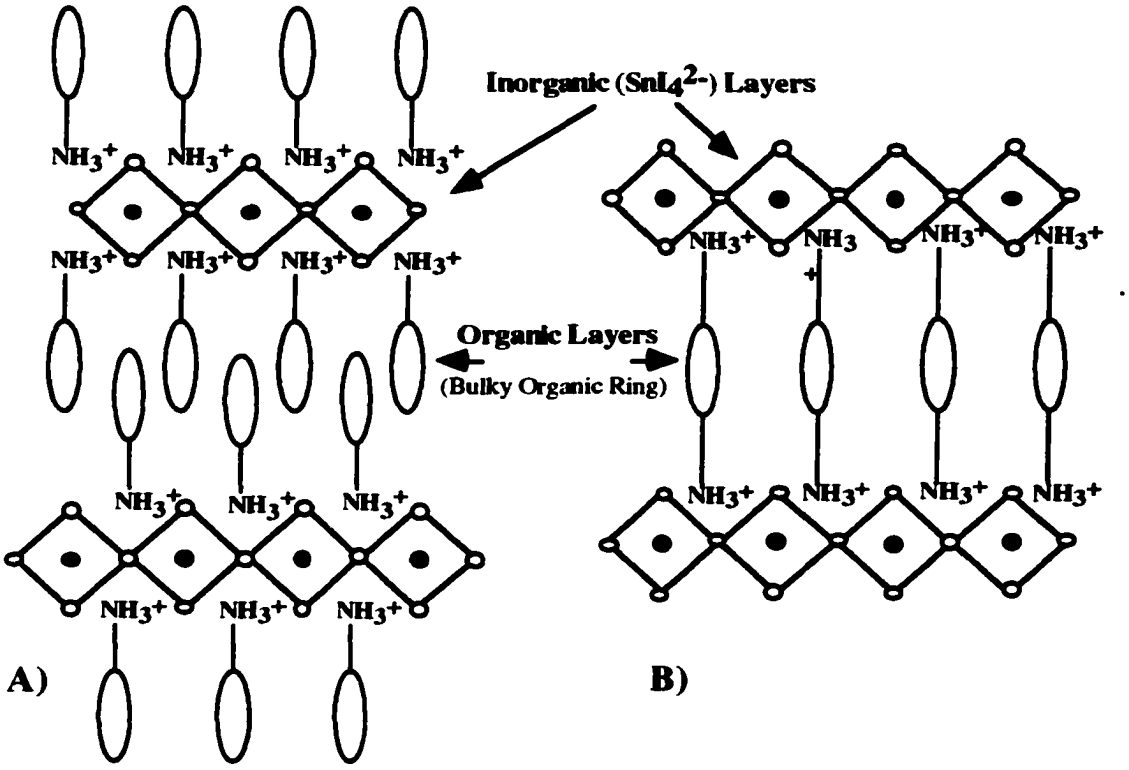


**Fig. B.2.** Schematic of a layered inorganic-organic perovskite film. The inorganic anions are charge-balanced by the organic ammonium cations. A) The stoichiometry is $A_2BX_4$ and is shown with the organic components interdigitated and the inorganic components staggered between adjacent layers. B) The diammonium organic cation has a $2^+$ charge yielding $ABX_4$ stoichiometry.

**Modification of the Organic Components**

The primary objective in this research proposal is to vary the chemistry of the organic component to explore the relationship between the organic component and the electronic properties of the hybrid film. There are three principle characteristics of interest for thin-film-transistor device applications. These are; 1) enhancing the self-assembly of the hybrid material to give a more extended and mechanically stronger film, 2) increasing the overall conductivity of the hybrid thin film, and 3) chemically tuning the electron energy levels. The hypothesis is that facilitation of self-assembly of the film will provide an extended ordered inorganic layer that will directly enhance the conductivity. If films made of the organic-inorganic hybrids are to be feasible for practical use, the carrier mobilities need to be increased to well over 1 $cm^2/V \cdot s$ [8]. Therefore, research will be focused on the mechanisms of self-assembly of the inorganic-organic hybrid films. In addition to creating more ordered films, the polarity of the organic moieties will also perturb the electron density and energy levels of the adjacent inorganic moieties, which may also lead to increases in conductivity. Modifying the organic component in the hybrid film will provide a means to control or tune the electron/hole energy levels. When cast into a thin film, the organic component forms adjacent to the substrate[15], which means that the polarity of the organic component can influence the injection barrier for carriers and the onset voltage at this interface [18-20]. Controlling, or more specifically lowering, the magnitude of the injection barrier between

the drain/source electrodes and the inorganic-organic hybrid material (Fig. B.3, inset) will lower the onset voltage and improve the switching behavior in FETs.

Previous research in organic-inorganic hybrid layered materials has included small organo-amines such as alkylammonium $(CH_3(CH_2)_nNH_3^+)_2PbI_4$ [12,21-23] and phenethylammonium $(C_6H_5C_2H_4NH_3^+)_2SnI_4$ [14,15,22]. There have been few studies involving other classes of organic components for use in the semiconducting films. The purpose of this project is to investigate a diverse group of organic molecules with different dipole moments, chemical functional groups, and/or hydrogen bonding capabilities. Through a series of instrumental techniques, which will be discussed below, the structural, chemical, and electronic characteristics of the material will be analyzed to elucidate the dependence of the organic component on the functionality of the hybrid thin films.

Table B.1 shows a representative, though not exhaustive, list of a few potential organic components that will be tested. The proposed organic compounds all consist of at least one amine group, which protonates to form an ammonium ion under the acidic conditions used when synthesizing the hybrid materials. Some critical factors that must be considered when determining which organic compounds to use are size, shape, and the attached functional groups [11]. The organic component must be small enough to fit into the lattice site of the unit cell for the perovskite structure. This means that the molecular

## Table 1 Proposed Organic Components

| Organic Compound | Self-Assembly Interactions | Approximate Molecular Dimensions 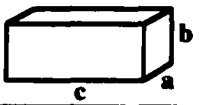 |
|---|---|---|
|  X = F,Cl,Br,I,OH,CN | van der Waals dipole-dipole | a = 5.0 Å<br>b = 5.0 Å<br>c = 5.3 - 6.4Å |
|  X = F,Cl,Br,I,OH,CN | van der Waals dipole-dipole | a = 5.0 Å<br>b = 5.0 Å<br>c = 6.3 - 6.9 Å |
| 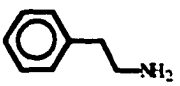 | van der Waals π-orbital stacking | a = 5.0 Å<br>b = 6.4 Å<br>c = 9.0 Å |
| 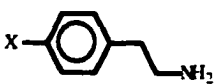 X = F,Cl,Br,I,OH,CN | van der Waals π-orbital stacking dipole-dipole | a = 5.0 Å<br>b = 6.4 Å<br>c = 9.3 - 11.8 Å |
| 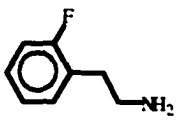 | van der Waals π-orbital stacking dipole-dipole | a = 5.0 Å<br>b = 6.7 Å<br>c = 9.0 Å |
| $H_2N(CH_2)_nNH_2$ (n = 1-8) | van der Waals ionic bonding (diammonium) | a = 5.1 Å<br>b = 5.0 Å<br>c = 3.9 - 9.3 Å |
| 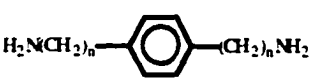 (n = 1-3) | ionic-bonding (diammonium) π-orbital stacking | a = 5.0 Å<br>b = 6.4 Å<br>c = 10.2 - 15.9 Å |
| 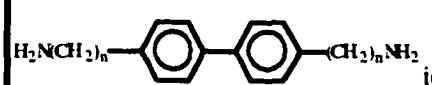 (n = 1-3) | ionic-bonding (diammonium) π-orbital stacking | a = 5.0 Å<br>b = 6.4 Å<br>c = 14.4 - 20.1 Å |
| 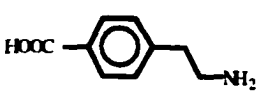 | hydrogen bonding π-orbital stacking | a = 5.0 Å<br>b = 6.4 Å<br>c = 11.2 Å |
| 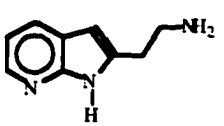 | hydrogen bonding π-orbital stacking | a = 5.0 Å<br>b = 7.1 Å<br>c = 9.8 Å |

width (a) and height (b) of the organic component must be within the range of the perovskite lattice constants in order for the structure to be formed. This essentially means that the a and b dimensions of the organic molecule must each be less than 5.6-8.6 Å, depending on the halide used in the inorganic component [24]. The c dimension, or the length of the molecule, is not as critical, however it needs to be relatively linear and rigid. Rod-like organic components are generally needed but be relatively long (40Å or more is feasible). The octahedral coordinated metal halide may exhibit some Jahn-Teller distortion enabling a limited degree of flexibility in the molecular shape. Since the geometric constraints are so critical to maintaining the perovskite structure, the molecular dimensions (to the nearest 0.1Å) are included for each of the proposed molecules in Table B.1. Some organic components will interdigitate between adjacent layers if it is geometrically and energetically favorable to do so. The organic components will otherwise arrange themselves with the organic head groups adjacent to each other. An important objective of this research is to distinguish the organic components that will interdigitate from those that will stack head to head. A primary aspect of the proposed research is to establish the effects of the intermolecular interactions, including interdigitiation, between organic components have on the mechanical strength of the hybrid film. Molecular modeling programs will be used to screen possible organic molecules and test how they will geometrically fit into the perovskite crystal structure.

The molecular models will also be used to study the intermolecular interactions between adjacent organic components.

Several specific types of chemical modifications to the organic components will be investigated. The first study will be to change the type and positions of functional groups on the organic cation [25]. For example, placing fluorine in the ortho- or meta-positions on a phenethylammonium will increase the dipole-dipole interactions between the different organic groups enhancing the stabilization of the self-assembled film. Halides or other functional groups influence the dipole moment of the organic cation. The effect of the dipole moment of the organic moieties, on both the self-assembly process and the positions of the electronic energy levels, will be the subject of detailed investigation in this research.

Another study involves attaching ammonium groups to each end of the organic moiety. The double cation changes the stoichiometry of the hybrid film to $ABX_4$ allowing just one organic moiety to have an ionic bond two inorganic anions in alternate layers as shown in Fig. B.2b. Attaching two ammonium groups to the organic components to strengthen the hybrid films has been the subject of some limited studies [26,27] although not with the conducting films. To accommodate the diammonium organic cations, the perovskite lattice structure of the films will stack with the metal halides "eclipsed" (Fig. B.2b) rather than "staggered" relative to each other as depicted in Fig. B.2a where monovalent cations are used [11].

Using organic compounds that have the potential of hydrogen bonding with adjacent organic compounds, could also facilitate self-assembly. Two proposed ways of accomplishing this are 1) attaching hydrogen-bonding functional groups such as a carboxylic acid to a phenylalkylammonium [28], or 2) using aromatic hydrogen-bond donor-acceptor complexes, each of which can form hydrogen-bonded bridges to adjacent organic moieties. Hydrogen bonded complexes such as 7-azaindole have been utilized in molecular self-assembly to strengthen films [29], although this has not been applied to inorganic-organic hybrids. The facilitation of self-assembly may not be effective for all of the currently proposed molecules since the orientations of adjacent organic molecules is critical for hydrogen-bonding to occur. The molecular geometry required for both ionic bonding to the inorganic sheets and hydrogen-bonding to adjacent organic moieties may not be compatible. This could, in fact, hinder the stabilization of a self-assembled film or prevent the formation of a perovskite crystal structure. As stated above, Table B.1 is just a representative list of the proposed molecules and extensive modification from the proposed organic compounds may be necessary to achieve the objective of creating more conducting films.

Structural characterization will primarily be conducted using thin film x-ray diffraction (XRD) to determine the bulk crystal structure of those hybrid materials that are cast into films. Atomic force microscopy (AFM) will be used to measure the surface topography and the domain sizes of the crystallized inorganic-organic hybrid

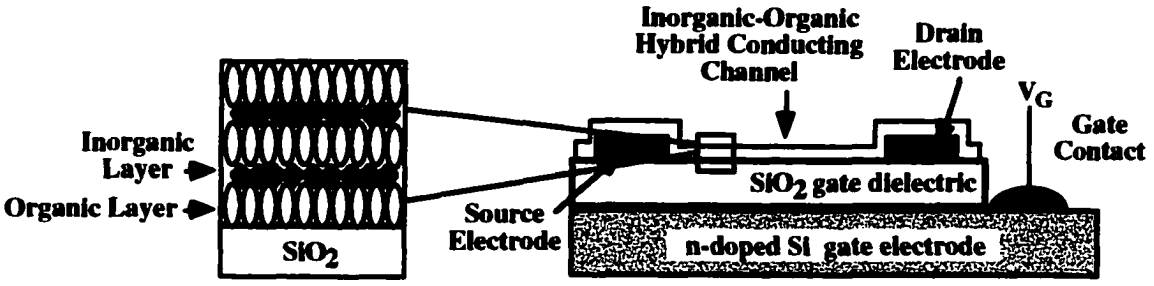


**Fig. B.3.** Schematic of a Field Effect Transistor (FET) using an inorganic-organic hybrid material as the conducting channel. The inset shows the molecular alignment of the hybrid film on the surface of the device.

film. This is critical for determining the efficiency of the self-assembly mechanism for each of the different compounds since AFM can easily be used to resolve grain boundaries in the film. Chemical analysis of the films will be performed using x-ray photoelectron spectroscopy (XPS).

The ultimate purpose of varying the organic component of the hybrid materials is to improve the electrical conductivity of thin film FET devices made with inorganic-organic hybrid films. To determine the electrical characteristics, thin films of the hybrid will be incorporated into a FET device as shown in Fig. B.3. The highly doped silicon substrate will serve as the gate electrode with $SiO_2$ as the gate dielectric. For the source and drain electrodes, a high work function metal such as gold will be evaporated onto the substrate, through a mask, prior to coating of the hybrid film. A commercial potentiostat will be used for probing the current-voltage behavior of the devices. Hall measurements will also be performed on films of the hybrid materials to obtain the carrier densities and mobilities.

The onset voltage of the FET will be determined from the current-voltage measurements. A reduced onset voltage indicates improved matching of the carrier injection barriers between the source/drain electrodes and the hybrid film. The polarity of the organic compounds in the hybrid films will be systematically varied to change the dipole at the interface to effectively "tune" the injection barriers for the mobile carriers. By establishing a relationship between dipole moment of the organic components used and the onset voltage of the FET, new organic molecules can be designed to further improve the performance of inorganic-organic hybrid FETs.

The potential optical [30-33] and magnetic [34-36] properties of these inorganic-organic hybrid films are outside the realm of the primary objectives of the proposed research, so discussion of the emphasis of these properties will be limited. It is essential that the optical and magnetic properties be investigated because there are many organic and inorganic components that have yet to be applied to perovskite structure hybrids. Use of novel components in these films could lead to interesting results and potentially useful materials.

The emerging organic-inorganic hybrid semiconducting materials have the strong potential of yielding devices with mobilities substantially higher than those of pure organic compounds. Thin film FETs made with inorganic-organic hybrids may be competitive with conventional inorganic semiconductors in some applications and could be used for new types of electronic devices.

**References:**


[1] Z. Bao, A. J. Lovinger, A. Dodabalapur, "Organic field-effect transisotrs with high mobility based on copper phthalocyanine", *Appl. Phys. Lett.*, **69**, 3066 (1996).

[2] T. R. Hebner, C. C. Wu, D. Marcy, M. H. Lu, J. C. Sturm, "Ink-jet printing of doped polymers for organic light emitting devices", *Appl. Phys. Lett.*, **72**, 519 (1998).

[3] F. Garnier, R. Hajlaoui, A. Yassar, P. Srivastava, "All-polymer field-effect transistor realized by printing techniques", *Science*, **265**, 1684 (1994).

[4] A. Dodabalapur, Z. Bao, A. Makhija, J. G. Laquindanum, V. R. Raju, Y. Feng, H. E. Katz, J. Rogers, "Organic smart pixels", *Appl. Phys. Lett.*, **73**, 142 (1998).

[5] A. R. Brown, A. Pomp, C. M. Hart, D. M. de Leeuw, "Logic gates made from polymer transistors and their use in ring oscillators", *Science*, **270**, 972 (1995).

[6] H. Sirringhaus, N. Tessler, R. H. Friend, "Intergrated optoelectronic devices based on conjugated polymers", *Science*, **280**, 1741 (1998).

[7] J. G. Laquindanum, H. E. Katz, A. J. Lovinger, A. Dodabalapur, "Morphological origin of high mobility in pentacene thin-film transistors", *Chem. Mater.*, **8**, 2542 (1996).

[8] H. E. Katz, Z. Bao, "The physical chemistry of organic field-effect transistors", *J. Phys. Chem. B*, **104**, 671 (2000).

[9] A. Dodabalapur, L. Torsi, H. E. Katz, "Organic transistors: Two-dimensional transport and improved electrical characteristics", *Science*, **268**, 270 (1995).

[10] S. M. Sze, *Physics of Semiconductor Devices*, 2nd ed. (John Wiley & Sons, 1981).

[11] D. B. Mitzi, in *Progress in Inorganic Chemistry*; *Vol. 48*, edited by K. D. Karlin (John Wiley & Sons, Inc., New York, 1999), p. 1.

[12] D. B. Mitzi, C. A. Feild, W. T. A. Harrison, A. M. Guloy, "Conducting tin halides with a layered organic-based perovskite structure", *Nature*, **369**, 467 (1994).

[13] D. B. Mitzi, S. Wang, C. A. Feild, C. A. Chess, A. M. Guloy, "Conducting layered organic-inorganic halides containing <110>-oriented perovskite sheets", *Science*, **267**, 1473 (1995).

[14] G. C. Papavassiliou, I. B. Koutselas, A. Terzis, M.-H. Whangbo, "Structural and electronic properties of the natural quantum-well system $(C_6H_5CH_2CH_2NH_3)_2SnI_4$", *Sol. State Comm.*, **91**, 695 (1994).

[15] C. R. Kagan, D. B. Mitzi, C. D. Dimitrakopoulos, "Organic-Inorganic hybrid materials as semiconducting channels in thin-film field-effect transistors", *Science*, **286**, 945 (1999).

[16] This is the procedure for synthesizing the phenethylammonium tin iodide film as given in Kagan et. al. (Ref. 15). Variations on this procedure are necessary depending on the organic and inorganic reagents used. Typically the hybrid material is created under acidic conditions using HCl, HBr, or HI keeping the halide consistent with that of the inorganic anion. To prevent oxidation, it is critical that the compounds are synthesized and the films are formed under inert ($N_2$) atomosphere.

[17] To date, the tin iodide is the only known anion to have promising high conductivity. Hybrids containing other inorganic anions may not be suitable for field effect transistors, but still may be applicable for their optical or magnetic properties. D.B. Mitzi, Progress in Inorg. Chem., Vol. 48. pp. 1-123 (1999).

[18] R. Cohen, N. Zenou, D. Cahen, S. Yitzchaik, "Molecular electronic tuning of Si surfaces", *Chem. Phys. Lett.*, **279**, 270 (1997).

[19] R. Cohen, L. Kronik, A. Shanzer, D. Cahen, A. Liu, Y. Rosenwaks, J. K. Lorenz, A. B. Ellis, "Molecular control over semiconductor surface electronic properties: Dicarboxylic acids on CdTe, CdSe, GaAs, and InP", *J. Am. Chem. Soc.*, **121**, 10545 (1999).

[20] R. Cohen, L. Kronik, A. Vilan, A. Shanzer, D. Cahen, "Frontier orbital model of semiconductor surface passivation: Dicarboxylic acids on n- and p-GaAs", *Adv. Mater.*, **12**, 33 (2000).

[21] D. B. Mitzi, K. Liang, "Preparation and properties of $(C_4H_9NH_3)_2EuI_4$: A Luminescent Organic-Inorganic Perovskite with a divalent rare-earth metal halide framework", *Chem. Mater.*, **9**, 2990 (1997).

[22] K. Liang, D. B. Mitzi, M. T. Prikas, "Synthesis and characterization of organic-inorganic perovskite thin films prepared using a versatile two-step dipping technique", *Chem. Mater.*, **10**, 304 (1998).

[23] D. B. Mitzi, M. T. Prikas, K. Chondroudis, "Thin film deposition of organic-inorganic hybrid materials using a single source thermal ablation technique", *Chem. Mater.*, **11**, 542 (1999).

[24] A. Poglitsch, D. Weber, "Dynamic disorder in methylammoniumtrihalogenoplumbates(II) observed by millimeter-wave spectroscopy", *J. Chem. Phys.*, **87**, 6373 (1987).

[25] Some of the proposed organic molecules are commercially available, and will require only a purification procedure prior to use. Others will have to be synthesized to give relatively pure yields of the compound with both the amine and the desired functional group(s). This can be accomplished through selective synthetic processes such as the Schmidt rearrangement or orientation controlled electrophilic aromatic substitution.

[26] J. K. Garland, K. Emerson, M. R. Pressprich, "Structures of four- and five- carbon alyldiammonium tetrachlorocuprate(II) and tetrabromocuprate(II) salts", *Acta Cryst.*, **C46**, 1603 (1990).

[27] K. Halvorson, R. D. Willett, "Structures of ethylenediammonium tetrabromocuprate(II) and propylenediammonium tetrabromocuprate(II)", *Acta Cryst.*, **C44**, 2071 (1988).

[28] Certain functional groups on the organic moieties may create competing reactions with the synthesis of the hybrid material. For example, the carboxylic acid in the para position relative to the ethylammonium could create a tendency to form a polypeptide. This, or other side reactions, can be prevented by adjusting the reaction conditions accordingly (e.g. keep the organic compound under acidic conditions).

[29] T. Koyama, A. Wakisaka, "Molecular self-assembly composed of aromatic hydrogen-bond donor-acceptor complexes", *J. Chem. Soc., Faraday Trans.*, **93**, 3813 (1997).

[30] X. Hong, T. Ishihara, A. V. Nurmikko, "Photoconductivity and electroluminescence in lead iodide based natural quantum well structures", *Sol. State. Comm.*, **84**, 657 (1992).

[31] C. Xu, H. Sakakura, T. Kondo, S. Takeyama, N. Miura, Y. Takahashi, K. Kumata, R. Ito, "Magneto-optical effects of excitons in $(C_{10}H_{21}NH_3)_2PbI_4$ under high magnetic fields up to 40 T", *Sol. State Comm.*, **79**, 249 (1991).

[32] M. Era, K. Maeda, T. Tsutsui, "Enhanced phosphorescence from naphthalene-chromophore incorporated into lead bromide-based layered perovskite having organic-inorganic superlattice structure", *Chem. Phys. Lett.*, **296**, 417 (1998).

[33] T. Ishihara, X. Hong, J. Ding, A. V. Nurmikko, "Dielectric confinement effect for exciton and biexciton states in PbI4-based two-dimenstional semiconductor structures", *Surf. Sci.*, **267**, 323 (1992).

[34] G. S. Long, M. Wei, R. D. Willett, "Crystal strucutres and magnetic properties of a novel layer perovskite system: (3-picoliniumylammonium)$CuX_4$ (X=Cl, Br)", *Inorg. Chem.*, **36**, 3102 (1997).

[35] J. R. Long, D. N. Haines, J. E. Drumheller, "Magnetic tricritical behavior of ethylammonium tetrachlorocuprate", *J. Appl. Phys.*, **8**, 3031 (1988).

[36] P. Zhou, J. E. Dumheller, B. Patyal, R. D. Willett, "Magnetic properties and critical behavior of quasi-two-dimensional systems $[C_6H_5(CH_2)_nNH_3]_2CuBr_4$ with n=1,2, and 3", *Phys. Rev. B*, **45**, 12365 (1992).